INTERLAMINAR DELAMINATION IN UNIDIRECTIONAL CARBON EPOXY COMPOSITES INDUCED BY STATIC AND FATIGUE LOADING

by

A.K. El-Senussi

Department of Aeronautical Engineering
University of Bristol

Thesis submitted for the Degree of Ph.D.

September 1986

In the name of Allah, the Beneficent, the Merciful.

. Who teacheth by the pen,
. Teacheth man that which he knew not.

KORAN

MEMORANDUM

The work contained in this thesis is the original work of the author, except where stated otherwise in the text. It has not been submitted for any other degree to any other University or examining body.

Signed 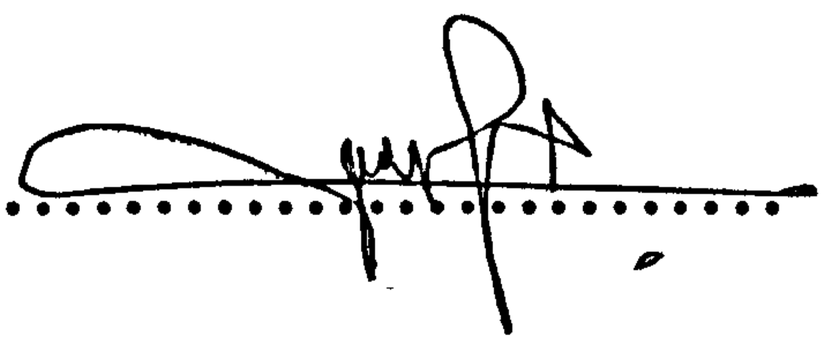

Abdelrasol K. El-Senussi

ACKNOWLEDGEMENTS

The work was carried out under the supervision of Dr. J.P.H. Webber of the Department of Aeronautical Engineering, University of Bristol. I would like to thank him for all his help and advice during the period of the research.

I would also like to thank the following:

Mr. J. Harris and all the staff of the Aeronautical Engineering Department Workshop.

Miss Alison Davies for skillfully tracing most of the graphs.

Prestridge Information Services for typing the manuscript.

My wife Mahmula for her patience and encouragement.

My small children Randa, Ziad and Ahmad for the many times I went to work while they wished I could stay with them.

SUMMARY

The research is concerned with the interlaminar delamination problem in unidirectional Carbon Fibre Reinforced Plastic (CFRP) laminates under static and fatigue loading. Analytical models backed by experimental techniques are employed to describe the delamination behaviour in 0° interfaces.

The problem of a semi-infinite elastic plate loaded along its straight boundary is persued to develop an analytical and realistic Double Cantilever Beam (DCB) Model which accounts for the end deflections associated with deformation beyond a crack tip. Comparisons with the predictions of existing models and with available experimental data show good agreement. The analysis is used to formulate the strain energy release rate (SERR) and the corresponding stress intensity coefficient. This shows excellent agreement with other results from more elaborate methods. The SERR is also formulated for a tapered double cantilever beam and this agrees well with experiment.

DCB type specimens were tested in load control where the SERR is measured and compared with theory for 0° CFRP. Other specimens were tested in fatigue and the delamination is described for various maximum loads. A Paris type formula is given for predicting crack growth in 0° CFRP.

A theoretical analysis is presented for the crack propagation in a layered fibre reinforced plastic strip in compression, in the presence of a blister. Account is taken of a resin rich layer at the delaminating edge and of an initial deflection in the blister geometry. Typical design curves are produced which show the

influence of blister length, applied strain and resin stiffness on loads required for delamination.

Blistered sandwich specimens were tested in static compression where debonding characteristics are explained. The loads required to initiate delamination are found to compare reasonably well with theory. Similar specimens were tested in constant amplitude fatigue compression loading and delamination behaviour is illustrated.

CONTENTS

LIST OF TABLES, FIGURES AND PLATES

TABLES

FIGURES

FIGURES (continued)

FIGURES (continued)

FIGURES (continued)

FIGURES (continued)

FIGURES (continued)

FIGURES (continued)

FIGURES (continued)

PLATES

PLATES (continued)

5.12 Fatigue delamination surface features for specimen TB-F3 (side 'B') (Total N = 2,250,000 cycles)

5.13 Fatigue delamination surface features for specimen TB-F4 (side 'A') (Inner edges represent the 'Front') (Total N = 1,502,040 cycles)

NOTATION

a	Crack length
a_o	Initial crack length
A	Crack surface
b	DCB specimen width
B	Constant in Eqn. (3.5)
c	Constant factor
c'	Half attached length of outer layer
C	Compliance
C_1, C_2, C_3, C_4	Constants of integration
$\overline{C}_1, \overline{C}_2$	Constants of integration
d	Distance beyond crack tip where displacements vanish
D	Flexural rigidity of blister
e	Distance between load line and TDCB apex
E	Young's modulus
E_1, E_2, E_r	Young's moduli of outer, inner and resin, respectively
E_1^*	Equivalent Young's modulus of outer layer
E_d	Overall Young's modulus for complete specimen
E_e	Equivalent Young's modulus of blister layer
E_ℓ	Young's modulus of laminate in absence of delamination
f	Frequency
$f_1(a/h)$	Function of a/h only
F	Defined below Eqn. (4.6)
F'	Defined below Eqn. (4.7)
F_1, F_2	Defined below Eqn. (4.31)
g	Energy release rate
g_c	Critical energy release rate
g_n	Normalized strain energy release rate

G	Shear modulus
h	DCB arm depth
h_1, h_2	Defined below Eqn. (4.11)
h_a	TDCB arm height at crack tip
J	Ratio of applied and buckling strains
k	Elastic foundation constant
K	Kinetic energy
K_I	Stress intensity factor
ℓ	Length of load action on straight boundary
ℓ'	Half span of outer layer
L	Distance between load line and DCB base
m	Constant exponent
M_1, M_2	Defined below Eqn. (4.11)
n	Constant exponent
n_p	Dimensionless g.s.f. coefficient in load control
n_{stp}	Number of PTFE layers
n_Δ	Dimensionless g.s.f. coefficient in displacement control
N	Number of cycles
$\bar{N}$	Number of blotting paper layers
p	Ratio of layer buckling load to its in-plane load
P	Applied load
P_1, P_2	Load/unit width in outer and inner layers, respectively
P_c	Critical applied load
P_c^*	Critical applied load/unit width
P_E	Euler buckling load for delaminated layer
P_E'	Buckling load for delaminated layer
P_{max}	Maximum of fatigue load

P_{mean}	Mean load
P_{min}	Minimum of fatigue load
P_{ov}	Overall applied load for TB specimen
q	Distributed load
Q	Defined below Eqn. (4.45)
r	Distance from elementary load to point examined
R	Small length
R_1, R_2, R_3, R_4 R_5, R_6	Defined below Eqn. (4.26)
$\bar{R}$	Ratio of min. and max. of fatigue load
s	Ratio of apex and base distances from load line
t	Total thickness of strip
t_1, t_2, t_r	Thickness of outer, inner and resin rich layers, respectively
T	Distance between knife edges
T_o	Distance between measuring points in released C.O.D. gauge
u	Axial displacement
$u_{1\ell}$	Displacement at any point to left of loading 1
$u_{2\ell}$	Displacement at any point to left of loading 2
$u_{3\ell}$	Displacement at any point to left of loading 3
u_{4r}	Displacement at any point to right of loading 4
u_{2u}	Displacement at any point under loading 2
u_{4u}	Displacement at any point under loading 4
U	Strain energy/unit width
U_{at}	Strain energy/unit width for attached portion
U_b	Strain energy/unit width of bending
U_c	Half of complementary strain energy
U_{dc}	Strain energy/unit width of direct compression
U_{in}	Strain energy/unit width for inner layer
U_t	Total strain energy/unit width for blister layer

v	Vertical displacement
V	Unit-wide strip volume
w	Deflection along z'-axis
w_1	Total deflection of blister layer
w_o	Initial deflection of blister layer
$\bar{w}_1$	Difference between total and initial deflections of blister layer
w_2	Deflection of attached portion (beam on elastic foundation)
W	Work against material resistance
W'	External work done
W_c	Complementary work
W_i	Initial pre-cure weight of CFRP plate
x	Longitudinal variable coordinate
$x_{1\ell}$	Local variable coordinate to left of loading 1
$x_{2\ell}$	Local variable coordinate to left of loading 2
$x_{3\ell}$	Local variable coordinate to left of loading 3
x_{4r}	Local variable coordinate to right of loading 4
x_{2u}	Local variable coordinate under loading 2
x_{4u}	Local variable coordinate under loading 4
$Y(\lambda')$	Function of λ' defined below Eqn. (4.36)
Y_1	Defined below Eqn. (4.11)
z	Ratio of crack length and base distance from load line
z'	Vertical axis
Z	Additional energy
α	Square root of ratio between in-plane load and flexural rigidity
β	Defined below Eqn. (4.9)
β_1, β_2	Defined below Eqn. (4.10)
γ	Specific surface energy per unit of crack surface

γ_o	Surface tension
Γ	Surface energy of fracture
Γ_o	Total surface tension
δ	DCB arm deflection
δ_o	Additional deflection due to DCB arm rotation
$\bar{\delta}_o$	Max. initial deflection of blister layer
δ^*_o	Max. of post-buckled deflection of debonded layer
δ_b	Bending deflection
δ_{mb}	Deflection in middle of blister layer
δ_s	Shear deflection
Δ	Crack mouth opening displacement
$\bar{\Delta}$	Shortening of blister
$\bar{\Delta}_o$	Shortening of undelaminated portion of outer layer
$\bar{\Delta}_1$	Total shortening of outer layer
ε	Applied longitudinal strain
ε'_E	Critical buckling strain for delaminated layer
ζ	Displacement micro-strain
ζ_o	Displacement micro-strain for initial setting
ζ_L	Loading micro-strain
η	Dimensionless ratio defined below Eqn. (4.10)
θ	Angle of taper
κ	Dimensionless ratio defined below Eqn. (2.23)
λ	Slope of taper for TDCB specimen
λ'	Dimensionless term defined below Eqn. (4.11)
λ_1	Dimensionless term defined below Eqn. (4.11)
Λ	Taper dependent implicit function
μ	Dimensionless term defined below Eqn. (4.7)
ν	Poisson's ratio
$\nu_{\ell t}$	Poisson's ratio with respect to longitudinal fibre and transverse fibre directions (stress in fibre direction)

$\nu_{t\ell}$	Poisson's ratio with respect to transverse fibre and longitudinal fibre directions (stress in transverse direction)
ξ	Constant factor
π	Common constant (=3.141593)
ρ	Defined below Eqn. (4.36)
σ	Applied stress
σ_o	Maximum tensile/compressive bending stress
σ_1	Stress in outer layer
σ_2	Stress in inner layer
σ_x	Bending stress
ϕ	Defined below Eqn. (4.10)
χ_1	Defined below Eqn. (4.11)
$\psi\ (\lambda)$	Explicit function of λ
ω	Reduction factor
ω^*	Defined below Eqn. (4.45)
Ω	Defined below Eqn. (4.26)

ABBREVIATIONS

App. strain	Applied strain
Ben. st. energy	Bending strain energy
CERR	Critical energy release rate
CFRP	Carbon fibre reinforced plastic
C.O.D.	Crack mouth opening displacement
DCB	Double cantilever beam
Direct st. energy	Direct strain energy
Nor. E.R.R.	Normalized energy release rate
PMMA	Polymethylmethacrylate
PTFE	Polytetraflouroethylene
TB	Twin blister
TDCB	Tapered double cantilever beam

C H A P T E R O N E

INTRODUCTION

1 1 WORK DEFINITION

Advanced fibrous composite materials such as carbon fibre reinforced plastic (CFRP) are becoming widely used in many structural applications. The Aerospace industry which is considered to be the main pioneer of this material had in 1984 a respectable 38% share of worldwide markets of advanced polymer composites (Ref. 1). High specific strength and stiffness combined with light weight and the ability of the manufacturer to tailor the materials, with minimum waste, to meet strength requirements in different directions, have made these composites very appealing to the structural analyst and designer alike. For example, a reduction of one pound in weight of a commercial aircraft can save up to 1000 Dollars over its lifetime from, *inter alia*, fuel saving (Ref. 1). A second example is offered by McDonnell Douglas' development of a 3 Kg light weight composite structure, that supports 43 Kg of electro-optical equipment which is subjected to 5g acceleration, through selective fibre orientation to resist loads and deflections. The result is a 25-40% cost reduction over a beryllium structure (Ref. 2). Typical aircraft applications include (apart from secondary components such as rudders, elevators, wing flaps, access doors, furniture, etc.) primary components such as horizontal stabilisers and elevators, fins, wings, engine and fuselage parts (Ref. 3). Probably the most dramatic application of carbon epoxy composites is in the U.S.A. Navy AV-8B Attack V/STOL aircraft with

approximately 26% saving in weight (Ref. 4).

Even though the future outlook seems to be very promising (Ref. 5), the use of CFRP composite materials in major aerospace components is still lagging behind conventional metallic counterparts such as Aluminium, Steel and Titanium. Two main reasons account for this; firstly the high cost of basic material production mainly due to the complex and often out-dated manufacturing processes (Ref. 6), and secondly because of lack of knowledge of the behaviour of these materials under static and fatigue loading. Though, the literature on the latter seems to be quite extensive (e.g. Refs. 7 and 8) more work needs to be done before many aspects of behaviour can be fully understood (Ref. 9).

Most of the CFRP composite used in the aerospace industry is supplied to manufacturers in pre-impregnated (pre-preg) form where the fibres are pre-impregnated with resin which is partially cured for ease of handling. This type of process allows closer control of the resin content during manufacture than the wet lay-up process where the impregnation takes place during manufacture. The pre-preg material (typical thickness; 0.125mm) is cut into sheets and these are layed up in predetermined orientations to meet the strength and stiffness requirements. After laying up, the material is consolidated under heat and pressure to produce a viable laminate (Ref. 10).

One of the main disadvantages with a CFRP laminated plate is that whilst its in-plane mechanical properties can be tailored to give very good strength and stiffness, its out-of-plane (or through the thickness) properties are poor compared with conventional metal plates. This is because the properties in this direction are obtained, in the main, from the relatively weak plastic resin matrix. The problem is made worse, by the presence of areas of poor inter-layer

bonding caused by voids and the inclusion of extraneous matter during manufacture or, a low energy impact induced delamination in the cured component (Ref. 11). An example of this type of behaviour is the blister problem (Ref. 12) where the initial voided area can spread rapidly when prone to buckling under compressive loading. The development of representative analytical models together with appropriate specimen testing, for studying the static and fatigue behaviour in unidirectional CFRP composites under cleavage and in-plane direct compression loading, is the main theme of this thesis.

An extensive bibliographical survey has been conducted by the author into the subject of damage in composite materials. It has revealed that a considerable amount of work has been done on damage emanating from sharp and blunt, through thickness notches under tensile static and tensile fatigue loads (e.g. Refs. 13 to 25). Also, the problem of edge delamination in laminated composites subjected to in-plane tension, has been undertaken by a number of authors (Refs. 26 to 28). On the other hand, work on delamination under either static in-plane direct compression or static cleavage is still relatively limited and mostly very recent. Moreover, the author is aware only of (Ref. 82) and his work (Ref. 29) on cyclic cleavage, and Refs. 30 and 31 on delaminatory fatigue damage propagating from an initial blister debond subjected to in-plane direct compressive load.

1.2 THE AIM OF THE WORK

Since layer interfaces are inherent planes of weakness in laminated composites, a comprehensive study which looks into the problem of delamination is an important area of research.

When a composite component is loaded statically, strain energy is

stored within and, if flaws are present they become sites for stress concentrations. If these reach or exceed the strength of the interlaminar bonds, delamination may ensue with strain energy being released to drive the crack. The result can be a catastrophic failure of the component. Even when the maximum stress within the component is below the interlaminar strength, damage may still grow under fatigue loading. The onset of delamination and its possible spread is very much dependent on the amount of strain energy needed to separate the bonded layers. The energy released at the crack front per unit of fracture area is known as the "critical energy release rate" (Ref. 12 Eqn. (29) and Ref. 32 Section 1.4) and is a basic laminate material property which can be measured from controlled two-dimensional opening mode tests on laminated strips.

The present work encompasses the following:-

a) the development of reliable and relatively simple theoretical models for the calculation of the strain energy release rate (SERR) during delamination;

b) the design and subsequent testing of specimens which represent the analytical models under static and fatigue loading. The experimental results are then discussed and compared where possible with the analytical predictions.

1.3 METHOD OF APPROACH

This thesis falls into two main areas of investigation. In the first part, the problem of delamination cleavage is studied using double cantilever beam (DCB) techniques. The author has developed a simple and realistic analytical model (Ref. 33) which can be employed in the study of fracture type cleavage. It accounts for the end

deflections associated with deformation beyond the crack tip. The model is directly applied to the design of DCB specimens for both static and fatigue studies of delamination along 0°/0° interfaces in CFRP laminates. A DCB specimen consists of two mild steel arms to which is glued an eight-layered, 0°, CFRP strip. An initial delaminated region is introduced at one end by means of a polytetrafluoroethylene (PTFE) sheet which is positioned at the plate mid-plane before the curing process.

The delamination growth from an initial through-width debond in a laminated component, subjected to in-plane compressive load, is addressed in the second area of investigation. Here, the through-width splitting problem of a typical fibre reinforced plastic orthotropic layer taking into account the effects of initial deflected shape and also the elastic end effects of a resin rich layer (Ref. 12) is modelled and formulated. The extent of delamination growth in the laminated component depends on whether the debond bridging layer is originally flat or whether a certain pre-load degree of bulging is present. In the former case, delamination will grow only after the layer has buckled (Ref. 12). However, delamination growth after buckling may or may not take place. The growth depends on many parameters, including layer dimension, layer in-plane and flexural stiffness and of course the interlaminar fracture toughness of the material. Layer local buckling behaviour can trigger rapid splitting growth and component collapse especially when the initial debond length is small. On the other hand, the pre-load bulging layer case may be less serious as far as the postbuckling behaviour is concerned. In fact, it is shown that, the strain energy is released in such a way that only limited delamination occurs when the in-plane applied strain reaches a critical value. An expression for the SERR is developed for

the above two configurations i.e., according to whether the pre-load layer is initially flat or bulging. In both cases, the inner layer is assumed to remain flat throughout the loading process. All 0° CFRP strips, each consisting of eight layers with a through-width blister which separates the strip into four layers each side, are glued on each side of an Aeroweb Type A1 honeycomb (supplied by Ciba-Geigy Ltd.) to form a sandwich. Equal end lengths of the twin-blister (TB) test specimen are resin moulded into mild steel end-fittings through which the compressive load is applied. This test method has been found to be both very effective and time saving.

1.4 PLAN OF THE THESIS

The bulk of the subject matter appears in Chapters 2, 3, 4 and 5. At the end of each Chapter are placed Figures, Tables and Pictures. A thorough discussion of the matters arising from the study and of the relevant literature appears in each Chapter where appropriate.

Chapter 2 contains the analytical details of the DCB model where the end deflections associated with deformation beyond the crack tip are accounted for and, the total deflection of the DCB arm along the load line is formulated for various DCB configurations. The SERR is expressed in terms of the mechanical and geometrical fracture parameters and, the criterion for the stability of crack propagation is documented.

Chapter 3 deals with the application of the theory developed in Chapter 2, to fabricate and test a number of DCB specimens for studying the cleavage behaviour between CFRP 0° layers under static and fatigue loading. The static SERR is measured in two different ways (the Gurney area method (Ref. 34) and the compliance method) and compared with

the theoretical calculation. Fatigue crack data are used in conjuction with the SERR expression to develop a Paris-type semi-empirical formula for the prediction of delamination growth.

Chapter 4 goes into the details of the splitting problem in the presence of a central through-width debond region when the bridging layer is subjected to an in-plane direct compressive load. The analysis takes into account the elastic end effects of a resin rich layer at the delaminating edges. Simple expressions are derived for the evaluation of the SERR in cases, with and without an initial bulge-out. Results are given for various compressive applied strains, blister span lengths and in-plane loads.

Chapter 5 includes the manufacture of the twin-blister test specimens and the experimental results obtained from a series of static and fatigue tests. The critical static compressive strain, corresponding to the start of delamination, is plotted versus the blister half span length and compared with the theoretical results, for three representative twin-blister test specimens. A similar set of specimens are tested in fatigue and the behaviour of the delamination growth is given in graphical form showing the blister span length versus the number of cycles. Serveral graphs allow the splitting growth rate to be measured and subsequently plotted versus the overall applied load.

Chapter 6 documents the general conclusions and the salient matters from the work, and also suggestions for prospective future work.

CHAPTER TWO

DOUBLE CANTILEVER BEAM (DCB) TECHNIQUES FOR STUDYING CRACK PROPAGATION

2.1 INTRODUCTION

The simple beam theory of bending has been found to be a convenient tool when dealing with many crack propagation problems. The method allows the use of the strain energy stored in a cantilever beam to obtain an energy balance at the onset of crack propagation. As early as 1930, Obreimoff (Ref. 35) employed this approach to assess the splitting strength of a thick sheet of mica. The same concept was used later by Benbow and Roesler (Ref. 36), with some sacrifice of simplicity for the sake of stable crack propagation. Other worthy works which followed these two publications are found in Refs. 37 and 38.

The double cantilever beam (DCB) specimen is used frequently in studying crack propagation characteristics because of its versatility in both theory and experiment. Therefore, it is no wonder, it has become so popular in the research for fracture characteristics of many materials.

In the past, various models have been developed for studying the behaviour of the DCB specimens. With reference to Fig. 2.1(a), one of the objectives behind the work contained in this Chapter is to establish a reliable theoretical relationship between the applied load P and the corresponding deflection δ, so that satisfactory crack propagation specimens can be designed. Mechanically, the system is

nearly equivalent to two built-in slender cantilever beams, and the end deflection due to bending and shear can be obtained from elementary beam theory. However, there remains the problem of trying to establish a satisfactory theory to account for the strains which occur beyond the crack tip. An early paper by Gillis and Gilman (Ref. 39) discussed this problem, and they observed that no satisfactory theory had been developed which takes these strains into account. However, they point out that this effect can be assessed by means of simultaneous force and end deflection measurements during testing. A later paper by Gillis (Ref. 40) on slotted double cantilever specimens treats the uncleaved part as a pair of beams elastically supported by the joining web. The strain energy of each beam and its foundation was then added to the bending strain energy. Further theoretical work by Srawley and Gross (Ref. 41) and Wiederhorn, Shorb, and Moses (Ref. 42) gives a linear elastic solution for the stresses around the crack in the double cantilever configuration, which stresses determine the stress intensity factor. The authors (Ref. 42) go on to calculate the resulting end displacement δ, and with this indirect approach they deduce the actual values of certain constants which are used by Gillis and Gilman (Ref. 39) to allow for the strains beyond the crack tip. Burns and Lawn (Ref. 43) attempt to account for the strain energy in the uncracked part by regarding the cantilever arms as effectively built-in at a beam length slightly greater than the crack length. Experimental compliance calibration (Ref. 44) showed that the arm of the DCB deflected more under a given load than was predicted by the specimen beam formula. The additional deflection was attributed to the fixed end rotation and was accounted for by regarding the specimen arm as a fixed amount longer than the actual crack length.

Raasch (Ref. 45) accounts for the elastic energy stored beyond the

crack by assuming that there would be no significant change in the test specimen if this strain energy were stored in a semicircular annulus of inner radius equal to the radius of the crack tip and outer radius equal to half the specimen thickness. The biharmonic equation for the stress function was solved for assumed stress-free boundary conditions at these radii, and the strain energy stored in the annulus was calculated. However, when comparing the theoretical predictions with his own experimental data, the author found that his theory over-estimated the strain energy by a considerable margin. Hence a factor was introduced to bring his theoretical results into line with experiment.

An augmented double cantilever beam model (Ref. 46) treats the region of the specimen beyond the crack tip as a beam on an elastic foundation. The author recognizes that the foundation modulus is established in an arbitrary way, but justifies his choice by the fact that the model is found to be in excellent agreement with established data. This agreement must be fortuitous because the model is not representative of the actual mechanical system. In fact, the elastic foundation model has been taken up by many investigators (Refs. 47 to 50) for studying both static, quasistatic, and dynamic crack propagation. Bonesteel, Piper and Davinroy (Ref. 51) and Green, Hawkins and Hirlinger (Ref. 52) throw some light on the agreement of the different models with experiment.

The object of this present Chapter is to develop a theoretical model of the specimen which takes into account the strains beyond the crack tip in a relatively simple but realistic way, although the strains in the immediate vicinity of the crack tip are neglected.

2.2 THEORETICAL MODEL

It is assumed that the deformation beyond the crack tip is induced primarily by the bending moment at the crack tip section of the beam. This is a reasonable assumption provided the arms are long compared with the beam depth [i.e., a >> h, Fig. 2.1(a)]. If they are not, then the shear strains beyond the crack tip would become significant. Fig. 2.1(a) shows the geometry and loading for the double cantilever beam, and Fig 2.1(b) shows the linear elastic bending stress distribution across the crack tip section. The main objects of the analysis which follows are to calculate the horizontal displacements u across the section AB due to the bending stresses and hence to find the resulting end rotations of each part of the section at AC and CB. These rotations can then be used to find the corresponding deflections at the loading points, which deflections must be added to those due to bending and shear of the specimen arms.

Consider the case of a distributed load q acting over a length ℓ on the straight boundary of a semi-infinite plate as shown in Fig. 2.2. The vertical displacement u produced at point 0, a distance r from the elementary load qdr, is given by (Ref. 53, Article 30).

$$\delta u = \frac{2q}{\pi E} \ln \frac{d}{r} \, dr - \frac{1 + \nu}{\pi E} \, dr,$$

where d is the distance beyond the crack tip where the displacements vanish, E is Young's modulus, and ν is Poisson's ratio.

The total deflection becomes

$$u = \frac{2}{\pi E} \int_{x}^{\ell+x} q \ln \frac{d}{r} \, dr - \frac{(1 + \nu)}{\pi E} \int_{x}^{\ell+x} q \, dr \qquad (2.1)$$

Eqn. (2.1) is valid for any point outside the loaded region. For a point O within the loaded region [see Fig. 2.2(b)] the lower and upper limits of integration in Eqn. (2.1) are replaced by $-x$ and $\ell-x$, respectively.

Eqn. (2.1) is used to calculate the horizontal displacements across the section ACB in Fig. 2.1. However, it must be remembered that, strictly speaking, the equation applies only to a semi-infinite plate. Thus whilst displacements in the central region of the beam will be estimated accurately, those in the outer regions near the edges will be subject to some error. It is convenient to divide up the loading diagram [Fig. 2.1(b)] into four separate triangular regions, and to calculate the displacements due to each portion of loading separately. The resulting displacements can then be found by superposition, noting symmetry about the point C. The letter u is used, with two subscripts, to denote the horizontal displacements due to any portion of the load distribution. The first subscript (a number) indicates the portion of the loading according to Fig. 2.1(b), whilst the second (a letter, either ℓ, u, or r) indicates "left", "under" or "right" respectively. Thus, for example, $u_{2\ell}$ is the displacement due to the loading 2 at any point to the left of the load triangle 2. The same subscripts are also conveniently employed in exactly the same way with the letter x to symbolize the local variable associated with each load triangle. From the above, it is clear that in order to obtain the total displacement at any point on the straight boundary, say to the left of the centre line, it is necessary to calculate:

$$u_{3\ell}\ ,\ u_{1\ell}\ ,\ u_{2\ell}\ ,\ u_{2u}\ ,\ u_{4r}\ ,\ \text{and}\ u_{4u}$$

Using Eqn. (2.1), it follows that

$$u_{3\ell} = \frac{2}{\pi E}\int_{x_{3\ell}}^{x_{3\ell}+(h/2)} \frac{2(r-x_{3\ell})}{h}\sigma_o \ln\left(\frac{d}{r}\right) dr - \frac{(1+\nu)}{\pi E}\int_{x_{3\ell}}^{x_{3\ell}+(h/2)} \frac{2(r-x_{3\ell})}{h}\sigma_o\, dr \qquad (2.2)$$

where the linearly varying stress $2\sigma_o(2-x_{3\ell})/h$ Fig. 2.3(a) has been substituted for the arbitrarily distributed load q. After integration, Eqn. (2.2) becomes

$$\frac{2u_{3\ell}}{h}\frac{\pi E}{\sigma_o} = -\left[\frac{4(h^2/4 - x_{3\ell}^2)}{h^2}\ln\left(\frac{h/2 + x_{3\ell}}{d}\right) + \frac{4x_{3\ell}^2}{h^2}\ln\left(\frac{x_{3\ell}}{d}\right) + \frac{2x_{3\ell}}{h} + \frac{\nu}{2}\right] \quad (2.3)$$

In Eqns. (2.2) and (2.3) the local coordinate $x_{3\ell}$ is measured from point D [Fig. 2.1(b)] to the left. In the same way, the following expressions are obtained for the other displacements $u_{1\ell}$, $u_{2\ell}$, u_{2u}, u_{4r} and u_{4u} (see Appendix A, Section 1).

$$\frac{2u_{1\ell}}{h}\frac{\pi E}{\sigma_o} = \left(\frac{h/2 + x_{1\ell}}{h/2}\right)^2 \ln\left(\frac{h/2 + x_{1\ell}}{d}\right) - \frac{4(x_{1\ell}^2 + hx_{1\ell})}{h^2}\ln\left(\frac{x_{1\ell}}{d}\right) - \frac{2(h/2 + x_{1\ell})}{h} + \frac{\nu}{2} \quad (2.4)$$

$$\frac{2u_{2\ell}}{h}\frac{\pi E}{\sigma_o} = \frac{4(h^2/4 - x_{2\ell}^2)}{h^2}\ln\left(\frac{h/2 + x_{2\ell}}{d}\right) + \left(\frac{x_{2\ell}}{h/2}\right)^2 \ln\left(\frac{x_{2\ell}}{d}\right) + \frac{2x_{2\ell}}{h} + \frac{\nu}{2} \quad (2.5)$$

$$\frac{2u_{2u}}{h}\frac{\pi E}{\sigma_o} = \left(\frac{h/2 - x_{2u}}{h^2}\right)^2 \ln\left(\frac{h/2 - x_{2u}}{d}\right) - \frac{4(x_{2u}^2 - hx_{2u})}{h^2}\ln\left(\frac{x_{2u}}{d}\right) - \frac{2(h/2 - x_{2u})}{h} + \frac{\nu}{2} \quad (2.6)$$

$$\frac{2u_{4r}}{h}\frac{\pi E}{\sigma_o} = -\left[\frac{4(h^2/4 - x_{4r}^2)}{h^2}\ln\left(\frac{h/2 + x_{4r}}{d}\right) + \left(\frac{x_{4r}}{h/2}\right)^2 \ln\left(\frac{x_{4r}}{d}\right) + \frac{2x_{4r}}{h} + \frac{\nu}{2}\right] \quad (2.7)$$

$$\frac{2u_{4u}}{h}\frac{\pi E}{\sigma_o} = -\left[\frac{4(h^2/4 - x_{4u}^2)}{h^2}\ln\left(\frac{h/2 - x_{4u}}{d}\right) + \left(\frac{x_{4u}}{h/2}\right)^2 \ln\left(\frac{x_{4u}}{d}\right) - \frac{2x_{4u}}{h} + \frac{\nu}{2}\right] \quad (2.8)$$

It will be found to be more convenient to express the local coordinates $x_{3\ell}$, $x_{1\ell}$, $x_{2\ell}$, x_{2u}, x_{4r} and x_{4u} in terms of the DCB arm depth h and a single variable x [Fig. 2.3(b)] as follows:

$$x_{3\ell} = x + h/2,\ x_{1\ell} = x,\ x_{2\ell} = x - h/2,$$

$$x_{2u} = x,\ x_{4r} = -x + h/2,\ x_{4u} = x - h/2$$

Thus, Eqns. (2.3) through to (2.8) become

$$\frac{2u_{3\ell}\,\pi E}{h\sigma_o} = \frac{4(x^2 + hx)}{h^2} \ln\left(\frac{h+x}{d}\right) - \left(\frac{h/2 + x}{h/2}\right)^2 \ln\left(\frac{h/2 + x}{d}\right) - \frac{h/2 + x}{h/2} - \frac{\nu}{2} \tag{2.9}$$

$$\frac{2u_{1\ell}\,\pi E}{h\,\sigma_o} = \left(\frac{h/2 + x}{h/2}\right)^2 \ln\left(\frac{h/2 + x}{d}\right) - \frac{4(x^2+hx)}{h^2} \ln\left(\frac{x}{d}\right) - \frac{h/2 + x}{h/2} + \frac{\nu}{2} \tag{2.10}$$

$$\frac{2u_{2\ell}\,\pi E}{h\,\sigma_o} = \frac{4(-x^2+hx)}{h^2} \ln\left(\frac{x}{d}\right) + \left(\frac{x - h/2}{h/2}\right)^2 \ln\left(\frac{x - h/2}{d}\right) + \frac{x - h/2}{h/2} + \frac{\nu}{2} \tag{2.11}$$

$$\frac{2u_{2u}\,\pi E}{h\,\sigma_o} = \left(\frac{h/2 - x}{h/2}\right)^2 \ln\left(\frac{h/2 - x}{d}\right) - \frac{4(x^2-hx)}{h^2} \ln\left(\frac{x}{d}\right) - \frac{h/2 - x}{h/2} + \frac{\nu}{2} \tag{2.12}$$

$$\frac{2u_{4r}\,\pi E}{h\,\sigma_o} = \frac{4(x^2-hx)}{h^2} \ln\left(\frac{h-x}{d}\right) - \left(\frac{h/2 - x}{h/2}\right)^2 \ln\left(\frac{h/2 - x}{d}\right) - \frac{h/2 - x}{h/2} - \frac{\nu}{2} \tag{2.13}$$

$$\frac{2u_{4u}\,\pi E}{h\,\sigma_o} = \frac{4(x^2-hx)}{h^2} \ln\left(\frac{h-x}{d}\right) - \left(\frac{x - h/2}{h/2}\right)^2 \ln\left(\frac{x - h/2}{d}\right) + \frac{x - h/2}{h/2} - \frac{\nu}{2} \tag{2.14}$$

The displacements, given by Eqns. (2.9) through to (2.14), can now be superimposed in the regions C-E and E-B (Figs. 2.1(b) and 2.3) to give

$$u_{C-E} = u_{3\ell} + u_{1\ell} + u_{2u} + u_{4r} \tag{2.15}$$

and

$$u_{E-B} = u_{3\ell} + u_{1\ell} + u_{2\ell} + u_{4u}\,, \tag{2.16}$$

where u_{C-E} and u_{E-B} give respectively the resultant displacement at any point in each of the regions C-E and E-B. Substitution from Eqns. (2.9) through to (2.14) into Eqns. (2.15) and (2.16) gives

$$u_{C-E} = u_{3\ell} + u_{1\ell} + u_{2u} + u_{4r} = \frac{h\sigma_o}{2\pi E}\left[\left(\frac{x}{h/2}\right)^2 \ln\left(\frac{h^2-x^2}{x^2}\right) + \frac{4x}{h}\ln\left(\frac{h+x}{h-x}\right) - 4\right] \tag{2.17}$$

and

$$u_{E-B} = u_{3\ell} + u_{1\ell} + u_{2\ell} + u_{4u} = \frac{h\sigma_o}{2\pi E}\left[\left(\frac{x}{h/2}\right)^2 \ln\left(\frac{h^2-x^2}{x^2}\right) + \frac{4x}{h}\ln\left(\frac{h+x}{h-x}\right) - 4\right] \tag{2.18}$$

It is seen from Eqns. (2.17) and (2.18) that u_{C-E} and u_{E-B} are identical. This is not surprising considering that the displacement is single-valued at any chosen point between C and B (Fig. 2.3).

Writing the total displacement u_{C-E} and u_{E-B} at any point as u, either of Eqns. (2.17) and (2.18) gives

$$\frac{u\pi E}{h\sigma_o} = 2\left[\left(\frac{x}{h}\right)^2 \ln\left(\frac{h^2-x^2}{x^2}\right) + \frac{x}{h}\ln\left(\frac{h+x}{h-x}\right) - 1\right] \tag{2.19}$$

for $0 < x < h$.

This simple equation gives a continuous variation of u between x=0 and h. It is interesting to note that neither the distance d nor Poisson's

ratio ν appear in the expression for the final displacement produced by this particular type of loading on a semi-infinite plate.

Using Eqn. (2.19), the parameter $u\pi E/h\sigma_o$ is plotted against (x/h) in Fig. 2.4. It is seen that the central part of the graph is linear. The slope of this part can be used to obtain the rotation of the section as follows (See Fig. 2.4):

the vertical and horizontal intercepts of the straight line mn, as shown in Fig. 2.4, give

$$u = \frac{2.5h\sigma_o}{\pi E} \qquad \text{and,} \qquad x = 0.58h$$

Thus, the section rotation is

$$\frac{u}{x} = \frac{4.3\sigma_o}{\pi E}$$

This gives rise to a deflection δ_o at the point of application of the load P equal to $(4.3\ \sigma_o\ a)/\pi E$, or

$$\delta_o = \frac{8.212\ Pa^2}{Ebh^3} \tag{2.20}$$

using the usual bending stress formula $\sigma_o = 6Pa/bh^2$, where b is the specimen width.

This same result can be obtained using the complementary energy principle in the form

$$\frac{\partial U_c}{\partial P} = \delta_o, \tag{2.21}$$

where U_c is half the complementary strain energy stored in the specimen beyond the crack tip. This energy can be put equal to the

complementary work W_c done by the bending stresses across the crack tip section. In this case,

$$U_c = W_c = \lim_{R \to 0} \frac{b}{2} \int_R^{h-R} \sigma_x \, u \, dx, \qquad (2.22)$$

where σ_x is the bending stress at x.

It should be noted that it is not possible to integrate Eqn. (2.22) between x=0 and h directly and therefore a very small length R has been introduced into the limits in order to overcome this problem. Substituting the linear expression $\sigma_x = \sigma_o [(2x/h)-1]$, $u = 4.3 \sigma_o / \pi E$ and $\sigma_o = 6Pa/bh^2$ in Eqn. (2.22) and carrying out the integration, it is found that Eqn. (2.21) yields Eqn. (2.20) as R→0 (see Appendix A, section 2).

However, this energy approach enables a more accurate theoretical estimate to be made for δ_o by using the nonlinear expression for u given by Eqn. (2.19). With this, and with $\sigma_x = \sigma_o [(2x/h)-1]$, it is found that Eqn. (2.22) becomes

$$U_c = \frac{bh^2\sigma_o^2}{\pi E}\left[\frac{\kappa^2(1-\kappa)^2}{2} \ln\left(\frac{\kappa}{1-\kappa}\right) + \frac{1}{6}(2-\kappa)^2 (1-2\kappa+3\kappa^2) \ln (2-\kappa)\right.$$

$$- \frac{1}{6}(1+\kappa)^2(2-4\kappa+3\kappa^2) \ln (1+\kappa) + (1-\kappa)^3 \left(\kappa-\tfrac{1}{3}\right) \ln (1-\kappa)$$

$$\left. + \kappa^3 \left(\kappa-\frac{2}{3}\right) \ln \kappa + \frac{2\kappa-1}{6}\right] \qquad (2.23)$$

where

$$\kappa = \frac{R}{h}$$

As $\kappa \to 0$, Eqn. (2.23) becomes

$$U_c \approx \frac{bh^2\sigma_o^2}{\pi E}\left(\frac{2}{3}\ln 2 - \frac{1}{6}\right), \qquad (2.24)$$

and substituting $\sigma_o = 6Pa/bh^2$ into Eqn. (2.24) leads to

$$\delta_o = \frac{6.77Pa^2}{Ebh^2} \qquad (2.25)$$

Compared with the previous result[Eqn. (2.20)] this deflection is 17.5% lower, reflecting the fact that the rotation of the arm about the built-in end had previously been overestimated.

Each of the deflections given by Eqns. (2.20) and (2.25) can now be added to the well known deflections due to bending, δ_b, and shear, δ_s, given by (Ref. 53, Article 17)

$$\delta_b = \frac{4Pa^3}{Ebh^3} \quad \text{and} \quad \delta_s = \frac{1.5Pa}{bhG},$$

where G is the shear modulus, to give the total deflection δ in the direction of P. Therefore,

$$\delta = \frac{4Pa^3}{Ebh^3} + \frac{8.212Pa^2}{Ebh^2} + \frac{1.5Pa}{bhG}, \qquad (2.26)$$

and

$$\delta = \frac{4Pa^3}{Ebh^3} + \frac{6.77Pa^2}{Ebh^2} + \frac{1.5Pa}{bhG}. \qquad (2.27)$$

These equations have the same form as Eqn. 9 of Ref. 39, but in this last reference the term relating to the rotation about the built-in end is not given explicitly. However, a more explicit equation is given by

Wiederhorn, Shorb, and Moses in Ref. 42 Eqn. (5) in their paper gives

$$\delta = \frac{4Pa^3}{Ebh^3} + \frac{12cPa^{n+1}}{Ebh^{n+1}} + \frac{3\xi Pa}{bhG} \quad , \tag{2.28}$$

where n, c and ξ are constants that depend upon the conditions at the fixed end of the cantilever.

Values of n, c and ξ were estimated from a number of calculated displacements δ for crack lengths of 2, 3 and 4h for soda-lime glass, fused-silica glass, and polycrystalline sapphire. In all cases they found that $n \simeq 1$ and $c \simeq 0.66$, allowing the second term in Eqn. (2.28) to be written in the form $7.92Pa^2/Ebh^2$. Comparison with the corresponding second terms in Eqns. (2.26) and (2.27) derived from the analysis in this present work reveals that, it is 14.5% higher than the term in Eqn. (2.27) and is only 3.5% lower than the term in Eqn. (2.26).

A further direct comparison can be made with the result from the elastic foundation model given by Kanninen (Ref. 46). Eqn. (7) of his paper gives

$$\delta = \frac{4Pa^3}{Ebh^3} + \frac{7.68Pa^2}{Ebh^2} + \frac{1.88Pa}{Gbh} + \frac{1.56P}{Eb} \quad , \tag{2.29}$$

when

$$E = 2.6G$$

Again, the second term in Eqn. (2.29) falls between the second terms in Eqns. (2.26) and (2.27), and is not in exact agreement with either of them. However, it is still closer to the former than to the latter.

Raasch (Ref. 45) gives the results of his theoretical analysis in

the final form

$$\frac{\delta E b h^3}{4Pa^3} = f_1 (a/h) \quad , \tag{2.30}$$

where

$$f_1 (a/h) = 1+0.78 \left(\frac{h}{a}\right)^2 + \left[3.65 \left(\frac{h}{a}\right) + 1.721 \left(\frac{h}{a}\right)^2 + 0.594 \left(\frac{h}{a}\right)^3\right] . \tag{2.31}$$

Eqn. (2.31) is plotted in Fig. 2.5 together with the experimental results reported in the same reference (Ref. 45), and also with the corresponding parameters from Eqns. (2.26) and (2.27). It is seen that Raasch experimental results lie below his theoretical curve. This discrepancy was explained by the author to be due to the fact that his initial simplifying assumptions that the uncleaved part of the specimen might be replaced by a semicircular disc did not quite correspond to the facts. Therefore, a conforming factor was introduced, in front of the square bracket, in Eqn. (2.31) and was later determined by fitting it to the measured values. Apart from being arbitrarily introduced, the factor depends on the ratio of the uncleaved portion length to the depth of the DCB arm making a sound physical explanation of the difference between theory and experiment rather obscure. On the other hand, the values of the parameters obtained from Eqns. (2.26) and (2.27), as shown in Fig. 2.5, lie below the experimental values. This is to be expected if the following points are considered. Firstly, the present theory assumes the specimen is infinitely wide and long at the roots of the DCB arms, and this would have the effect of providing greater constraint against rotation than would be the case in practice. Secondly, the strains due to the root shear stresses are neglected (they would become significant for small values of a/h), as

are the local elastic/plastic strains at the crack tip itself. Finally, an exact elasticity solution would predict vertical displacement v as well as the horizontal displacements u in the root region. In practice, therefore, small vertical displacements which have not been accounted for in the present theory would be expected to exist. This would give rise to an additional small deflection at the loaded end. It is thus not surprising that the present theory gives results which fall below the experimental values obtained by Raasch (Ref. 45).

2.3 STRAIN ENERGY RELEASE RATE (SERR)

It was mentioned in the general introduction of this thesis that one of the aims of the present study was to develop a reliable and simple energy formula for studying the delamination characteristics in unidirectional CFRP laminates.

In the early 1920's, Griffith (Ref. 54) was confronted with the problem of finding out why the actual strength of glass was so much lower than what was expected from its molecular structure. He eventually came to the conclusion that, the discrepancy might be due to small internal defects which acted as stress raisers within the material, degrading in this way its overall strength. In order to tackle the problem, Griffith came out with what later became one of the most versatile methods in studying the behaviour of crack propagation in engineering solids; namely, he equated the strain energy released per unit of fracture area at the onset of crack propagation to the surface energy of fracture. The Griffith energy balance equation has the following form:

$$U - Z = W + K \quad , \tag{2.32}$$

where, U is the elastic strain energy stored in the body, Z is any additional energy supplied to the body during crack propagation, W is the work done against the resistance of the material and, K is the kinetic energy.

Let A be the extent of the crack; thus, differentiation of Eqn. (2.32) with respect to A gives

$$\frac{dU}{dA} - \frac{dZ}{dA} = \frac{dW}{dA} + \frac{dK}{dA} \tag{2.33}$$

At the onset of crack propagation $\frac{dZ}{dA} = \frac{dK}{dA} = 0$, and Eqn. (2.33)

becomes

$$\frac{dU}{dA} = \frac{dW}{dA} \tag{2.34}$$

Griffith identified the term dW/dA as the work done against the total surface tension $\Gamma_o = 2\gamma_o$, where γ_o is the specific surface energy. Following the above approach, Griffith successfully explained why there was a large difference between the theoretical and experimental tensile strength in glass. However, for the purpose of the present study, Eqn. (2.34) will be used in the updated modified context as explained in Ref. 55. In this context dW/dA is no longer simply regarded as the surface tension but as the total work done against the resistance of the material. Other names are often attached to this work; namely, the fracture toughness of the material g_c (= the critical energy release rate), and the surface energy of fracture $\Gamma=2\gamma$ (γ being the specific surface energy of fracture per unit of area). In the analysis which follows; $g_c = \Gamma$ and, $g = dU/dA$, will be taken to represent the critical energy release rate at the onset of crack propagation and the energy release rate respectively. Having

said this, the strain energy release rate g is next evaluated for the DCB specimen in a straight-forward manner.

With reference to Fig. 2.1(a), the total end deflection δ given by either of Eqns. (2.26) and (2.27) can be used in the strain energy formulation. In this present analysis, Eqn. (2.26) will be taken in preference to Eqn. (2.27) because of the former close agreement with experiment (Fig. 2.5).

The elastic strain energy stored in one arm of the DCB specimen is simply half the work done by the applied load P through the total arm deflection δ [Eqn. (2.26)]. The strain energy U of the entire specimen is twice this. Thus,

$$U = P\delta = \frac{P\Delta}{2} \tag{2.35}$$

where, $\Delta = 2\delta$ is the crack opening displacement (COD). The ratio, Δ/P, of the COD to the applied load P is defined as the compliance C of the specimen, which is characteristic of the considered crack length a. Therefore,

$$C = \frac{\Delta}{P} \tag{2.36}$$

or,

$$C = \frac{8a^3}{Ebh^3} + \frac{16.424a^2}{Ebh^3} + \frac{3a}{bhG} \tag{2.37}$$

Substitution for Eqn. (2.36) into Eqn. (2.35) gives

$$U = \frac{P^2 C}{2} \tag{2.38}$$

It is reiterated here that, in essence, the energy principle is

applied here in the sense that, when a crack extends in a stressed body, some of the elastic stored strain energy is lost to the growing crack and that the rate of the released strain energy g_c at the onset of crack propagation is equal to the material toughness, or equivalently to the surface energy of fracture Γ. Thus, differentiation of Eqn. (2.38) with respect to the crack area, A = ab, gives

$$g = \frac{dU}{d(ab)} = \frac{P^2}{2b}\left(\frac{dC}{da}\right) \tag{2.39}$$

Substitution from Eqn. (2.37) into the above equation yields,

$$g = \frac{P^2}{Eb^2}\left(\frac{12a^2}{h^3} + \frac{16.424a}{h^2} + \frac{1.5E}{hG}\right) \tag{2.40}$$

At the onset of crack propagation Eqn. (2.40) gives the critical energy release rate g_c, i.e.,

$$g_c = \Gamma = \frac{P_c^2}{Eb^2}\left(\frac{12a^2}{h^3} + \frac{16.424a}{h^2} + \frac{1.5E}{hG}\right) \tag{2.41}$$

where P_c is the critical load at the start of crack extension. The reliable physical ground on which Eqn. (2.41) is based, combined with its simplicity are two important credits to this expression in undertaking fracture toughness measurements for a certain material.

It is well known that the strain energy release rate g is related to the corresponding opening mode stress intensity factor K_I as shown in the following relations (Ref. 55):

$$K_I^2 = Eg \quad \text{(for plane stress)},$$

and (2.42)

$$K_I^2 = \frac{E}{1-\nu^2}g \quad \text{(for plane strain)}$$

There is no clear cut reason for choosing one form or the other from Eqns. (2.42). However, for relatively thin specimens, it is more appropriate to adopt the plane stress formula. Assuming that is so in our case, thus, substitution from Eqn. (2.40) into the first Eqns. (2.42) yields

$$\frac{K_I bh^{3/2}}{Pa} = 2\sqrt{3}\left[1 + 1.37\left(\frac{h}{a}\right) + 0.3125\left(\frac{h}{a}\right)^2\right]^{\frac{1}{2}} \qquad (2.43)$$

where, the typical value for steel, E/2.5, has been substituted for the shear modulus G. The left hand side of Eqn. (2.43) is often called the dimensionless stress intensity coefficient. The non-dimensional factor $K_I bh^{2/3}/Pa$ for several values of a/h is shown in Table 2.1 along with the corresponding results from Refs. 41, 42 and 46. These references were commented upon early in this Chapter. It is seen from the table that the results from the various methods are very close. However, the present method outweighs the others on the grounds of simplicity and physical understanding.

2.4 TAPERED DOUBLE CANTILEVER BEAM (TDCB) ANALYSIS

The model developed in the previous section for accounting for the strains past the crack tip in a DCB specimen, offers another major advantage; it can be easily extended to other double cantilever beam configurations. One of these; namely the tapered double cantilever beam specimen (TDCB) (Fig. 2.6), is of practical interest because it can offer a linearly varying compliance C with the crack length a. This can be very useful, because testing may be simplified considerably, while the critical energy release rate g_c is being measured for a certain material. In fact, a constant dC/da

allows the operator to monitor only the critical load P_c at the onset of crack propagation without being concerned with the crack length a [Eqn. (2.39)], unlike the parallel-arm DCB specimen where P_c and a must be monitored simultaneously. The TDCB specimen can also give slow and stable crack propagation; a feature desired in many test situations. Previously, the TDCB specimen was used, as pointed out in Ref. 56, in fatigue studies and environmental cracking investigations. Convenient use of the specimen has also been found in the study of crack propagation characteristics in adhesive joints.

In Fig. 2.6, there are shown two TDCB versions. The first [Fig. 2.6(a)] has been widely employed unlike the second where only very limited use is reported in the literature. In fact, the author is only aware of the work of Mai et al. (Ref. 56), where a specimen of the latter type was used. The authors (Ref. 56) employed a PMMA TDCB specimen as shown in Fig. 2.6(b) and, found that it gave better control of crack path and stability of cracking over the TDCB configuration shown in Fig. 2.6(a). However, the extension of the analysis detailed in the previous sections will be limited to the TDCB specimen shown in Fig. 2.6(a). Let us anticipate that this choice is not arbitrary as it will be made clear in Chapter 3; it is in fact the product of some experimental test trials to select a suitable DCB specimen for the delamination study of CFRP laminates.

With reference to Fig. 2.6(a), the total deflection δ given by Eqn. (2.26) can be easily modified to accommodate the effect of the taper angle θ. The second and third terms in the right hand side of Eqn. (2.26) are changed through the replacement of the DCB arm depth h by the variable arm depth of the TDCB $h_a = (a+e)\lambda$; where λ is the slope of the taper and, e is the distance between the load line and the apex of the specimen as shown in Fig. 2.6(a). Assuming a small taper

angle θ, the simple bending deflection represented by the first term in the right hand side of Eqn. (2.26), can be replaced by the corresponding expression for the tapered shape (Ref. 57), i.e.,

$$\delta_b = \frac{12P}{Eb\lambda^3}\left[\ln\left(\frac{a+e}{e}\right)+\frac{e(4a+3e)}{2(a+e)}-\frac{3}{2}\right]$$

Thus, the total arm deflection δ for the TDCB is

$$\delta = \frac{12P}{Eb\lambda^3}\left[\ln\left(\frac{a+e}{e}\right)+\frac{e(4a+3e)}{2(a+e)}-\frac{3}{2}\right]+\frac{8.212Pa^2}{Ebh_a}+\frac{3.75Pa}{Ebh_a} \qquad (2.44)$$

where, $G = E/2.5$

Therefore, the specimen compliance is given by

$$C = \frac{24}{Eb\lambda^3}\left[\ln\left(\frac{a+e}{e}\right)+\frac{e(4a+3e)}{2(a+e)}-\frac{3}{2}\right]+\frac{16.424}{Eb}\left(\frac{a}{h_a}\right)^2+\frac{7.5}{Eb}\left(\frac{a}{h_a}\right) \qquad (2.45)$$

In Fig. 2.7 the compliance C is plotted versus the crack length a for various taper slopes. These graphs show that beyond a crack length of 20mm the behaviour of C is approximately linear. As already stated earlier, a linearly varying compliance is beneficial, in that it gives a constant dC/da. On the other hand, the value of λ should not go beyond the validity of the simple theory of flexure.

The strain energy release rate for the TDCB specimen can be obtained readily by substituting the right hand side of Eqn. (2.45) into Eqn. (2.39), i.e.,

$$g = \frac{P^2}{Eb^2h_a^2}\left[\frac{12a^2}{h_a} + 16.424e\lambda\left(\frac{a}{h_a}\right) + 3.75e\lambda\right] \qquad (2.46)$$

or, at the onset of crack propagation Eqn. (2.46) becomes,

$$g_c = \frac{P_c^2}{Eb^2h_a^2}\left[\frac{12a^2}{h_a} + 16.424e\lambda\left(\frac{a}{h_a}\right) + 3.75e\lambda\right] \qquad (2.47)$$

In terms of the stress intensity factor K_I [see the first of Eqns. (2.42)], Eqn. (2.46) becomes

$$\frac{K_I\, bh_a^{\frac{1}{2}}}{P} = 2\sqrt{3}\left[(1-1.37\lambda)\left(\frac{a}{h_a}\right)^2 + (1.37-0.313\lambda)\left(\frac{a}{h_a}\right) + 0.313\right]^{\frac{1}{2}} \qquad (2.48)$$

The stress intensity factor coefficient $K_I bh_a^{\frac{1}{2}}/P$ is plotted in Fig. 2.8 for various values of λ. It is seen that the lines form a bunch like shape. These are entirely linear for relatively small tapers, and they depart gradually from linearity near $a/h_a = 0$ as the taper is increased. For the range of taper considered the lines meet the a/h_a-axis at $a/h_a \simeq -0.685$. Therefore, for small tapers we may write

$$\frac{K_I\, bh_a^{\frac{1}{2}}}{P} = \psi\left(\frac{a}{h_a} + 0.685\right) \qquad (2.49)$$

where ψ is a λ-dependent function representing the slopes of the lines shown in Fig. 2.8. Srawley and Gross (Ref. 41) found, from their boundary collocation analysis, that the intercept $a/h_a = 0.7$. Srawley and Gross (Ref. 41) derived the following formula from fitting their elasticity results to a set of straight lines such as those shown

in Fig. 2.8:

$$\frac{K_I b h_a^{\frac{1}{2}}}{P} = \Lambda\left(\frac{a}{h_a} + 0.7\right) \qquad (2.50)$$

where Λ is a taper dependent implicit function which represents the slopes of the lines in the $K_I b h_a^{\frac{1}{2}}/P$ versus a/h_a graphs of Ref. 41. The suspicion of Srawley and Gross that the linear relation (2.50) would not apply to actual specimens with small a/h_a (i.e., higher taper angle), is confirmed by the results shown in Fig. 2.8 wherein a departure from linearity can be detected as λ grows bigger.

An attempt to estimate the factor ψ in Eqn. (2.49), by comparing the compliance C given by Eqn. (2.45), and another corresponding expression obtained through integration from combining Eqns. (2.39), the first of (2.42) and (2.49), gives

$$\psi = 2\sqrt{3}\ (1 + 1.37\lambda + 0.47\lambda)^{-\frac{1}{2}} \qquad (2.51)$$

It must be mentioned however that the above estimate is quite crude because it has been obtained by comparing the coefficients of $\ln\ [(a+e)/e]$ in the two compliance expressions. However, besides its simplicity, Eqn. (2.49) follows quite well the graphs shown in Fig. 2.8 for $\lambda \leq 0.4$.

Let us recall one particular assumption which remains at the origin of the present analysis; the specimen containing the crack has a semi-infinite uncracked portion beyond the crack tip. In practice, the double cantilever beam specimen has finite dimensions and, therefore, we are bound to explain how much length the uncracked portion has before the end hinge effects are felt. Srawley and Gross (Ref. 41) approached the problem and identified two hinge-effected and non affected regions within the specimen, depending on the range of a/L, where a/L is the ratio of the crack length to the distance between

the load line and the specimen base ahead of the crack tip [see Fig. 2.6(a)]. Their conclusions are:

1. for $a/L < 0.7$; the dimensionless stress intensity factor, $K_I bh_a^{\frac{1}{2}}/P$, follows Eqn. (2.50), and
2. for $a/L \geq 0.7$, the behaviour is governed by the following equation, which the authors (Ref. 41) obtained by reformulating and adopting Eqn. (181) of Ref. 58 so that

$$\frac{K_I bL^{\frac{1}{2}}}{P_c} = \frac{0.537 + 2.17\ (1 + a/L)\ /\ (1 - a/L)}{(1-a/L)^2} \qquad (2.52)$$

Let us now examine our theory in the light of the above conclusions and the experimental results of Mai, Atkins and Caddell (Ref. 56) by reformulating Eqn. (2.47) as follows:

$$\frac{P_c^*}{(ELg_c)^{\frac{1}{2}}} = \frac{\lambda^{3/2}\ (z + s)^{3/2}}{[12z^2 + 16.424\ sz\lambda + 3.75(z+s)\ s\lambda^2]} \qquad (2.53)$$

where [see Fig. 2.6(a)], $P_c^* = P_c/b$ is the critical applied load per unit width, $s = e/L$ and $z = a/L$.

The dimensionless load coefficient $P_c^*/(ELg_c)^{\frac{1}{2}}$ is plotted versus z in Fig. 2.9 along with the experimental results, for the PMMA tapered double cantilever beam test specimens, taken from Ref. 56. The dotted curve in Fig. 2.9 represents Eqn. (2.52) after being arranged as in Eqn. (2.53). It is seen from the graphs that the agreement of the present analysis with the experimental data is very good up to a value of a/L around 0.7 and, that for higher values of this ratio the experimental data tend to follow Eqn. (2.52) as concluded by Srawley and Gross (Ref. 41). The simplicity and the remarkable agreement with experiments of Eqn. (2.47) [or equivalently Eqn. (2.53)] make this a

reliable candidate in future fracture toughness measurement of a certain material.

2.5 CRACK STABILITY

In conclusion of this Chapter, the crack stability criterion is established for the TDCB specimen shown in Fig. 2.6(a). Atkins et al. Ref. 59 state that crack stability means different things to different people. This statement is somehow vague, however, and it reflects the author's view that some misunderstanding surrounds the notion. For example, 'Stability of Cracking' is used occasionally to describe whether a propagating crack deviates from its original path, as pointed out in Ref. 61. A second example is given by Ripling et al. in Ref. 44, where the authors used the words 'Stability' and 'Instability' in a somewhat misleading context in their study of adhesive joints employing double cantilever beam techniques. They called 'Stable' and 'Unstable', respectively, the flat and saw-like behaviours of the applied load versus the crack opening displacement. This contradicts clearly the stability statement as laid out in Ref. 55. It is more appropriate in fact to call the saw-like behaviour as a mixture of instability and stability behaviour as shown in Ref. 61.

A crack is said to be in a stable, neutral equilibrium, or unstable condition according to whether the rate of change of the kinetic energy [see Eqn. (2.33)] per unit of fractured area is negative, zero or positive respectively (Ref. 55), i.e.,

$$\frac{dU}{dA} < \frac{dW}{dA} + \frac{dZ}{dA} \qquad \text{(for stability)}$$

$$\frac{dU}{dA} = \frac{dW}{dA} + \frac{dZ}{dA} \qquad \text{(for neutral equilibrium)}$$

and $\frac{dU}{dA} > \frac{dW}{dA} + \frac{dZ}{dA}$ (for instability)

The above are very general statements, and are not limited by any particular body shape nor by any particular boundary conditions. The interested reader may find Ref. 63 particularly valuable for a better understanding of the crack stability problem.

The crack stability concept is not intended usually for finite structural components. The concept has been brought about by the need to be able to design crack-tractable test specimens which can be reliably used in studying the fracture characteristics of a certain material. On the other hand, a finite structural component should not contain cracks unless it is intended to, otherwise, the designer should make sure that a crack will not propagate under service loading conditions.

A typical application of the crack stability is offered by Gurney's irreversible work area method (Ref. 34) for measuring the critical energy release rate g_c, where, a quasi-static stable crack propagation is necessary for the method to suffice, as pointed out by Mai and Atkins in Ref. 60.

All stability criteria are subject to certain constraints such as the stiffness of the testing rig. Two cases of practical interest are considered here (Ref. 34)

1) a monotonically increasing load ($dP>0$) which occurs with a continuously operated soft testing machine, and

2) a monotonically increasing deflection ($d\Delta > 0$) which occurs for a continuously operated hard testing machine.

The above stability conditions may be written as (Ref. 62)

$$\frac{1}{g_c}\frac{dg_c}{da} > \frac{d^2C/da^2}{dC/da} \qquad \text{(for } dP>0\text{)} \tag{2.54}$$

and,

$$\frac{1}{g_c}\frac{dg_c}{da} > \frac{d^2C/da^2}{dC/da} - 2\frac{dC/da}{C} \qquad \text{(for } d\Delta > 0\text{)} \tag{2.55}$$

After substituting for the compliance from Eqn. (2.45) the inequalities (2.54) and (2.55) become respectively

$$\frac{1}{g_c}\frac{dg_c}{da} > \frac{1}{a}\left[\frac{12z^2(2s-z)+16.424zs\lambda(s-2z)-7.5zs\lambda^2(z+s)}{(z+s)(12z^2+16.424zs\lambda)+3.75s\lambda^2(z+s)^2}\right] \tag{2.56}$$

and,

$$\frac{1}{g_c}\frac{dg_c}{da} > \frac{1}{a}\left[\frac{12z^2(2s-z)+16.424zs\lambda(s-2z)-7.5zs\lambda^2(z+s)}{(z+s)(12z^2+16.424zs\lambda)+3.75s\lambda^2(z+s)^2} - 2\frac{12z^3+16.424z^2s\lambda+3.75zs\lambda^2(z+s)}{12(z+s)[(z+s)^3\ln(1+z/s)-zs-1.5z^2]+8.212z^2\lambda(z+s)+3.75z\lambda^2(z+s)^2}\right] \tag{2.57}$$

The righthand sides of expressions (2.56) and (2.57) are known as the geometrical stability factors (g.s.f), which may be given, respectively, the contracted notations (n_P/a) and (n_Δ/a); where n_P and n_Δ are dimensionless numbers given by the expressions enclosed between brackets. The above statements [(2.56) and (2.57)] may also be written, respectively, in contracted notation as follows:

$$\frac{a}{g_c}\frac{dg_c}{da} > n_P \tag{2.58}$$

and,

$$\frac{a}{g_c}\frac{dg_c}{da} > n_\Delta \qquad (2.59)$$

The dimensionless critical energy release rate $(a/g_c)(dg_c/da)$, which appears in both the lefthand sides of expressions (2.58) and (2.59), can be evaluated through straightforward substitution from Eqn. (2.47). This quantity is plotted versus z (=a/L) in Figs. 2.10 and 2.11, for two values of s (=e/L = 0.25, 0.4) and various values of the taper slope λ. The dimensionless g.s.f. coefficients n_P and n_Δ are evaluated, respectively, from the right hand sides of expressions (2.56) and (2.57) and, plotted versus z for s=0.25, 0.4, and for several λ's as shown in Fig. 2.12 through to 2.15. For the load control case such as using a servo-hydraulic testing machine, comparison of the results from the left and right hand sides of expression (2.58) (Figs. 2.10 through to 2.13), reveals that, theoretically speaking, the stability in the load controlled situation improves with increasing z and increasing slope of taper λ, and that further improvement is obtained when s is increased which is equivalent to increasing h_a leaving the taper angle θ and z unchanged. These conclusions fall in line with those of Mai et al. (Ref. 56) for similar conditions. However, the stability margin in the load controlled case is quite small especially for lower z values and small angles of taper. On the other hand, the deflection controlled case ($d\Delta>0$), which is equivalent to using a hard testing machine such as 'a screw driven apparatus', shows negative values over the whole range of the parameters considered as shown in Figs. 2.14 and 2.15. These results fall well below the corresponding graphs of $(a/g_c)(dg_c/da)$ versus z shown in figs. 2.10 and 2.11. Therefore, it seems that, theoretically, the deflection controlled case offers a wider margin of stability

than the load controlled situation. However, unlike the latter, stability decreases with increasing z as shown clearly by the mutual approach of the corresponding graphs for n_Δ , and $(a/g_c)(dg_c/da)$ versus z (compare Figs. 2.10 and 2.11 with Figs. 2.14 and 2.15). It is also seen from examining Figs. 2.14 and 2.15 that the increase of the angle of taper reduces the stability and that a higher value of s has a beneficial effect in this respect. Therefore, for a hard testing machine ($n_\Delta > 0$), it is suggested that a test specimen with a relatively low angle of taper be used with the obvious advantage of remaining within the boundary of the simple theory of bending.

2.6 CONCLUSIONS

A simple theoretical elastic analysis has been given of the load deflection relationship for the DCB specimens. This analysis accounts approximately for the strains beyond the crack tip section. The analysis is based on a realistic model wherein the direct stresses due to bending at the crack tip section are used to find the corresponding horizontal displacements. These displacements are then used with the bending stresses, either directly or in a simplified graphically derived linear form, to calculate an expression for the strain energy stored beyond the root section. This energy in turn is equated to the external work done to obtain the tip deflection. Comparisons of the predicted deflection with the results of a previous elasticity solution wherein the complete strain field is obtained, and with a beam-on elastic foundation model, show reasonable agreement. Further comparisons with some published experimental work show that the present solution underestimates the deflection, as is expected when the limitations of the theory are considered. However, closer agreement

with the established data has been found for the calculated deflection using a linear displacement distribution along the specimen root section. This latter formulation of the end deflection has been followed through, and also adapted to a tapered double cantilever beam specimen (TDCB). The strain energy of bending stored in the arms of the DCB specimen, has been evaluated for both the tapered and straight shapes. Simple formulae which may be used reliably to calculate the fracture toughness of a certain material, have been derived for the strain energy release rate for the two considered geometries. For the parallel-arm DCB specimen, comparison of several computed stress intensity factors shows excellent agreement with the corresponding results from two elasticity solutions, as well as one from the elastic foundation model.

The dimensionless fracture strength of the TDCB, is compared with established experimental data, and very good agreement is found for values of z ranging up to 0.7.

The stability criterion has been established for the TDCB specimen with regard to both load and deflection controlled situations. In load control tests, the specimen is expected to be stable, but the stability margin is quite narrow. However, this margin widens as the angle of taper is increased, and stability is improved as the value of z grows bigger. As for the deflection controlled case, it has been found that the stability margin is wider; but an increase in the taper angle, and also in the value of z reduce stability, but not to the point to judge the specimen as unstable.

TABLE 2.1: DIMENSIONLESS STRESS INTENSITY COEFFICIENTS, $K_I bh^{3/2}/Pa$

a/h	$K_I bh^{3/2}/Pa$			
	Present analysis	Ref. 41	Ref. 42	Ref. 46
2	4.60	4.67	4.62	4.57
3	4.23	4.27	4.24	4.20
4	4.04	4.07	4.05	4.02
5	3.93	3.94	3.93	3.91
10	3.70	3.70	3.70	3.69

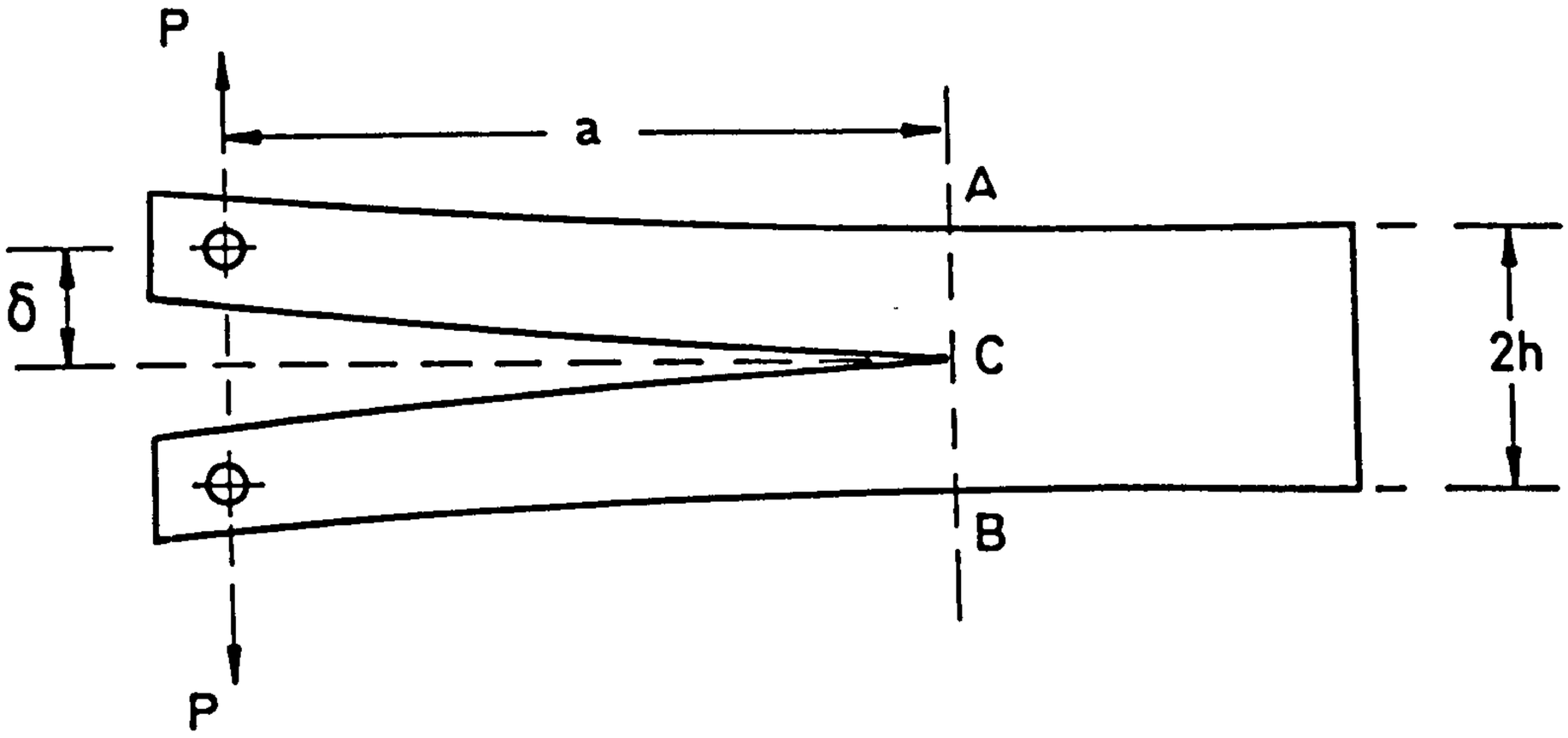

Fig. 1a Geometry and loading

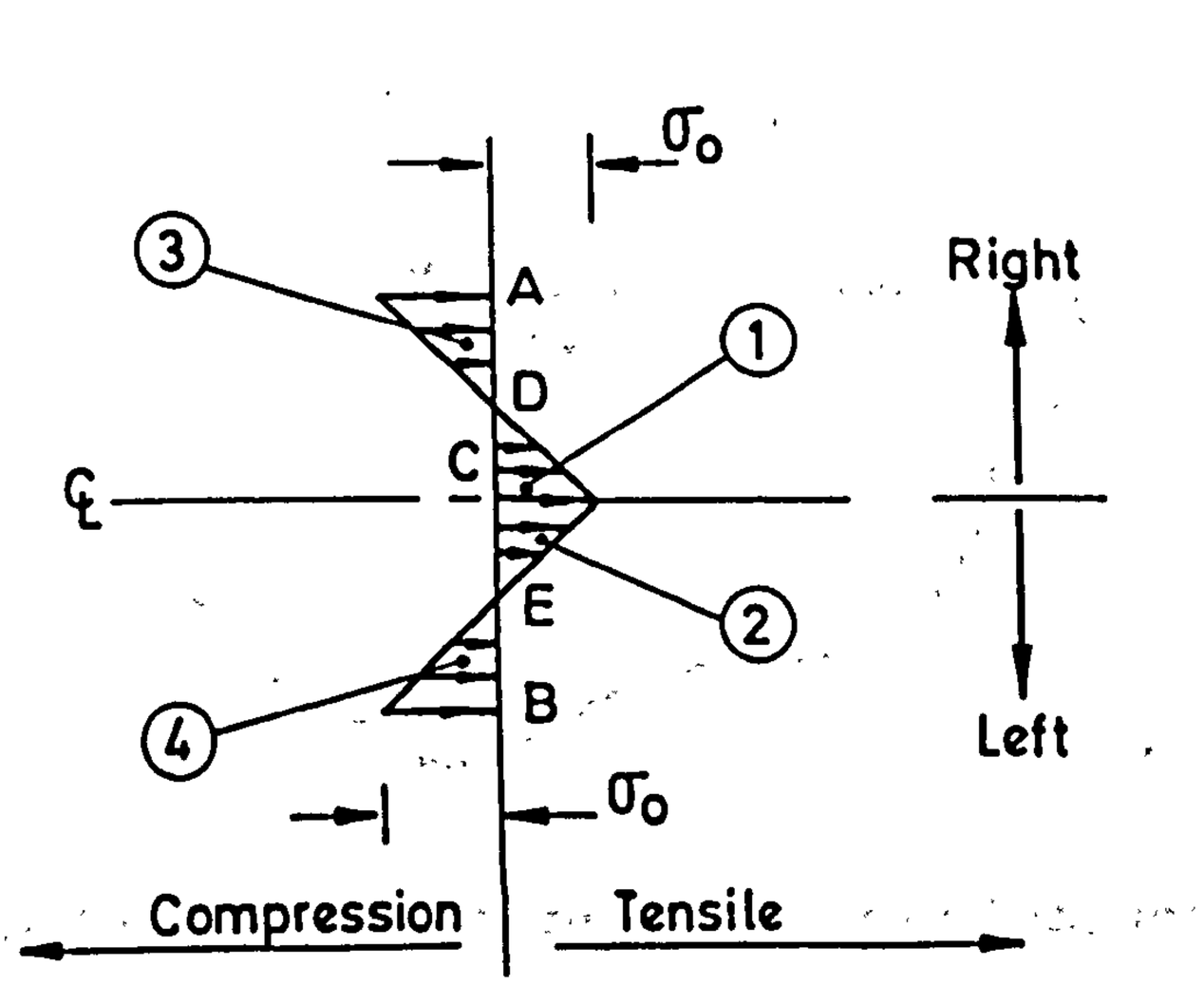

Fig. 1b Bending stress distribution across ACB

FIG. 2.1 DOUBLE CANTILEVER BEAM SPECIMEN

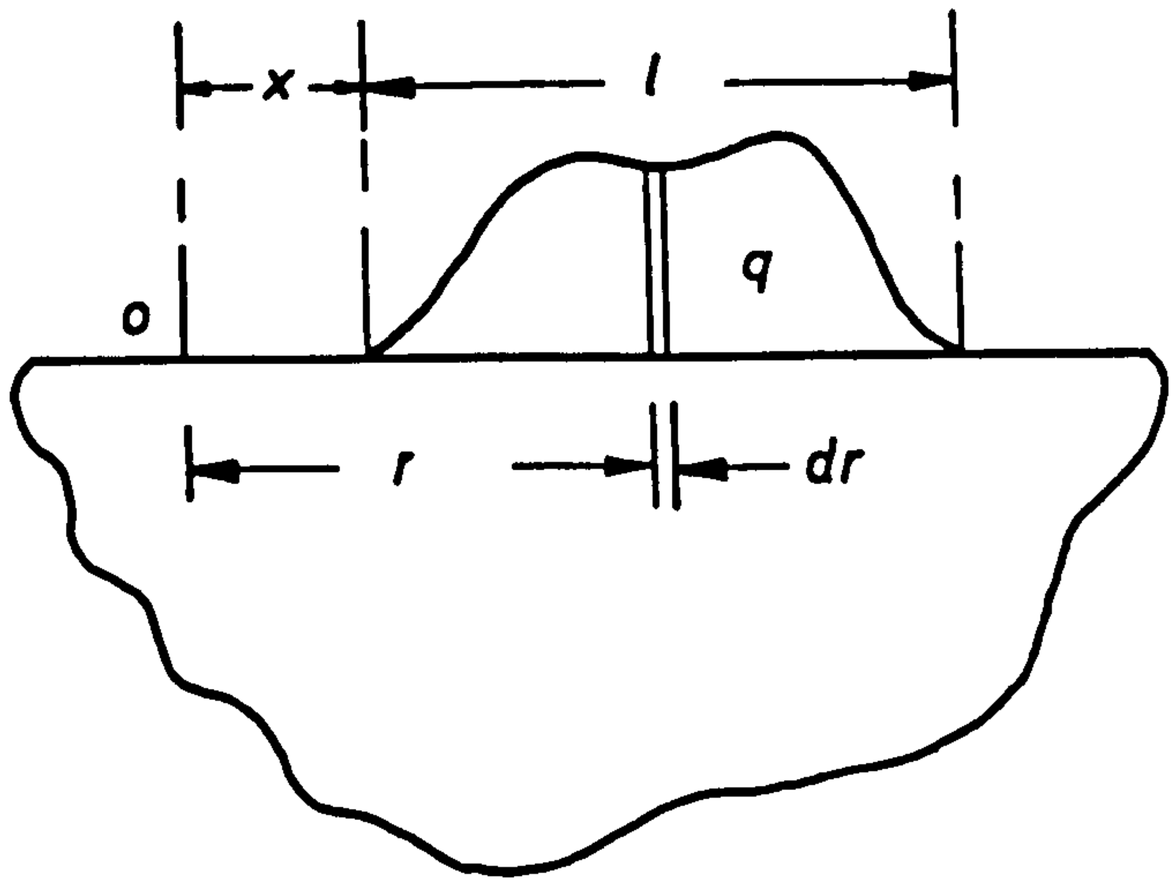

(a) Point 'o' outside the region of load distribution

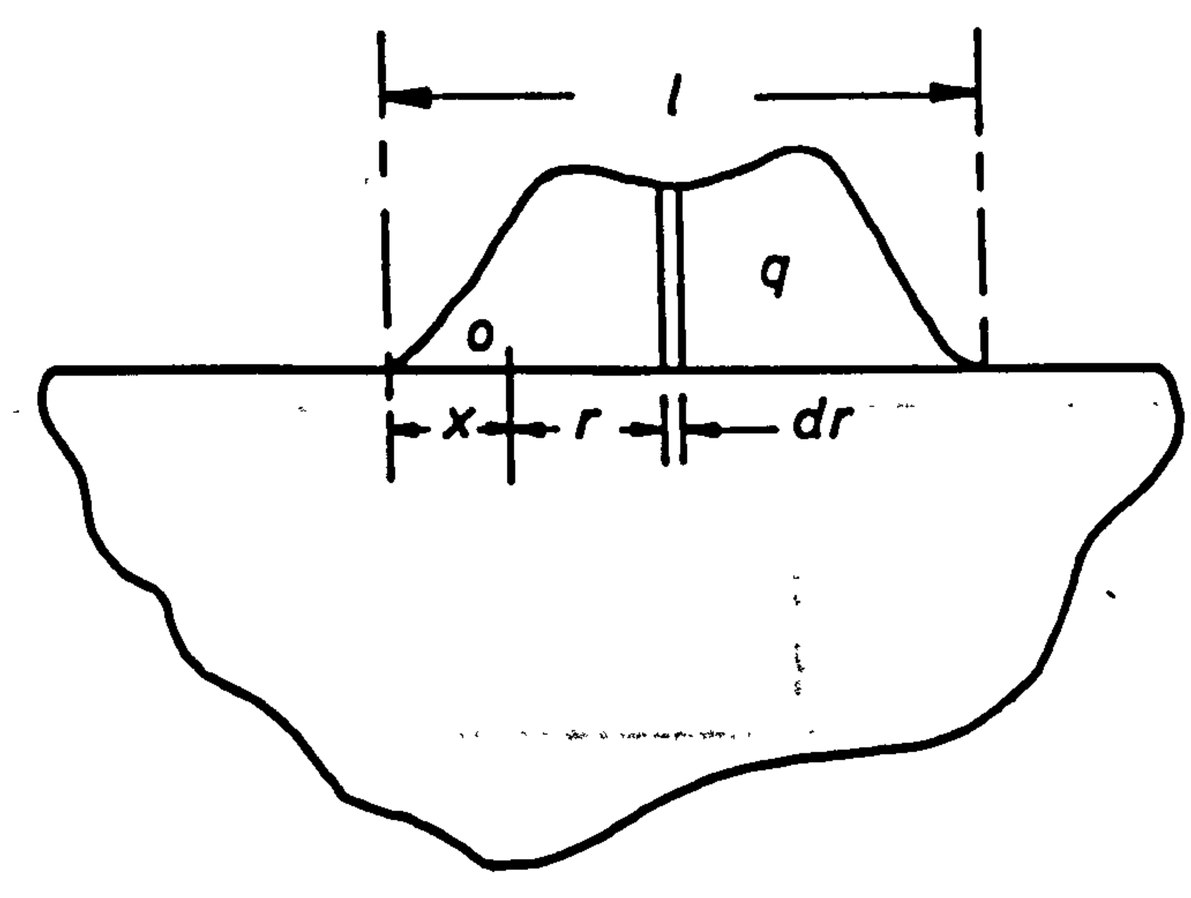

(b) Point 'o' inside the region of load distribution

FIG. 2.2 DISTRIBUTED LOADING ON SEMI-INFINITE PLATE

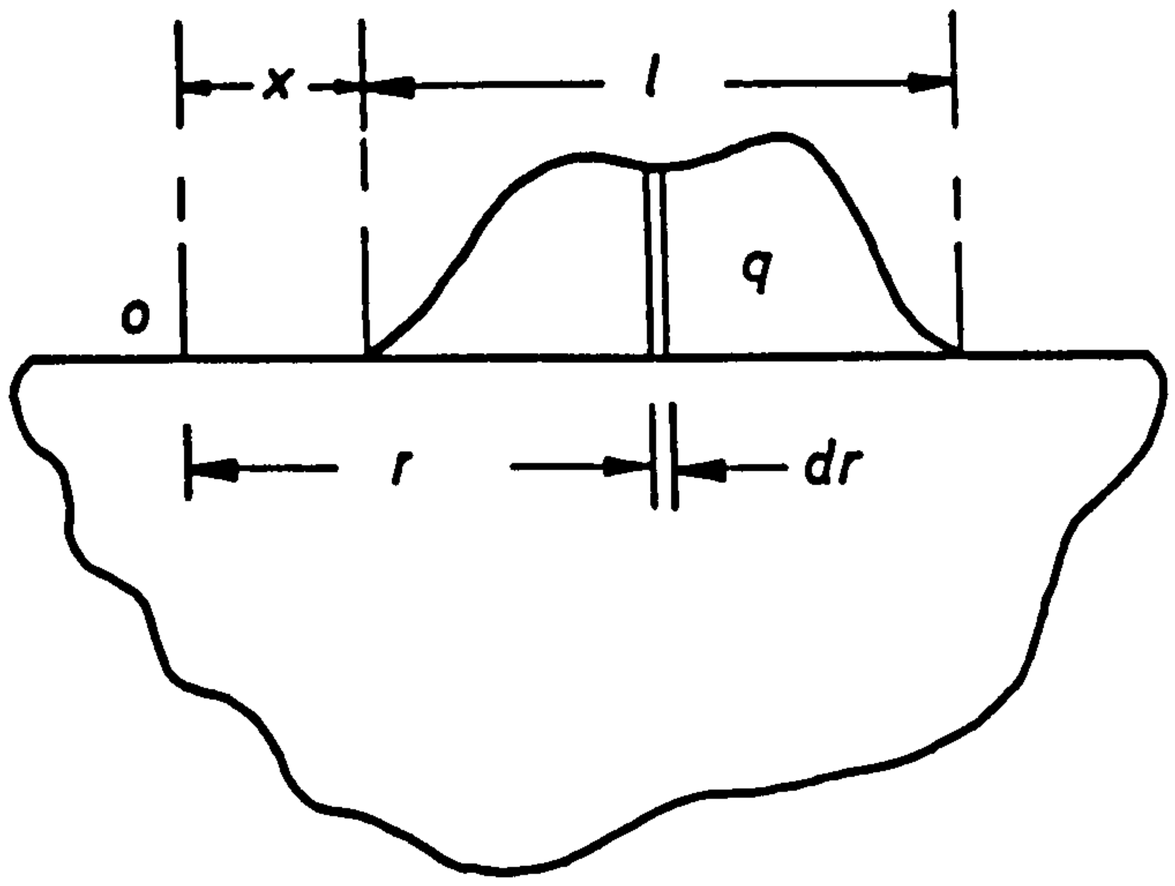

(a) Point 'o' outside the region of load distribution

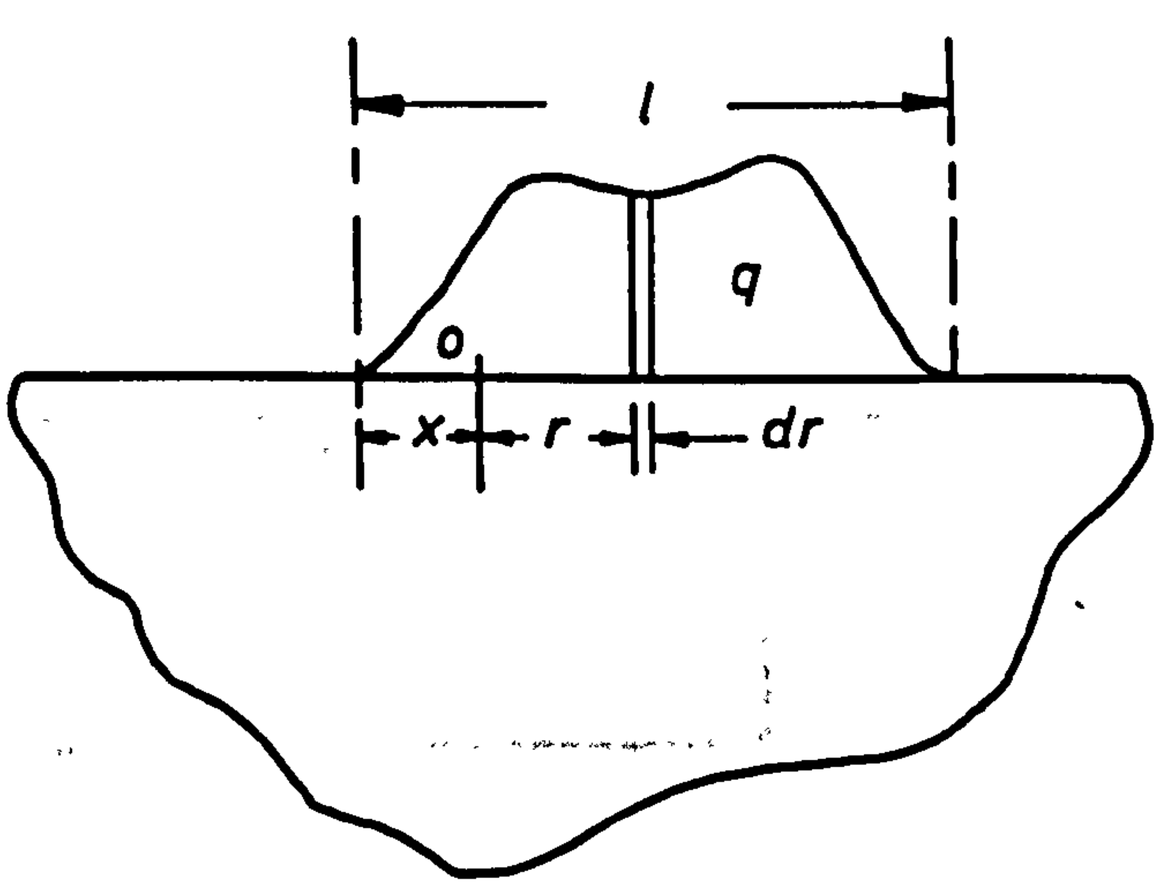

(b) Point 'o' inside the region of load distribution

FIG. 2.2 DISTRIBUTED LOADING ON SEMI-INFINITE PLATE

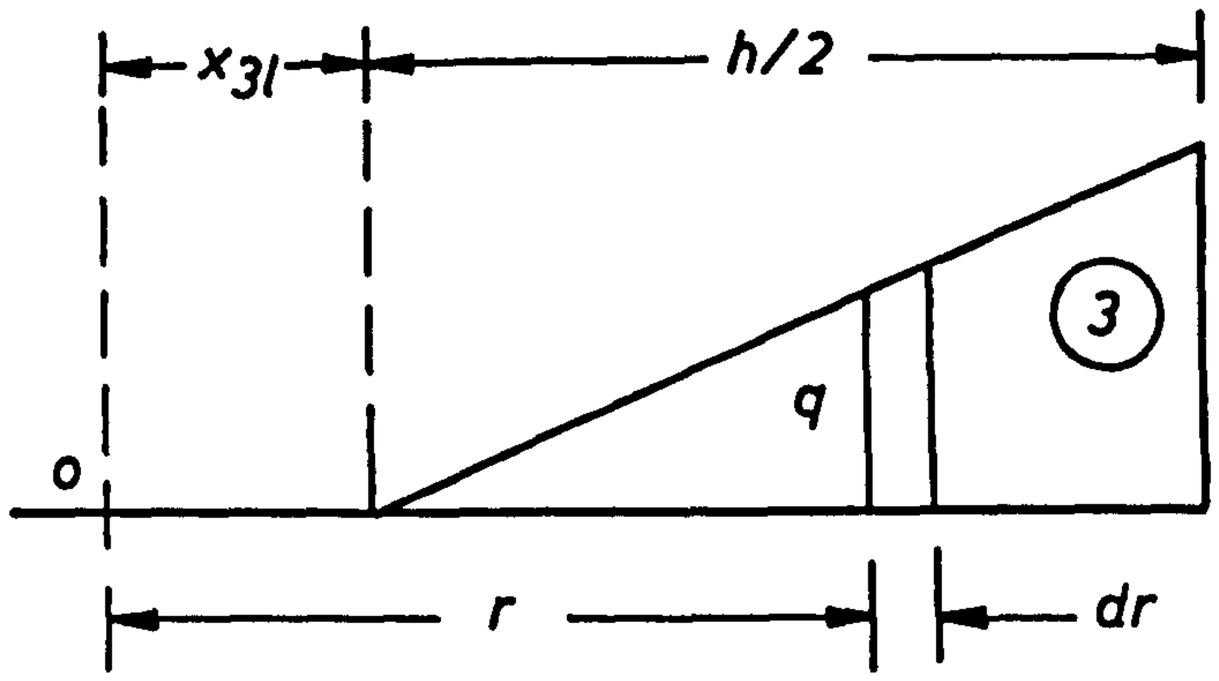

$$q = \frac{2(r - x_{31})}{h}\,\sigma_o$$

(a)

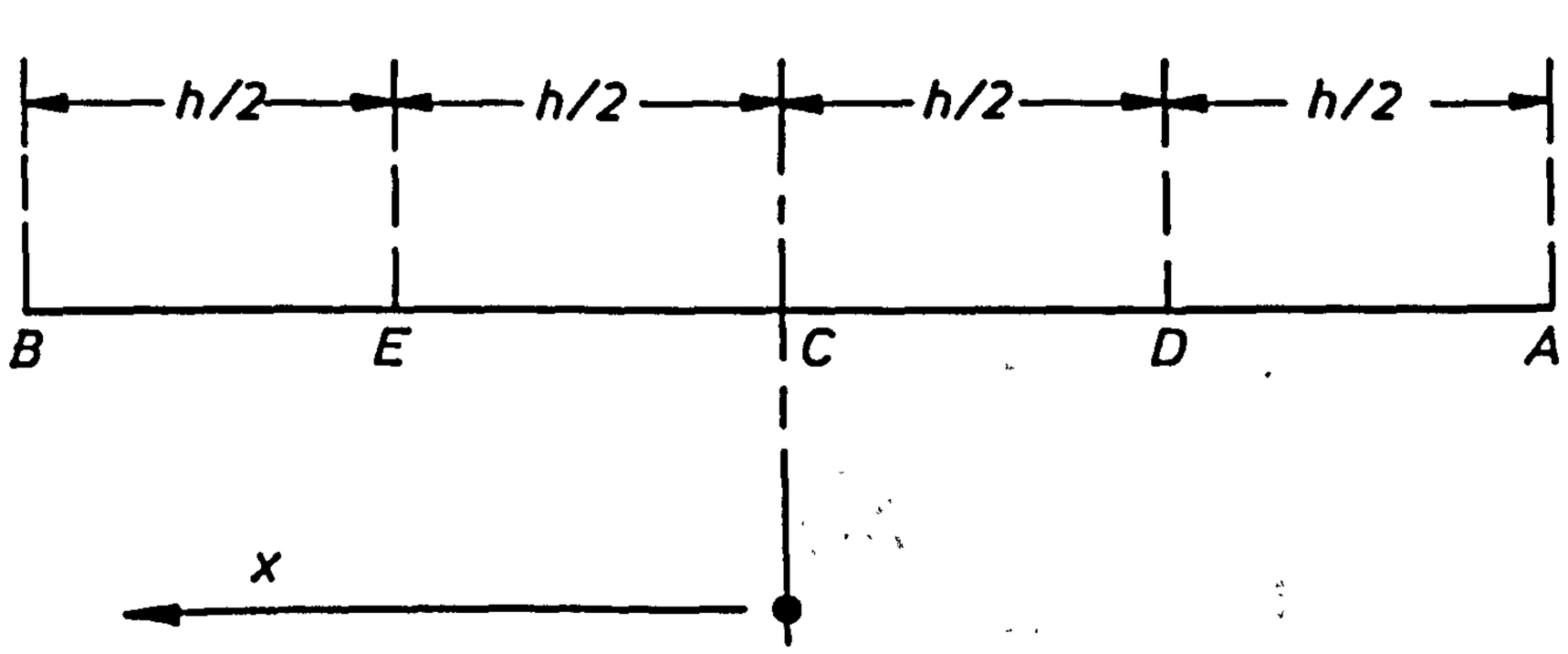

(b)

FIG. 2.3 (a) LOAD TRIANGLE No.3

(b) x - COORDINATE REPRESENTATION

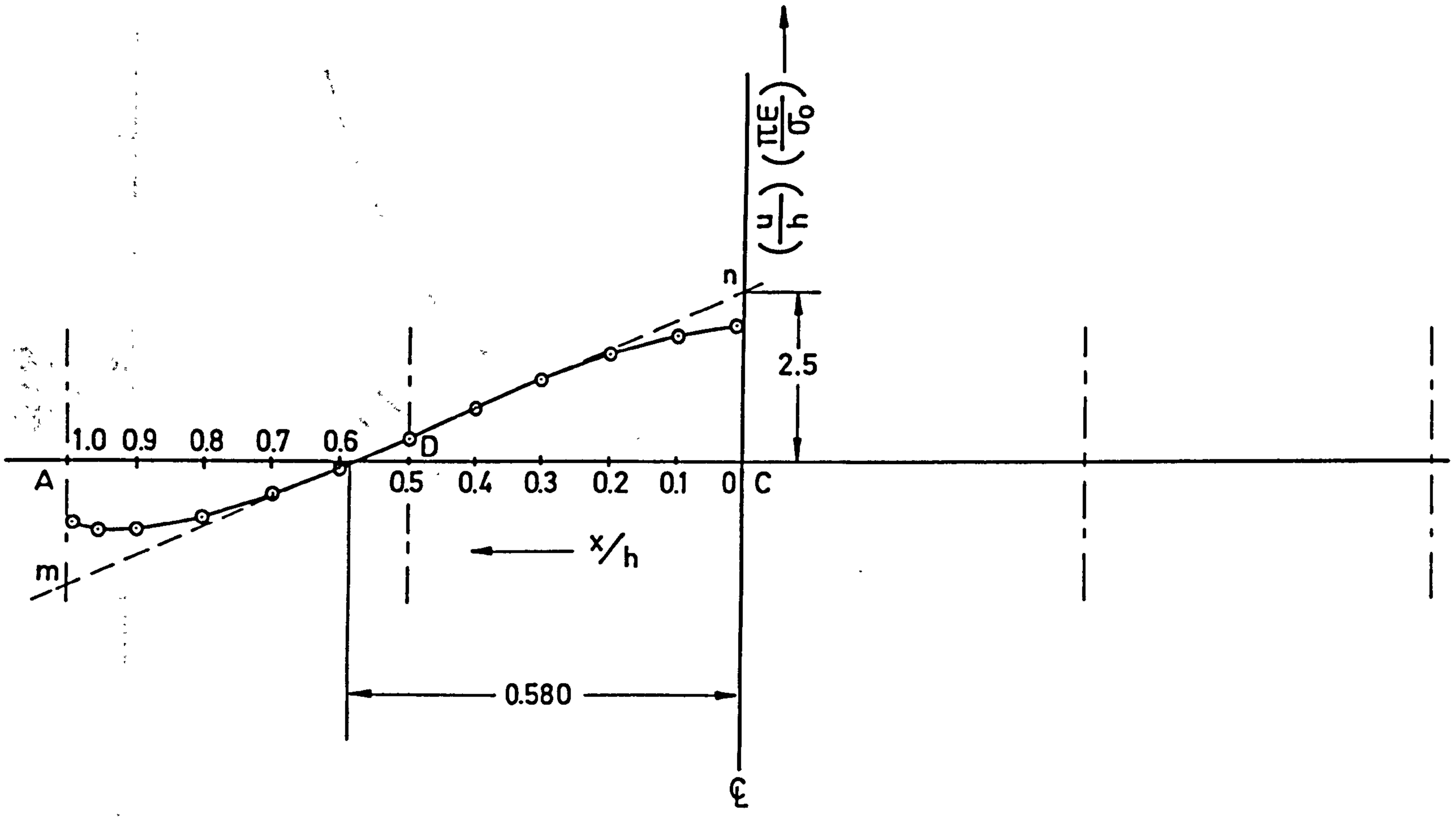

FIG. 2.4 THE NON-DIMENSIONAL DISPLACEMENT FACTOR $\left(\frac{u}{h}\right)\left(\frac{\pi E}{\sigma_o}\right)$ v x/h ALONG THE ROOT CROSS SECTION OF ONE DCB ARM

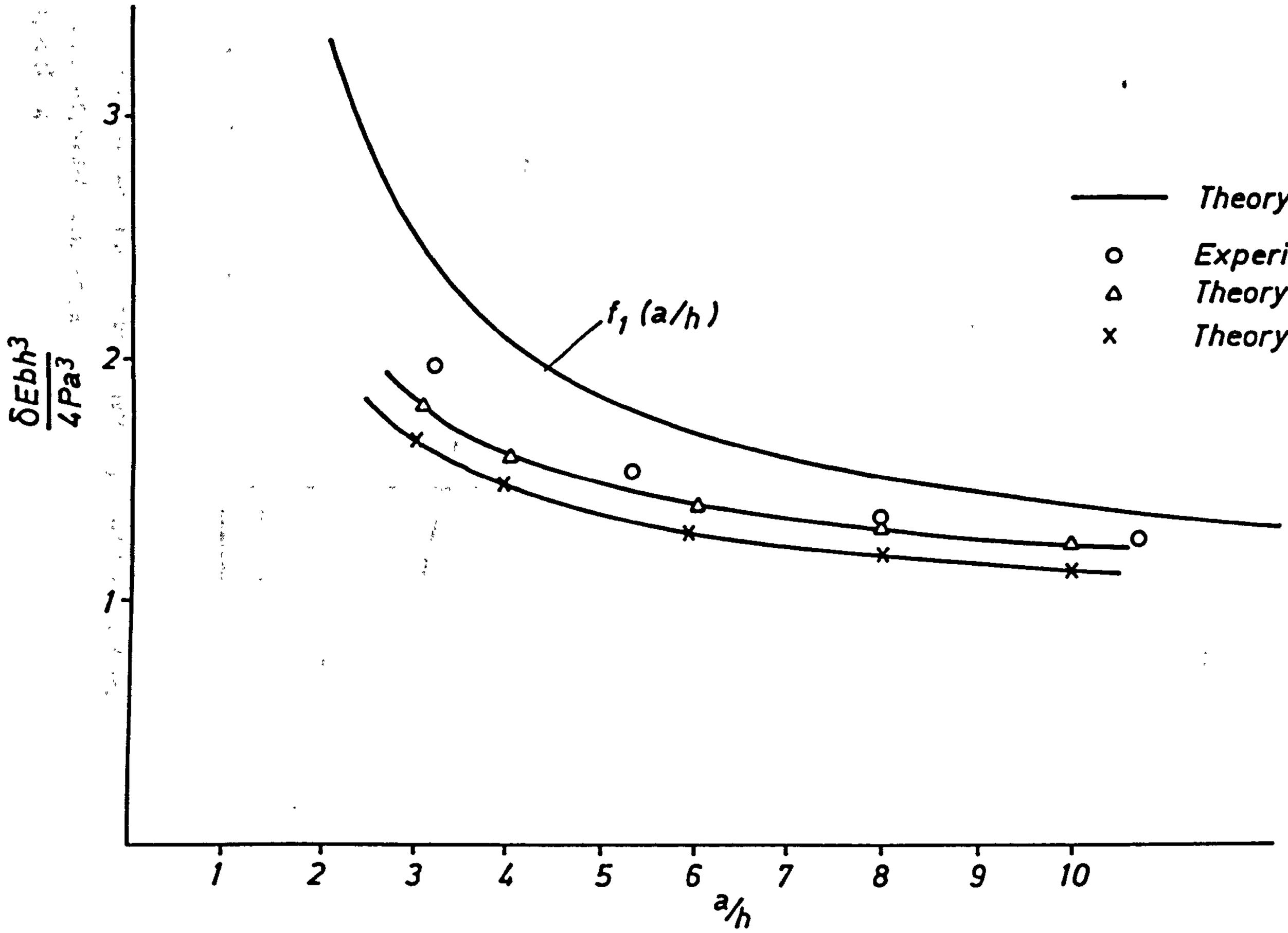

FIG.2.5 NON-DIMENSIONAL TIP DEFLECTION vs. a/h

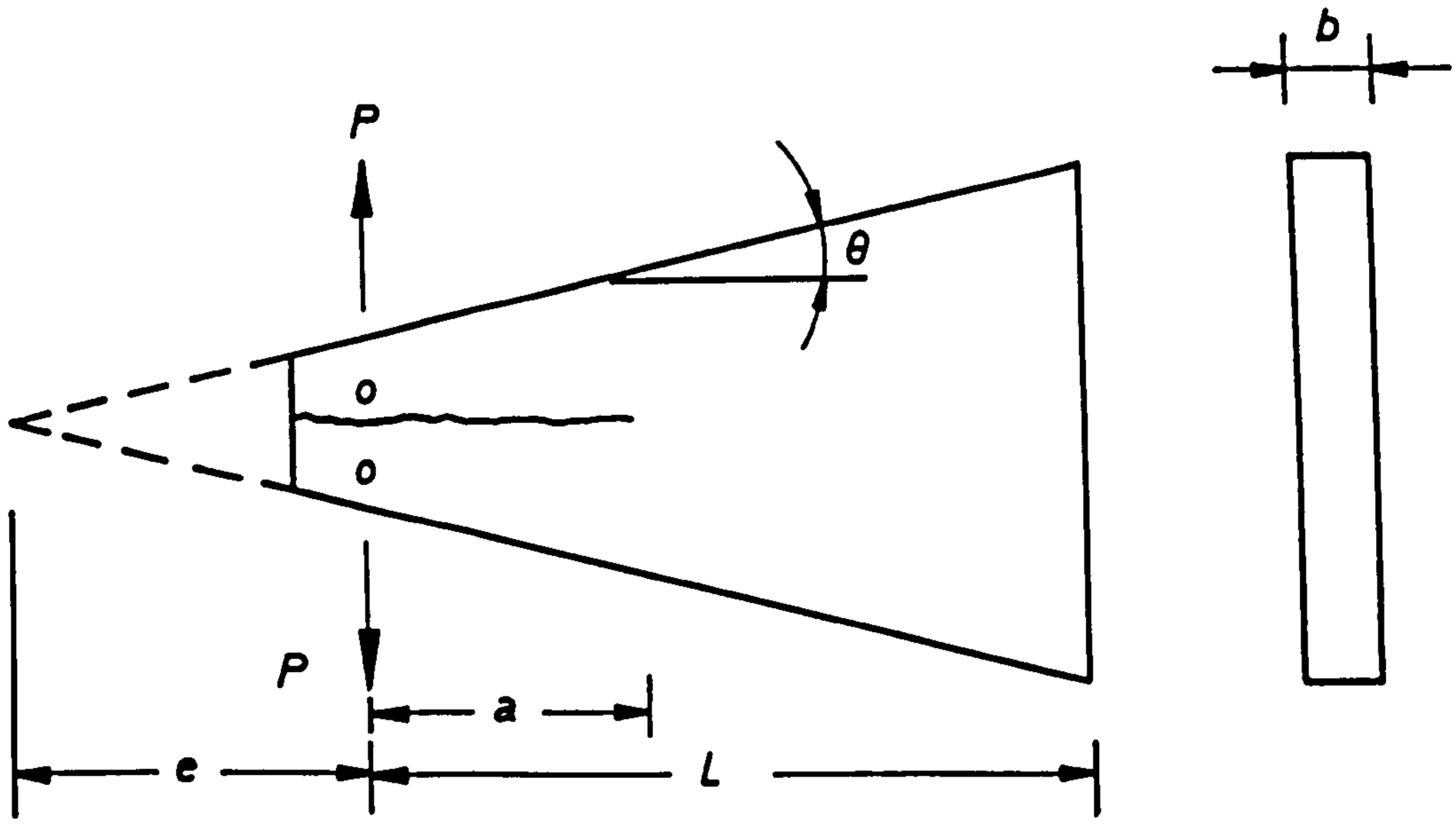

(a) Tapered double cantilever beam specimen (TDCB)
Load applied near the apex
$\tan \theta = \lambda$

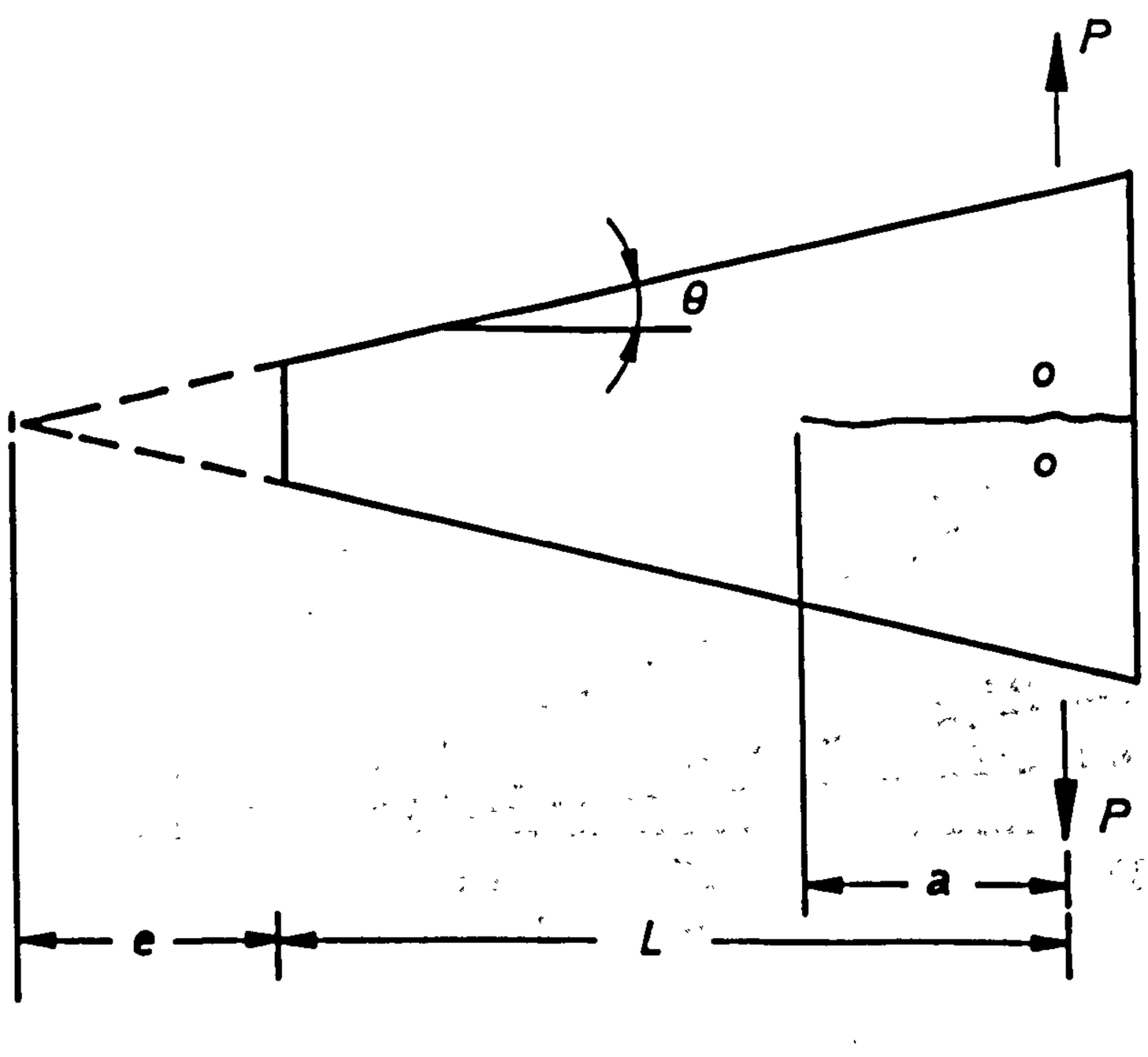

(b) Tapered double cantilever beam specimen (TDCB)
Load applied near max. height
$\tan \theta = \lambda$

FIG. 2.6 TAPERED DOUBLE CANTILEVER BEAM SPECIMEN (TDCB) CONFIGURATIONS AND LOADING

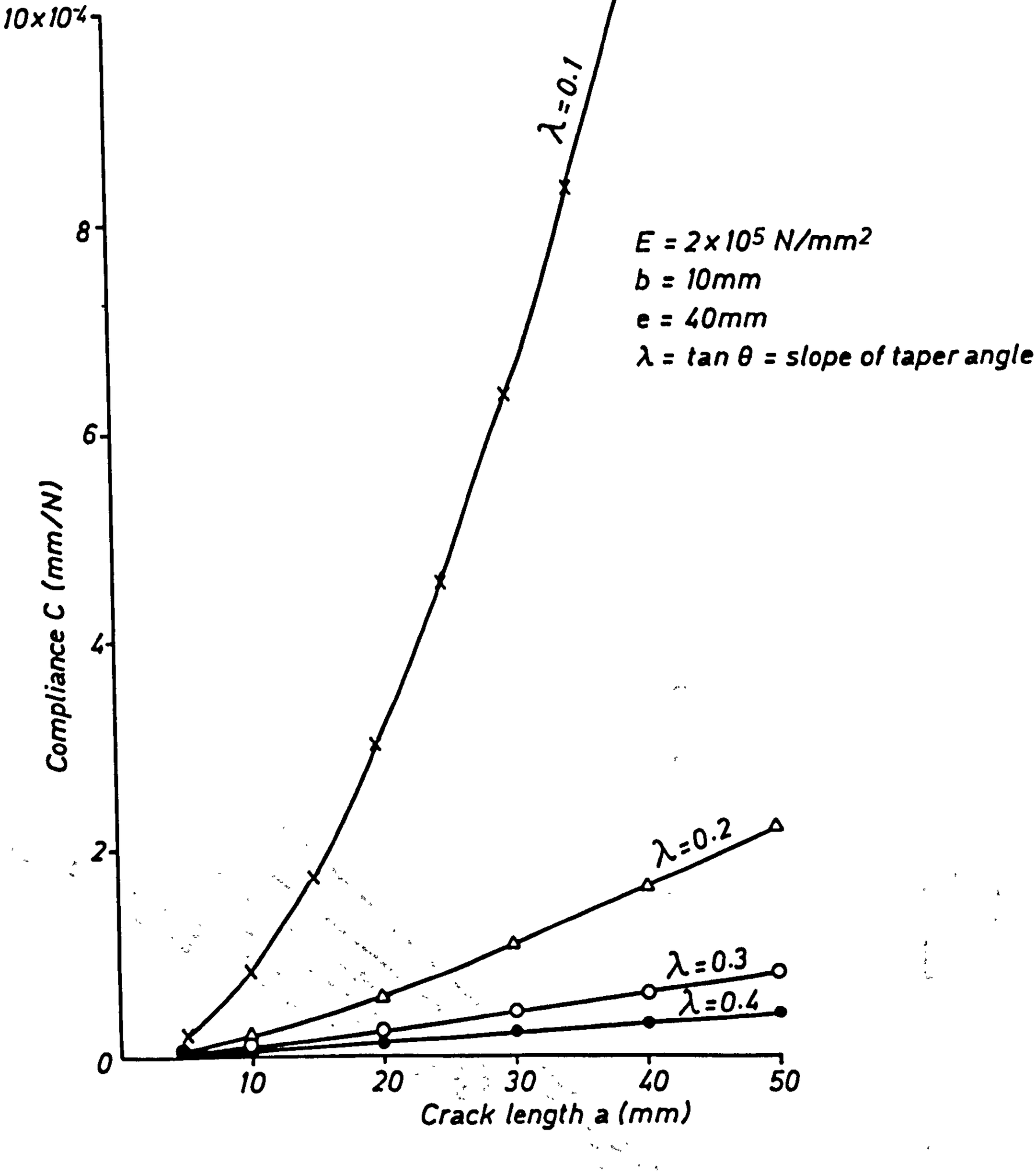

FIG. 2.7 TDCB COMPLIANCE VERSUS CRACK LENGTH

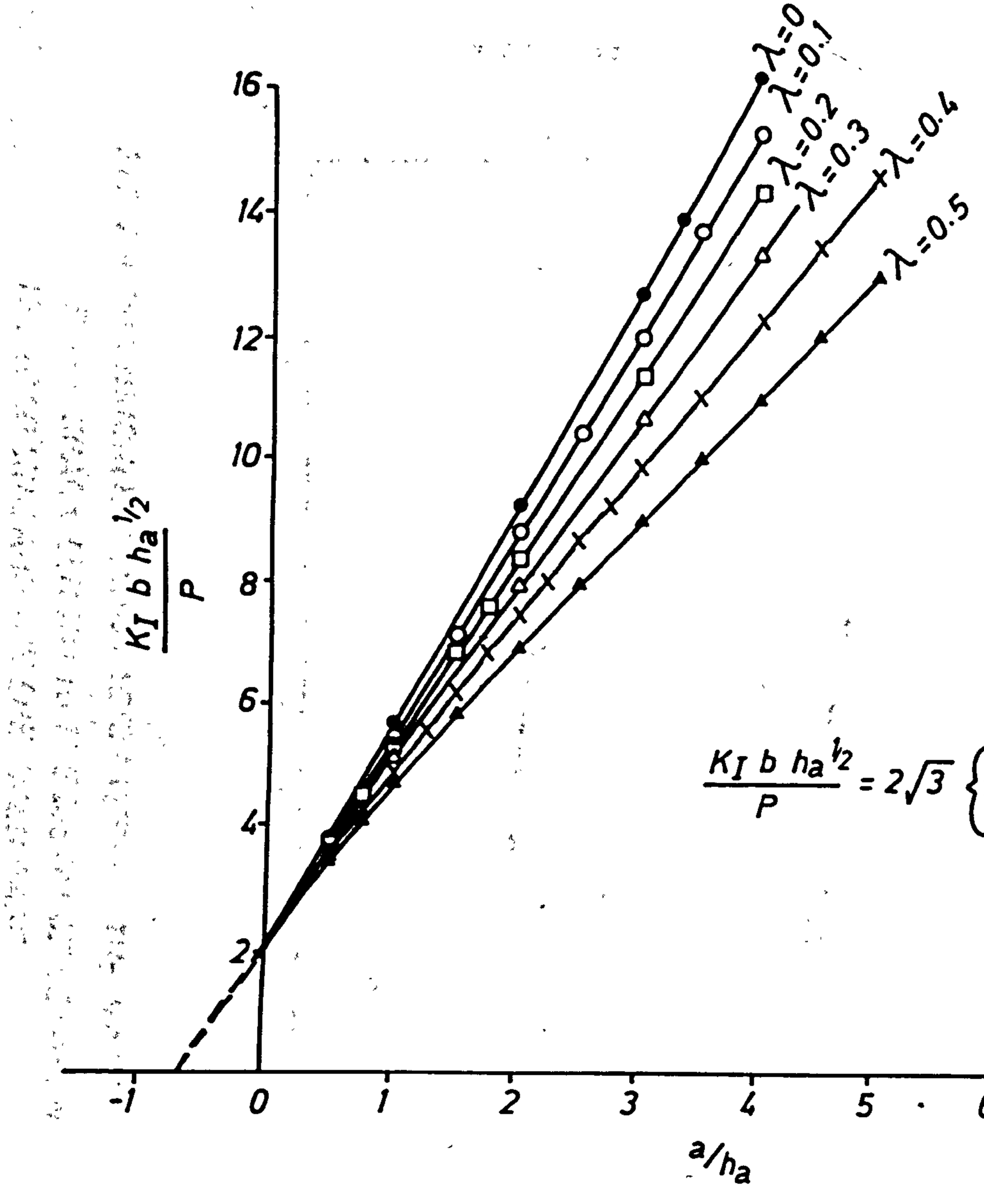

$$\frac{K_I\, b\, h_a^{1/2}}{P} = 2\sqrt{3}\left\{(1-1.37\lambda)\left(\frac{a}{h_a}\right)^2+(1.37-0.313\lambda)\left(\frac{a}{h_a}\right)+0.313\right\}^{1/2}$$

FIG. 2.8 STRESS INTENSITY COEFFICIENT VERSUS RATIO OF CRACK LENGTH TO TDCB ARM HEIGHT

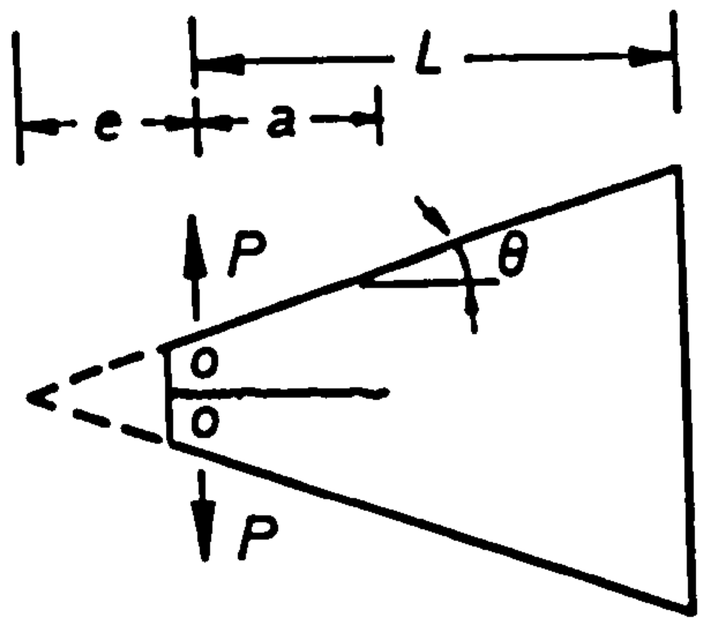

$\lambda = \tan\theta$

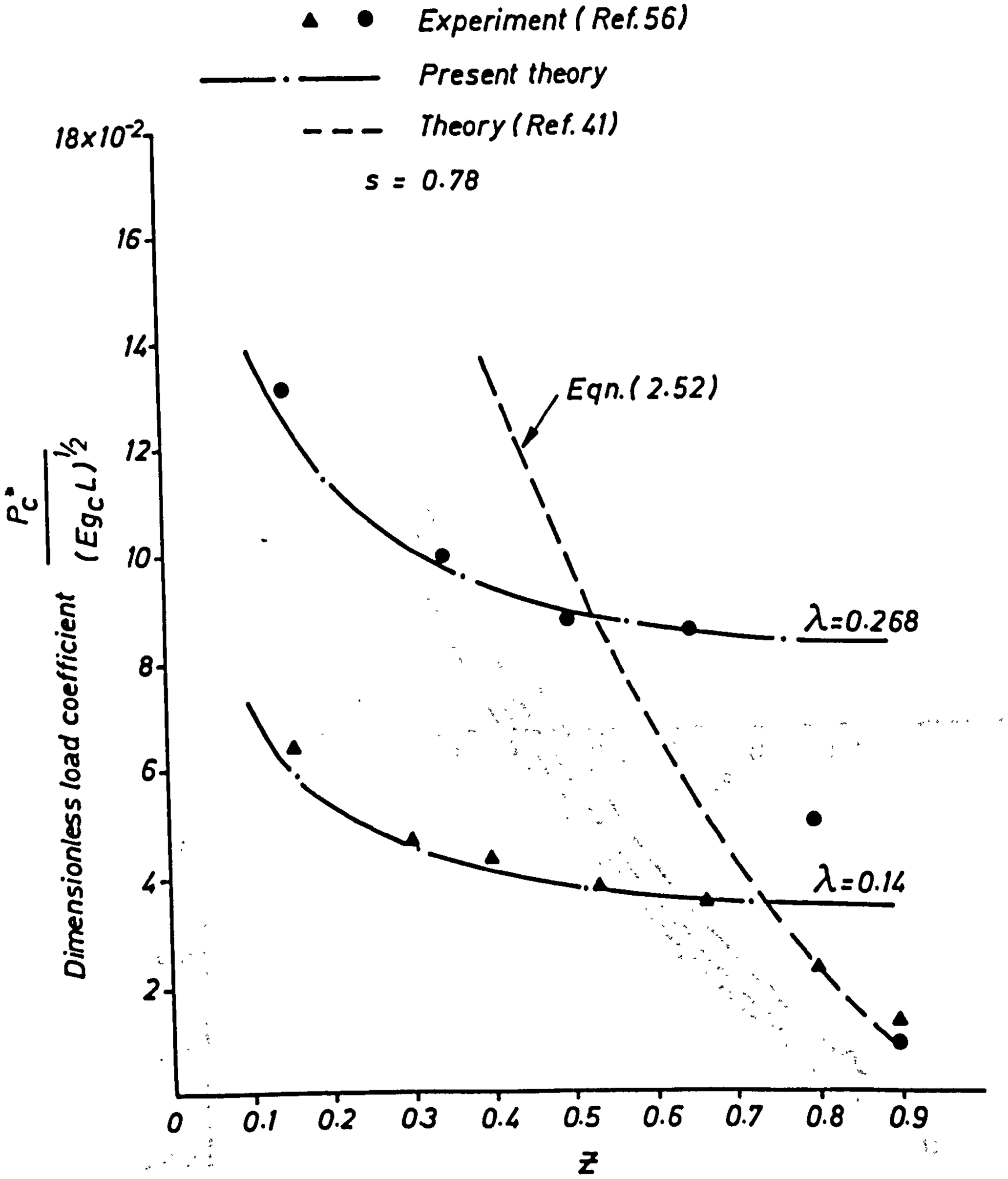

FIG. 2.9 DIMENSIONLESS LOAD FACTOR VERSUS THE RATIO OF THE CRACK LENGTH TO THE DISTANCE BETWEEN THE LOAD LINE AND THE SPECIMEN BASE

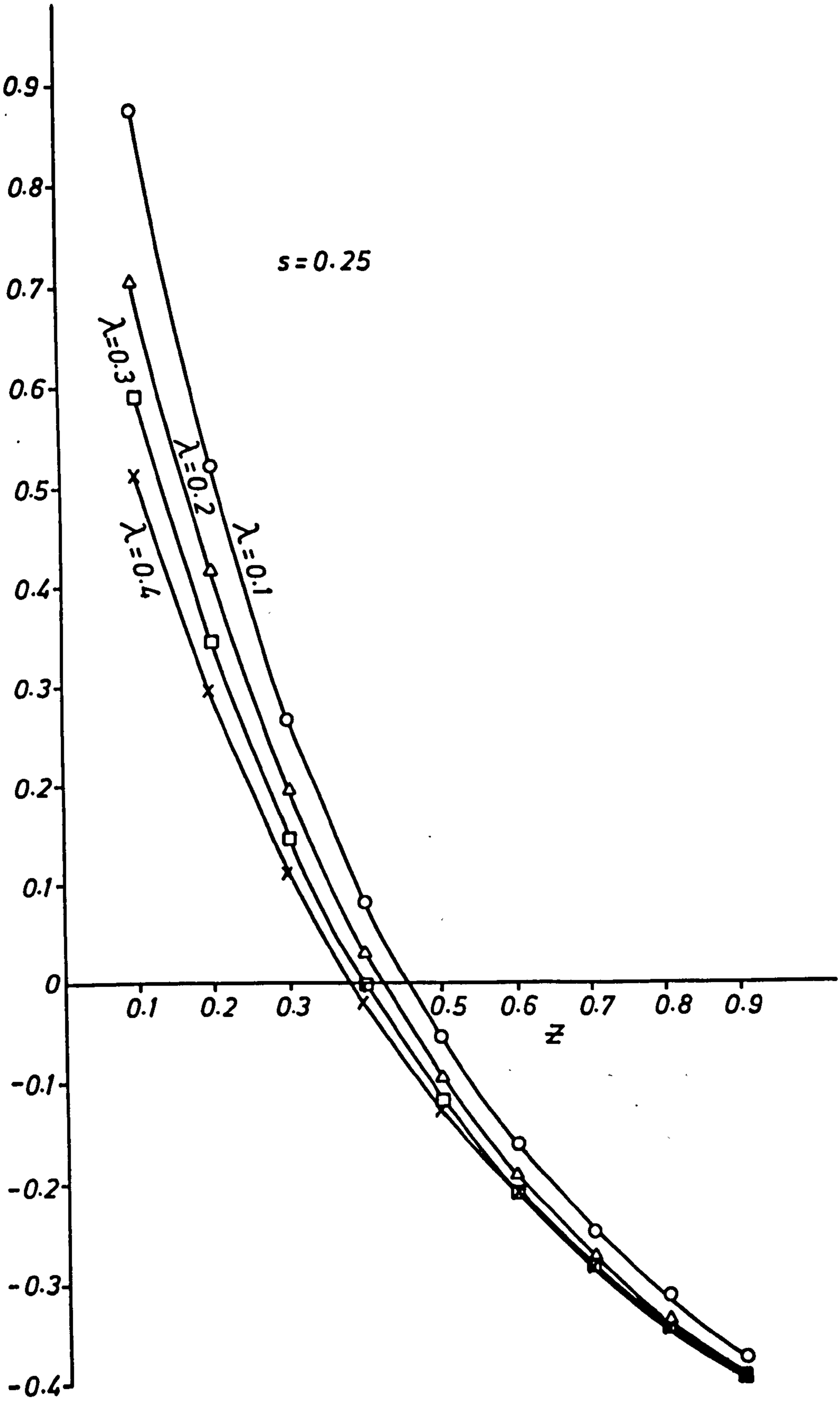

FIG. 2.10 DIMENSIONLESS CRITICAL ENERGY RELEASE RATE CHANGE $\frac{a}{g_c}\ \frac{dg_c}{da}$ VS z

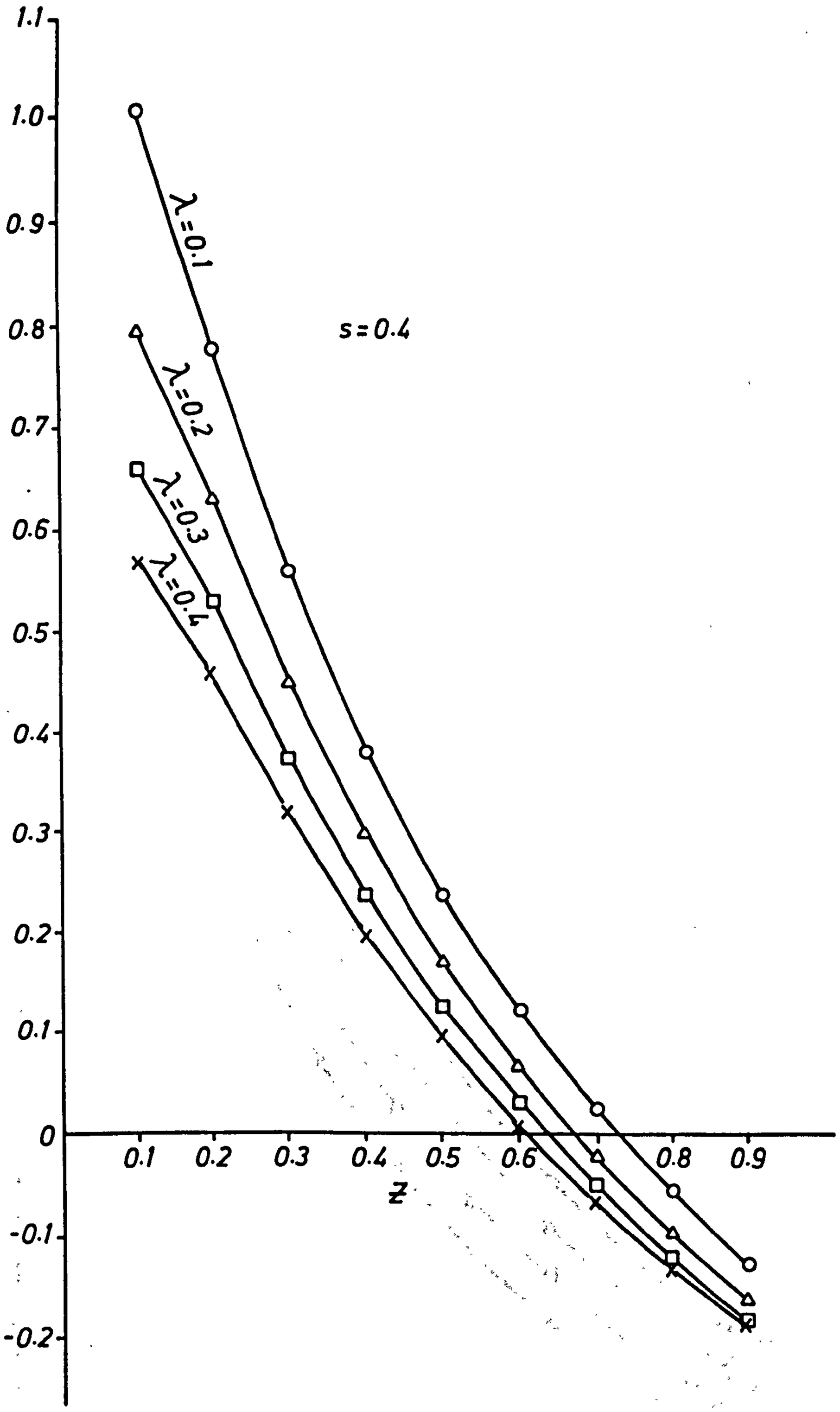

FIG. 2.11 DIMENSIONLESS CRITICAL ENERGY RELEASE RATE CHANGE $\frac{a}{g_c}\frac{dg_c}{da}$ VZ

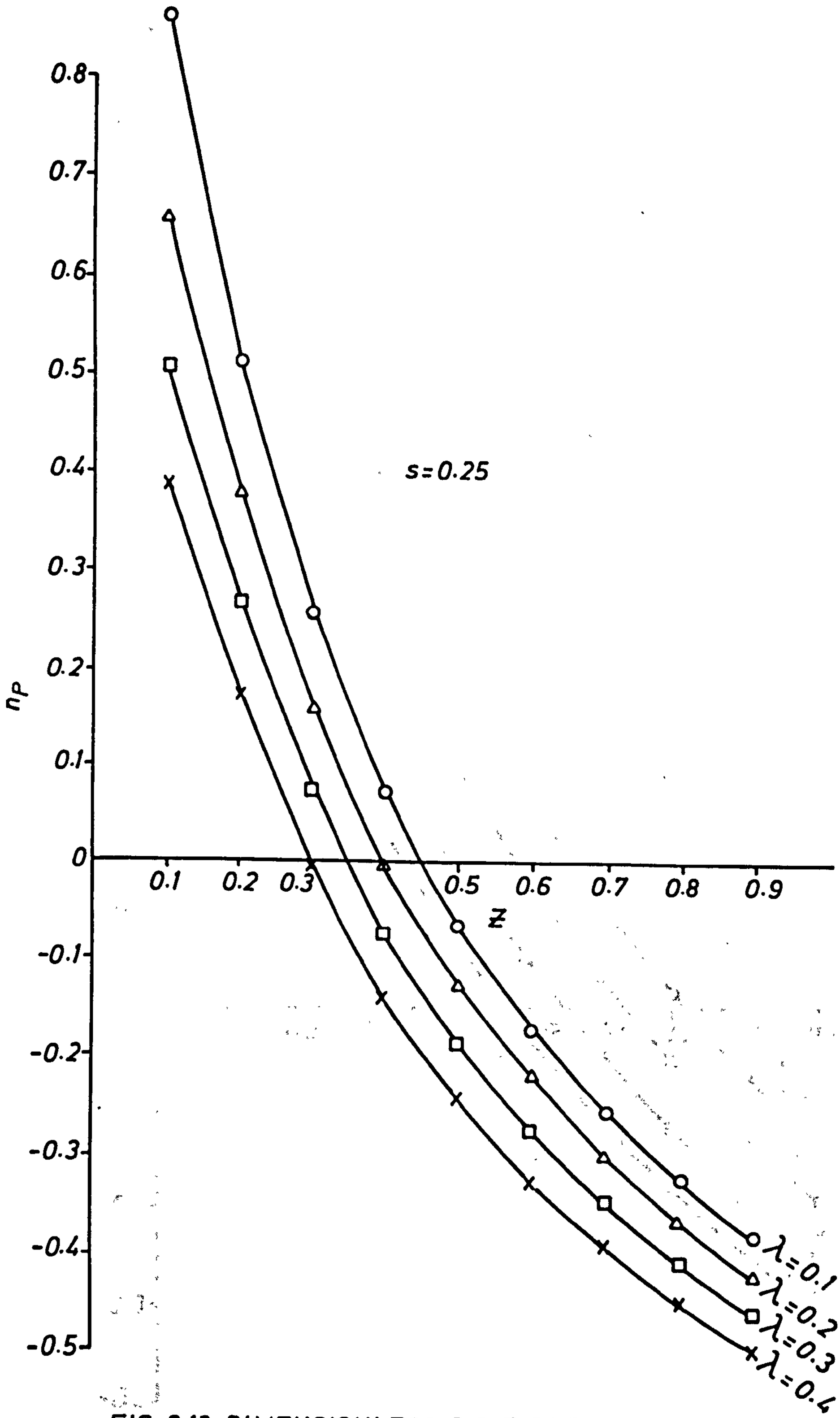

FIG. 2.12 DIMENSIONLESS G.S.F. COEFFICIENT IN LOAD CONTROL n_P VZ

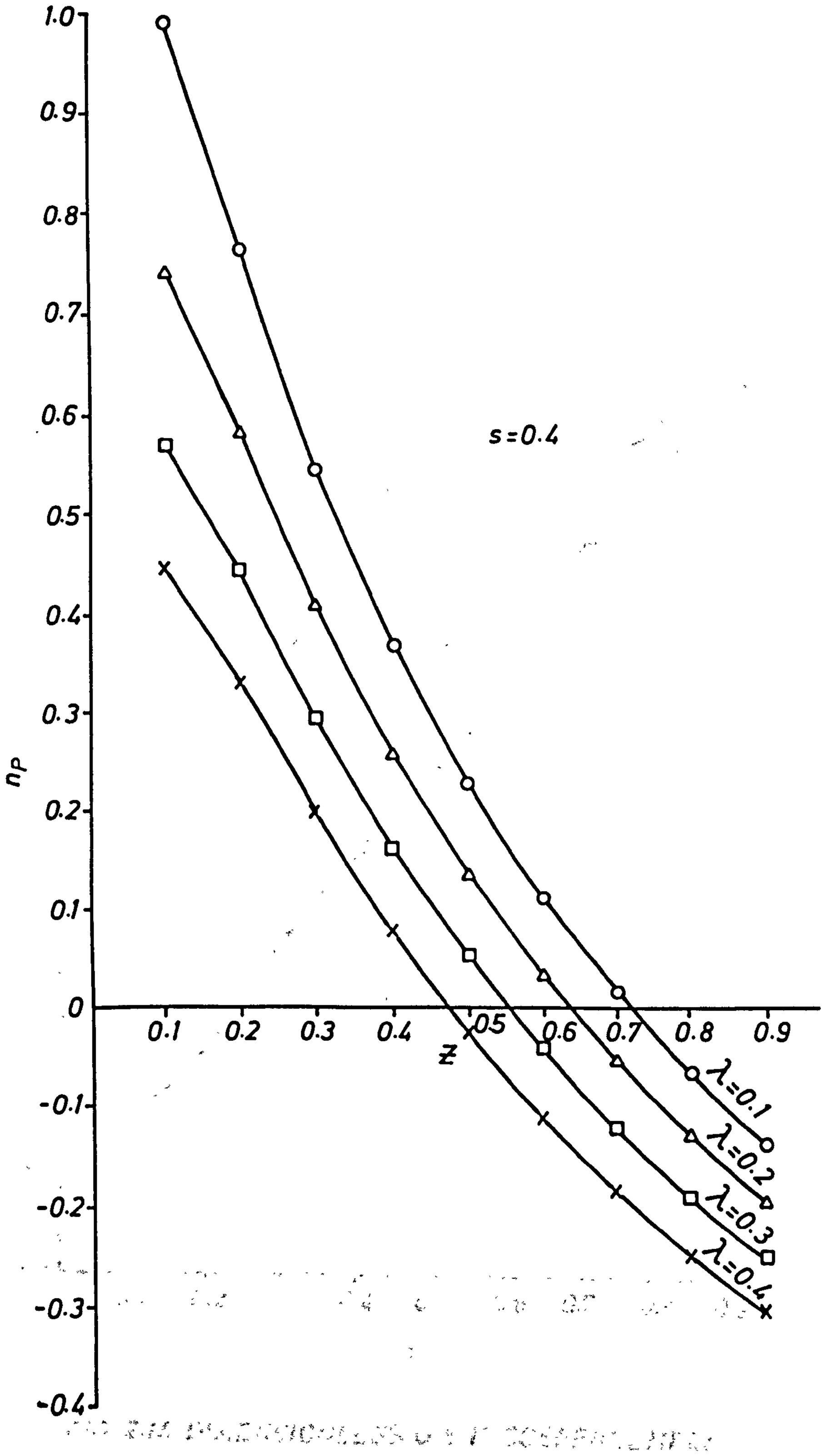

FIG. 2.13 DIMENSIONLESS G.S.F. COEFFICIENT IN LOAD CONTROL n_P Vz

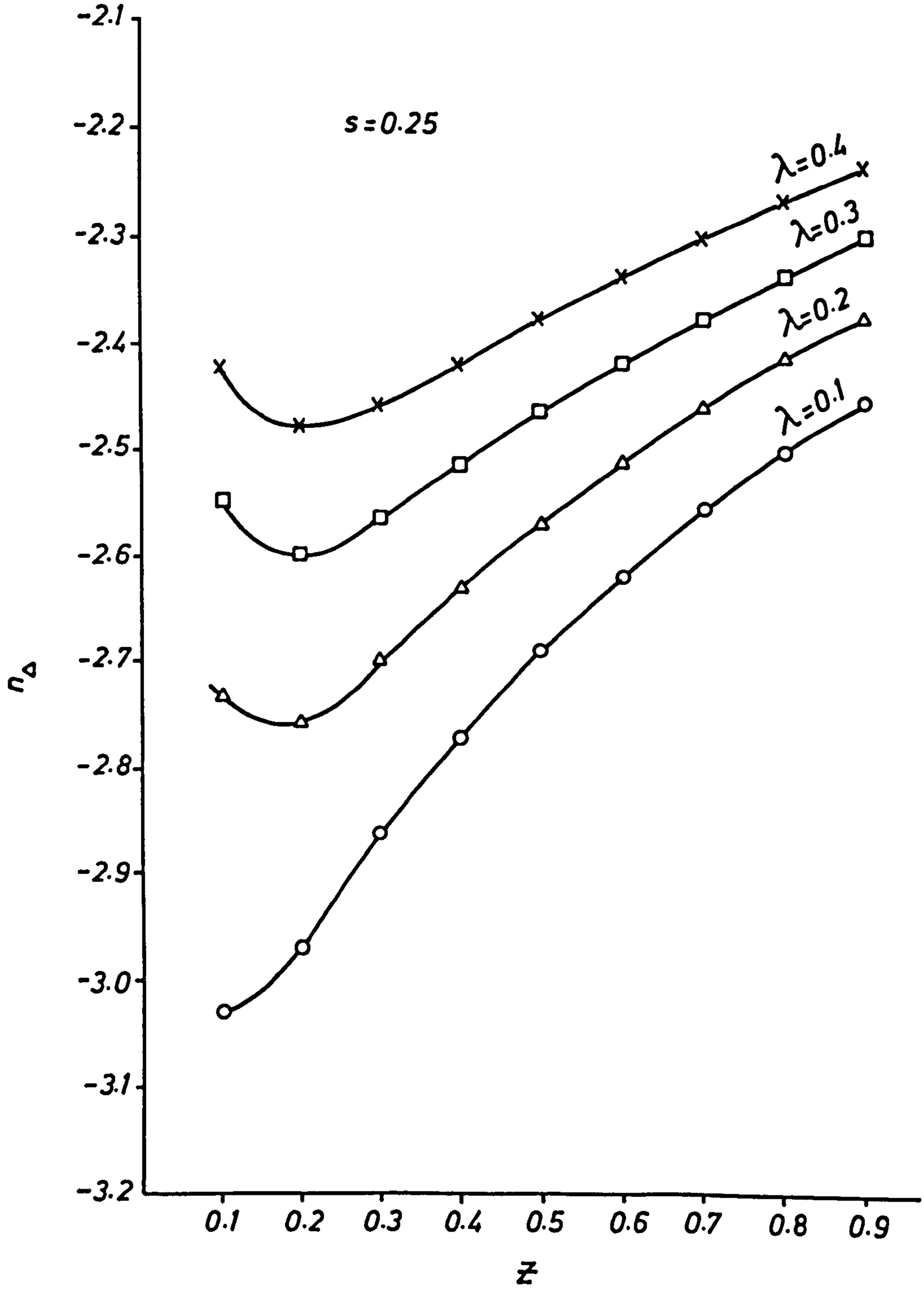

FIG. 2.14 DIMENSIONLESS G.S.F. COEFFICIENT IN DEFLECTION CONTROL n_Δ VZ

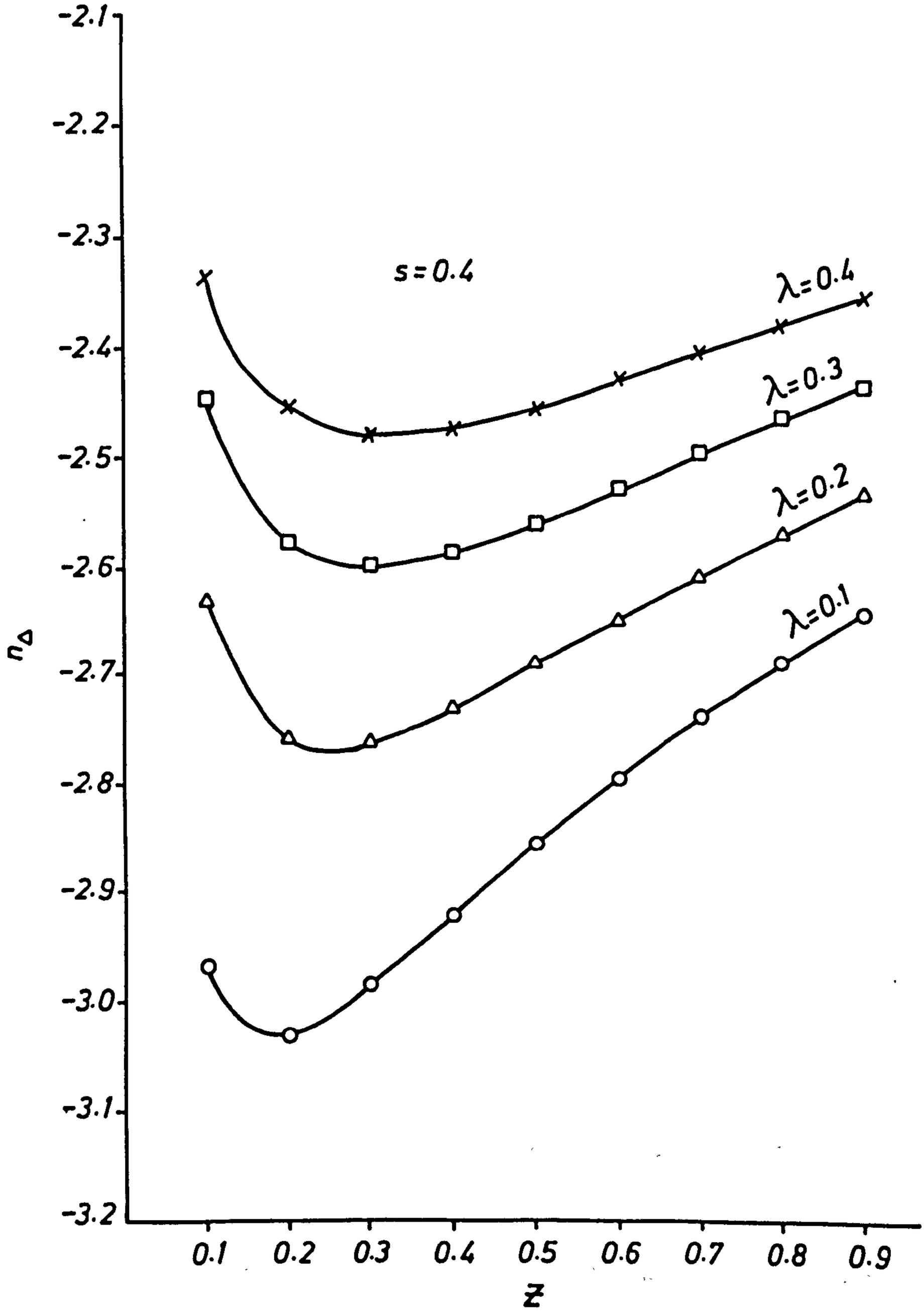

FIG. 2.15 DIMENSIONLESS G.S.F. COEFFICIENT IN DEFLECTION CONTROL n_Δ VZ

C H A P T E R T H R E E

OPENING MODE DELAMINATION IN CARBON FIBRE REINFORCED PLASTIC (CFRP) LAMINATES

3.1 INTRODUCTION

One of the main disadvantages with a carbon fibre reinforced plastic (CFRP) laminated plate is that, whilst its in-plane mechanical properties can be tailored as required to give very good strength and stiffness, its out-of-plane (or through the thickness) properties are poor compared with conventional metal plates. This is because, the properties in this direction are dominated by the relatively weak plastic resin matrix. The problem worsens in the presence of flaws such as areas of poor inter-layer bonding caused by voids, the inclusion of extraneous matter during manufacture, and impact induced delamination. These areas can give rise to stress concentrations and subsequent delamination under load. The blister problem (Ref. 12) is an example of such behaviour, where the initial voided area can spread rapidly when prone to buckling under compressive loading. In static testing conditions, the onset of delamination and spread is very much dependent on the amount of strain energy needed to separate the bonded layers. In general, the rate of change of this energy with crack growth, is not constant for a particular material, it depends on many factors such as fracture mode, test environment (temperature, moisture content, etc.), specimen geometry and the rate of straining (Ref. 64). In the case of a fibrous composite laminate, there are other factors which must be considered. These may be classified into two categories according to whether the effects are related to a particular component

(e.g., fibre misalignment, matrix porosity, etc.) or as a result of the interactions between the constituents of the composite (e.g., fibre-matrix debonding and pull-out of the fibres from the matrix). The above behaviour is summarized in Ref. 65 in the following statement 'a composite material can suffer any of the modes of failure of its constituents together with a few more arising from their combination.'

The energy released in the opening mode to drive the crack by a unit of newly created fracture area, is known as the 'Critical Energy Release Rate' (CERR)** g_c, and is characteristic of the same mode of fracture, as explained in Chapter 2 (see also, Ref. 32, Sec. 1.4). In principle, it is a basic laminate material property which can be measured from controlled two-dimensional opening mode tests on laminated strips as shown in Fig. 3.1(a) (the other two configurations shown in Figs. 3.1(b) and (c) will be shown to be unsuitable), wherein a laminated CFRP strip is glued on both sides to a pair of tapered mild-steel adherends (Ref. 29). Similar specimens have been used by some researchers for studying the fracture properties of adhesive joints (Refs. 44, 66, 67 and 68).

Whilst, the specimen shown in Fig. 3.1(a) may lend itself to the interlaminar (delamination) study of crack growth, it cannot be used for the opening mode where the plane of the crack is perpendicular to the fibres because of the large energy needed to propagate the notch across the fibres. This latter case is not considered in this study, and the interested reader may find Refs. 65, 69 and 70 useful in approaching the problem.

** In this Chapter, g and g_c are taken to represent, respectively, the strain energy release rate (SERR) and its critical value (CERR), in the opening mode (Mode I) type splitting. For simplicity, the mode subscript 'I' is omitted.

The (CERR) g_c can also be measured from opening mode tests on pure CFRP strips without any backing medium (Ref. 29, and Refs. 72 through to 75). These specimens are in the form of slender cantilever beams for economic and ease of manufacture reasons. Consequently, the delamination critical loads are very small making these specimens unsuitable for fatigue testing on large servohydraulic machines. Furthermore, the large deflections suffered by the specimen before the onset of splitting may give rise to nonlinear and even plastic effects (Ref. 74). The TDCB specimen shown in Fig. 3.1(a) enables the delamination critical load to be raised to about 100 times the value obtained from the pure CFRP strip specimen, and keeps at the same time the critical deflection to a very small level.

The critical energy release rate g_c may be obtained by following one of three main approaches (Ref. 71), namely, the Irwin-Kies equation $[(P_c^2/2b)(dC/da)]$, Berry's method, and Gurney's irreversible work area method. The first two lines of study are based on crack initiation, and their equivalence is supported by experimental data obtained from TDCB specimens (Ref. 60). The third method gives lower values for the CERR, if the crack jumps (stick-slip behaviour) following its initiation, as in the case of epoxy resin TDCB specimens (Refs. 60 and 71). However, if a stable quasi-static crack growth is achieved in the course of a test it is expected the Gurney's method falls into line with the other two approaches, and therefore consistent CERR data can be obtained by any one of the three methods.

The Irwin-Kies equation together with Gurney's irreversible work method are employed in this Chapter for the measurement of the critical energy release rate (CERR) g_c of delamination in unidirectional CFRP laminated strips (Fig. 3.1). The g_c data are plotted versus the crack length and compared with the analytical predictions.

An interlayer notch within a loaded laminated composite plate can still propagate to catastrophic dimensions under repeated loads even though the maximum stress concentration level along its front is well below the static interlaminar strength. For this reason, a study of the delamination behaviour in fatigue is included using a number of TDCB specimens [Fig. 3.1(a)]. Each test is characterized by a well defined maximum of the alternating load and the load amplitude. Several graphs, representing the crack length versus the number of elapsed cycles, are given and discussed. These graphs are then used in conjunction with the compliance expression for the TDCB specimen [Chapter 2, Eqn. (2.45)] to give a semi-empirical Paris type formula for the prediction of delamination growth rate under repeated loads.

3.2 GENERAL FEATURES OF TEST SPECIMENS

With reference to Fig. 3.1, for each specimen configuration, the CFRP strip is joined to the steel adherends by means of thin adhesive layers. These consist of two bonds on each side of the strip, giving adherend-adhesive and adhesive-CFRP interfaces. The steel faces were shot-blasted and all the bond surfaces were thoroughly degreased prior to the gluing operation. It is very important, for a delamination test to be valid, to ensure that no secondary cracking takes place along any bond interface. If this happens alongside the main delamination in the CFRP strip, some of the released strain energy will be diverted to propagate the secondary cracking with consequent misleading results. It is obvious, therefore, that the strength of any interface adhesive bond must be higher than the CRFP interlaminar strength.

A common adhesive system (Araldite Epoxy Resin; supplied by Ciba-Geigy) was used as directed by the company to prepare some TDCB

test specimens [Fig. 3.1(a)]. All of these specimens failed along the steel adhered-adhesive interface before any delamination could be detected. So, longitudinal channels were machined into the adherends to bury the CFRP strip by about a third thickness from each side so that the shear forces introduced along the strip edges might cure the problem. From the start, the new technique was bound to be discarded because the edges of the channels shadowed the delamination line along the CFRP strip making very difficult the detection of any possible delamination. However, the technique failed to cure the original problem. At this stage, other adhesives were introduced and an experimental programme was set up for the selection of the most suitable adhesive system to be used in the bonding process of the various DCB test specimen components (see Appendix B, Section 2). The task was accomplished through the selection of the high shear and peel strength adhesive system (Araldite 2005).

3.3 TEST SPECIMENS

(a) *Adherends.* These were machined from mild-steel strips and finished to the desired dimensions as shown in Fig. 3.1. Care was taken to ensure complete flatness of the bond surfaces. Shallow channels were machined into the ends of the adherends near the loading line to act as guides for a pair of adjustable distance slotted knife-edges for the crack opening displacement (C.O.D.)Δ measurement. These were kept apart at the desired distance by means of small bolts screwed through the slots into the adherends (Fig. 3.2).

The steel arms were first degreased, using Trichloroethylene solution, then the bond surfaces were shot-blasted, degreased again and dried using hot air. At this stage, the adherends were picked up,

by tongs to avoid contact with the bond surfaces, placed inside a container and sealed ready for the gluing operation.

(b) CFRP *strips*. These were cut from a unidirectional CFRP plate, which was made up from eight all-0° pre-preg layers and cured by the vacuum/pressure bag method. The pre-preg material (0.125mm thick) which was supplied by Ciba-Geigy, consisted of the XAS/914 resin system and contained Courtaulds high strength surface treated fibres. Details of the CFRP plate manufacturing process are given in Appendix B, Section 1. An initial delaminated region was introduced at one end by means of a full width thin strip (0.0125mm thick) of PTFE which was positioned at the plate mid-plane before the curing process. The cured plate measured 150mm x 190mm with a nominal thickness of 1mm.

The problem of void content within the plate was not assessed. However, it was assumed that the void content would be within acceptable limits [based on previous work (Ref. 76)] provided a 10mm wide marginal strip was trimmed off from each side of the plate. In fact, ultrasonic scanning techniques (Ref. 76) reveals that the boundary regions (a 10mm wide) of a cured plate are of poor quality because of heavy void content.

The trimmed plate was cut into strips along the fibre direction, starting at the far side from the initial debond, using a diamond circular saw. The dimensions for each strip (width x length) were matched exactly with those for the bond surfaces of the steel adherends. To avoid possible blunting effects at the front of the initial delamination, a crack was propagated beyond the debond front by wedging longitudinally a thin sharp blade along the CFRP strip mid-plane. No mechanical surface treatment was needed for the bond surfaces of the CFRP strip specimens. These were, in fact, cleaned thoroughly, degreased in a Trichloroethylene solution, dried by blowing

warm air, placed into a clean container and sealed ready for the gluing operation.

(c) *Adhesive.* A high shear and peel strength adhesive (Araldite 2005) was chosen from a number of alternatives following a selective "test for the highest strength" procedure, based on a butt-joint type test wherein a small CFRP square plate was glued, through the adhesive under examination, to a pair of small steel blocks through which an axial tensile load was applied. Details of the various adhesive systems and the test criteria for comparing their strengths are given in Appendix B, Section 2. Araldite 2005 was found to be the best adhesive for gluing CFRP to steel provided the bond surfaces were prepared as explained in steps (a) and (b).

The selected adhesive was mixed in a shallow container with the right proportions following the manufacturer's instructions, and applied evenly to the bond surfaces, using a plastic spatula. The three specimen components (CFRP strip and adherends) were brought together and the assembly secured in a specially designed rig. This enabled control to be maintained over the thickness of the adhesive layer and also kept the bonded parts in perfect alignment. Three hours were allowed for the adhesive to settle at room temperature before placing the assembly in an oven to cure for six hours at 40!C. At the end of the cure cycle, the specimen was removed from the rig and the excess adhesive was removed. A metric scale was engraved on one of the adherends using a vernier height gauge. The expected crack propagation path was painted using thin Snopake correction liquid for easy and accurate measurements (see Plate 3.1). Finally, a pair of knife-edges was attached to the test specimen at equal distances from the specimen mid-plane as shown in Fig. 3.2. The overall distance between the knife-edges was predetermined to be within the C.O.D. gauge

range.

3.4 TEST APPARATUS

3.4.1 *Monitoring the Crack Extension*

The crack propagation measurements were read directly against the engraved metric scale with the help of an X10 spherical magnifying glass. The Snopake background revealed a very clear picture of the crack extent so that delamination growth readings, accurate to ∿±0.2mm, at the edge, were obtained.

3.4.2 *Loading Record*

The test specimen shown in Fig. 3.2(a) was loaded through fork-pin joints (Fig. 3.3) using a Hounsfield Tensometer as shown in Plate 3.2. A more efficient way than the direct use of the Tensometer's mercury scale was devised for measuring the applied load. This was accomplished as follows:-

(a) An electrical resistance 6mm - active strain gauge (type FLA, manufactured by Tokyo Sokki Kenkyujo Co. Ltd.), was attached to the beam of the Hounsfield Tensometer so that strains proportional to the longitudinal beam deflections and therefore to the applied loads were obtained.

(b) A second identical dummy strain gauge for temperature change compensation, was mounted on a steel plate of similar size to that of the Tensometer's beam.

(c) The two strain gauges were connected to a digital Strain Indicator type 1526, manufactured by Bruel and Kjaer, to form a half bridge arrangement.

(d) A steel strip was loaded in the Tensometer and the digital strain

readings on the Strain Indicator were related to the direct load measurements from the mercury scale, as shown in Fig. 3.4. This figure served to convert the micro strain displays to the actual loads during the delamination tests.

The above procedure was found to be advantageous for two main reasons. Firstly, the mercury tube alongside the load scale was sensitive to temperature changes such as those caused by a lamp light source. Secondly, the output strain signal from the Strain Indicator was easily routed to drive a pen of an Instron Recorder, the travel of which could be related to the applied load and was therefore able to keep a continuous track of the load record even during a possible crack jump.

3.4.3 C.O.D. *Measurements*

The crack opening displacement (C.O.D.) at the mouth of the crack was measured using a 10mm Instron Crack Opening Gauge, Model A1367 1001B, with 4mm maximum travel. The principles of operation for the C.O.D. gauge are explained in Ref. 77 and are reported in the next paragraph for completeness.

The ends of the arms of the C.O.D. gauge are machined to clip on to knife-edges. These are machined at 60° to the vertical as shown in Fig. 3.2(b). A Vernier Dial Caliper can be used to centralize the sliding knife-edges at the correct distance within the gauge range. The lightweight gauge is easily clipped on to the test specimen [Fig. 3.2(b)], is self-supporting before and during testing, and is self released on specimen failure. It gives a precise indication of the relative displacement of two accurately located gauge points (knife-edges) which span the crack starter notch of the specimen, and provides an electrical linear output signal in proportion to the

displacement. The C.O.D. gauge incorporates foil type resistance strain gauges which are bonded to cantilever bending beam elements to form a Wheatstone bridge circuit. Bending the C.O.D. gauge arms to span the crack in the specimen applies a strain to the strain gauges. This strain is reduced when the crack in the specimen grows, opening the gauge arms and causing an unbalance in the Wheatstone bridge circuit which provides the output signal.

The C.O.D. gauge in the released condition (i.e. no strain is present in either of the arms) has a distance T_o between the bottoms of the grooves on its arms [Fig. 3.2(c)], and a distance T (equal to the length between the knife-edges) when it is in the strained configuration [Fig. 3.2(a) and (b)]. The difference (T_o-T) is proportional to the output strain. However, it should not exceed the C.O.D. gauge range of 4mm recommended by the manufacturer. In the same way as for the load output signal, during the delamination tests the strain signal from the C.O.D. gauge was conditioned by a Bruel and Kjaer Strain Indicator Type 1526 to provide the servo-drive input to an Instron Recorder. This, as was the case for the applied load, enabled a continuous C.O.D. record to be obtained even during any possible crack jump.

3.5 QUASI-STATIC DELAMINATION TESTING

A trial test programme was conducted, under stiff testing conditions, on several specimens representing the various configurations shown in Fig. 3.1. This was done to select the geometry which would meet the requirements of stable and quasi-static crack propagation. The type of specimen geometry shown in Fig. 3.1(c) which Mai et al. (Ref. 56) judged to be stable for bulk

polymethylmethacrylate (PMMA), was found to be highly unstable. This specimen measured 15mm in width by 170mm in length (angle of taper = 10°) and had an initial crack length of 16mm. It sustained the highest critical load (285ON) amongst the other configurations. At this load the crack started to propagate and took just a few seconds to split the specimen completely. The parallel-arm test specimen shown in Fig. 3.1(b) measured 15mm in width by 170mm in length with an initial crack length of 16mm. This specimen showed neutral behaviour in that even a slight increase in loading beyond a critical value (∿150ON), corresponding to the onset of crack propagation, triggered unstable extensive delamination. Because only a few specimens from the configurations shown in Figs. 3.1(b) and (c) were tested, the above findings are far from conclusive. However, judging from their behaviour, the two specimens were excluded from the fracture toughness data contained in this thesis as the kinetic energy released during delamination for these two cases could be considerable. This would bear on the accuracy of the strain energy release rate measurements assuming slow and stable crack propagation.

The quasi-static delamination characteristics were obtained from the TDCB test specimen shown in Fig. 3.1(a). This was loaded in the Hounsfield Tensometer as seen from Plate 3.2. Before setting the various measuring scales, a small load was applied and then reduced to zero to take off any backlash in the loading string. The load P in Fig. 3.2(a) was progressively applied up to a critical value P_c, just sufficient to propagate the existing crack. At crack arrest, the amount of propagation was measured, followed by a progressive load release. The crack propagation was signalled by a simultaneous automatic fall in load and displacement micro-strains. Throughout the load envelope, a complete load versus C.O.D. record could be obtained.

Crack propagation was very stable and quasi-static.

Two TDCB test specimens, S1 and S2, were used for all the results reported in this section. They measured 10mm and 20mm in width respectively, by 170mm in length, with the loading line distant 10mm from the knife-edges. Twelve and twenty seven complete load C.O.D. envelopes were obtained, respectively, from the S1 and S2 specimens, with an average crack extension per cycle of 3.5mm for the first and 0.63mm for the second. At the end of each crack growth, the test specimen was unloaded and P rezeroed so that accumulated components of permanent deflection from previous delaminations did not enter into the calculations of the critical strain energy release rate g_c. This effect could be significant especially if large crack growths were involved in earlier loading cycles.

The digital micro-strain readings, corresponding to the applied load and the crack opening displacement, were converted to the actual quantities using, respectively, the following formulae:

$$P = 1250\zeta_L / 1457 \qquad \text{(N), for the load}$$

and,

$$\Delta = \text{C.O.D.} = [(T_o - T)(\zeta_o - \zeta)]/\zeta_o \qquad \text{(mm), for the displacement}$$

where, $(T_o - T)$ is the pre-test amount of displacement by which the C.O.D. gauge is compressed when it is clipped on (Fig. 3.2), $(\zeta_o - \zeta)$ is the difference of displacement micro-strain relative to the initial setting and ζ_L is the loading micro- strain.

Figs. 3.5 and 3.6 show the sets of results obtained from specimen S1. A predominant linear behaviour, apart from the topmost portion, is common to all the graphs. In the cycles from 8 to 12 with the exception of cycle 11, at the start of the load release line, the C.O.D. was actually lower than its value on the load line for the same

load level, resulting in a small triangular area on top of the envelope. This area represented a small amount of energy absorbed back by the system at the start of the load release. Therefore, it was taken with negative sign during the measurement of the critical energy release rate. It was noticed that the above behaviour was accompanied by relatively small crack extensions where fibre bridging was suspected to be responsible for such behaviour. Also, it is interesting to note that on comparing the load deflection graphs with the results given in Ref. 29 for the pure CFRP strip, the critical loads shown in Figs. 3.5 and 3.6 actually increase as the delamination length increases, whilst the opposite is true in Ref. 29. This is due to the fact that the TDCB specimen is tapered in depth giving a larger cross-section at the crack tip as the crack progresses. This is a very important characteristic of this type of specimen, especially in closed loop fatigue experiments, since it ensures stable crack growth under load control testing.

The critical energy release rate g_c was evaluated in two different ways. The area method (Gurney's irreversible work method), described in Ref. 29, gives the following equation;

$$g_c = \frac{1}{b} \frac{\text{ENVELOPE AREA}}{\delta a} \qquad (3.1)$$

where "ENVELOPE AREA" (examples are shown by the shaded regions in Fig. 3.5) refers to the area enclosed by the loading line and the straight line joining the point of crack arrest and the origin of the load envelope. The rest of the loop area is associated with permanent deformations and therefore excluded in Eqn. (3.1), otherwise an overestimation of g_c could result if the whole area of the load envelope is considered.

The compliance method as documented in Ref. 66 gives,

$$g_c = \frac{P_c^2}{2b}\left(\frac{\partial C}{\partial a}\right) \qquad (3.2)$$

where P_c and $\partial C/\partial a$ are experimental values taken from the graphs of P_c and C versus the crack length a.

For the S1 specimen, the critical load P_c versus the crack length a (Fig. 3.7), shows a generally linear behaviour. The experimental compliance is shown in Fig. 3.8 along with its theoretical curve based on Eqn. (2.45). Here also, linearity is in evidence underlining an early mentioned advantage with TDCB specimens (constance of dC/da). It is interesting to see from Fig. 3.8 that both curves are almost parallel for most of the crack propagation. Consequently, the experimental and theoretical compliances differ by a quantity which is independent of the crack length and, therefore, may be dependent only on the mechanical and geometrical properties of the CFRP strip. In fact, the theoretical curve in Fig. 3.8 represents the compliance for a pure steel ($E = 2 \times 10^5$ N/mm^2) specimen and, therefore, the crack opening displacement (C.O.D.) is governed by the steel cohesive stiffness. On the other hand, the experimental compliance, represented by the upper curve in Fig. 3.8, is affected by the interlaminar stiffness between the 0^o layers of the CFRP strip. This stiffness is matrix (resin) dominated which has a Young's modulus $E_r = 3380$ N/mm^2 (Ref. 76). Also the adhesive layers between the CFRP and steel will add to the compliance value. In the light of the above argument, it can be concluded that for a certain crack length, the test specimen opened more under the same applied load than the pure steel specimen. Equivalently, the theoretical specimen should have its crack length increased by about 35mm over that for the experimental case in order to achieve the same compliance as shown in Fig. 3.8. However, the

difference between the two curves is not likely to affect the g_c values because their slopes (=dC/da) are about the same.

The g_c results for the S1 specimen from the foregoing methods together with a theoretical curve are plotted in Fig. 3.9. The latter was obtained from the formula given by Eqn. (2.47) of Chapter 2. Very good agreement between experiment and theory is achieved over the first 20mm of crack extension as shown in Fig. 3.9. For further crack growth the critical energy release rate from both the experimental methods lies above the theoretical curve. This increase is thought to be due to non linear material behaviour and fibre bridging. The critical energy release rate g_c is initially around 0.26 N/mm. As the delamination grows however misaligned fibres bridge the crack faces behind the crack front as discussed in Refs. 14 and 78. Extra energy is needed to break this tied zone and propagate the crack further. This is shown by the trend of the pronounced rise of g_c after about 20mm of crack growth. The curves through the data points in Fig. 3.9 tend to flatten after a further 20mm of crack extension with a g_c value of around 0.6 and 1.0 N/mm for the area and compliance methods respectively. Similar findings are reported by Dorey in Ref. 14 wherein a pure CFRP strip representing a parallel-arm double cantilever beam specimen was split parallel to the fibres. He concludes that fibre fracture processes absorb most energy in the fracture of composites. It is seen however from Fig. 3.9 that the g_c values from the area method agree fairly well with the theory of Chapter 2 (Eqn. 2.47) during the late crack extensions. As mentioned earlier, the average energy release rate from the area method during the first 20mm crack extension is about 0.26 N/mm. This value is higher than g_c = 0.15 N/mm obtained using the method of Ref. 29 for the pure CFRP strip with the same resin system (XAS/914). This difference may be attributed to the following factors:

(a) The knife edge supports for the TDCB specimen were 10mm to one side of the load line as shown in Fig. 3.2. It was found from simple flexure theory that this arrangement gave deflection measurements, at the largest crack length considered, higher than the corresponding values at the load line by an estimated 2%. This error is thought to have only a small effect on the measured g_c values.

(b) The enhancement of fibre bridging in the TDCB specimen with consequent increase in the measured g_c values. This conclusion was reported by Russell and Street in Ref. 79. The authors pointed out that since thicker specimens were less compliant a greater degree of fibre bridging was allowed.

In fact, the TDCB specimen considered here conforms to the case of a very thick laminate with an internal delamination. However, while this explanation may be true for late delaminations it is not so obvious for early crack propagation where close agreement with theory is achieved.

The twenty seven load C.O.D. envelopes for the S2 test specimen are shown in Figs. 3.10 through to 3.16. The behaviour of this specimen, as far as these figures are concerned, is very similar to that of the S1 specimen. Only in two envelopes (6 and 16) at the start of the load release, does the actual C.O.D. reduce its value on the loading line for the same load level. Obviously, given the specimen had twice the width of the S1 test piece, the associated critical loads were relatively high making this specimen suitable for testing on large servo-hydraulic machines. The crack propagation was extremely slow and stable with almost no audible clicking. The critical load P_c remained nearly constant during delamination and increased as the crack grew longer as shown in Fig. 3.17. The average crack growth for the first twelve cycles is about 1.2 mm which is small compared with 6.5mm

for the S1 specimen.

There are some disadvantages in using a wider test specimen. Firstly, a wide specimen is more prone to non-equal crack extensions from the two sides. This may introduce slight errors in the measurement of the delamination extent especially when the crack is monitored from only one side of the specimen as in the case of the tests documented in this Chapter wherein it had been assumed that the crack had a straight front and that it extended by the same amount from both sides of the specimen. Secondly, voids, poorly bonded patches and other flaws as well as secondary failure mechanisms on a micro-mechanical scale are likely to increase as a result of the extended area of the specimen with consequent effect on the critical energy release rate measurement. This latter case is clearly reflected by the scatter of the delamination data shown in Figs. 3.17 and 3.18 for the S2 specimen. It is interesting to see from Fig. 3.18 that the values of g_c obtained over the first 10mm extension are close to those obtained from the S1 specimen over twice the above length (i.e. 20mm). Both test specimens show the trend of rising critical energy release rate after a certain delamination growth length (20mm for S1 and 10mm for S2). This is due mainly to the establishment of a tied zone (nesting effect) consisting of fibres and even whole bundles (as was found on inspection of the fracture surface of the S2 specimen) bridging the mouth of the crack as was discussed in Ref. 79. However, apart from the early test stages, it is observed that the g_c values, for the S2 specimen, are mainly characterized by relatively small crack growths which may particularly affect their accuracy because of non-even crack front advance. Fig. 3.19 shows the experimental compliance versus the crack length for the test specimen S2. The curve drawn through the data can be used at a certain crack length to obtain

$\partial C/\partial a$. This may be substituted into Eqn. (3.2) together with the corresponding P_c taken from Fig. 3.17 to yield the critical strain energy release rate g_c as shown in Fig. 3.18 by the middle curve which lies below the scatter band of g_c values from the area method. This behaviour underlines the complex mechanism of energy dissipation which takes place following the formation of the tied zone.

3.6 FATIGUE TEST RESULTS AND DISCUSSION

Early investigations into the fatigue behaviour of advanced fibrous composites started with tension-tension constant amplitude loading. The majority of fatigue studies in the field of composites still have this experimental base (Ref. 80). However, a broadening of the field of study has been brought about by the development of advanced test techniques and more demanding design requirements. At present, fatigue testing includes: tension-compression and compression-compression, variable amplitude loading, environmental effects, etc. More recently, efforts have been directed towards the study of the interactions between the composite components and fatigue failure mechanisms.

Whereas metals usually fail by crack initiation and growth in a manner predictable by fracture mechanics principles, fibrous composites exhibit several modes of damage (Ref. 80) including fibre breakage, resin crazing and cracking, interfacial debonding and interlaminar delamination. Cyclic damage in the form of a progressive degradation of the mechanical properties of an otherwise unotched composite laminate may ensue from the early beginning of life. However, this damage is often not perceptible visually unless either some sort of a separate conventional test is carried out to assess the accumulated damage or suitable means of detection are introduced during cycling. It can happen, however, that the laminate may not survive up to a

degenerative type failure as a result of an earlier fracture through a pre-existing notch of certain severity within the composite. This is not a prelude to a halt of the degenerative process, however, the associated parameters may take secondary importance especially if the original notch is propagating along a favourable path such as an interlaminar interface (plane of weakness). This mode of failure is matrix dominated and may be similar in this respect to that for a bulk material such as a metal.

Delamination in composite laminates may take place as a result of different loading conditions; tension, compression, shearing or any combination of these. It may start at free edges (Refs. 28 and 81) or around notches such as an initial interlayer debond (Refs. 12, 30 and 31), central through thickness holes and slits (Refs. 16, 17 and 18), surface notches (Ref. 22) or as a result of direct delamination cleavage. This latter case is of immediate particular interest because of the following reasons:

(1) The interlayer planes in a unidirectional composite are planes of weakness and the energy of separation is least. Still lower energy is needed to separate the layers, if the interlaminar stresses are periodic.

(2) Very limited fatigue data are available in the open literature. In fact, the author is aware only of Ref. 82 and his work in Ref. 29.

(3) The cyclic data may be easily correlated with the analytical analysis developed in Chapter 2.

All various configurations (Fig. 3.1) for the DCB test specimen were considered in the fatigue study programme. The test specimens were identical to those for the static tests except that no restriction was made on the initial crack length. In fact, each CFRP strip

consisted of eight 0° layers with a PTFE film at the laminate mid plane so that delamination between 0° layers could be studied. Also, the steel adherends were the same as those used for the static tests after they had been cleaned and passed through the various manufacturing stages to obtain a viable fatigue test specimen.

The tests were carried out in "load control" on a two-column servo-hydraulic Instron testing machine Model 1342 employing a 10 kN dynamic capacity load cell. Before the start of each testing session, the machine response was optimized and the various test parameters were dialled into the closed loop system through an Instron desk-top version control console.

The loading fixures were modified to cope with the machine hydraulic grips (see Plate 3.3). Here, the loading fork was assembled from three pieces of steel held together and fixed to the specimen by nuts and bolts. Ordinary and locking washers were used to prevent movement by the specimen during cycling and also to centralize the loading fixures. Each test specimen was fitted with knife-edges for measuring the variation in the C.O.D. amplitude (difference between max. and min.). This offered a further check on the delamination growth during load cycling. The C.O.D. gauge was used in the same way as for the static tests and a similar formula to that given earlier { C.O.D. = $[(T_o - T)(\zeta_o - \zeta)]/\zeta_o$} was employed for the displacement measurements.

Throughout the test programme a sinusoidal tension-tension (Fig. 3.20) constant amplitude loading, at a frequency of 6Hz, was selected for all the specimens. The load signal was routed to be displayed on the screen of an Oscilloscope for optimization while setting up and also for continuous load monitoring during cycling. One tapered double cantilever beam specimen with an initial crack length of

17mm, loaded close to the base [Fig. 3.1 (c)] was fatigued at different stages, each characterized by an increased load amplitude over its predecessor. The results from this specimen are given in Table 3.1. It must be said that the data shown here are incomplete and of an exploratory nature and, therefore, are difficult to discuss. However, note may be taken of the effects of the gradual increase of the maximum load and the cycling amplitude, wherein delamination seemed to be sensitive to both. It is also seen from the results shown that, apart from the first stage, no significant delamination growth took place during the late stages. This may be due to the shielding effect of a tied zone behind the crack front. At the start of the last setting, the specimen delaminated completely at the top of the first stroke. This was a result of the specimen being statically unstable (the system wanted to restore the load but the specimen was incapable of maintaining it, therefore, failure occurred).

The set of results given in Table 3.2 was obtained from the parallel-arm test specimen shown in Fig. 3.1 (b). As in the earlier case, the mean load level and the cycling amplitude were increased simultaneously as the specimen passed from one setting to the next. For this specimen, there was no sign of delamination growth. The specimen failed suddenly through delamination along the original split. Even though there were no apparent reasons for the sudden fracture it was suspected that a voltage spike in the load signal might be the cause. However, the above results gave the false impression that CFRP laminates were not after all sensitive to fatigue delamination along 0° interfaces.

After the poor performance shown by the two foregoing test specimens, it was decided to exclude them from further cleavage fatigue testing and to concentrate instead on the TDCB specimen shown in

Fig. 3.1 (a) in view of its stable behaviour during crack propagation. Seven TDCB test specimens (F1, F2, F3, F4, F5, F6 and F7) of the type shown in Fig. 3.1 (a) were tested in cleavage fatigue. All the specimens were similar to the static test specimen S2; i.e., each had a taper angle θ of 10° and measured 20mm in width by 170mm in length, with the loading line 10mm distant from the knife-edges. At regular intervals, the delamination growth was monitored and measurement taken against the engraved scale using an X20 Stereo Microscope, supplied by Griffin and George Ltd. The maximum and minimum of the C.O.D. gauge output were taken at the same intervals to double check the crack growth. A quasi-static pre-fatigue test was carried out on each specimen to find its delamination strength, P_c. This served as a ceiling for the maximum of the alternating load, besides giving extra information on the quasi-static behaviour.

Figs. 3.21, 22 and 23 show the number of cycles versus the crack length for the test specimens F1, F2 and F3. These had their mean load, P_{mean}, varied between 32% and 43% of P_c with the maximum of the alternating load varying between 53% and 80% of P_c. These variations were motivated mainly by the need to increase either or both the amplitude ΔP and the maximum of the alternating load without pushing the minimum load to compressive values. The test specimen F1 ($P_{max} \sim 71\%$ of P_c) showed that, after an early delamination growth, no further crack movement was detected beyond 15,000 cycles for a further 25,000 cycles. This pattern of behaviour was repeated with specimen F2 during the last two settings where the specimen was cycled at a larger number of cycles as shown in Fig. 3.22. The limited delamination growth, for the specimen F2, took place after the original split was statically extended to greater values comparable to those of specimen F1.

The third specimen (F3) was subjected to more severe loading conditions characterized by relatively high loading amplitudes and ratios P_{max}/P_c . The tendency of an earlier crack extension followed by a lull was also found here, however, the specimen showed sensitivity to large P_{max} values, as percentages of P_c, and high ΔP's. Unfortunately, the test specimen F3 did not survive long enough to give more data; it failed along the interface of one of the steel adherends and the contiguous adhesive layer. The fracture surfaces for the foregoing specimens were visually featureless, however, they seemed slightly smoother than for the quasi-static case. Even though the elapsed number of cycles, for any particular setting for the specimens F1, F2 and F3, did not go beyond 100,000 cycles, the idea that the material might not be "sensitive" after all to fatigue cleavage was growing stronger.

Against the above background, another test specimen (F4) was fatigued with the intention of increasing the number of cycles. The specimen accumulated 170,000 cycles as shown in Fig. 3.24. It was only after 100,000 cycles that the crack showed signs of advancement. This result, although limited, showed the early limitations in the notion of the insensitivity of the material to fatigue delamination under cleavage loading. However, considering that the growing crack might have encountered some of the inevitable inherent flaws such as, poorly bonded patches, voids, etc., the test was not considered conclusive. The test was ended after load control became problematic because of the specimen loss of stiffness as a result of its large crack length.

A clearer picture of the behaviour of delamination by cyclic cleavage was given by the last three test specimens (F5, F6 and F7). These were cycled at 6Hz (as before) at a mean load level = 50% of the maximum initial static splitting load, P_c. The cycling amplitude for

each case was determined by taking (90%, 80%, and 70%) of the initial splitting strength to represent the maximum of the fatigue load. Linear-log graphs were used for plotting crack length versus the number of cycles as shown in Figs. 3.25 and 3.26. An approximate linear behaviour is observed beyond 100,000 cycles, where the rate of crack increase with the number of cycles, increases as P_{max} increases. Even with the most unfavourable case, no crack extension was observed before the lapse of several thousand cycles, confirming the trend found with earlier test specimens. The crack growth was one of pure delamination except in one specimen (F6) which had an initial crack length (= 33.5mm) and a maximum fatigue load (= 90% of the corresponding static strength, P_c). Here, a rather unexpected fracture mechanism accompanied the delamination growth. In fact, the crack propagated in a step-wise fashion as shown in Fig. 3.27 (see also Plate 3.4). First, delamination started along the original split, then it jumped to the next interface without breaking the layer and a second delamination took place. The crack then jumped again to the next level up until it finally settled between the two topmost layers. The average step length delamination was ∿ 1.5mm. This type of behaviour had been observed in the static tests given in Ref. 29 and points to a region of poor interlaminar bonding.

The graphs of a versus N (Figs. 3.25 and 3.26) show occasionally as if the crack growth has temporarily stopped. It is thought that the complex nature of the fracture process (fibre pulling, matrix cracking, fibre-matrix debonding, local fibre breaking, etc.) is the main factor behind this behaviour. It is possible that no crack extension can be visually detected before the various phases of fracture are totally or partially encountered and broken by the stress concentration at the crack front. This explains clearly the reluctance of the crack to grow

during the tests for the specimens (F1, F2, F3 and F4). Seen in the above context, the notion of the material being insensitive is meaningless, given that the material is actually sensitive at microscopic level before macroscopic damage appears to the naked eye.

The slopes of the linear portions of a versus N graphs (Figs. 3.25 and 3.26) represent the crack extension rates for the same regions. These are plotted versus the stress intensity factor range ΔK_I in Fig. 3.28. The latter is obtained from its relationship with the energy release rate g (Ref. 78) as follows:

$$K_I^2 = Eg \qquad (3.3)$$

where E is the adherend Young's modulus. The energy release rate g is given by Eqn. (3.2); where $\partial C/\partial a$, is a constant ($= 4.541 \times 10^{-6}\ N^{-1}$) $= \frac{1}{2}$ slope of the theoretical line in Fig. 3.8. Straightforward substitution into Eqn. (3.3) gives:

$$\Delta K_I = 0.151\ (P_{max} - P_{min})\quad N\ mm^{-3/2} \qquad (3.4)$$

where, P_{max} and P_{min} are respectively the maximum and minimum of the alternating fatigue load.

A semi-empirical formula which fits the experimental data in Fig. 3.28 very well is obtained using a Paris type equation (Ref. 83):

$$\frac{da}{dN} = B(\Delta K_I)^m \qquad (3.5)$$

From the above equation the experimental constants B and m are found to be:

$B = 3.216 \times 10^{-8}$

$m = 1.271$, in Nmm units.

Eqn. (3.5) then becomes,

$$\frac{da}{dN} = 3.216 \times 10^{-8} (\Delta K_I)^{1.271} \qquad (3.6)$$

with ΔK_I in $Nmm^{-3/2}$

Eqn. (3.6) may be used to predict the rate of crack growth, given ΔK_I. The fatigue-induced changes in C.O.D. from the test specimens F5 and F6 are plotted versus the crack length in Figs. 3.29 and 3.30, showing a well behaved and mainly linear relationships.

3.7 CONCLUSIONS

(i) CFRP specimens and test procedures have been given for the determination of the critical energy release rate, g_c, in the opening delaminating mode between 0° layers for the resin system XAS/914.

(ii) TDCB type-specimens capable of raising the critical splitting load and consequently suitable for controlled stable tests on a servo-hydraulic machine were used to study both static and fatigue delamination.

(iii) The critical energy release rate g_c was initially constant (around 0.26 N/mm with very good agreement with theory. The early stages of delamination growth were followed by a continuous increase in the value of g_c before this became again nearly constant. It has been generally found that g_c from the TDCB tests was higher than the value obtained from pure CFRP strips given in Ref. 29.

(iv) Delamination was essentially the mode of fracture during the fatigue tests. However, one specimen with a relatively small initial crack length showed an additional mechanism of fracture in that the delamination spread into adjacent layers, indicating a region of poor interlayer bonding.

(v) A semi-empirical Paris type formula has been found for fatigue delamination growth rate prediction in the linear region of "crack length vs number of cycles" graphs. This formula gives:

$$\frac{da}{dN} = 3.216 \times 10^{-8} (\Delta K_I)^{1.271}.$$

Table 3.1 Fatigue data for one TDCB test specimen loaded close to the base. b = 15mm; a_o = 17mm; θ = 10°

P_{mean} (N)	P_{min} (N)	P_{max} (N)	ΔP (N)	$\bar{R}$, P_{min}/P_{max}	Crack length, a (mm)	Number of cycles, N
200	100	300	200	0.33	17	0
					18.5	1500
					19	2000
					19	30000
500	400	600	200	0.67	19	0
					19	10000
500	200	800	600	0.25	19	0
					20	30000
1000	500	1500	1000	0.33	20	**

** the specimen delaminated completely, approximately at the top of the first tensile stroke (∿ 1500N)

Table 3.2 Fatigue data for one parallel-arm test specimen.

$b = 15mm$; $a_o = 25.5mm$

P_{mean} (N)	P_{min} (N)	P_{max} (N)	ΔP (N)	$\bar{R}$, P_{min}/P_{max}	Crack length, a (mm)	Number of cycles, N
300	200	400	200	0.50	25.5 25.5	0 20000
400	200	600	400	0.33	25.5 25.5	0 10000
500	250	750	500	0.33	25.5 25.5	0 10000
700	440	960	520	0.46	25.5 25.5	0 120000
850	600	1100	500	0.55	25.5 25.5	0 75000
900	600	1200	600	0.50	25.5 25.5	0 22000
1000	700	1300	600	0.54	25.5 25.5	0 18000

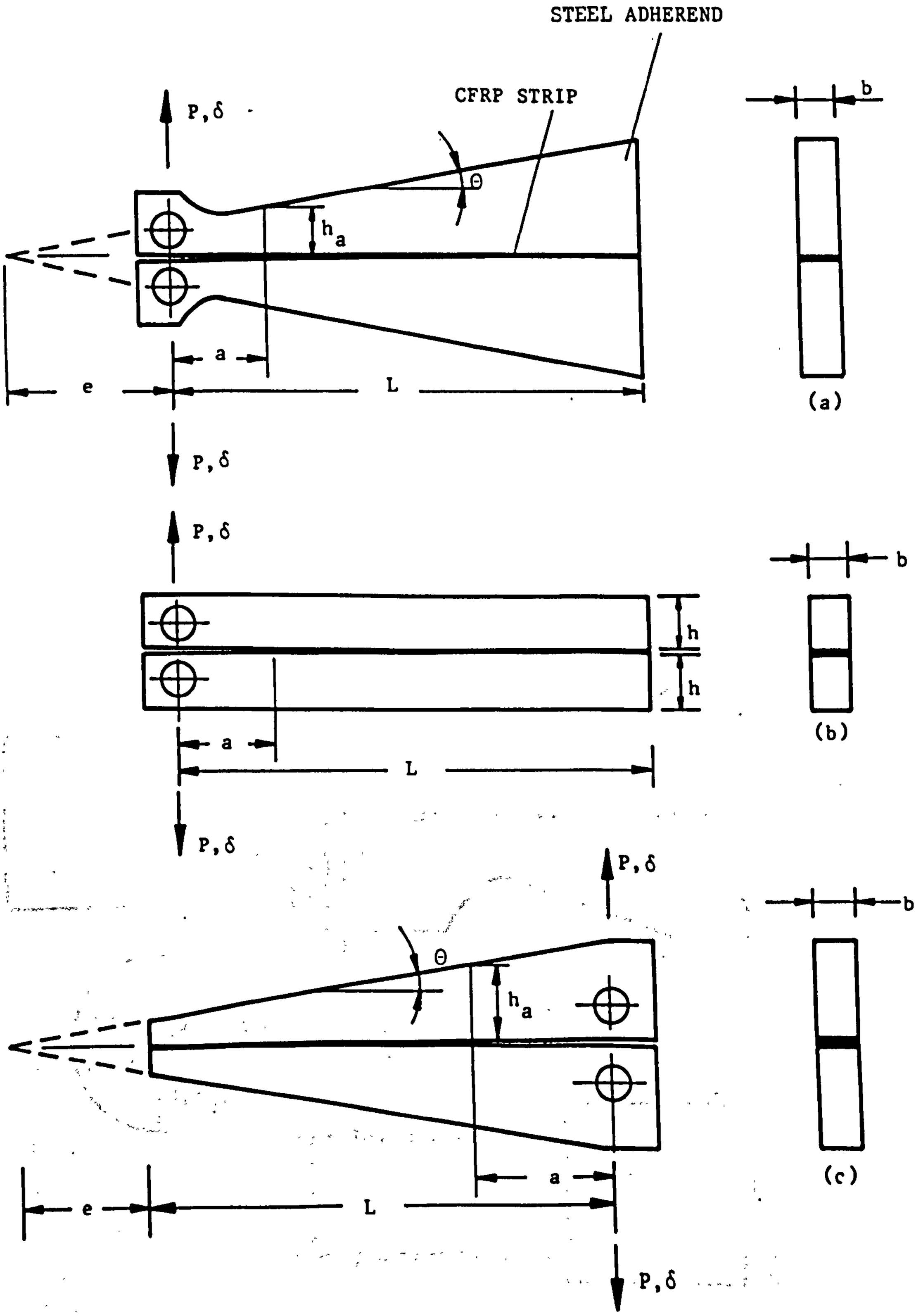

Fig. 3.1 DCB SPECIMENS: GEOMETRY AND LOADING

a. TDCB LOADED CLOSE TO THE APEX
b. DCB WITH PARALLEL ARMS
c. TDCB LOADED CLOSE TO THE BASE

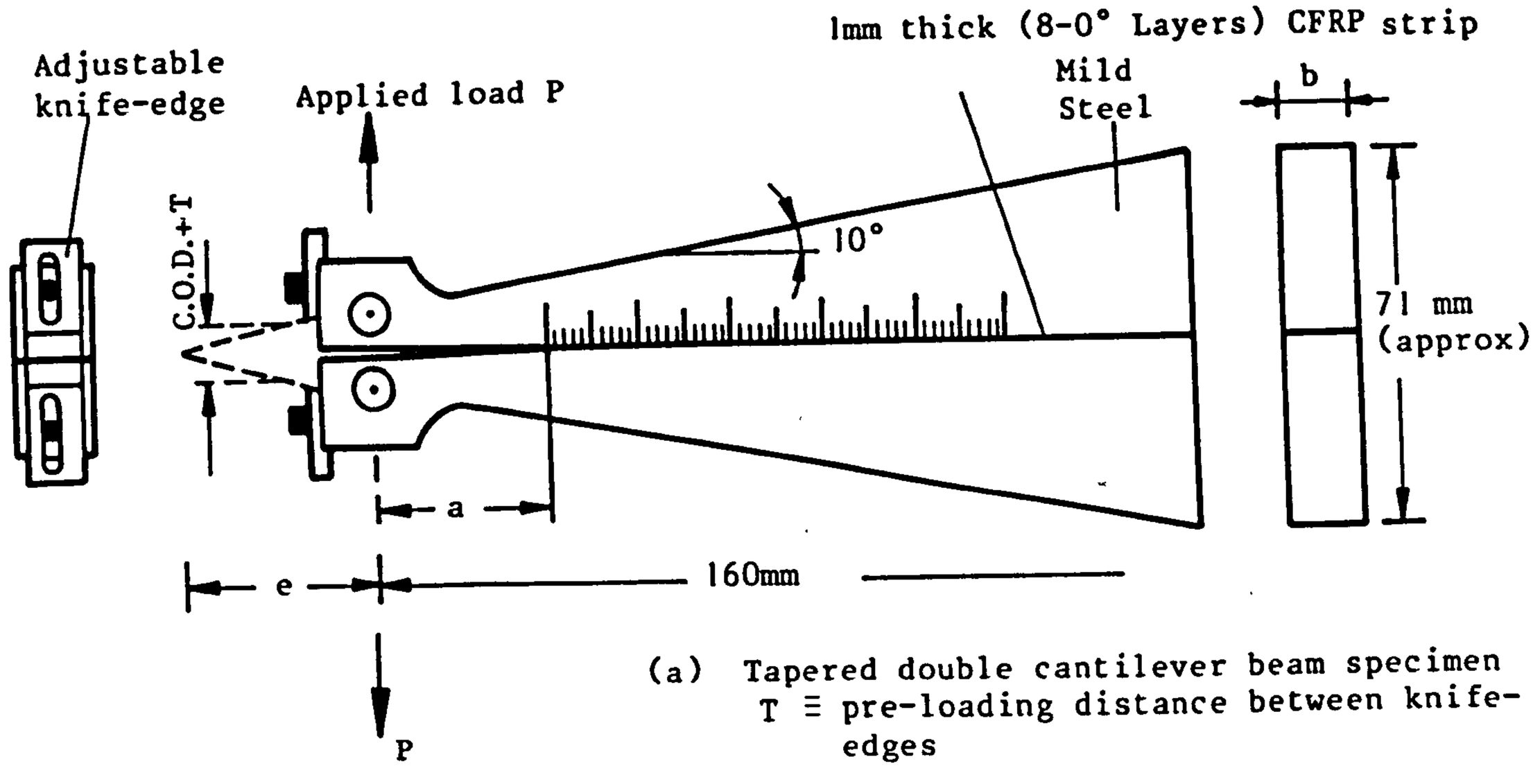

(a) Tapered double cantilever beam specimen
T ≡ pre-loading distance between knife-edges

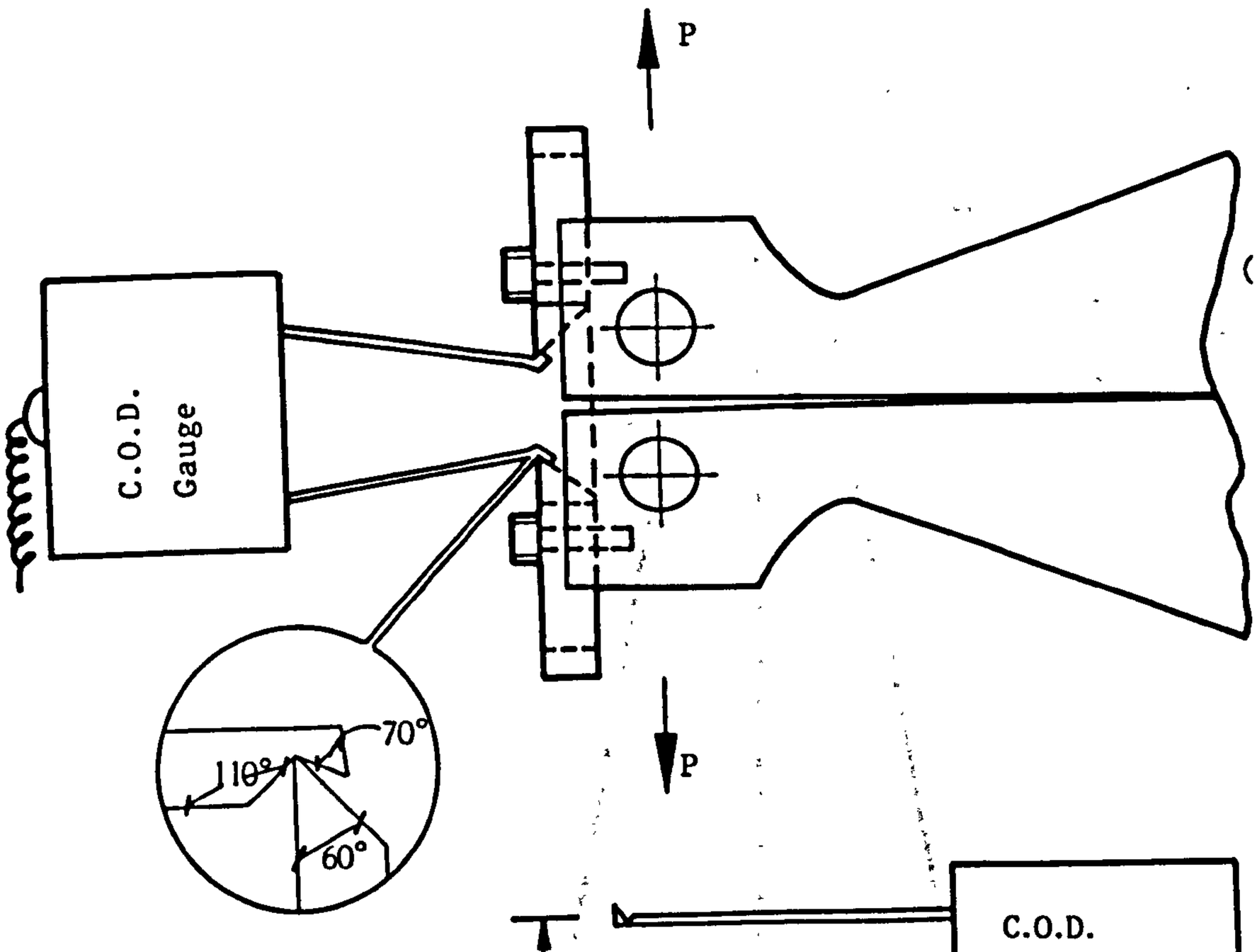

(b) Crack Opening Displacement Gauge mounting

(c) C.O.D. Gauge in released position

Fig. 3.2 TDCB TEST SPECIMEN; GEOMETRY, LOADING AND C.O.D. GAUGE MOUNTING

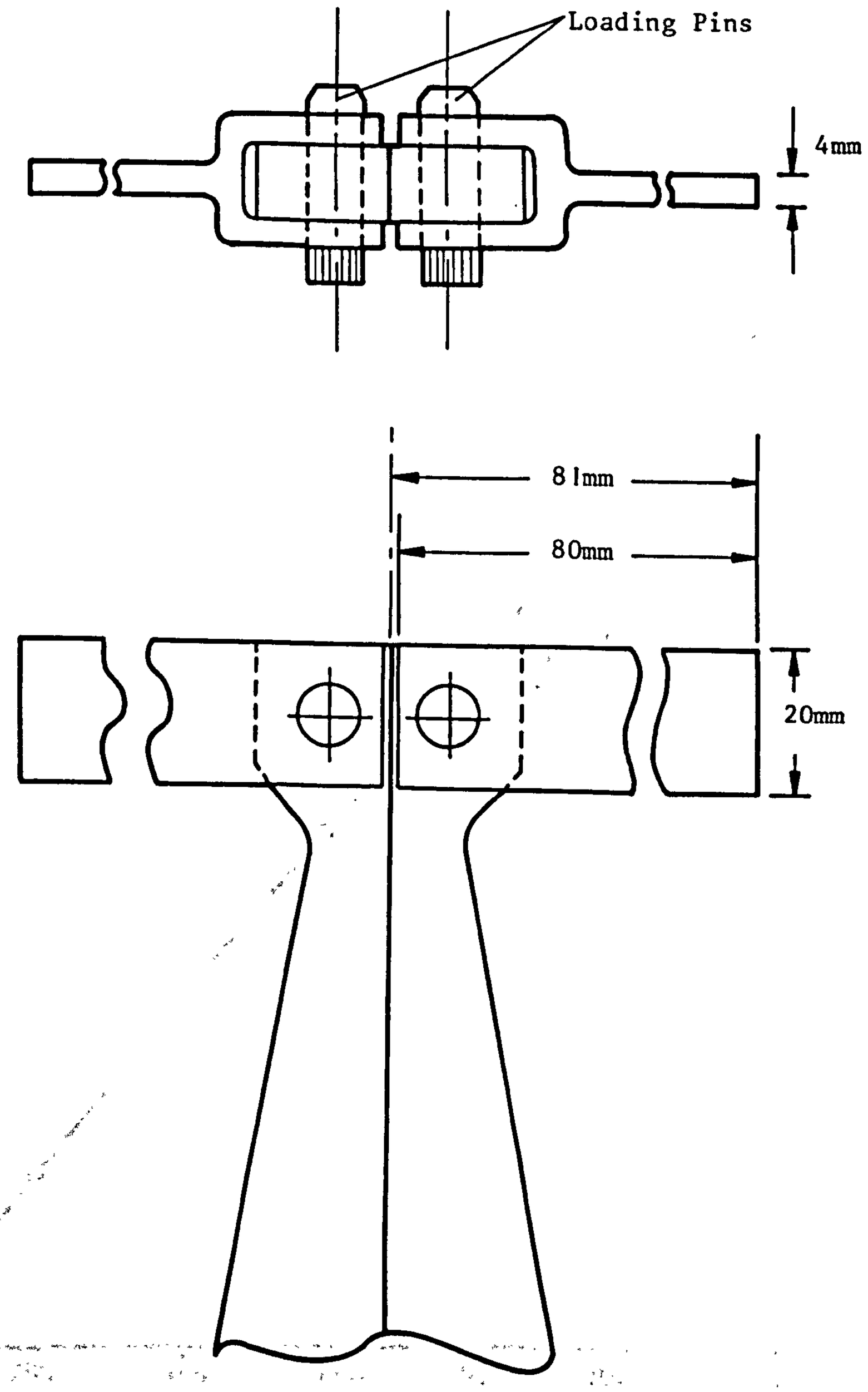

Fig. 3.3 FORK-PIN JOINTS FOR LOADING TDCB SPECIMENS IN A HOUNSFIELD TENSOMETER

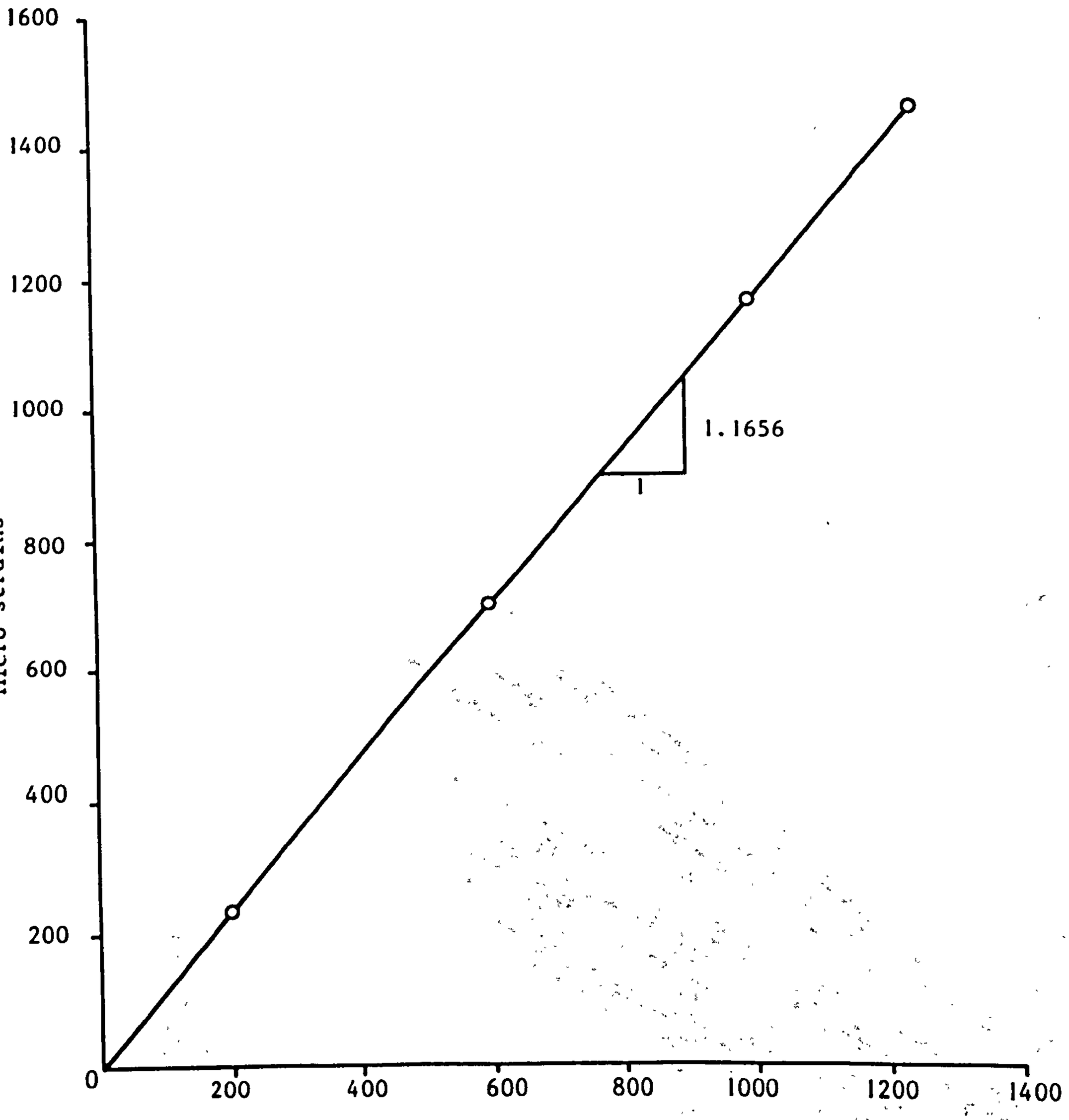

Fig. 3.4 MICROSTRAIN READINGS VERSUS DIRECT LOADS MEASURED ON THE MERCURY SCALE OF THE HOUNSFIELD TENSOMETER

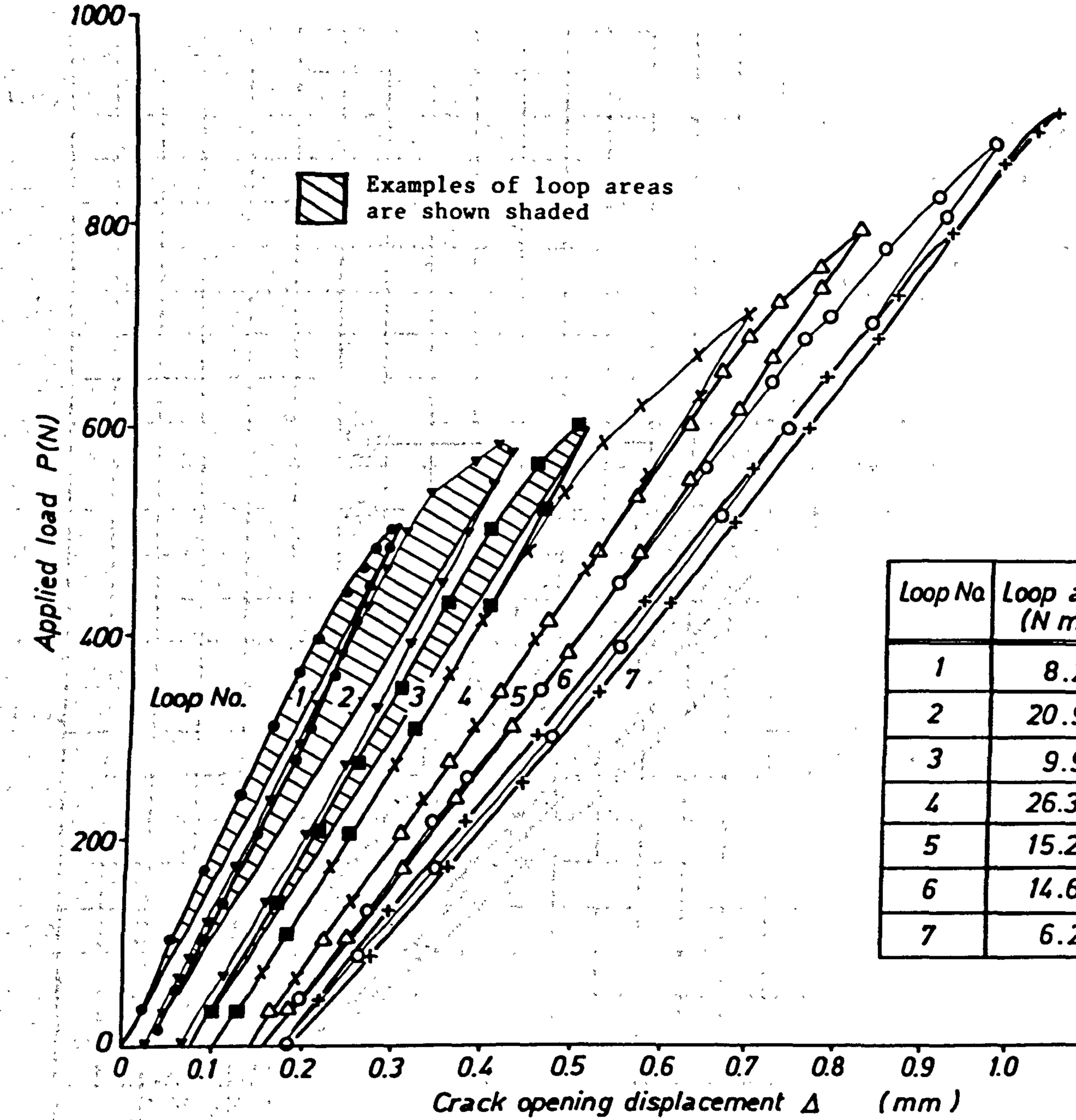

Loop No.	Loop area (N mm)	Crack length (mm)	Crack ext. (mm)	g_c (N/mm)
1	8.26	37.38	3.52	0.23
2	20.9	40.90	7.50	0.28
3	9.9	48.40	3.0	0.33
4	26.34	51.40	9.75	0.27
5	15.29	61.15	3.75	0.40
6	14.69	64.90	2.75	0.53
7	6.24	67.65	1.25	0.50

FIG. 3.5 DETERMINATION OF DELAMINATION GROWTH CHARACTERISTICS FOR TDCB SPECIMEN

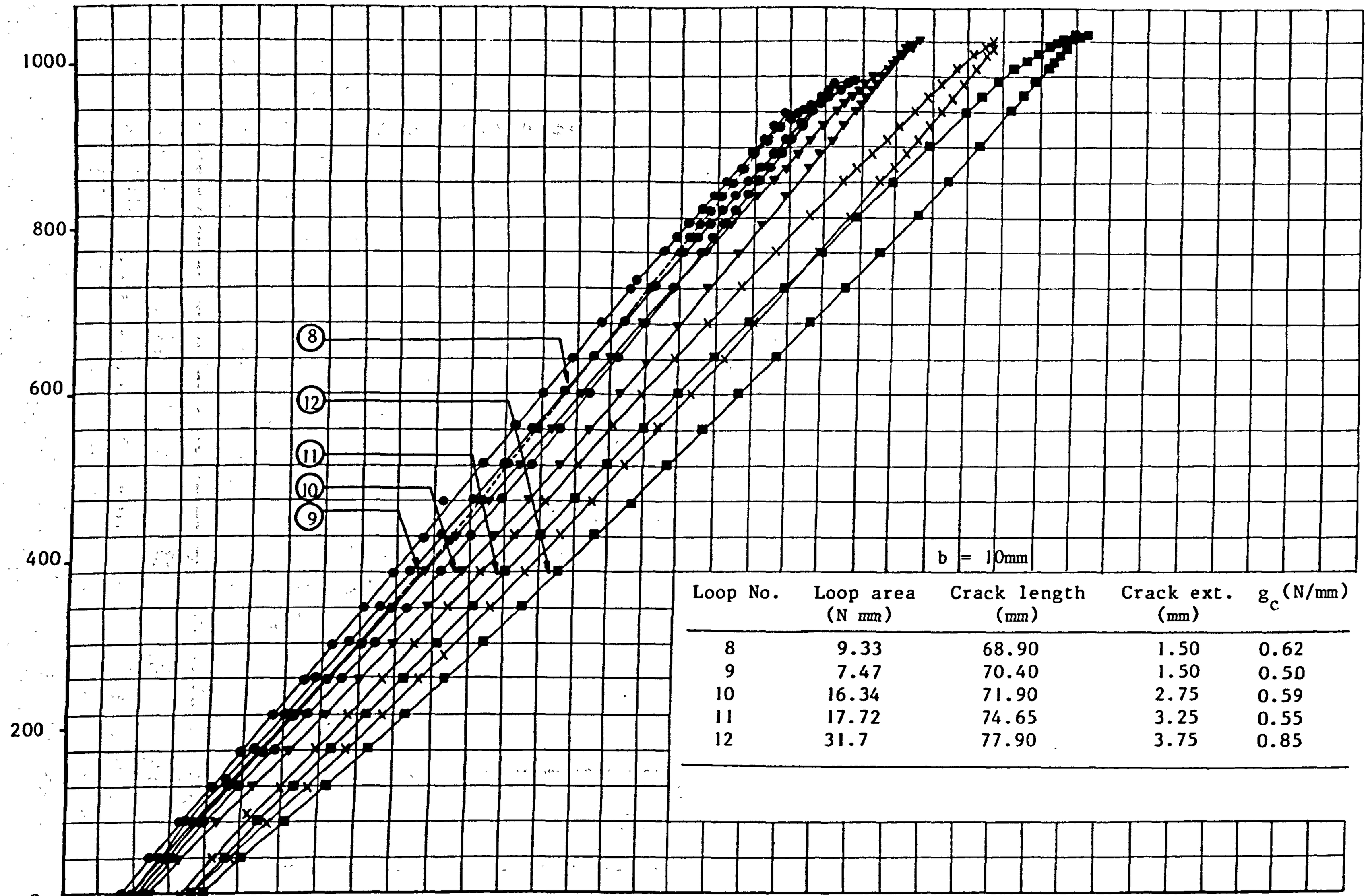

Loop No.	Loop area (N mm)	Crack length (mm)	Crack ext. (mm)	g_c (N/mm)
8	9.33	68.90	1.50	0.62
9	7.47	70.40	1.50	0.50
10	16.34	71.90	2.75	0.59
11	17.72	74.65	3.25	0.55
12	31.7	77.90	3.75	0.85

Fig. 3.6 DETERMINATION OF DELAMINATION CHARACTERISTICS FOR TDCB SPECIMEN, S1

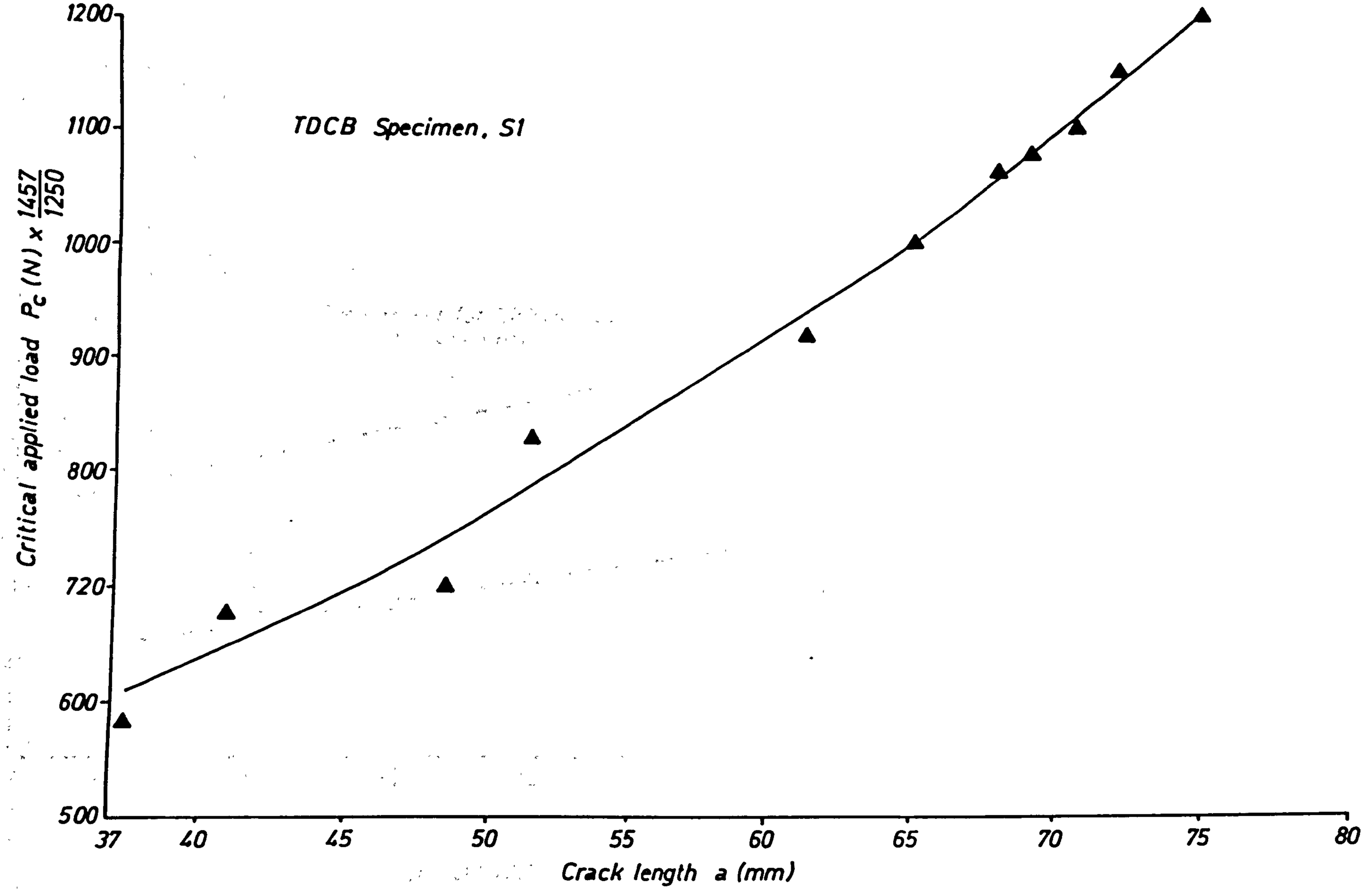

FIG.3·7 CRITICAL DELAMINATION LOAD vs CRACK LENGTH

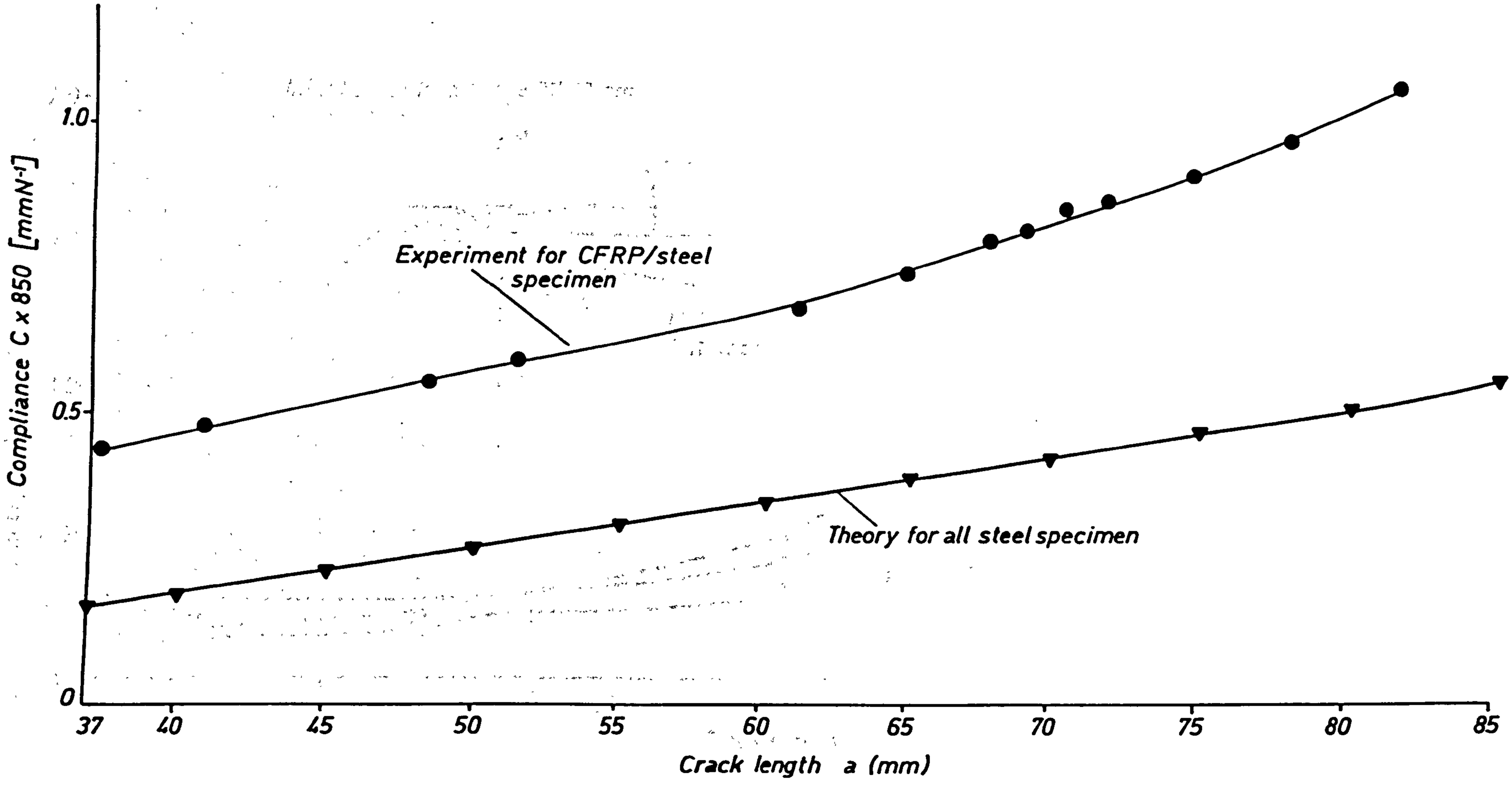

FIG. 3.8 COMPLIANCE vs. CRACK LENGTH FOR TDCB SPECIMEN

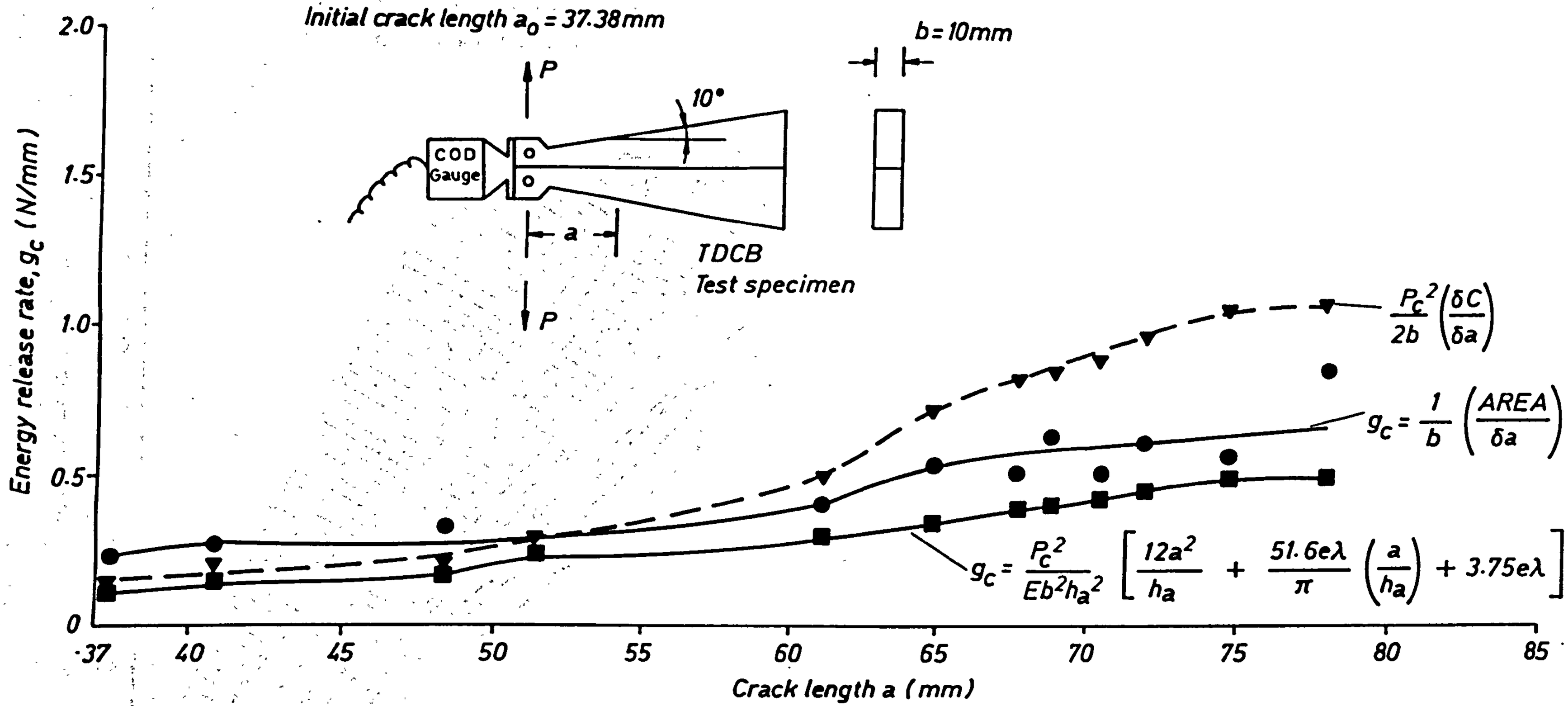

FIG. 3.9 CRITICAL ENERY RELEASE RATE vs. CRACK LENGTH FOR TDCB SPECIMEN, S1

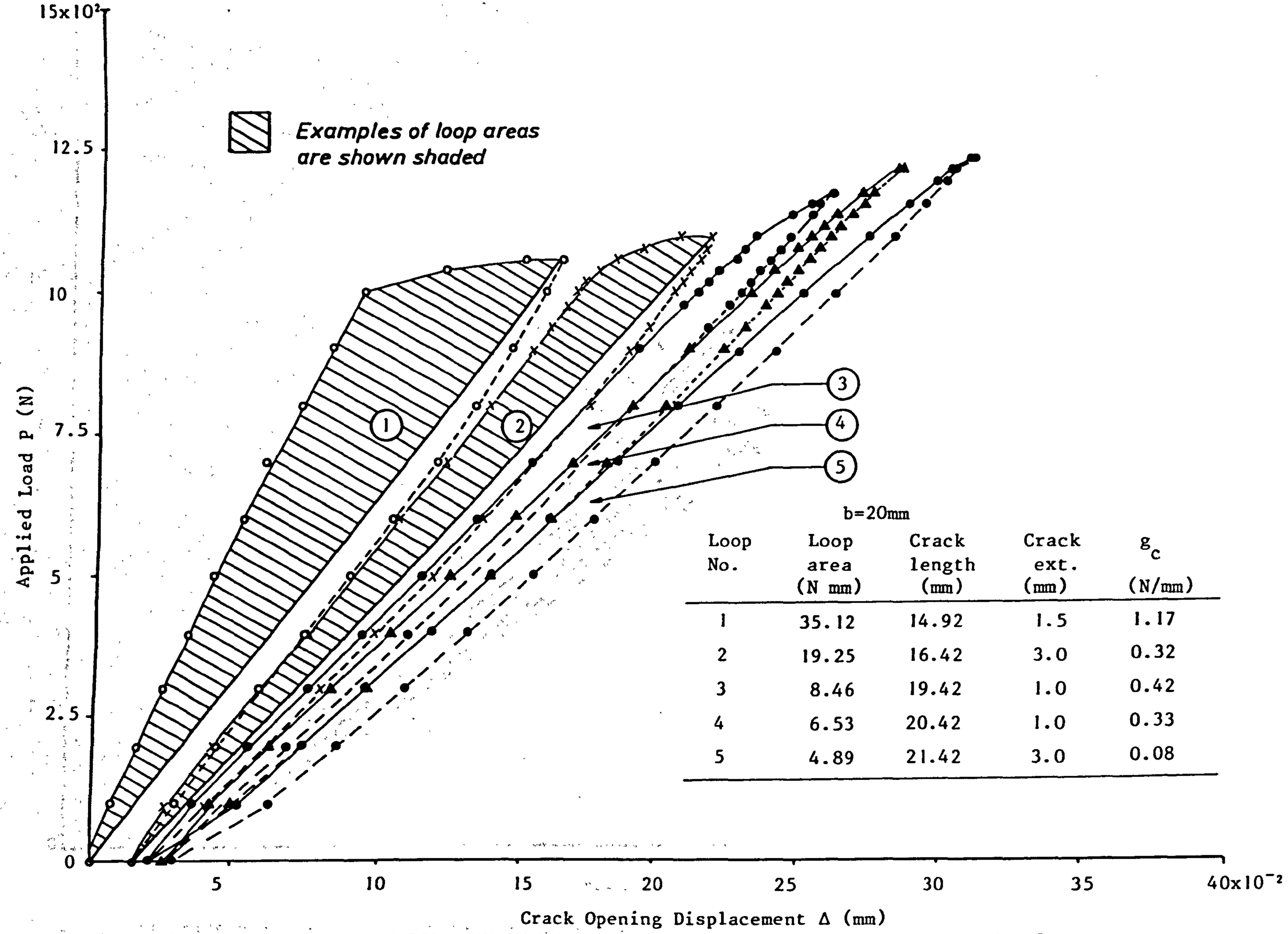

b=20mm

Loop No.	Loop area (N mm)	Crack length (mm)	Crack ext. (mm)	g_c (N/mm)
1	35.12	14.92	1.5	1.17
2	19.25	16.42	3.0	0.32
3	8.46	19.42	1.0	0.42
4	6.53	20.42	1.0	0.33
5	4.89	21.42	3.0	0.08

Fig. 3.10 DETERMINATION OF DELAMINATION GROWTH CHARACTERISTICS FOR TDCB SPECIMEN, S2

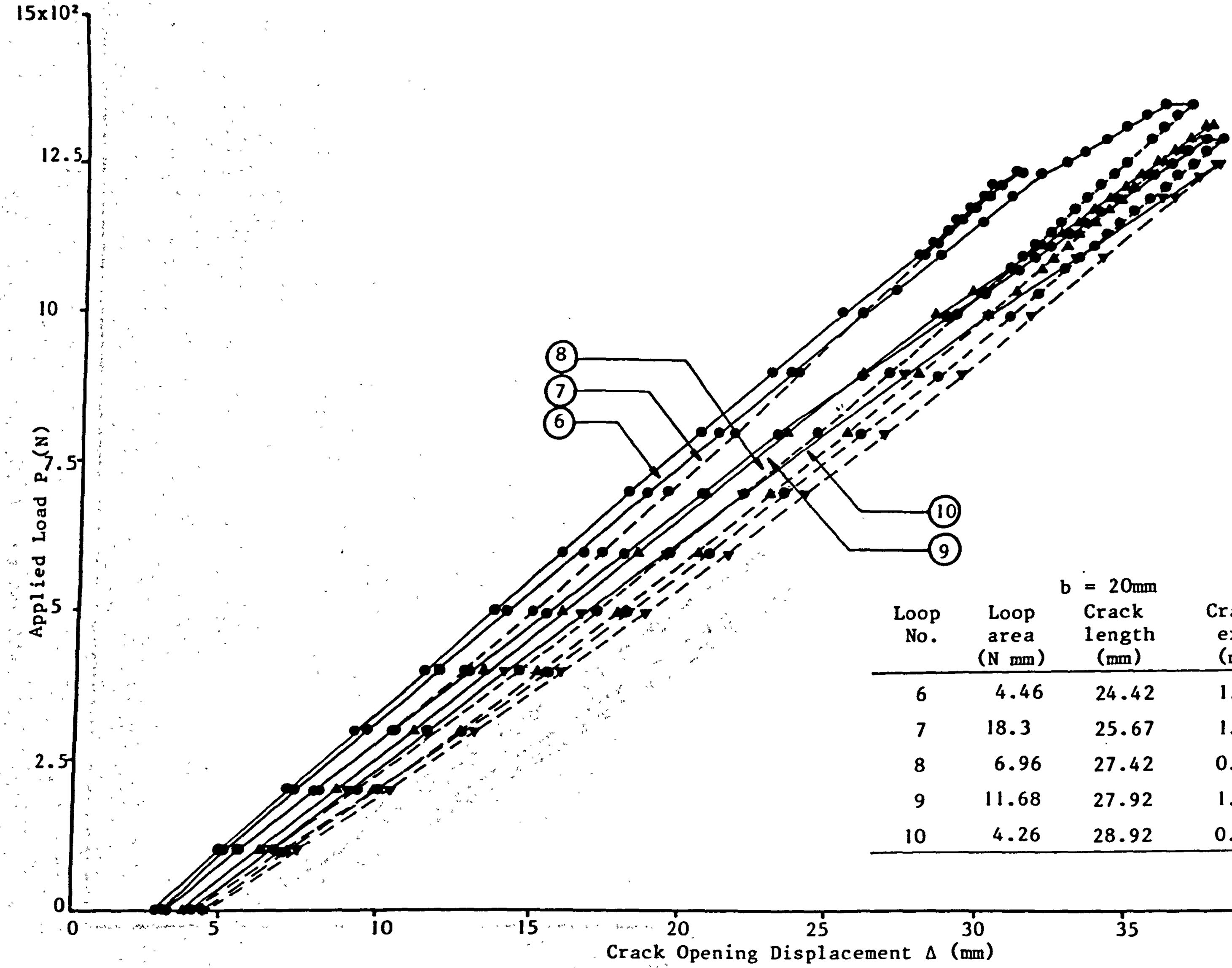

b = 20mm

Loop No.	Loop area (N mm)	Crack length (mm)	Crack ext. (mm)	g_c (N/mm)
6	4.46	24.42	1.25	0.18
7	18.3	25.67	1.75	0.52
8	6.96	27.42	0.50	0.69
9	11.68	27.92	1.0	0.58
10	4.26	28.92	0.25	0.85

Fig. 3.11 DETERMINATION OF DELAMINATION CHARACTERISTICS FOR TDCB SPECIMEN, S2

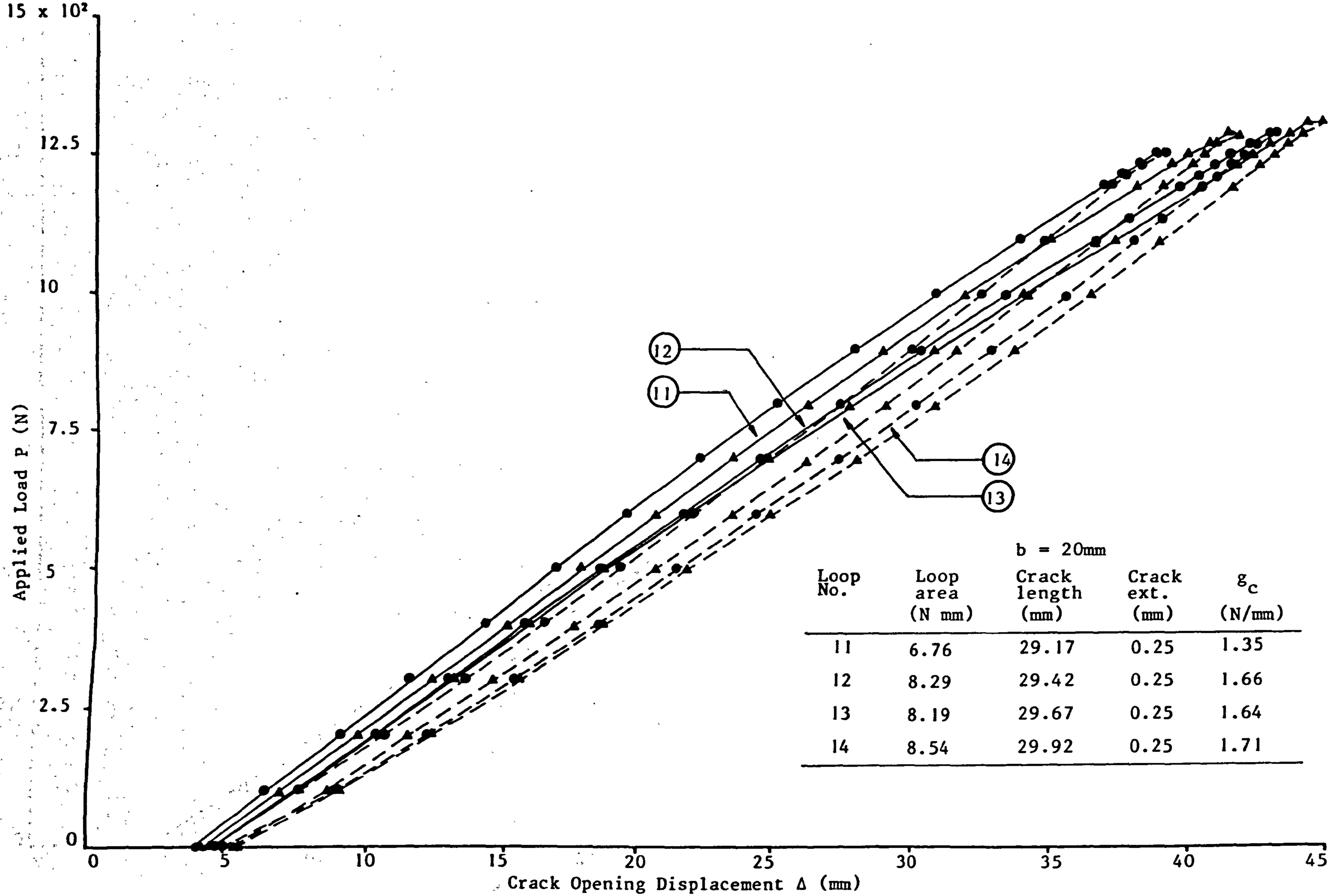

b = 20mm

Loop No.	Loop area (N mm)	Crack length (mm)	Crack ext. (mm)	g_c (N/mm)
11	6.76	29.17	0.25	1.35
12	8.29	29.42	0.25	1.66
13	8.19	29.67	0.25	1.64
14	8.54	29.92	0.25	1.71

Fig. 3.12 DETERMINATION OF DELAMINATION CHARACTERISTICS FOR TDCB SPECIMEN, S2

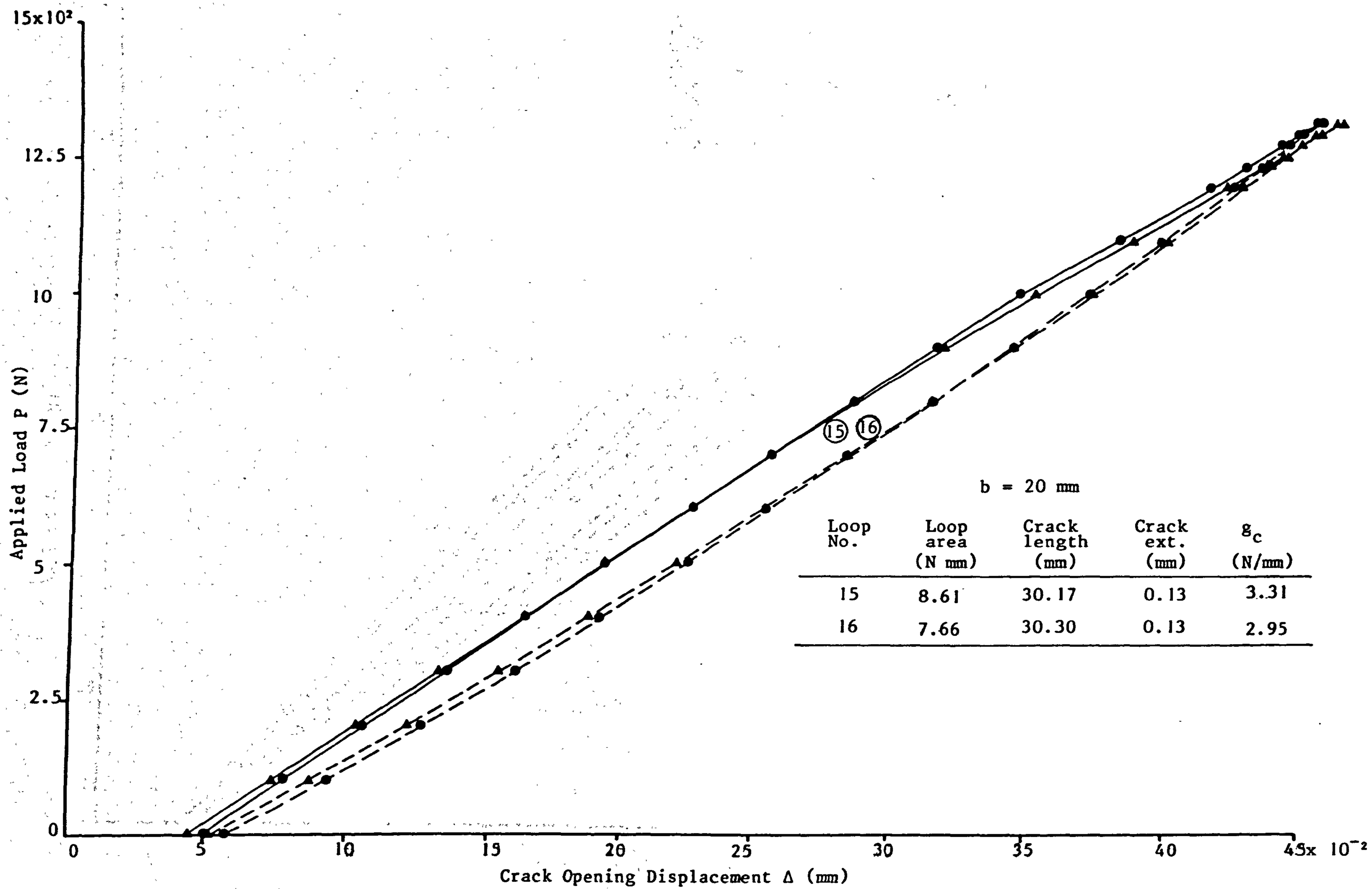

b = 20 mm

Loop No.	Loop area (N mm)	Crack length (mm)	Crack ext. (mm)	g_c (N/mm)
15	8.61	30.17	0.13	3.31
16	7.66	30.30	0.13	2.95

Fig. 3.13 DETERMINATION OF DELAMINATION CHARACTERISTICS FOR TDCB SPECIMEN, S2

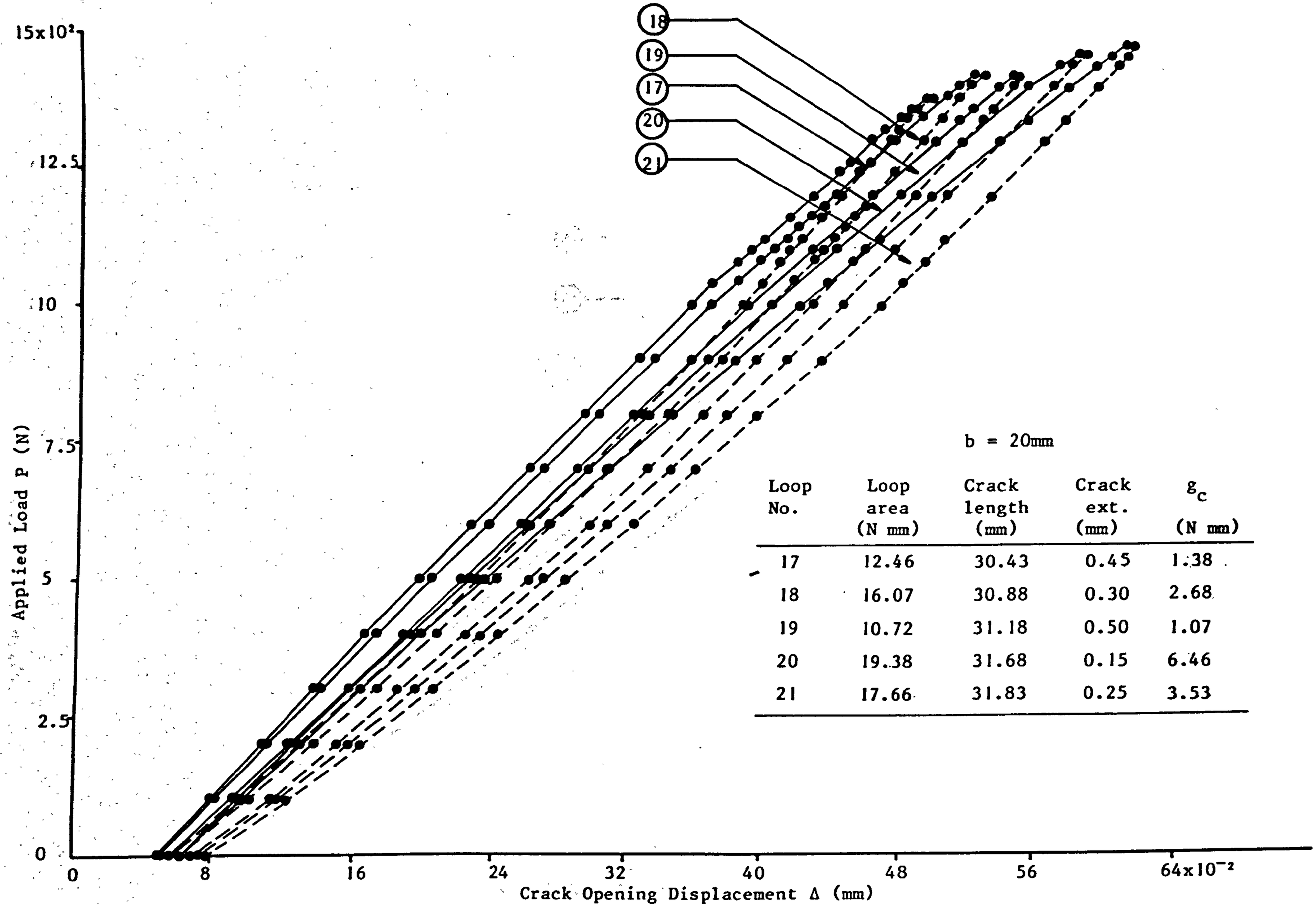

Loop No.	Loop area (N mm)	Crack length (mm)	Crack ext. (mm)	g_c (N mm)
17	12.46	30.43	0.45	1.38
18	16.07	30.88	0.30	2.68
19	10.72	31.18	0.50	1.07
20	19.38	31.68	0.15	6.46
21	17.66	31.83	0.25	3.53

Fig. 3.14 DETERMINATION OF DELAMINATION CHARACTERISTICS FOR TDCB SPECIMEN, S2

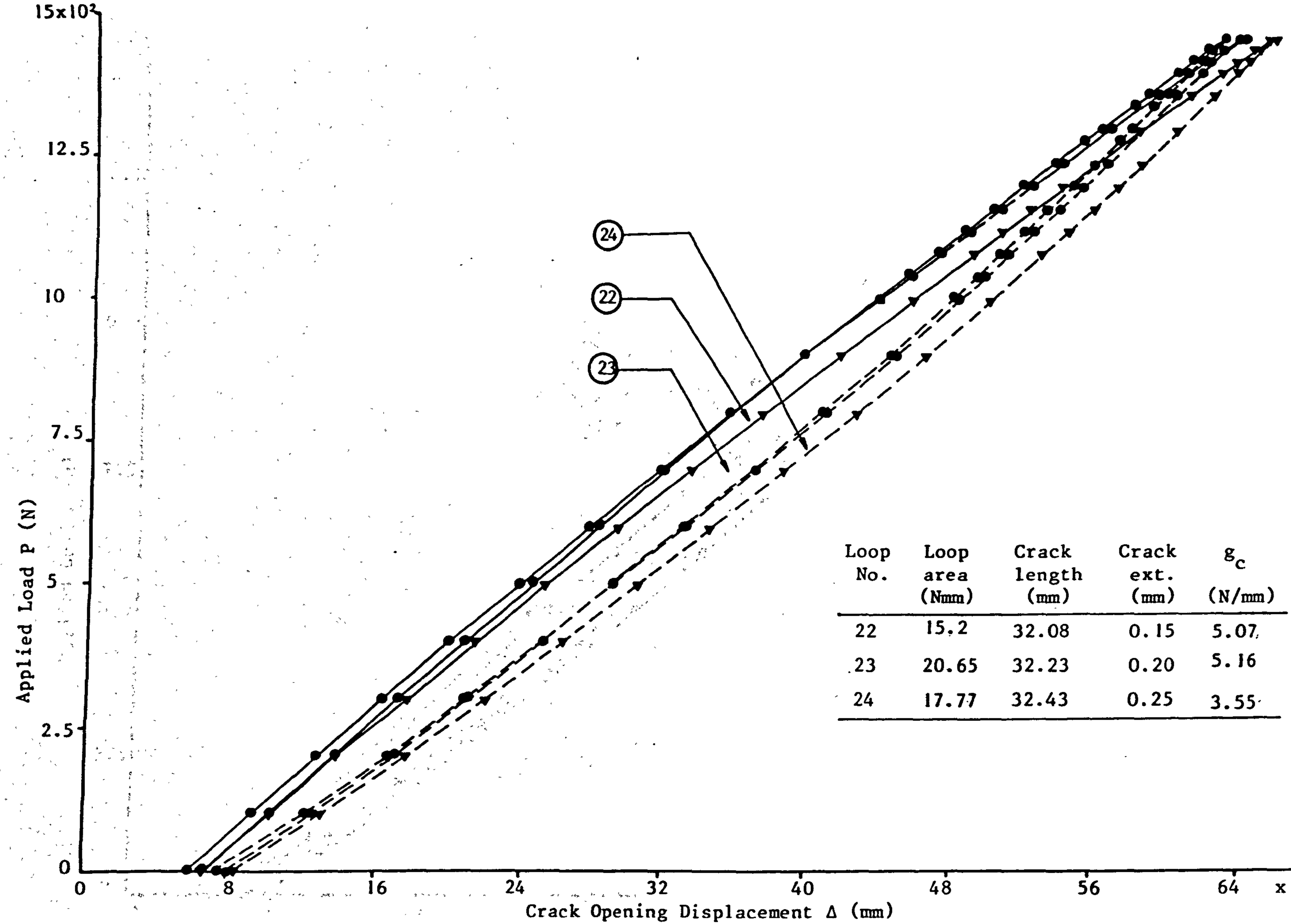

Loop No.	Loop area (Nmm)	Crack length (mm)	Crack ext. (mm)	g_c (N/mm)
22	15.2	32.08	0.15	5.07
23	20.65	32.23	0.20	5.16
24	17.77	32.43	0.25	3.55

Fig. 3.15 DETERMINATION OF DELAMINATION CHARACTERISTICS FOR TDCB SPECIMEN, S2

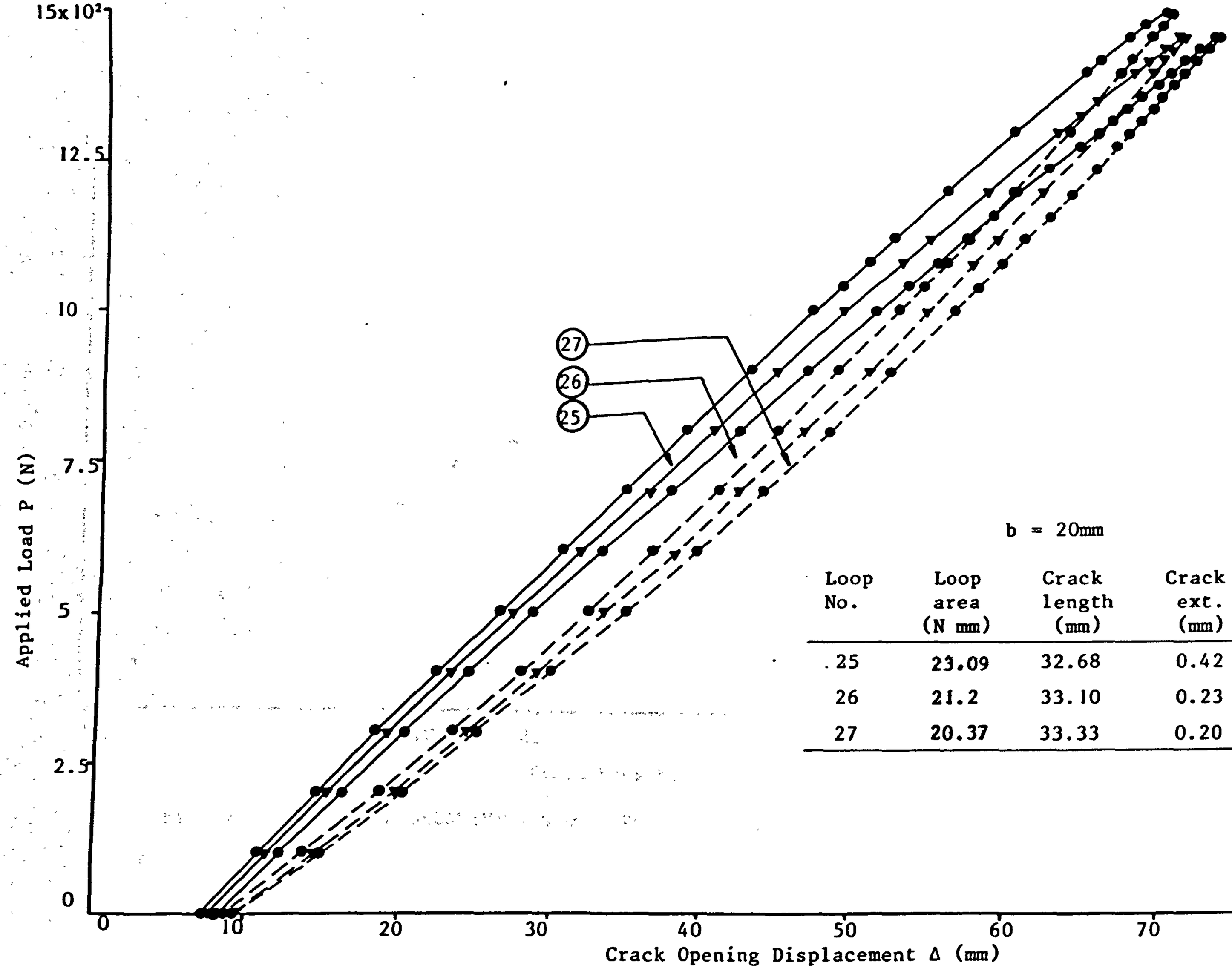

b = 20mm

Loop No.	Loop area (N mm)	Crack length (mm)	Crack ext. (mm)	g_c (N/mm)
25	23.09	32.68	0.42	2.75
26	21.2	33.10	0.23	4.61
27	20.37	33.33	0.20	5.09

Fig. 3.16 DETERMINATION OF DELAMINATION CHARACTERISTICS FOR TDCB SPECIMEN, S2

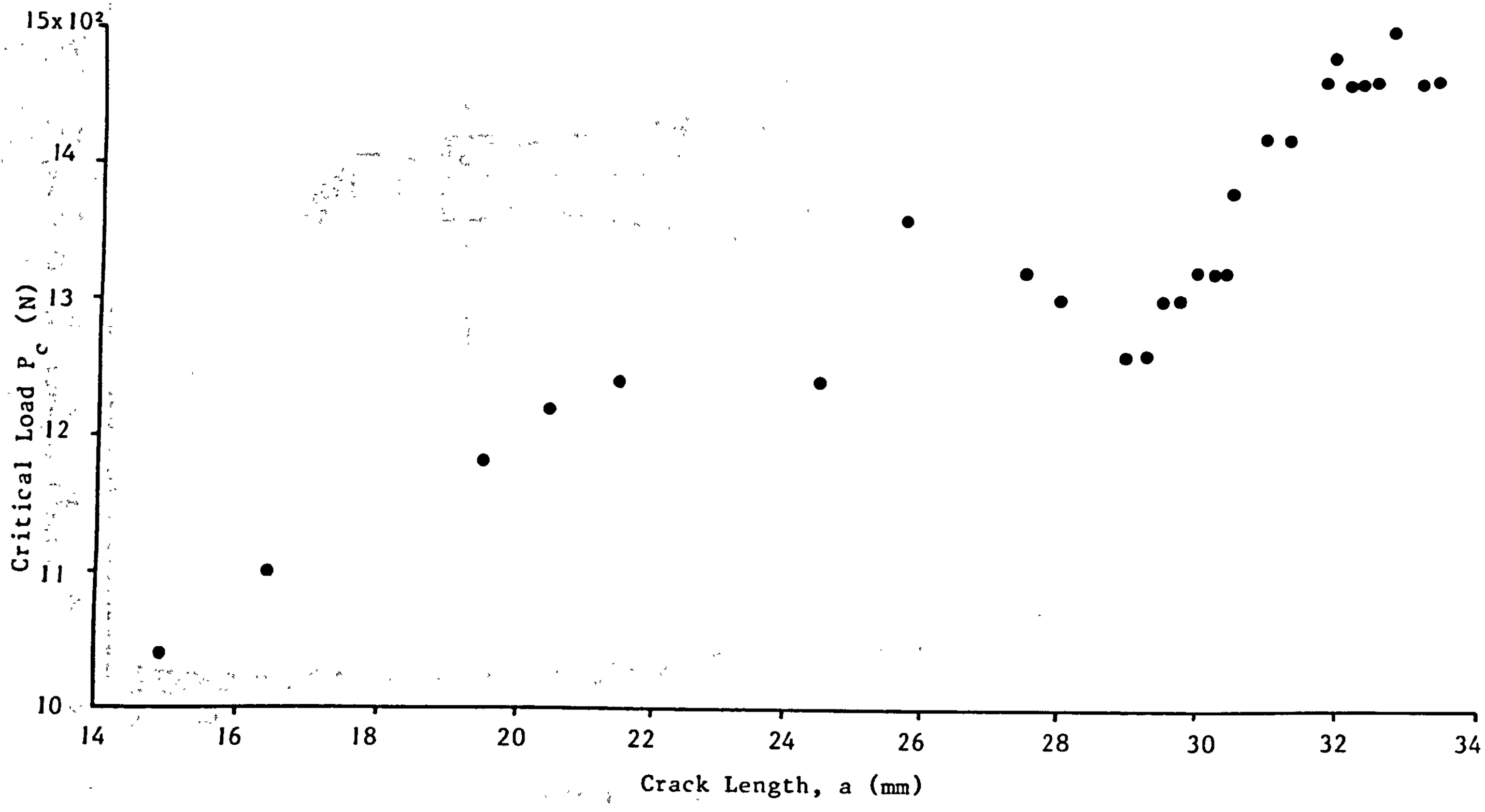

Fig. 3.17 CRITICAL DELAMINATION LOAD VS. CRACK LENGTH FOR S2 TDCB SPECIMEN

TDCB Test specimen, S2

Initial crack length a_o = 14.92mm

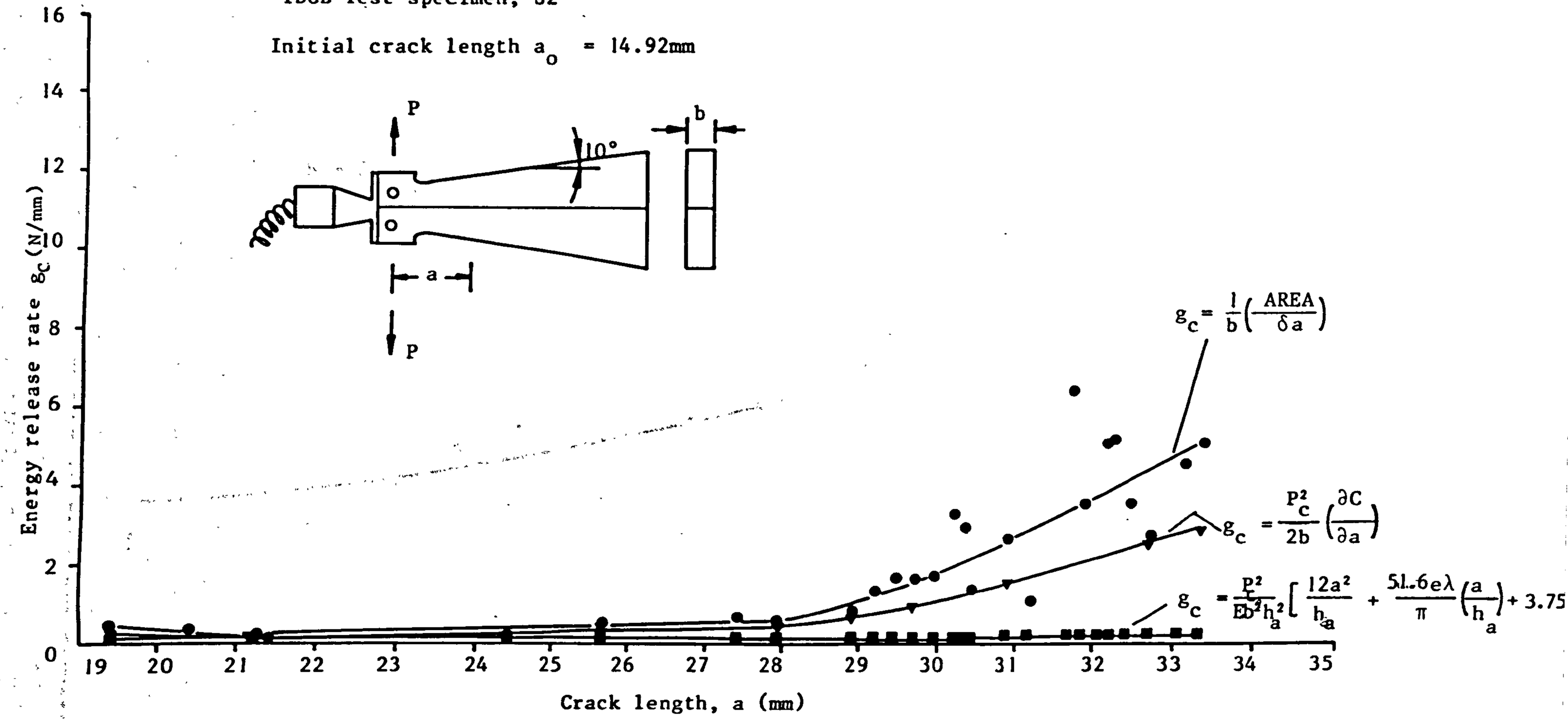

Fig. 3.18 CRITICAL ENERGY RELEASE RATE VS. CRACK LENGTH

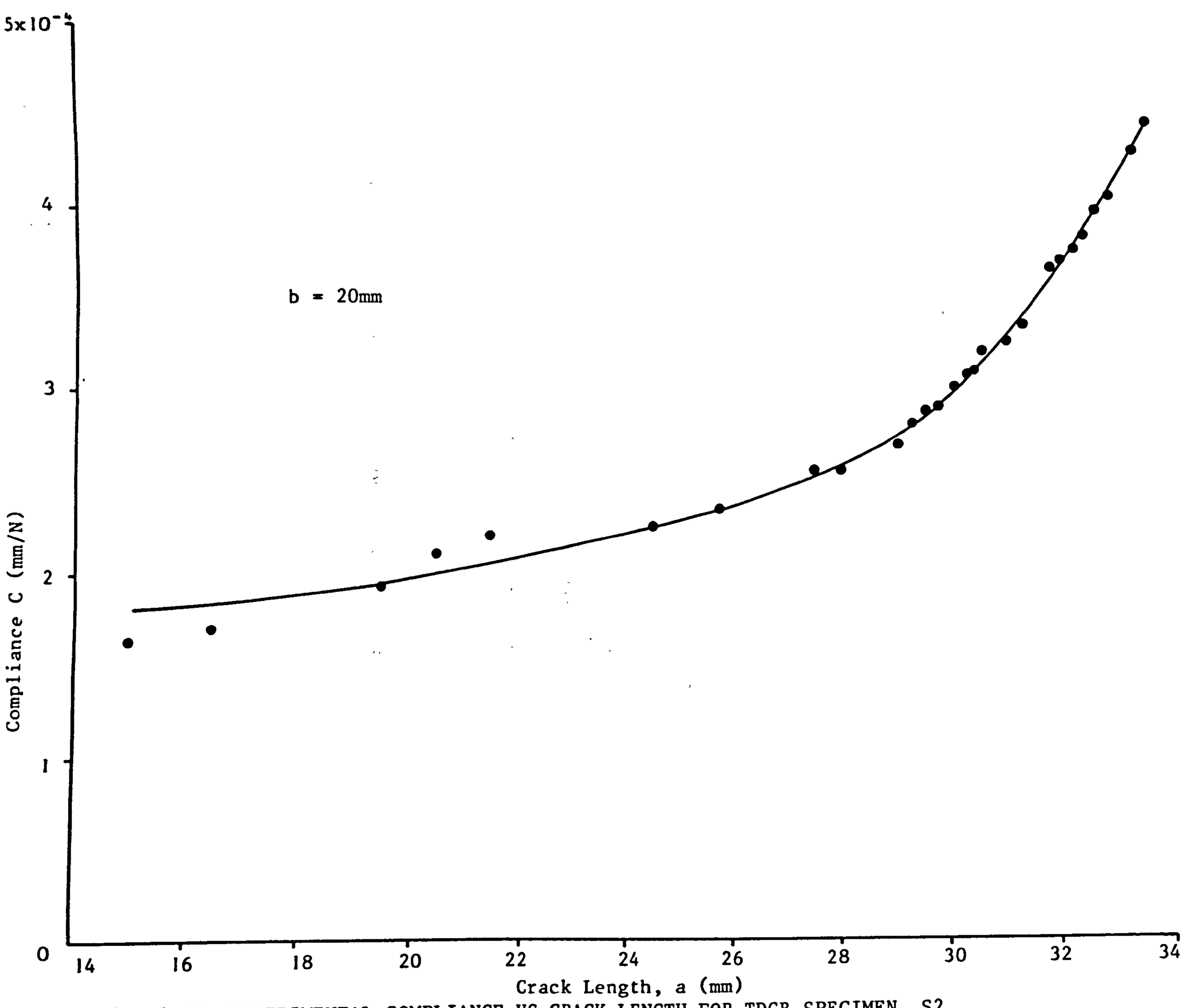

Fig. 3.19 EXPERIMENTAL COMPLIANCE VS CRACK LENGTH FOR TDCB SPECIMEN, S2

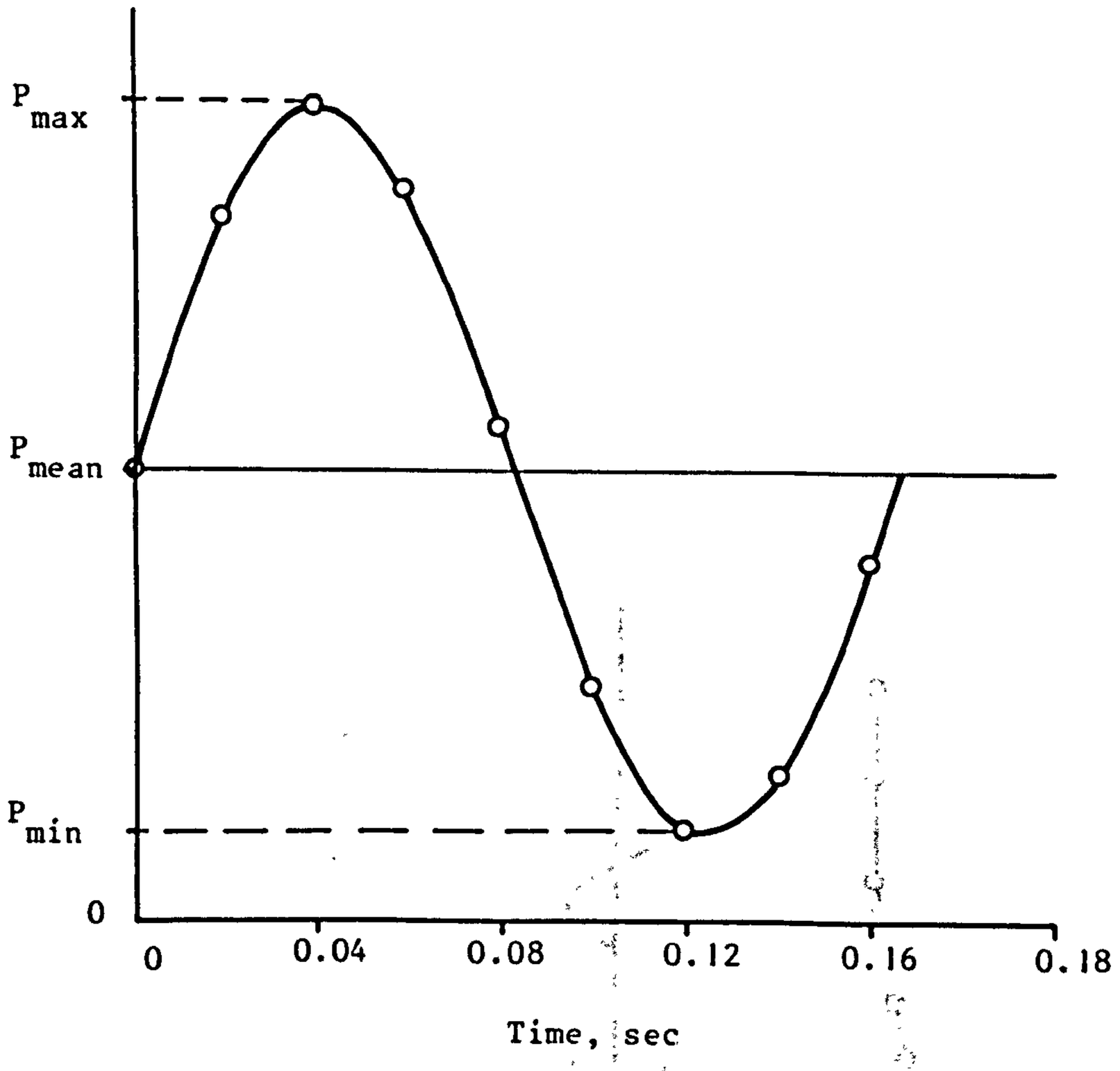

Fig. 3.20 LOAD VS TIME FOR FATIGUE TESTS

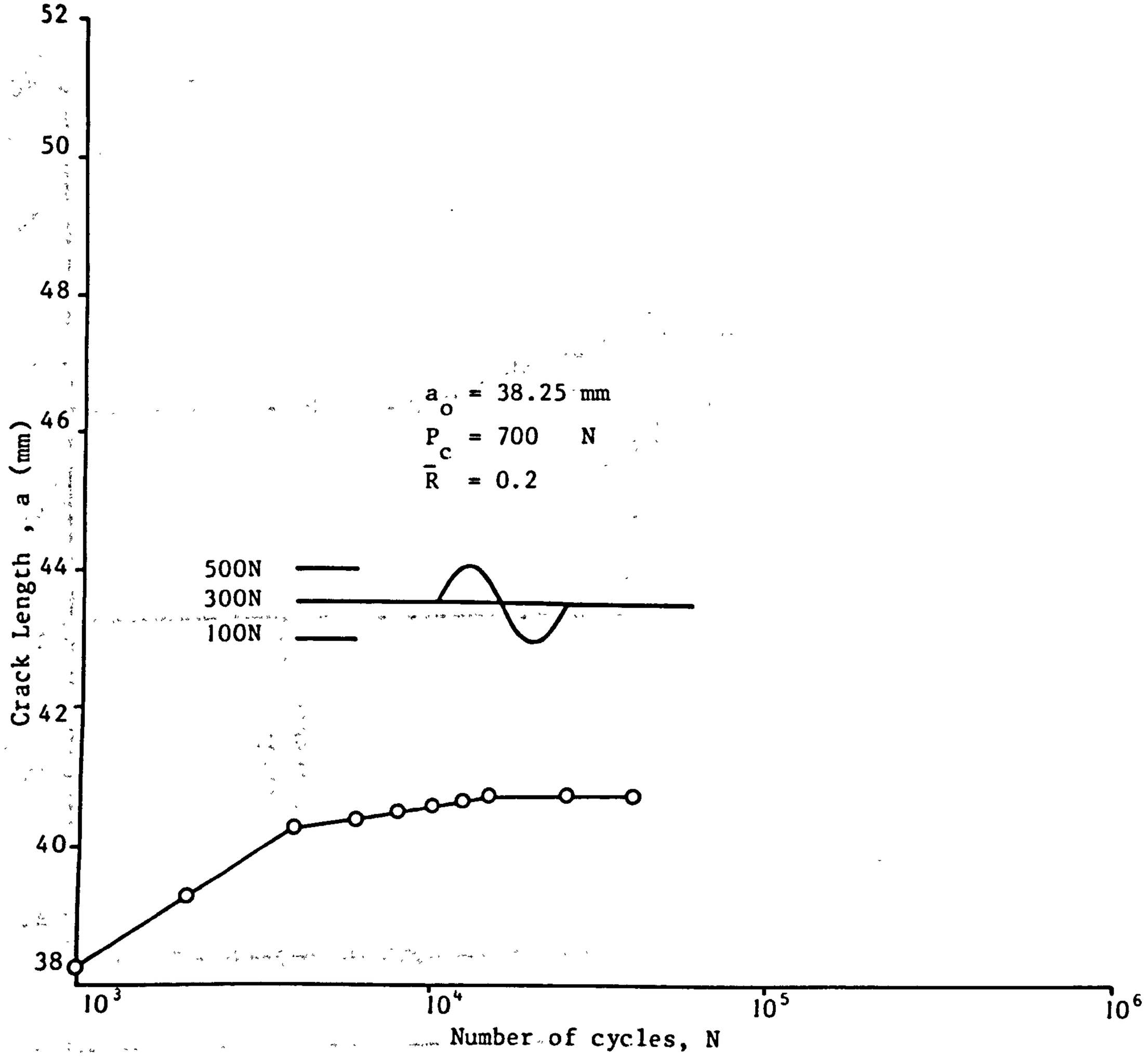

Fig. 3.21 FATIGUE CRACK PROPAGATION DATA FOR TDCB TEST SPECIMEN, F1

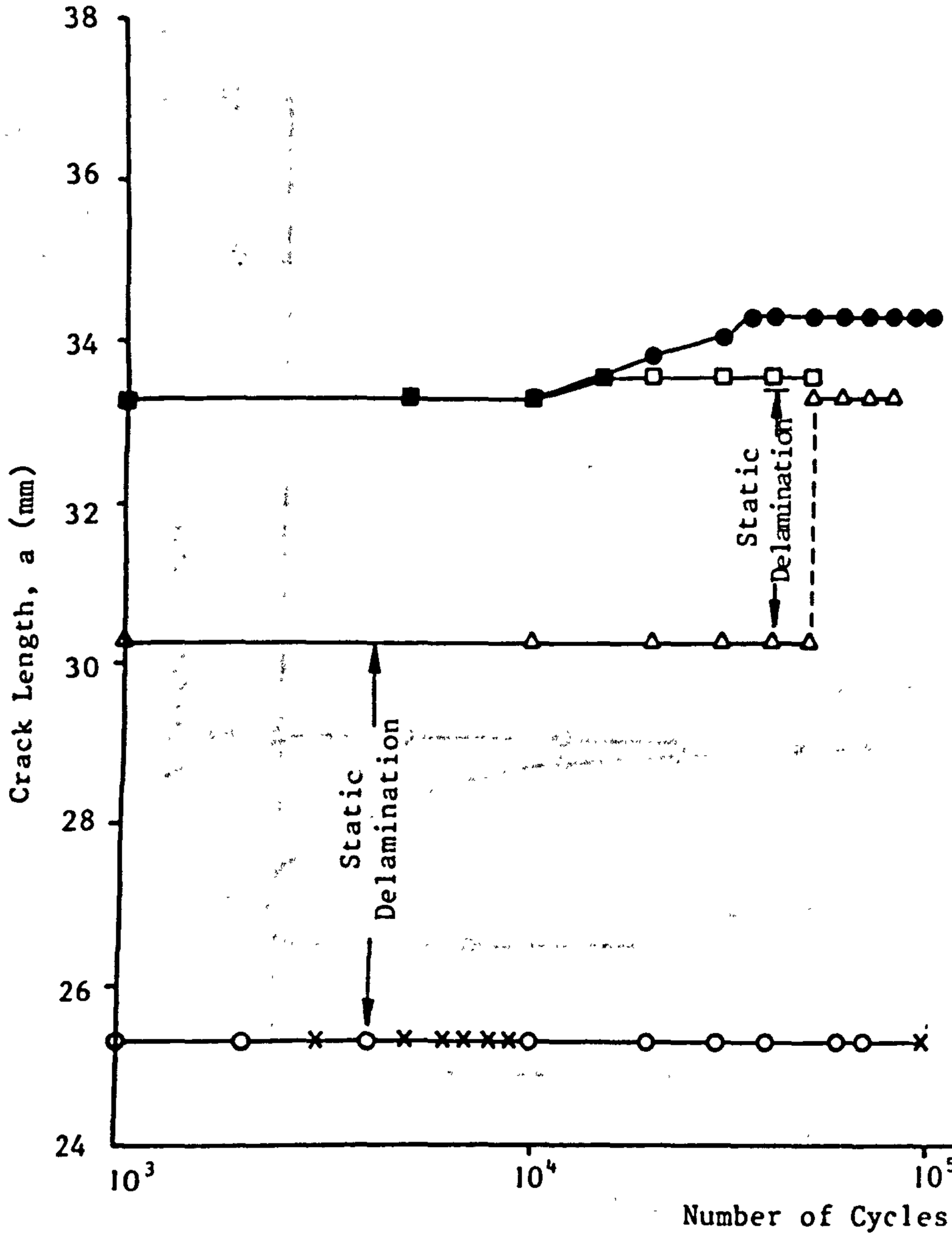

a_o = 25.3 mm

P_c = 800 N

Symbol	P_{min} (N)	P_{max} (N)	ΔP (N)	P_{mean} (N)	$\bar{R}$
×	100	300	200	200	0.33
○	100	600	500	350	0.17
△	100	300	200	200	0.33
□	100	400	300	250	0.25
●	100	500	400	300	0.20

Fig. 3.22 FATIGUE CRACK PROPAGATION DATA FOR TDCB TEST SPECIMEN, F2

a_o = 18.3 mm

P_c = 940 N

Symbol	P_{min} (N)	P_{max} (N)	ΔP (N)	P_{mean} (N)	$\bar{R}$
△	100	500	400	300	0.20
×	100	700	600	400	0.14
○	50	750	700	400	0.07

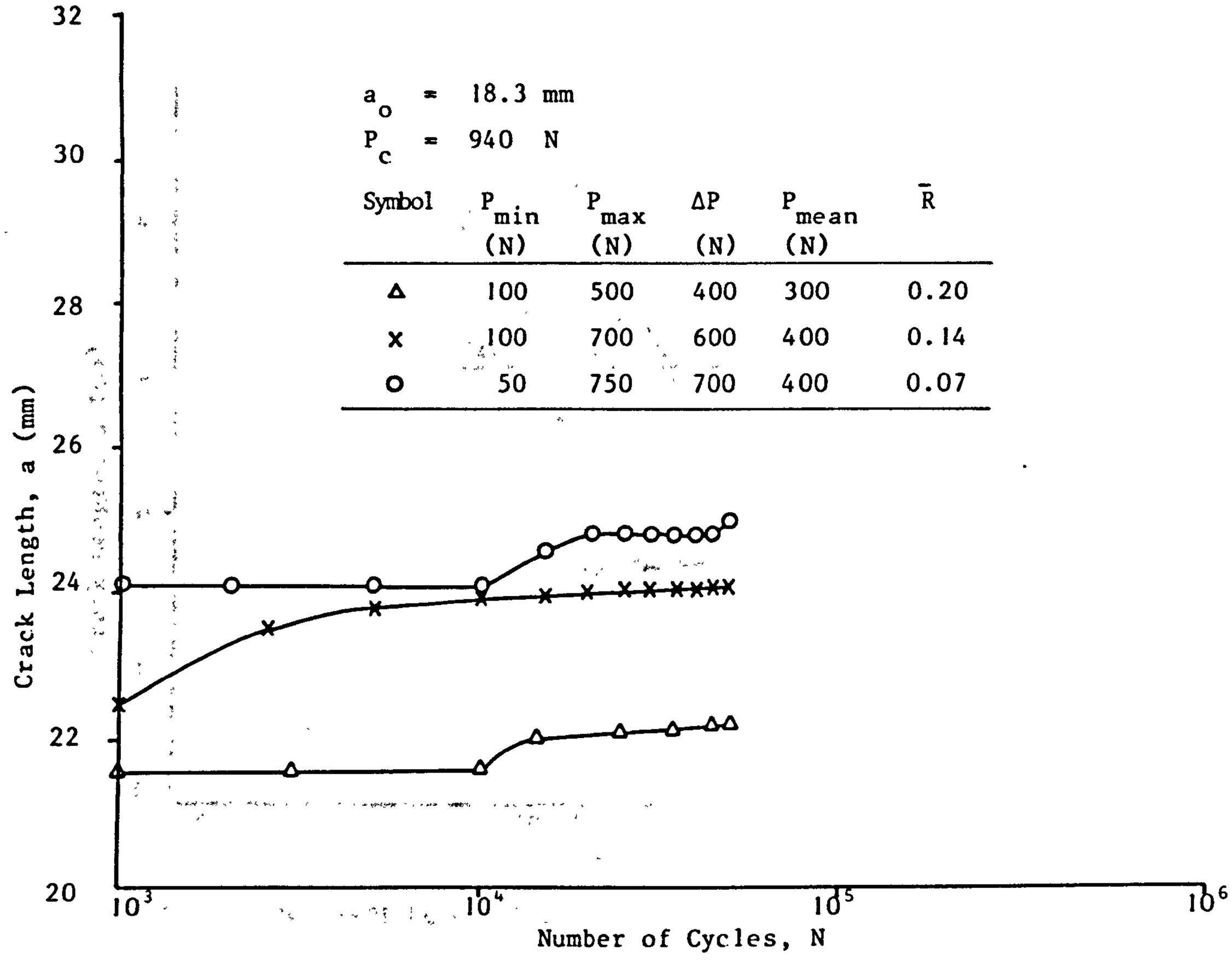

Fig. 3.23 FATIGUE CRACK PROPAGATION DATA FOR TDCB TEST SPECIMEN, F3

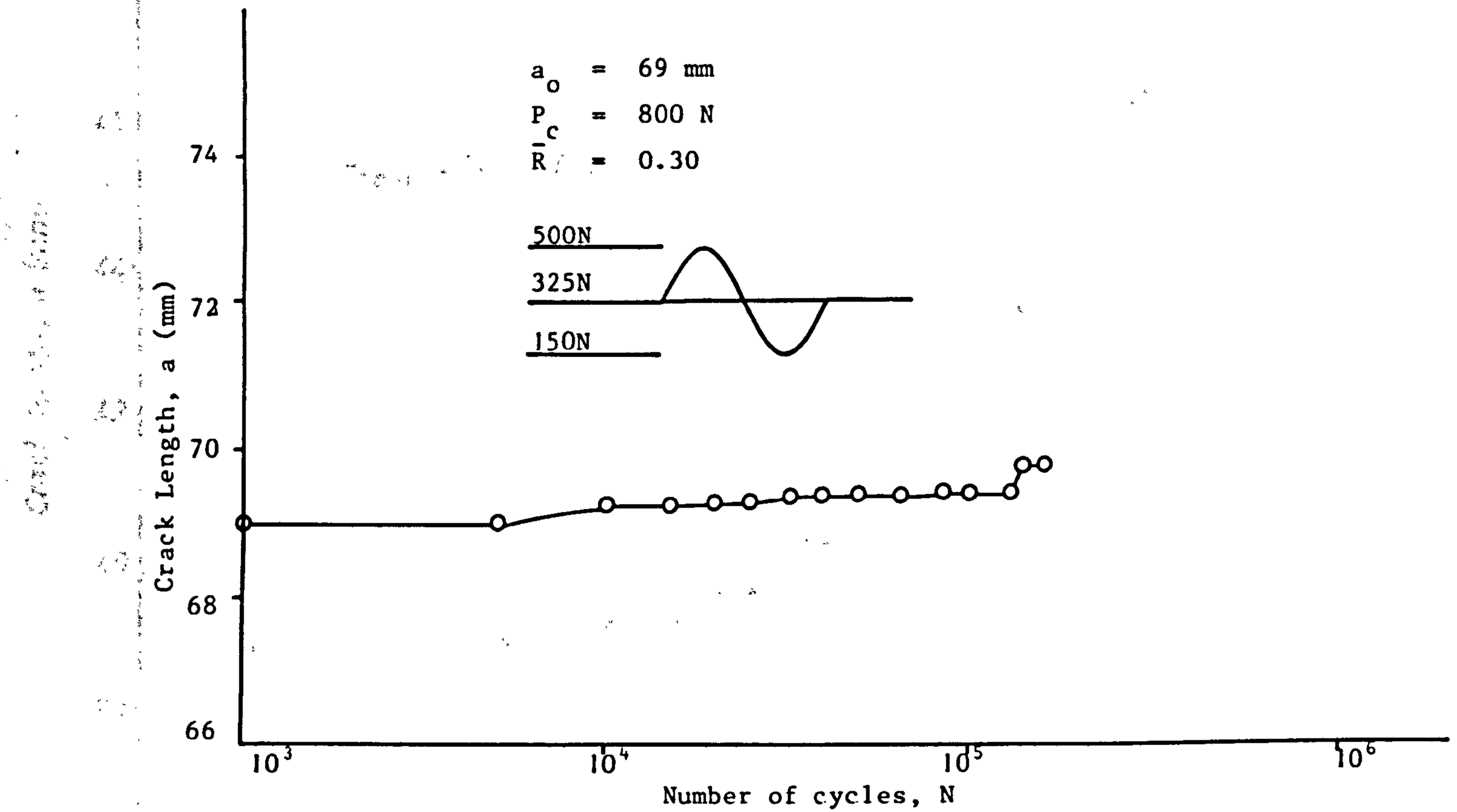

Fig. 3.24 FATIGUE CRACK PROPAGATION DATA FOR TDCB TEST SPECIMEN, F4

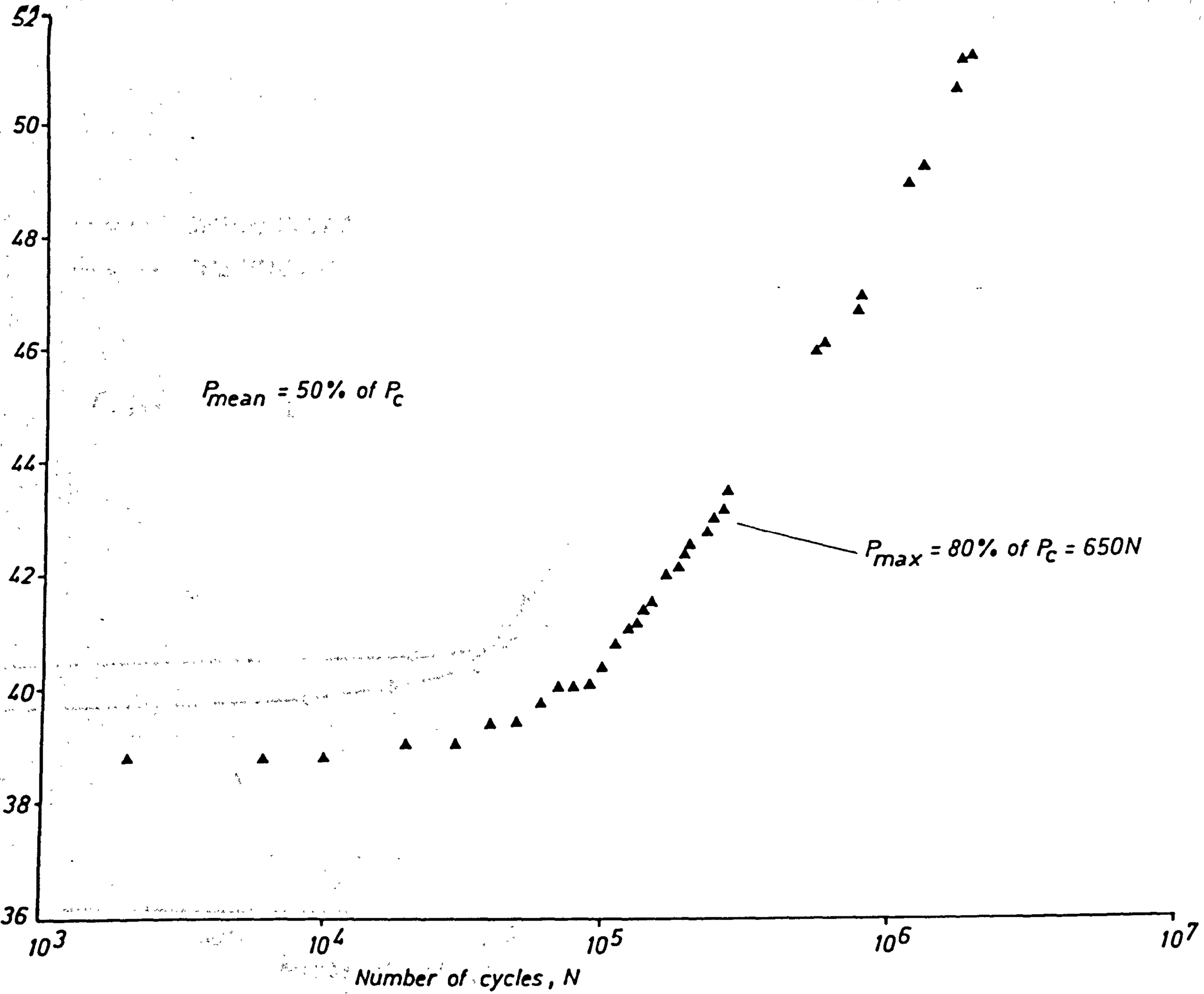

FIG 3.25 FATIGUE CRACK PROPAGATION DATA FOR ONE TDCB SPECIMEN (F5)

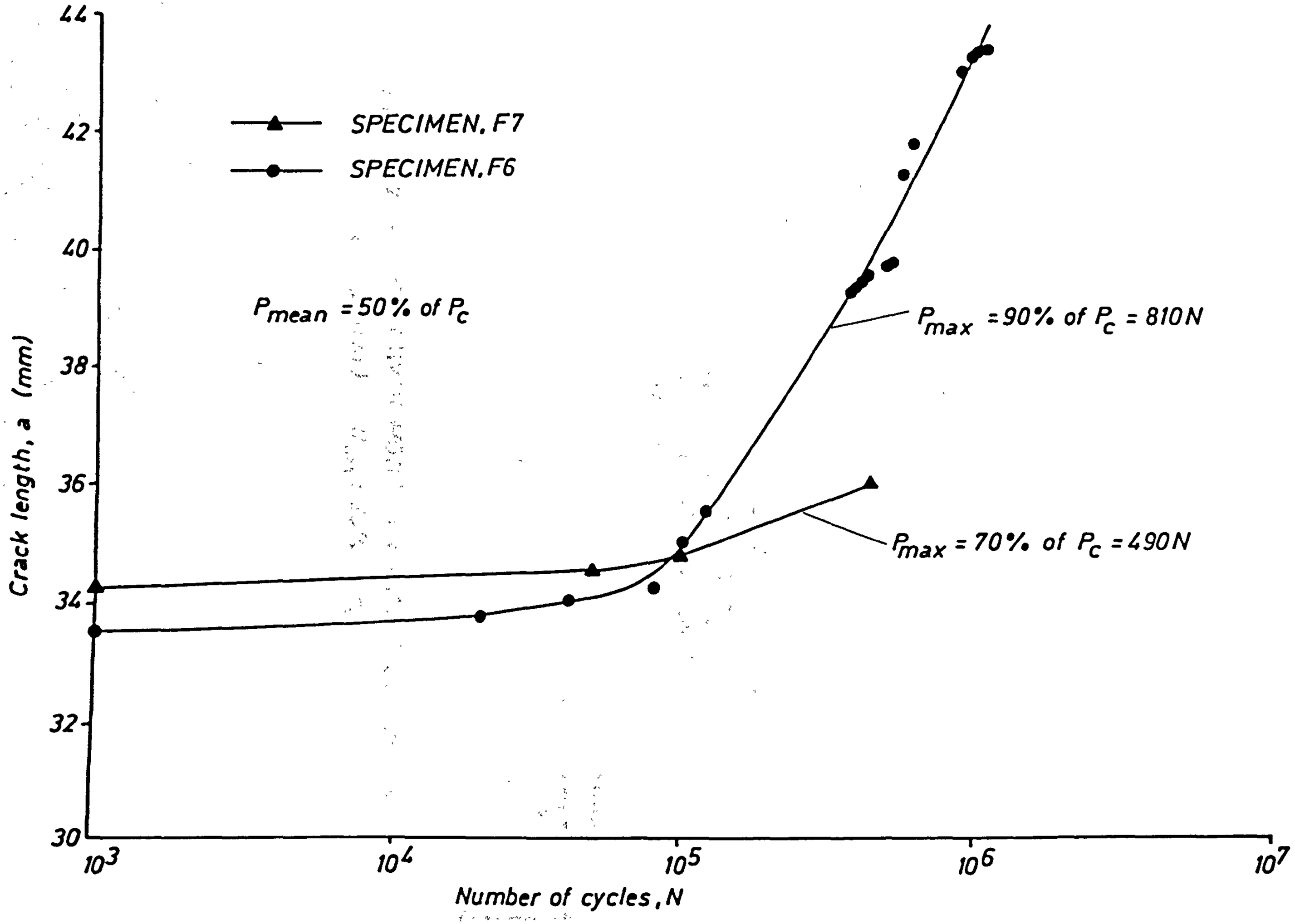

FIG 3.26 FATIGUE CRACK PROPAGATION DATA FOR TWO TDCB SPECIMENS (F6 AND F7)

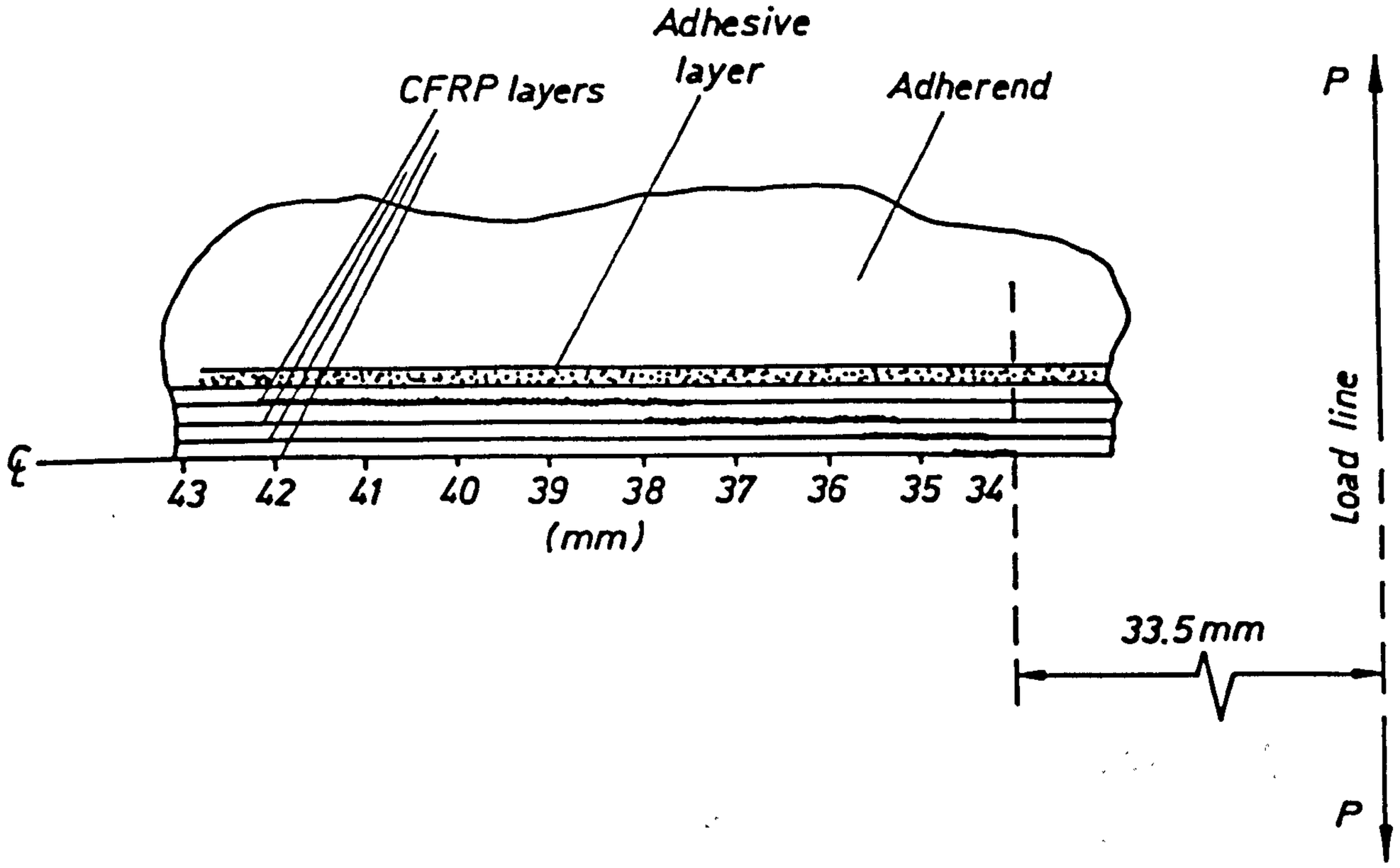

FIG. 3.27 CRACK GROWTH MODE FOR TDCB SPECIMEN. F6
($b = 20\,mm$), ($P_{max} = 90\%$ of P_c)

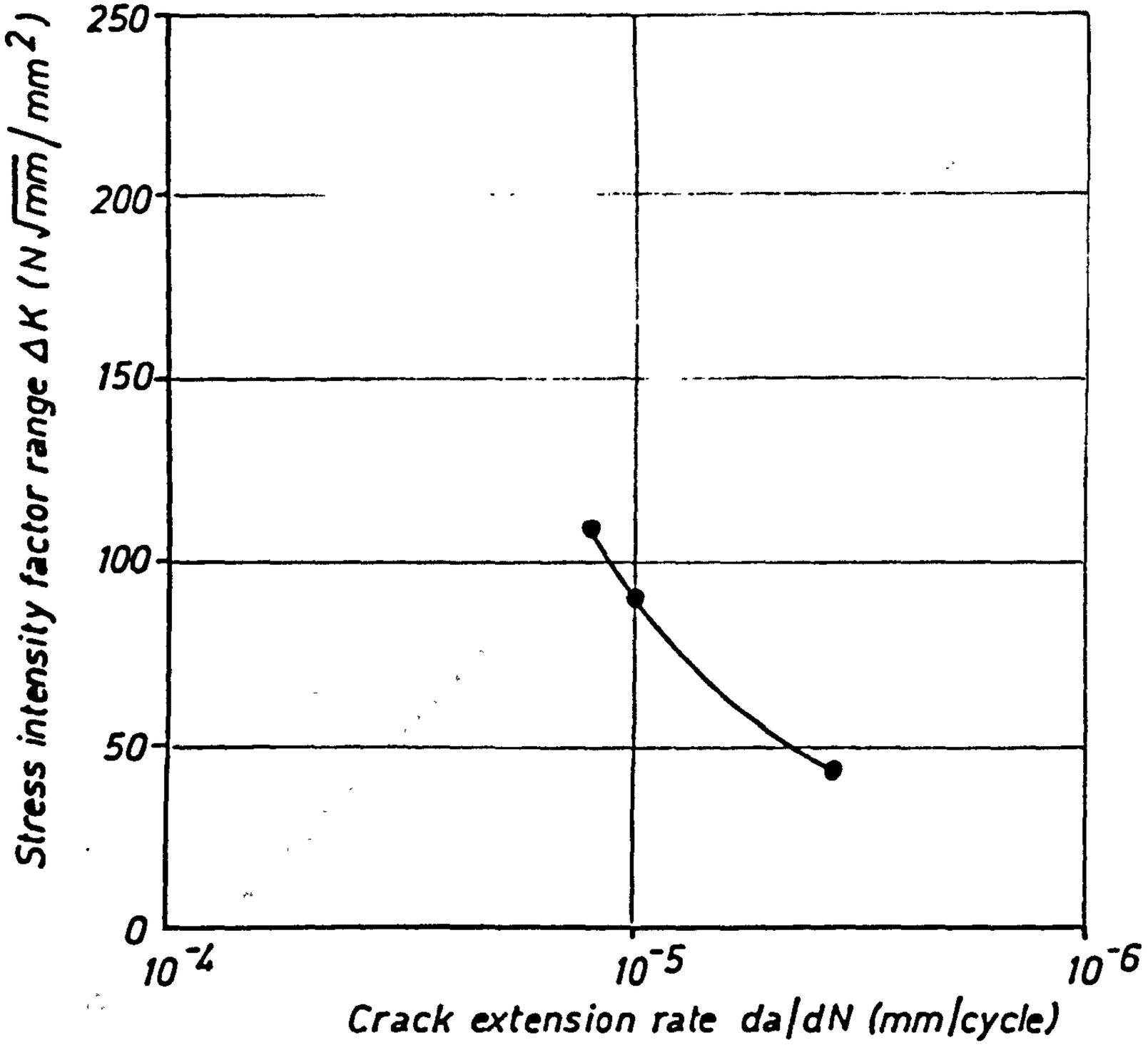

FIG. 3.28 FATIGUE CRACK GROWTH RATE FOR THREE TDCB SPECIMENS WITH (P_{max} = 90%, 80% AND 70% OF P_c)

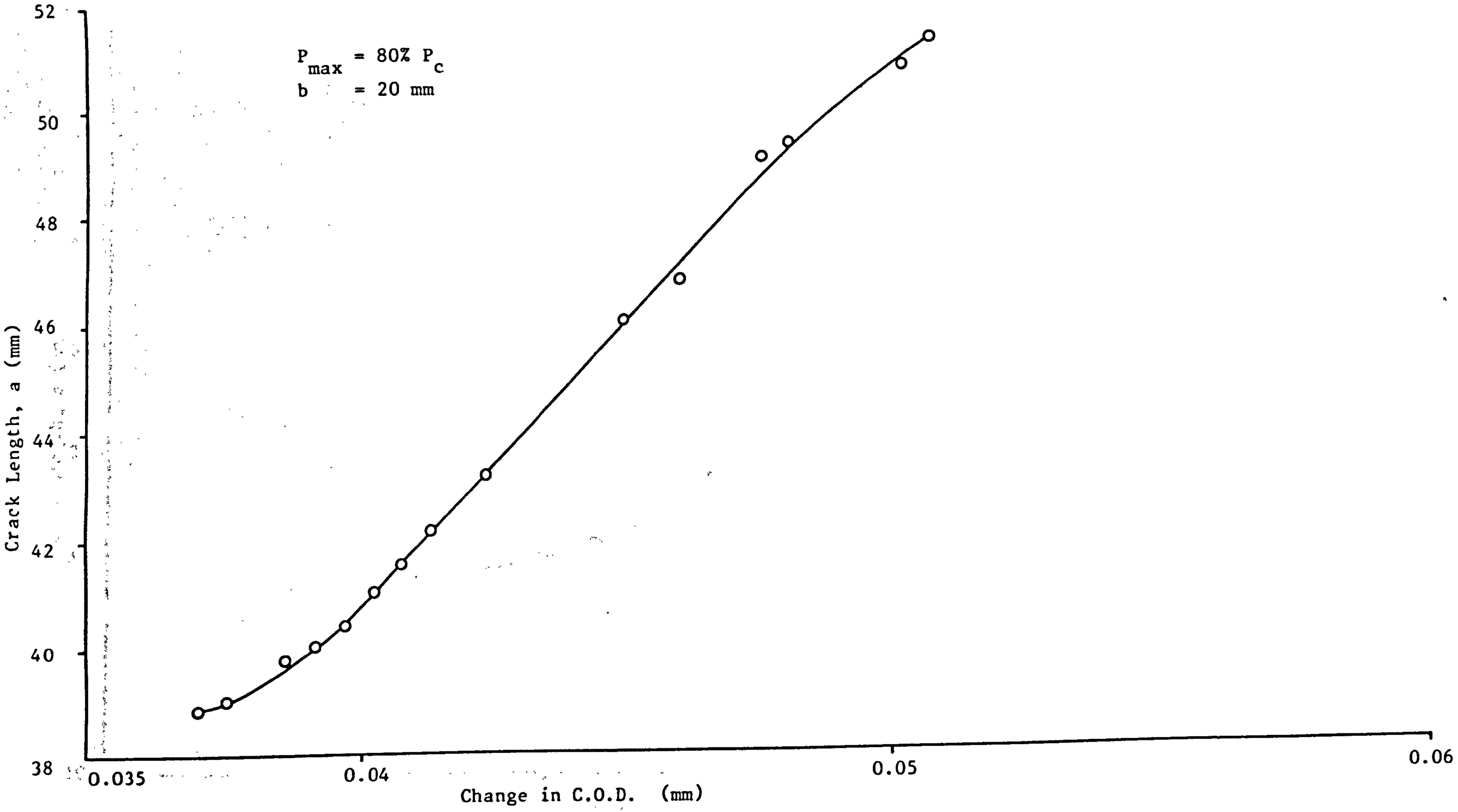

Fig. 3.29 FATIGUE-INDUCED CHANGE IN C.O.D. VS CRACK LENGTH FOR TDCB SPECIMEN, F5

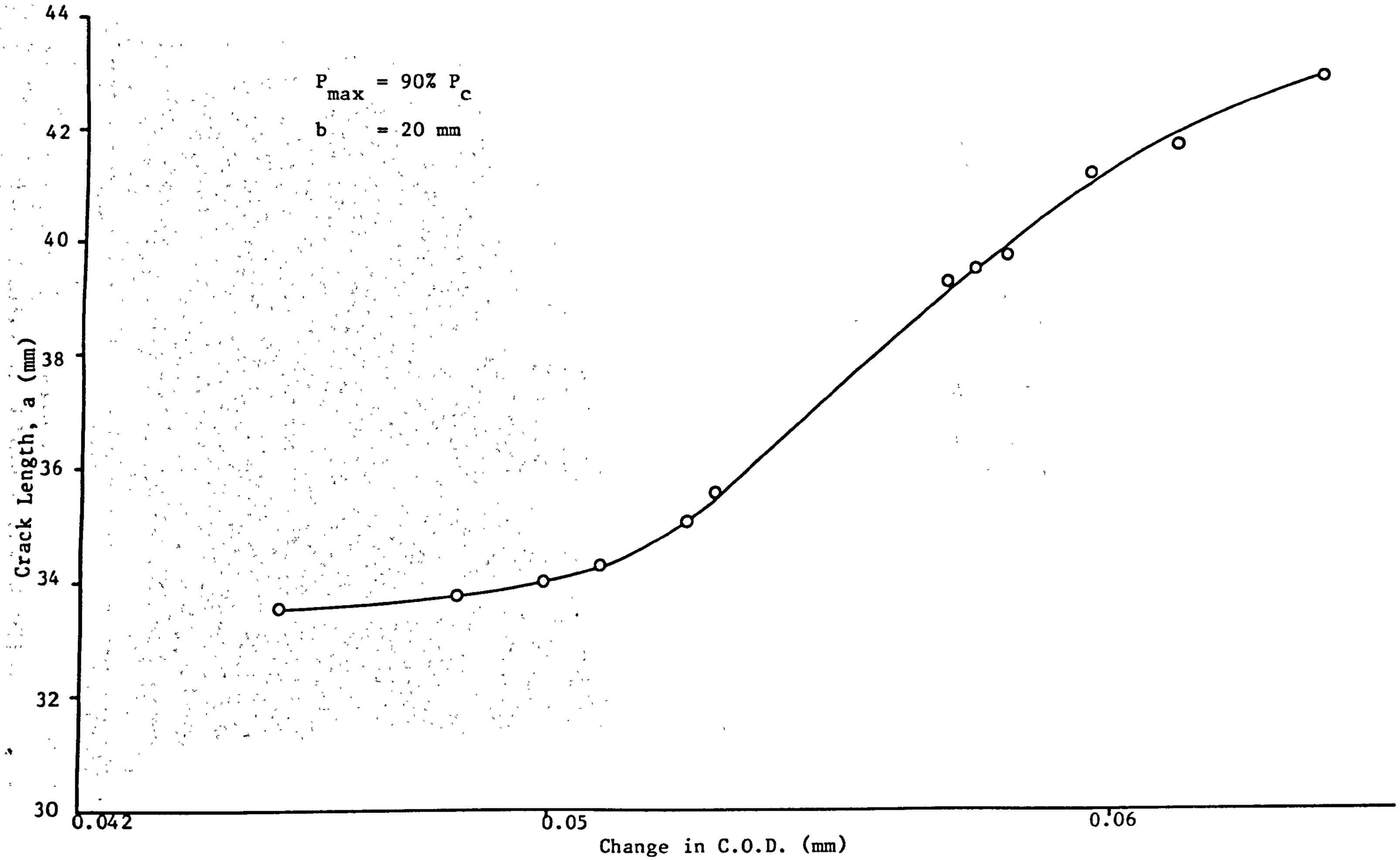

Fig. 3.30 FATIGUE INDUCED CHANGE IN C.O.D. VS CRACK LENGTH FOR TDCB SPECIMEN, F6

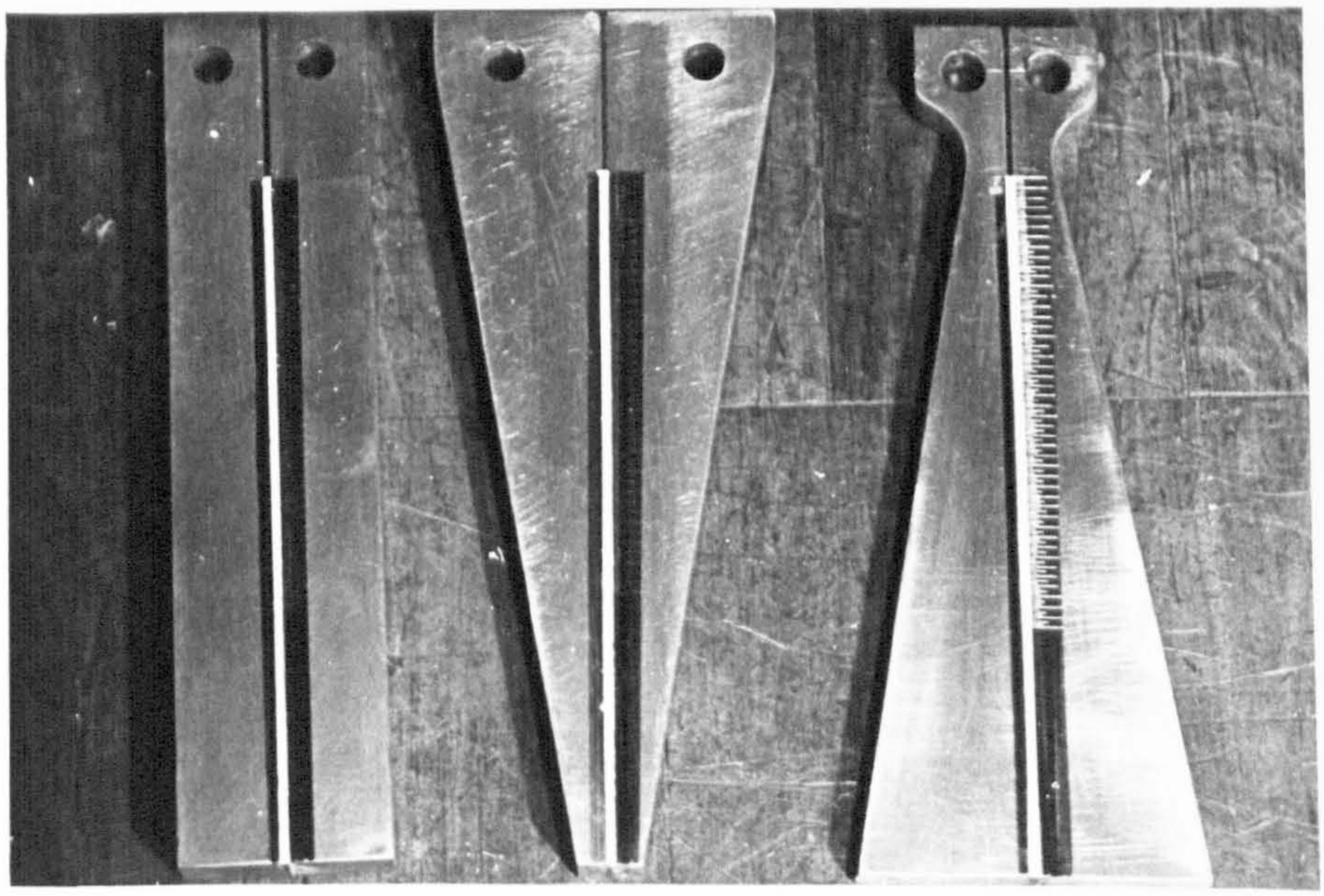

PLATE 3.1
DCB TEST SPECIMENS WITH ENGRAVED METRIC SCALE FOR CRACK MEASUREMENTS

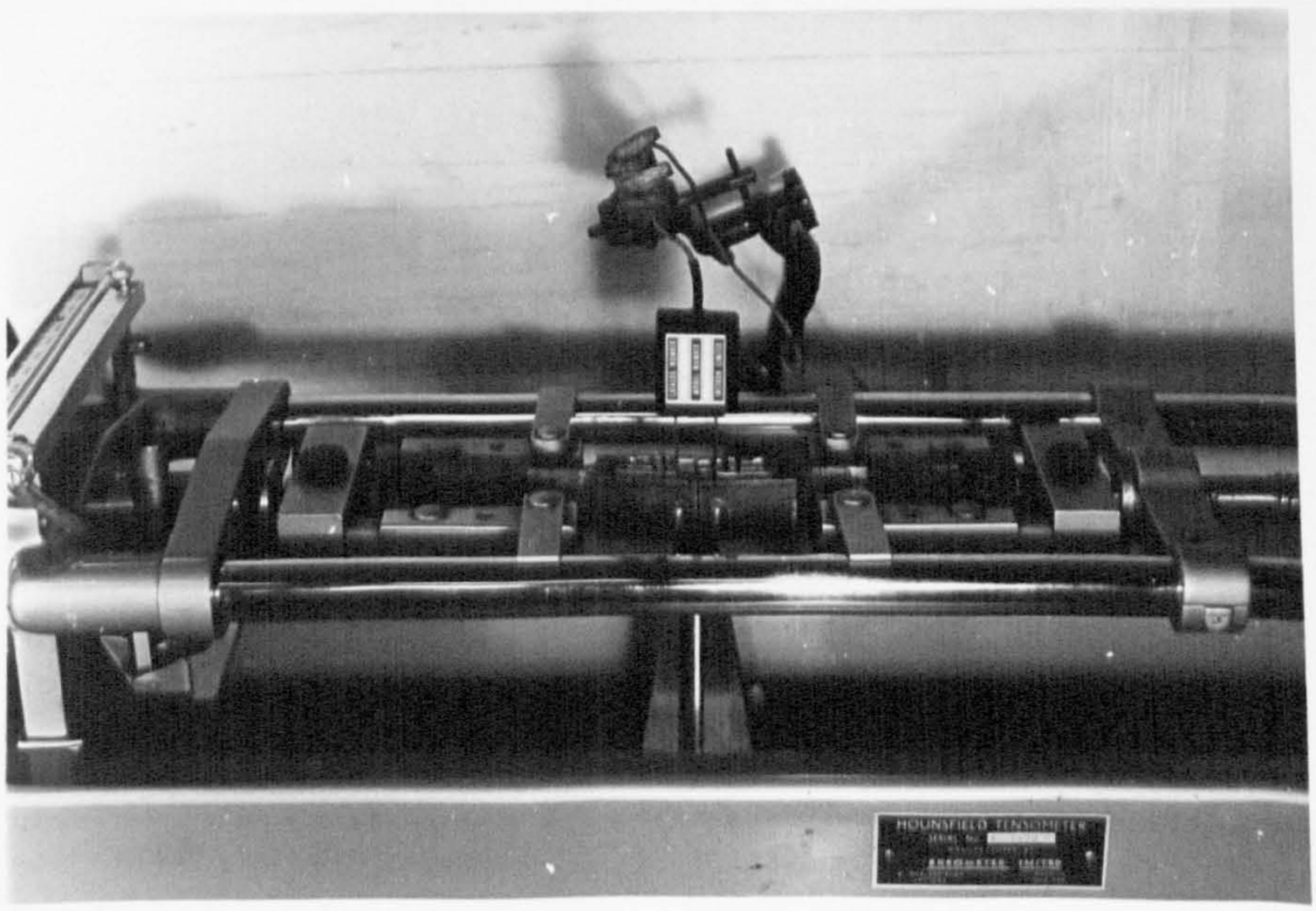

PLATE 3.2
TDCB TEST SPECIMEN IN LOADING CONFIGURATION

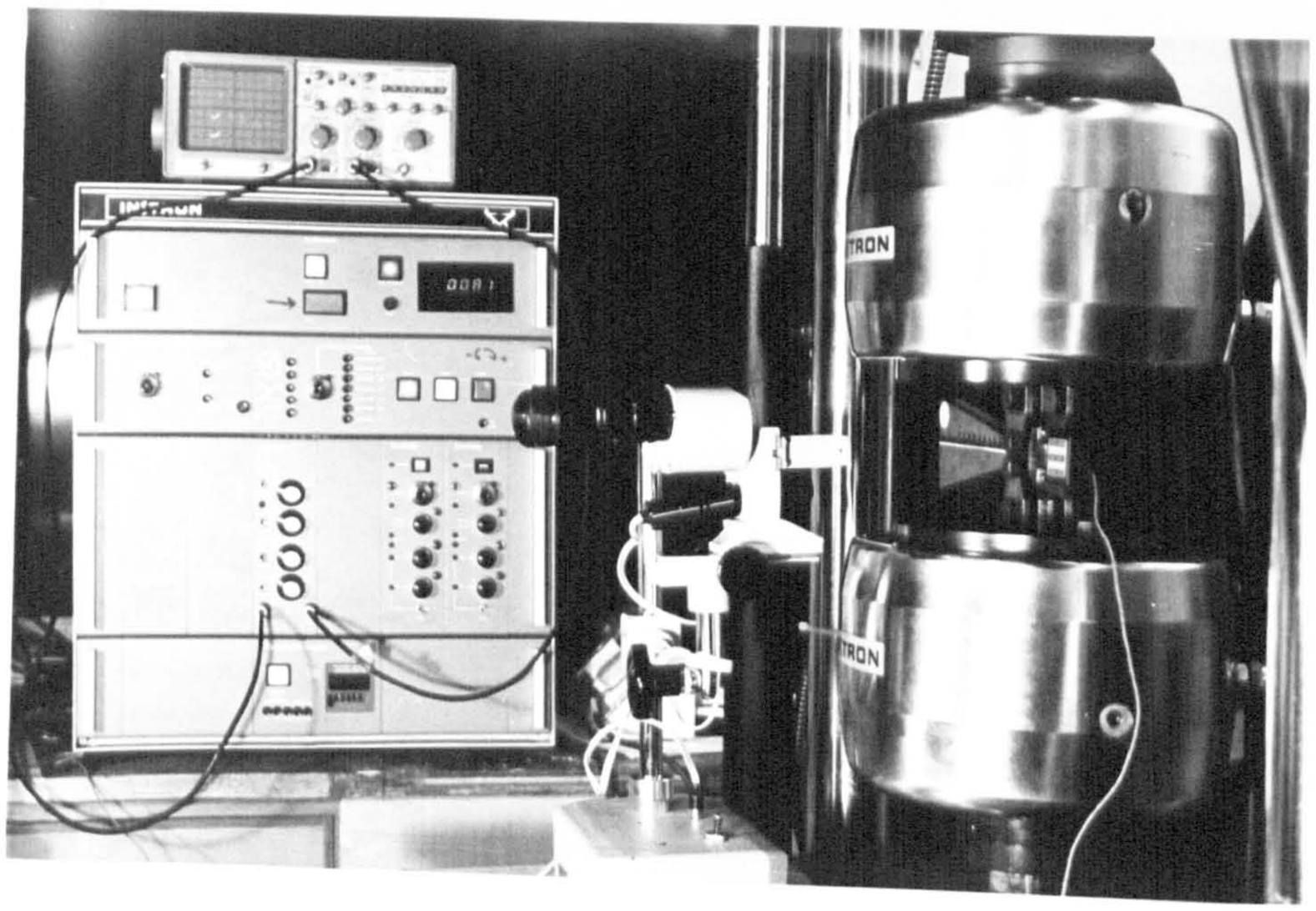

PLATE 3.3
TDCB FATIGUE TEST SPECIMEN IN LOAD SETTING

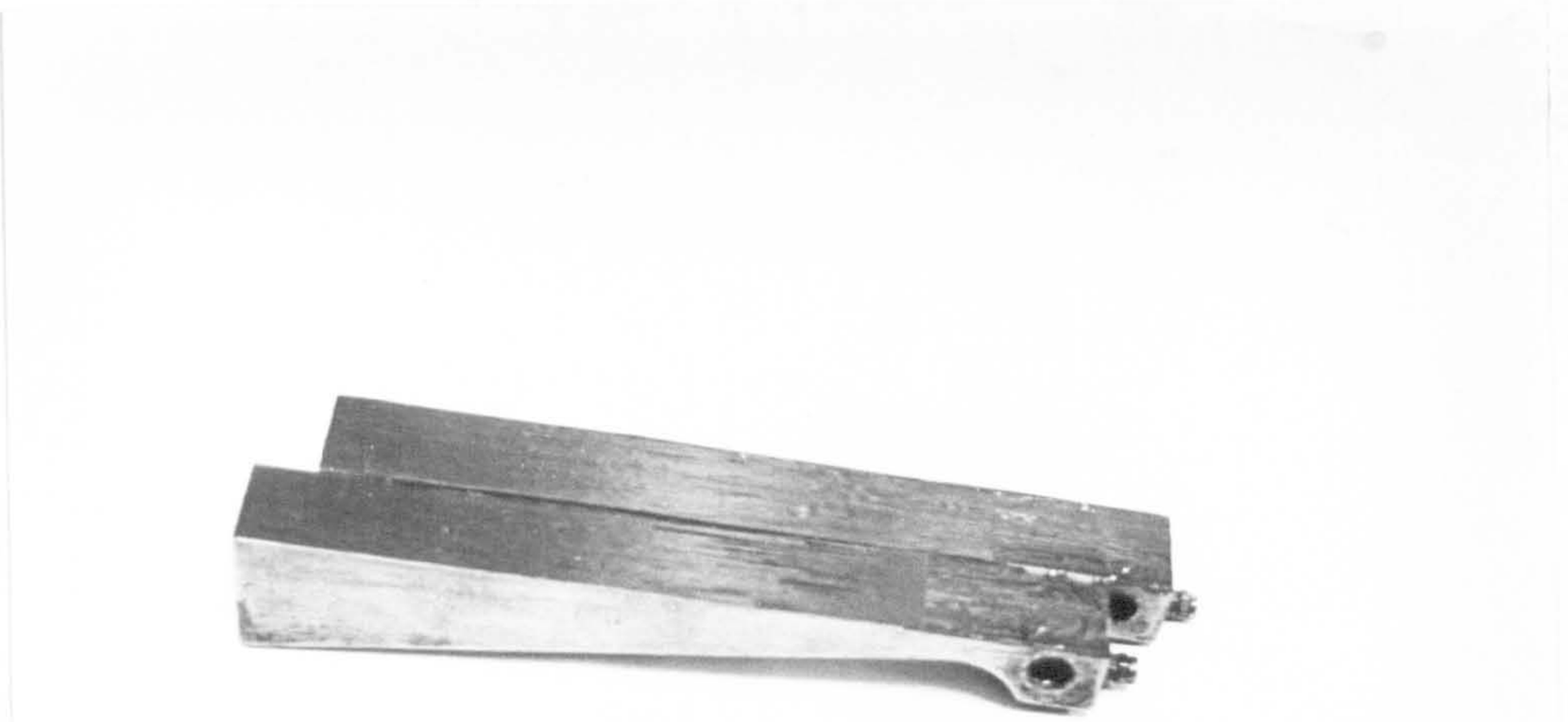

PLATE 3.4
DELAMINATION SURFACE FEATURES FOR TDCB FATIGUE TEST SPECIMEN, F6
($b = 20mm$; $P_{max} = 90\% P_c$)

C H A P T E R F O U R

BLISTER DELAMINATION ANALYSIS IN FIBRE REINFORCED PLASTICS USING BEAM-COLUMN THEORY WITH AN ENERGY RELEASE RATE CRITERION

4.1 INTRODUCTION

During recent years the important problem of ply delamination in carbon fibre reinforced plastics (CFRP) has been considered by many researchers. One aspect of this problem: delamination under compressive applied loading, deserves careful assessment because of the likelihood of catastrophic failure as a result of extensive delamination, following buckling of an initially debonded area. In this mode, if some critical conditions are met in the delaminated layer (e.g. debond size and shape, in-plane load in the layer, etc.), the elastic fracture surface energy or equivalently the stress intensity factor, and not the overall compressive strength, is the fundamental laminate property dictating compression failure. The blister problem, in particular, has received much attention because of the relative ease with which the initial damaged area can spread as a consequence of stress concentration, at its front, exceeding the interlaminar strength. The onset and extent of delamination depend on numerous parameters, including the initial size of the delaminated layer, the in-plane and flexural stiffness of the layer itself and of course the interlaminar toughness of separation. The latter, in turn, depends on factors associated with the manufacturing process such as inclusions, voids, fibre misalignment, etc. In one of the early papers Chai et al. (Ref. 84) construct some one-dimensional theoretical models which

consider a through width delaminated portion as an end-clamped beam. The strain energy in the delaminated layer is evaluated and then the energy release rate is calculated for a given compressive strain. It is shown that the delamination will grow only after the layer has buckled. Whitcomb (Ref. 30) addresses the same problem but uses geometrically nonlinear finite elements to analyse the large deflection post-buckled problem. Some experimental results of growth rates on a number of specimens subjected to fatigue loading with implanted delaminations are also reported, but no direct comparisons could be made with the analytical work. In Refs. 85 and 86 the delamination region is taken as a circular plate with clamped edges. A combination of fracture mechanics and post-buckling theory is used to study the interlaminar delamination characteristics. In Ref. 87 Gillespie and Pipes investigate the detrimental effects of the local instabilities (buckling of initial interlaminar defects) on the compressive strength of composite laminates.

The aim of the analysis developed in this Chapter is to consider the through width delamination problem of a typical fibre reinforced plastic orthotropic layer taking into account the effects of initial deflected shape, and also the elastic end effects of a resin rich layer at the delaminating edges A and B as shown in Fig. 4.1(a). Thus instead of taking the delaminated region as a clamped beam, some degree of elastic restraint is offered at the ends depending on the stiffness of the resin. In fact the end conditions for the beam are determined by matching deflection, slope, shear force and bending moment with those obtained from the solution to the 'beam on elastic foundation' equations. The result is to provide a solution to the problem which allows the strain energy release rate to be obtained which is not dependent on the buckling behaviour of the delaminated strip. A simple

Winkler foundation was also used by Williams in Ref. 88 to investigate adhesive failure between a pressurized disk and a rigid substrate.

Numerical results are given for an eight-layered carbon fibre reinforced plastic (CFRP) strip (Fig. 4.1) with a through width blister which separates the strip into four layers each side. The straight side of the strip is assumed to be held straight throughout the loading process by means of a honeycomb or foam backing medium which has zero longitudinal stiffness. Graphs are obtained showing how the normalized strain energy release rate varies with blister length for various values of P_1/P_E (ratio of the in-plane and buckling loads in the bulge-out layer) for different strains. These are then used to obtain crack propagation curves from which critical applied loads can be predicted. The post-buckling analysis for the case of an initially pre-loading flat debond is given at the end of the Chapter where it is shown that delamination will not take place unless the debonded layer buckles.

4.2 THEORY (A PRELOADING BLISTER SHAPE IS PRESENT: $\bar{\delta}_o \neq 0$)

4.2.1 Beam/Column and Elastic Foundation Equations

Consider the blister geometry shown in Figs. 4.1(a) and 4.1(b). The straight layer is taken to remain straight during loading because it is assumed to be attached to a support medium such as a honeycomb or foam backing material, whilst the blister shape before loading is assumed to be given by

$$w_o = \frac{\bar{\delta}_o}{2}\left[1 + \cos\left(\pi x/a\right)\right] \tag{4.1}$$

This expression is symmetrical about the Oz'-axis and gives the end conditions

$$(w_o)_{x=\pm a} = \left(\frac{dw_o}{dx}\right)_{x=\pm a} = 0 \qquad (4.2)$$

The applied load P may be distributed between the outer and inner layers as shown in Fig. 4.1 so that the differential equation governing the behaviour of the deflected shape of the blister when loaded by P_1 will be (Ref. 89)

$$\frac{d^4\bar{w}_1}{dx^4} + \left(\frac{P_1}{D}\right) \frac{d^2(\bar{w}_1 + w_o)}{dx^2} = 0 \qquad (4.3)$$

with the total deflection w_1 given by

$$w_1 = \bar{w}_1 + w_o \qquad (4.4)$$

Integrating the above equation twice gives

$$\frac{d^2\bar{w}_1}{dx^2} + \left(\frac{P_1}{D}\right) \bar{w}_1 = \bar{C}_1 + C_2 - \left(\frac{\bar{\delta}_o P_1}{2D}\right) [1+\cos(\pi x/a)] \qquad (4.5)$$

This has the general solution

$$\bar{w}_1 = C_1\cos(\alpha x) + \bar{C}_2\sin(\alpha x) + F\cos(\pi x/a) + \bar{C}_1 \frac{x}{\alpha^2} + \frac{C_2}{\alpha^2} - \frac{\bar{\delta}_o}{2} \qquad (4.6)$$

where

$$\alpha^2 = \frac{P_1}{D}$$

and

$$F = \frac{\bar{\delta}_o \alpha^2}{2(\frac{\pi^2}{a^2} - \alpha^2)}$$

Now because $\bar{w}_1$ is symmetrical about Oz' it follows that it should be an even function of x. Therefore $\bar{C}_1 = \bar{C}_2 = 0$ and the total deflection w_1 can be obtained from Eqns. (4.1), (4.4) and (4.6) to give

$$w_1 = C_1 \cos(\alpha x) + \frac{C_2}{\alpha^2} + F'\cos(\pi x/a) \qquad (4.7)$$

where

$$F' = \frac{\bar{\delta}_o \pi^2}{2(\pi^2 - \mu^2)}$$

and

$$\mu = \alpha a$$

The constants C_1 and C_2 will be determined from the end boundary conditions for the blister taking into account the elasticity of the resin rich layer. The attached portion of the top layer (Fig. 4.2) may be regarded as two identical beams on elastic foundations, with a foundation constant given by the resin modulus E_r divided by the resin film thickness t_r (corresponding to a simple Winkler foundation stiffness). The governing differential equation may be shown to be (Ref. 90)

$$D \frac{d^4 w_2}{d^4 x} + P_1 \frac{d^2 w_2}{dx^2} + k w_2 = 0 \qquad (4.8)$$

where

$$k = E_r/t_r$$

or

$$\frac{d^4 w_2}{dx^4} + \alpha^2 \frac{d^2 w_2}{dx^2} + 4\beta^4 w_2 = 0 \qquad (4.9)$$

where

$$\beta^4 = \frac{k}{4D}$$

In practice $\alpha^4 << 16\beta^4$; and also as x becomes large $w_2 \to 0$. This requires the vanishing of the two constants which appear with the positive exponential terms. Thus

$$w_2 = e^{-\beta_1 x}[C_3\cos(\beta_2 x) + C_4\sin(\beta_2 x)] \qquad (4.10)$$

where

$$\beta_1 = \sqrt{2}\,\beta\sin(\phi/2); \quad \beta_2 = \sqrt{2}\,\beta\cos(\phi/2)$$

and

$$\phi = \arctan\sqrt{(16\eta^4 - 1)}; \quad \eta = \beta/\alpha$$

The constants C_1 to C_4 in Eqns. (4.7) and (4.10) may now be determined by imposing the continuity conditions of deflection, slope, bending moment and shear force at point B in Fig. 4.1. After some algebraic manipulation we obtain

$$C_1 = \left(\frac{F'\pi^2}{\mu^2}\right) \frac{2\chi_1\eta}{2\chi_1\eta\cos\mu + (2\eta^2-1)\sin\mu}$$

$$C_2 = F'\alpha^2 \left\{1 + \frac{\pi^2[1+2\eta^2(2\chi_1^2 -1)-4\chi_1\eta^3\cot\mu}{2\lambda'^2[2\chi_1\eta\cot\mu+2\eta^2-1]}\right\}$$

$$C_3 = \frac{F'\pi^2}{a^2\beta_2 Y_1}\left\{\frac{\alpha^2(-\beta_1 M_1+\beta_2 M_2)+h_1 M_1+h_2 M_2}{2\beta^2\alpha^2(2\chi_1\eta\cot\mu-1)+4\beta^4}\right\} \qquad (4.11)$$

$$C_4 = \frac{F'\pi^2}{a^2\beta_2 Y_1}\left\{\frac{\alpha^2(\beta_1 M_2+\beta_2 M_1)-h_1 M_2+h_2 M_1}{2\beta^2\alpha^2(2\chi_1\eta\cot\mu-1)+4\beta^4}\right\}$$

where

$$\lambda' = \beta a \; ; \quad \lambda_1 = \beta_1 a \; ; \quad \chi_1 = \sqrt{2}\,\sin(\phi/2)$$

$$M_1 = \sin\beta_2 a \; ; \quad M_2 = \cos\beta_2 a$$

$$h_1 = 3\beta_1\beta_2^2 - \beta_1^3 \; ; \quad h_2 = 3\beta_1^2\,\beta_2 - \beta_2^3 \; ; \quad Y_1 = e^{-\lambda_1}$$

from which the deflected shapes w_1 and w_2 can be obtained for a given load.

4.2.2 Energy Release Rate and Elastic Strain Energy

Because of the pre-load configuration of the delaminated region [Fig. 4.1(a)] the original delamination may spread when the direct load P_1 in the blister layer is well below the Euler buckling load for that layer. For this reason, a method of solution based on a buckling analysis combined with an energy criterion, as given in Ref. 84, will not be able to solve the problem.

The main requirement is for the determination of the energy release rate of fracture g, given by the well-known equation

$$g = \frac{dW'}{da} - \frac{dU}{da} \tag{4.12}$$

Assuming a uniform overall applied strain ε just sufficient to extend the already existing delamination with fixed grip conditions, then $dW'/da = 0$ and Eqn. (4.12) becomes

$$g = -\frac{dU}{da} \tag{4.13}$$

Now the total strain energy of the system per unit width, U, can be expressed in terms of an overall Young's modulus, E_d, and the applied strain, ε, to give

$$U = \frac{V}{2}\varepsilon^2 E_d = \ell' t \varepsilon^2 E_d \tag{4.14}$$

Substituting into Eqn. (4.13) and noting that ε will not be a function of a gives

$$g = -\ell' t \varepsilon^2 \frac{dE_d}{da} \tag{4.15}$$

A simple 'rule of mixtures' formulation is now used to find E_d in terms of the Young's moduli for the inner and outer layers.

The applied load P is assumed to be divided between the inner and outer layers to give

$$P = P_1 + P_2 \tag{4.16}$$

with the load P_1 in the outer layer remaining constant along the entire length of the specimen. Thus the blister portion of the outer layer is assumed to carry the same load as the attached portions of the outer layer.

From the simple uniaxial stress/strain equations, and introducing an equivalent Young's modulus E_1^* for the complete outer layer (including the blister) we can use the following equations

$$\sigma = E_d\varepsilon \; ; \quad \sigma_1 = E_1^*\varepsilon \qquad \text{and} \qquad \sigma_2 = E_2\varepsilon \tag{4.17}$$

so that Eqn. (4.16) becomes

$$E_d\varepsilon t = E_1^*\varepsilon t_1 + E_2\varepsilon t_2$$

or

$$E_d = E_1^*\left(\frac{t_1}{t}\right) + E_2\left(\frac{t_2}{t}\right) \tag{4.18}$$

E_1^* can now be found in terms of an equivalent Young's modulus for the blister, E_e and E_1 by writing the total shortening ($\bar{\Delta}_1$) of the outer layer as the sum of the shortening for the blister ($\bar{\Delta}$) [Fig. 4.1(c)] and the undelaminated portion ($\bar{\Delta}_o$) giving

$$\bar{\Delta}_1 = \bar{\Delta} + \bar{\Delta}_o$$

or

$$\frac{2\ell' P_1}{E_1^* t_1} = \frac{2aP_1}{E_e t_1} + \frac{2c' P_1}{E_1 t_1} \tag{4.19}$$

so that

$$E_1^* = \frac{E_1 E_e}{\left(\frac{a}{\ell'}\right)E_1 + \left(\frac{c'}{\ell'}\right)E_e} \tag{4.20}$$

Substituting Eqn. (4.20) into Eqn. (4.18) gives

$$E_d = \frac{E_1 E_e (t_1/t)}{\left(\frac{a}{\ell'}\right)E_1 + \left(\frac{c'}{\ell'}\right)E_e} + E_2\left(\frac{t_2}{t}\right) \qquad (4.21)$$

and this part of the analysis will be completed when E_e is found as a function of a. This may be achieved from strain energy considerations as follows.

If U_t is the total elastic strain energy per unit width of the blister then this may be equated to the work done by P_1 moving through the shortening distance $\bar{\Delta}$

$$U_t = \frac{P_1 \bar{\Delta}}{2} \qquad (4.22)$$

with

$$\bar{\Delta} = \frac{2aP_1}{E_e t_1} \qquad \text{[Eqn. (4.19)]}$$

Thus

$$E_e = \left(\frac{a}{t_1}\right)\frac{P_1^2}{U_t} \qquad (4.23)$$

Substituting Eqn. (4.23) into Eqn. (4.21) and the result in Eqn. (4.15) (nothing that c' and U_t will both be functions of a) gives

$$g = \frac{-\varepsilon^2 E_1 t_1 \left(1 - \frac{E_1 t_1}{P_1^2}\frac{dU_t}{da}\right)}{\left(\frac{c'}{\ell'}\right)^2\left(1 + \frac{E_1 t_1}{c' P_1^2}U_t\right)^3} \qquad (4.24)$$

It now only remains to find U_t as a function of the blister half span a. Now the total strain energy per unit width of the blister will be

the sum of the direct compression energy U_{dc} and the bending energy U_b. The expression for U_{dc} may be written

$$U_{dc} = E_1 t_1 \int_0^a \left[\varepsilon + \frac{1}{2} \left(\frac{d\bar{w}_1}{dx} \right)^2 \right]^2 dx \qquad (4.25)$$

where $\varepsilon = du/dx \equiv$ overall applied strain, u being the axial displacement, and $\bar{w}_1 = w_1 - w_o$. The appearance of $\bar{w}_1$ in Eqn. (4.25) is a second order effect, due to the layer curvature. Substitution for $\bar{w}_1$ from Eqns. (4.1) and (4.7) into Eqn. (4.25) and integrating yields

$$U_{dc} = aE_1 t_1 \varepsilon^2 + \frac{E_1 t_1 F^4 \alpha^4}{4} \left(2p^8 \Omega^4 R_1 + \frac{3ap^2}{8} + 6p^5 \Omega^2 R_2 + 32p^7 \Omega^3 R_3 + 48p^5 \Omega R_4 \right) + E_1 t_1 F^2 \alpha^2 \varepsilon \left(p^4 \Omega^2 R_5 + 4p^3 \Omega R_6 + \frac{ap}{2} \right) \qquad (4.26)$$

where the following abbreviations have been adopted

$$\frac{\pi^2}{\mu^2} = \frac{\pi^2 D}{a^2 P_1} = p \quad \text{(ratio of layer buckling load to its in-plane load)}$$

$$\Omega = \frac{\chi_1 \eta}{2\chi_1 \eta \cos\mu + (2\eta^2 - 1)\sin\mu} \; ; \; R_1 = 3a - \frac{(3+2\sin^2\mu)\sin 2\mu}{2\alpha}$$

$$R_2 = a - \frac{p \sin 2\mu}{2\alpha(\mu - 1)} \; ; \; R_3 = \frac{[(p-1)\sin^2\mu - 6]\sin\mu}{\alpha(p-1)(p-9)}$$

$$R_4 = \frac{\sin\mu}{\alpha(p-1)(9p-1)} ; \; R_5 = 2a - \frac{\sin 2\mu}{\alpha} \; ; \; R_6 = \frac{\sin\mu}{\alpha(p-1)}$$

The bending strain energy U_b in the blister can be expressed as

$$U_b = D \int_0^a \left(\frac{d^2 \bar{w}_1}{dx^2} \right)^2 dx \qquad (4.27)$$

Eqn. (4.27) can now be integrated after substitution for $\bar{w}_1$, giving

$$U_b = \frac{Dp^2\alpha^3\bar{\delta}_o^2}{8(p-1)^2}\left[2p^2\Omega^2(2\mu+\sin 2\mu) + \frac{8p\Omega\sin\mu}{(p-1)} + \mu\right] \qquad (4.28)$$

Thus $U_t = U_{dc} + U_b$ [using Eqns. (4.26) and (4.28)] which can now be used in Eqn. (4.24) to evaluate g.

For a particular material and lay-up configuration it is possible to measure the energy release rate for crack propagation (the critical energy release rate) g_c, which is often given the symbol Γ (= surface energy of fracture). Thus Eqn. (4.24) can be normalized with respect to Γ to give

$$g_n = \frac{-\varepsilon E_1 t_1\left[1 - \frac{E_1 t_1 p^2}{P_E}\left(\frac{dU_t}{da}\right)\right]}{\Gamma\left(\frac{c'}{\ell'}\right)^2\left[1 + \left(\frac{E_1 t_1 p^2}{c' P_E^2}\right) U_t\right]^2} \qquad (4.29)$$

When g_n is greater than or equal to unity, the blister will split and numerical results which predicted this behaviour are given in the next section for various values of ε, a and p.

It is interesting to note from Eqn. (4.29) that splitting is only possible when g_n is positive, that is when

$$1 - \frac{E_1 t_1 p^2}{P_E^2}\left(\frac{dU_t}{da}\right) < 0$$

or, after integration, when

$$U_t > \frac{P_1^2 a}{E_1 t_1}\left(= \frac{P_E^2 a}{p^2 E_1 t_1}\right)$$

The right hand side of the above relation is equal to the direct strain energy stored in the outer layer over the length 2a when $\bar{\delta}_o = 0$. This shows that no splitting is possible for an originally

straight delamination unless it buckles and in so doing gives rise to additional energy components which make U_t greater than $P_1^2 a/E_1 t_1$. This same conclusion can be reached as follows: Let E_ℓ be the Young's modulus of the laminate in absence of an initial delamination. This modulus will be reduced to E_d [Eqn. (4.21)] as a result of introducing the interlaminar debond. Substituting Eqn. (4.23) into Eqn. (4.21) and noting that [$E_\ell = E_1(t_1/t) + E_2(t_2/t)$] yields

$$E_\ell - E_d = \left(\frac{E_1 t_1}{t}\right) \frac{\left(\frac{t_1}{\ell'}\right) E_1 U_t - \left(\frac{a}{\ell'}\right) P_1^2}{\left(\frac{t_1}{\ell'}\right) E_1 U_t + \left(\frac{c'}{\ell'}\right) P_1^2}$$

Therefore a reduction of E_ℓ following delamination will necessitate

$$\left(\frac{t_1}{\ell'}\right) E_1 U_t > \left(\frac{a}{\ell'}\right) P_1^2$$

or,

$$U_t > \frac{P_1^2 a}{E_1 t_1} \quad \text{, thus the earlier result.}$$

4.2.3 Numerical Results and Discussion

The following data, for unidirectional CFRP laminates, were used for the numerical work:

$E_1 = 138500$ N/mm^2; $E_r = 3380$ N/mm^2

$\nu_{\ell t} = 0.3352$; $\nu_{t\ell} = 0.0223$

$t_1 = 0.5$mm ($=t_2$); $t_r = 0.105\text{x}10^{-4}$mm

$\ell' = 75$mm ; $\bar{\delta}_o = 0.1$mm

$\Gamma = 0.26$ N/mm (from Ref. 29)

The above data, except where specified, were taken from Ref. 76.

The direct strain energy of compression U_{dc} is shown versus the blister half span a in Figs. 4.3, 4.4 and 4.5, for three different values of the applied strain ϵ and several parameters representing P_1/P_E values. Figs. 4.6 through to 4.10 depict U_b versus a for various values of ϵ and load ratio P_1/P_E. It is seen that for relatively high values of a and low load ratios, U_b becomes very small. However, a dramatic increase in U_b is noticed as P_1 approaches P_E. This behaviour is also confirmed in Fig. 4.11 where the load ratio P_1/P_E is plotted versus the bending strain at the middle point of the blister layer (obtained by using simple bending theory formulation) for several a values. Typical graphs for the total strain energy per unit width U_t in the bulge-out layer, together with its components,, are plotted versus the blister half span, in Fig. 4.12, for a particular applied strain, ϵ ($=0.7\times10^{-3}$), and load ratio P_1/P_E. The direct stain energy of compression is fairly constant over a wide range of a and it is the main component for relatively high values of a. However, for small values of a the bending strain energy dominates (as $\bar{\delta}_o/a$ increases) giving rise to a rapid increase in the total strain energy. This type of behaviour is also shown in Fig. 4.13 where the variation of total strain energy with a is plotted for various load ratios P_1/P_E. As the load P_1 in the bulge-out approaches the Euler buckling load, so the bending energy increases causing a relatively large increase in the total strain energy. Superimposed on these curves is a dotted line which gives the critical strain energy required for splitting. There is a rapid increase in this quantity around a=25mm as P_1/P_E approaches unity, again due to large bending effects.

The normalized strain energy release rate for several applied

strains ε is plotted in Figs. 4.14 through to 4.21 for different load ratios P_1/P_E. Critical values for laminate splitting lie on the 1.0 horizontal line. It is seen from Fig. 4.14 ($\varepsilon=0.3\times10^{-3}$) that delamination will not occur for P_1/P_E < 0.75 and 2mm<a<30mm. For higher applied strain values, in order to prevent delamination growth from an initial blister half span within the above range the load ratio P_1/P_E should be kept to lower levels as shown in Figs. 4.15 through to 4.21. Equivalently, the range of non-delamination for the initial blister half span will be narrowed if certain high values of the load ratio P_1/P_E are established. For example, for an applied $=0.9\times10^{-3}$ (Fig. 4.17), the range of non-delamination is reduced to 16mm < a < 32mm for an allowed maximum load ratio P_1/P_E = 0.65. However, the critical value of P_1/P_E is always less than unity for the range of a considered. This is to say, the critical in-plane load in the blister layer will never reach the layer buckling load P_E. This behaviour is shown clearly by the sinking of the curve for P_1/P_E = 0.95 (see figures). Theoretically however, for relatively high values of ε and a delamination growth may occur at values of the load ratio P_1/P_E around 0.95 as shown in Figs. 4.19, 4.20 and 4.21.

The set of curves shown in Fig. 4.22 are produced from graphs such as those shown in Figs. 4.14 through to 4.21, and represent the energy release rate paths. The area enclosed by each individual curve, or between branches of the same curve, is a crack propagation instability region. As the applied strain is increased so the wider becomes the related instability region. It is seen that the instability problem is more serious between P_1/P_E = 0.8 and 0.95. Thus for example, an initial blister half span of 2mm, which carries an in-plane load given by P_1/P_E = 0.90, will propagate to about 27mm without stopping when

the applied strain ε=0.0007. This large amount of propagation may lead to the upper blister layer becoming completely delaminated with consequent collapse of the laminated component. Values of P_1/P_E below 0.55 are less serious for the range of strain considered. In fact, here, the critical initial delamination is higher than the previous case for low 'a' values and the crack arrests after a relatively short length depending on the applied strain. It is clear from the above that delamination depends strongly on ε and may occur at in-plane loads in the bulge-out layer which are well below the Euler buckling load.

The effect of an infinitely stiff elastic foundation is shown in Fig. 4.23 for ε=0.0005 and 0.0007. The difference between the two cases is very small in the central region of the curves corresponding to P_1/P_E ranging from 0.75 to 0.90. However, a significant difference is evident below and above this P_1/P_E interval. For thicker and more flexible resin rich layers the difference between the two curves could be appreciable.

4.3 THEORY (FLAT INITIAL DEBOND, $\bar{\delta}_o$= 0)

4.3.1 Beam/Column and Elastic Foundation Equations

The blister case characterized by the presence of an initial pre-loading bulge in the delaminated layer was analysed in the last section. It was seen that delamination could well take place while the in-plane load in the blister layer P_1, was below the Euler buckling load P_E. This may not be the case when the initial debonded layer is perfectly flat ($\bar{\delta}_o$=0) when the load is first applied. If a uniform applied strain ε is assumed, delamination will not grow as long as the initially debonded area is flat (Ref. 84). However, delamination is possible if the debonded portion buckles. Therefore, the problem

can only be assessed through post-buckling analysis. If the extent of delamination and its consequences on the integrity of a certain laminate are the main concern, then, the problem is far more serious than the case analysed earlier where $\bar{\delta}_o \neq 0$. In fact, the behaviour is progressive where a pre-loading bulge is present and therefore, can be controlled unlike the initially flat debond case ($\bar{\delta}_o=0$) when post-buckling events may be sudden and catastrophic. However, it may happen that delamination will not occur following buckling, in which eventuality, the problem can be treated exactly in the same way as when $\bar{\delta}_o \neq 0$ as long as the maximum post-buckling deflection $\bar{\delta}_o$ is small. The other possibility is that delamination will take place following buckling of the debonded region. This is the subject of the analysis contained in this section.

There is one major assumption which lies at the root of the problem: the post-buckling configuration is taken to have a defined shape. This assumption has been adopted throughout researches on the problem (e.g. Ref. 84 and 30). The present analysis takes the problem a step forward by assessing the effect of a resin rich layer on the post-buckling behaviour and delamination.

The general solution for Eqn. (4.3), remembering that $\bar{\delta}_o=0$, reduces to

$$w_1 = C_1\cos(\alpha x) + \frac{C_2}{\alpha^2} \qquad (4.30)$$

The deflection w_2 for the attached portion of the top layer is still given by Eqn. (4.10). The constants C_1 to C_4 in Eqns. (4.10) and (4.30) may now be determined, as was done in Section 4.2, by imposing the continuity conditions of deflection, slope, bending moment and shear force along the delamination front between debonded and attached portions (point B in Fig. 4.1). The continuity conditions yield,

$$C_1\cos\mu + \frac{C_2}{\alpha^2} = Y_1(C_3M_2 + C_4M_1)$$

$$-C_1\alpha\sin\mu = Y_1[-C_3(\beta_1M_2 + \beta_2M_1) + C_4(-\beta_1M_1 + \beta_2M_2)] \qquad (4.31)$$

$$-C_1\alpha^2\cos\mu = Y_1[C_3(F_1M_2 + F_2M_1) + C_4(F_1M_1 - F_2M_2)]$$

$$C_1\alpha^3\sin\mu = Y_1[C_3(h_1M_2 - h_2M_1) + C_4(h_2M_2 + h_1M_1)]$$

where

$$F_1 = \beta_1^2 - \beta_2^2 \quad ; \quad F_2 = 2\beta_1\beta_2$$

The last three of Eqns. (4.31) contain only C_1, C_3 and C_4 and may be solved simultaneously for these constants. The condition for a non-trivial solution is given by the vanishing of the determinant of the coefficients for C_1, C_3 and C_4. Thus

$$\begin{vmatrix} -\alpha\sin\mu & \beta_1M_2 + \beta_2M_1 & \beta_1M_1 - \beta_2M_2 \\ -\alpha^2\cos\mu & -F_1M_2 - F_2M_1 & -F_1M_1 + F_2M_2 \\ \alpha^3\sin\mu & -h_1M_2 + h_2M_1 & -h_1M_1 - h_2M_2 \end{vmatrix} = 0 \qquad (4.32)$$

Expanding the determinant and simplifying, Eqn. (4.32) reduces to

$$\tan\mu = \frac{2\chi_1\mu\ \lambda'}{\mu^2 - 2\lambda'^2} \qquad (4.33)$$

Eqn. (4.33) may be solved graphically to yield the critical buckling load, as shown in Fig. 4.24 where both sides of the equation are plotted versus μ, noting that at buckling $\alpha = \sqrt{(P'_E/D)}$, where P'_E is the critical buckling load for the delaminated layer. The load P'_E may differ from the Euler critical load P_E for a built in strut because it incorporates the hinge effect offered by the elastic

foundation. This effect, though small, manifests itself in smaller critical loads corresponding to lower values of E_r as shown in Fig. 4.24. Given that in general $P'_E < P_E$ for the problem under examination, it is permissible to write

$$\alpha = \sqrt{(P'_E/D)} \quad = \omega\pi/a$$

or

$$P'_E = \frac{\omega^2 \pi^2 D}{a^2} \tag{4.34}$$

as a solution to Eqn. (4.33), corresponding to the least buckling load; where ω is less than unity and, for a certain material, is dependent upon the debond half span length a as shown in Fig. 4.24. The above dependence is clearly seen from Fig. 4.25 where $\omega \to 1$ as $a \to \infty$. This is to say, for large values of 'a' the critical load P'_E approaches the Euler buckling load P_E. Another occasion when $P'_E \to P_E$ is that when the elastic foundation is infinitely stiff ($E_r \to \infty$). In fact, if E_r is very large $\chi_1 \to 1$ [see below Eqns. (4.10) and (4.11)], also $\lambda' = \beta a \to \infty$ [see below Eqn. (4.9)]; then Eqn. (4.33) becomes, $\tan \mu = 0$ which is possible if $\mu = a\sqrt{(P'_E/D)} = \pi$ or $P'_E = \pi^2 D/a^2 = P_E$, i.e. the Euler buckling load for a built-in strut.

4.3.2 Post-Buckling Shape

The constants C_2, C_3 and C_4 may be expressed in terms of the constant C_1 using Eqns. (4.31). Thus

$$C_2 = \alpha^2 \cos\mu \left[\frac{1 + 4\eta^4 + 4\eta^2(\chi_1^2 - 1)}{2\eta^2\ (1-2\eta^2)}\right] C_1$$

$$C_3 = \frac{\cos\mu}{2Y_1\beta_2\beta^2}\left[\frac{\alpha^2(\beta_2 M_2 - \beta_1 M_1) + h_2 M_2 + h_1 M_1}{1 - 2\eta^2}\right] C_1 \qquad (4.35)$$

$$C_4 = \frac{\cos\mu}{2Y_1\beta_2\beta^2}\left[\frac{\alpha^2(\beta_1 M_2 + \beta_2 M_1) + h_2 M_1 - h_1 M_2}{1 - 2\eta^2}\right] C_1$$

From Eqns. (4.35) and (4.30), remembering that at buckling $\alpha = \omega\pi/a$, we obtain

$$w_1 = \frac{\delta_o^*}{1 + Y(\lambda')} \cos(\rho x/a) + Y(\lambda') \qquad (4.36)$$

where, $\delta_o^* = (w_1)_{x=0}$ is the debond mid-span maximum deflection, $\rho = \omega\pi$, and $Y(\lambda')$ is a function of λ' given by the following expression

$$Y(\lambda') = \frac{\rho^4 + 4\lambda'^4 + 4\lambda'^2\rho^2(\chi_1^2 - 1)}{2\lambda'\beta(\rho^2 - 2\lambda'\beta)} \cos\rho \qquad (4.37)$$

It is seen from Eqns. (4.36) and (4.37) that for an infinitely stiff elastic foundation $\lambda' \to \infty$; $\omega \to 1$; $\cos\rho \to -1$, therefore

$$w_1 \to \frac{\delta_o^*}{2}\ [1 + \cos(\pi x/a)] = \text{deflection for the built-in case.}$$

The post-buckling maximum deflection shape given by Eqn. (4.36) will be completely defined once δ_o^* is known. Referring to Fig. 4.26, the loading sequence which leads to buckling consists of assigning a uniform strain ε to the laminate which shortens as shown in Fig. 4.26 (b), then, the delaminated layer buckles Fig. 4.26(c) when the critical strain $\varepsilon_E' = \omega^2\pi^2 D/a^2 E_1 t_1$ is reached. If we assume that,

in going from Fig. 4.26(b) to 4.26(c), the length of the delaminated layer remains unchnaged and its in-plane direct stress is the same as the buckling stress, (provided δ_o^* is relatively small) then we may write from the formula which gives the approach of the ends of the split as it buckles,

$$\overline{\Delta} = (2a)(\varepsilon - \varepsilon_E') = \frac{1}{2}\int_{-a}^{a}\left(\frac{dw_1}{dx}\right)^2 dx \qquad (4.38)$$

Eqn. (4.38), after substituting for w_1 from Eqn. (4.36) and integrating, gives

$$\delta_o^* = \frac{8a^2\,(\varepsilon - \varepsilon_E')\,\left[1 + Y(\lambda')\right]^2}{\rho\,(2\rho - \sin 2\rho)} \qquad (4.39)$$

Substitution from Eqn. (4.39) into Eqn. (4.36) yields

$$w_1 = 2a\sqrt{\frac{2\,(\varepsilon - \varepsilon_E')}{\rho(2\rho-\sin 2\rho)}}\left[\cos(\rho x/a) + Y(\lambda')\right] \qquad (4.40)$$

4.3.3 Energy Release Rate and Elastic Strain Energy

The critical energy release rate g_c can be evaluated once the total strain energy per unit width in the laminate U is formulated. U may be split into four components U_b, U_{dc}, U_{at} and U_{in}; where U_b and U_{dc} are, respectively, the bending and direct compression energies for the delaminated layer, U_{at} is the strain energy of the attached portion and U_{in} is the strain energy of the inner layer (layer 2, as shown in Fig. 4.26). The strain energy component U_b may be evaluated using Eqn. (4.27), where $\overline{w_1} = w_1$ is given by Eqn. (4.40), therefore

$$U_b = \frac{2aE_1t_1(\varepsilon\varepsilon_E' - \varepsilon_E'^2)(2\rho + \sin 2\rho)}{2\rho - \sin\,2\rho} \qquad (4.41)$$

The other components of energy (U_{dc}, U_{at} and U_{in}) may be evaluated using the usual energy formula for direct stress and strain. Thus

$$U_{dc} = \frac{aE_1 t_1 \varepsilon_E'^2}{1-\nu_{\ell t}\,\nu_{t\ell}} \tag{4.42}$$

$$U_{at} = \frac{(\ell'-a)E_1 t_1 \varepsilon^2}{1-\nu_{\ell t}\,\nu_{t\ell}} \tag{4.43}$$

$$U_{in} = \frac{\ell' E_2 t_2 \varepsilon^2}{1-\nu_{\ell t}\,\nu_{t\ell}} \tag{4.44}$$

The total strain energy in the laminate $U = U_b + U_{dc} + U_{at} + U_{in}$, given by the components from Eqns. (4.41) through to (4.44), can now be used in Eqn. (4.13) to evaluate the strain energy release rate g, with the tacit assumption that the strain in the inner layer and the attached portion will remain unchanged (= ε) after the debonded layer has buckled. Thus, the normalized strain energy release rate g_n is

$$g_n = \frac{E_1 t_1^5 \pi^4 \omega^4}{144 a^4 \Gamma (1-\nu_{\ell t}\,\nu_{t\ell})^3}\left\{3+J^2+2Q(J-3) - \left(\frac{4a\omega^*}{\omega}\right)\left[1+Q(J-2)\right] - 2aQ(J-1)\right\} \tag{4.45}$$

where, $Q = [(1-\nu_{\ell t}\nu_{t\ell})(2\rho+\sin 2\rho)]/(2\rho-\sin 2\rho)$; $J=\varepsilon/\varepsilon_E'$;

$\omega^* = d\omega/da$ (plotted in Fig. 4.27 using the graph of ω versus a).

4.3.4 Numerical Results and Discussion

The same set of data given in Section 4.2.3 are also used here to study the delamination characteristics of an initially straight debonded layer. Numerical computation of Eqn. (4.45) revealed that for $J<1$ (i.e. $\varepsilon < \varepsilon_E'$) the normalized strain energy release rate was always negative, thus, no energy was released to propagate the existing

split. Only after $J \geq 1$ (i.e. $\varepsilon \geq \varepsilon'_E$) does g_n become positive and therefore delamination is possible. The normalized strain energy release rate is plotted versus 'a' in Fig. 4.28 for various values of J. The 1.0 horizontal dotted line represents the threshold for delamination growth. For points above this line splitting is always possible given that the energy release rate exceeds the toughness of separation Γ. It is also seen from Fig. 4.28 that for an applied strain value $\varepsilon \leq 1.5\ \varepsilon'_E$ no delamination will occur for any $a \geq$ 12.75mm. The separation between possible and not-possible regions of delamination is shown in Fig. 4.29 where the critical load ratio J is plotted versus the debond half span a.

4.4 CONCLUSIONS

A theoretical analysis based on beam-column theory and an energy release rate criterion, has been presented for the crack propagation of a layered fibre reinforced plastic strip in compression, in the presence of a blister. Account has been taken of a resin rich layer at the delaminating edge and of an initial deflection in the blister geometry. The beam-column and beam on elastic foundation differential equations have been solved, respectively, for the blister layer and the attached portion and the constants which appear in the solution have been determined through continuity conditions along the delamination front. The total strain energy has been evaluated for the blister layer and later used in conjunction with a law of mixtures to determine an overall Young's modulus for the whole laminate. This modulus has been used to calculate the total strain energy in the laminate and therefore the strain energy release rate. A typical set of design curves is given and discussed which shows the influence of blister

length, applied strain and resin stiffness on loads required for splitting. It has been found that delamination may occur at in-plane load in the blister layer well below the Euler buckling load for a built-in strut.

The case with no pre-loading initial deflection has also been analysed along the same line of thinking and the effect of the elastic foundation on the post-buckling behaviour and delamination is pointed out and discussed. Design curves are given for the prediction of the critical applied strain knowing the initial half debond length. It has been found here that delamination is not possible unless the delaminated layer buckles.

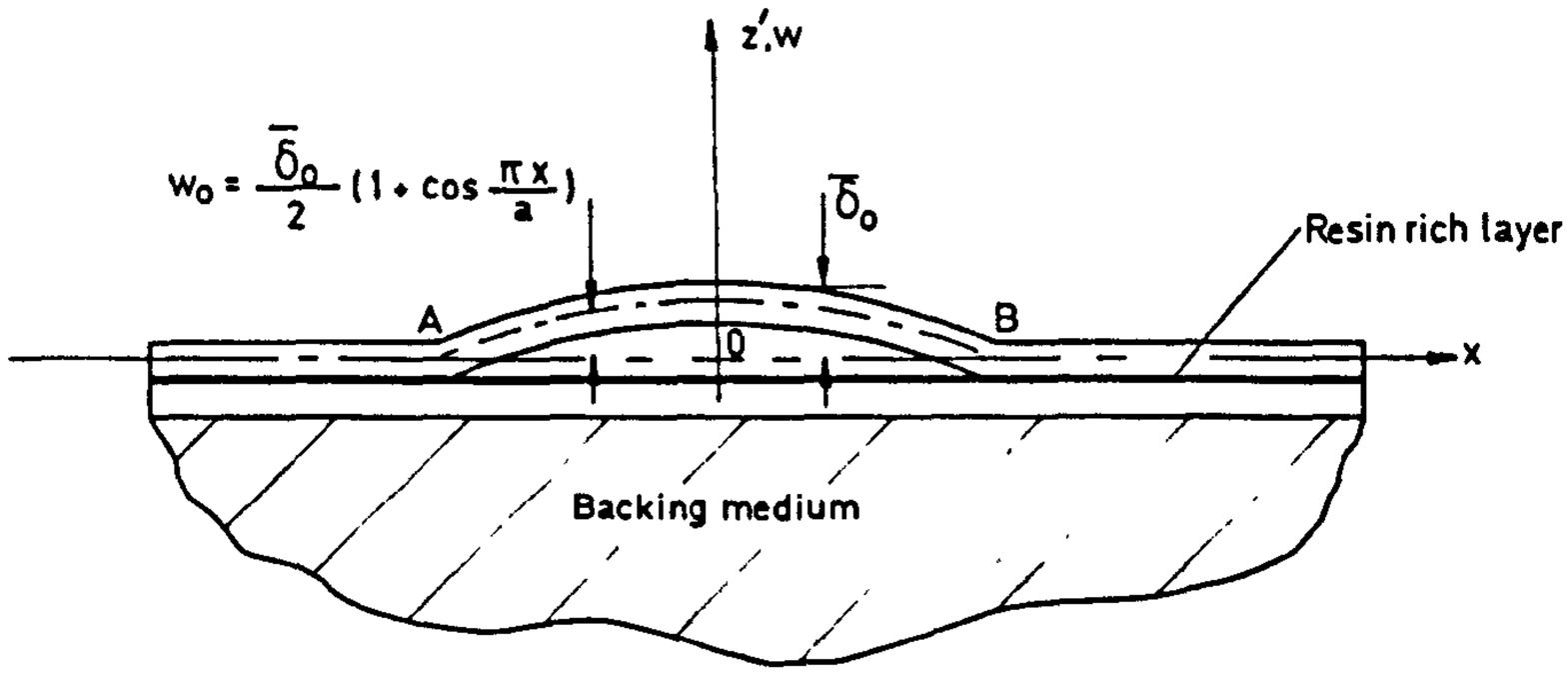

(a) Before load application

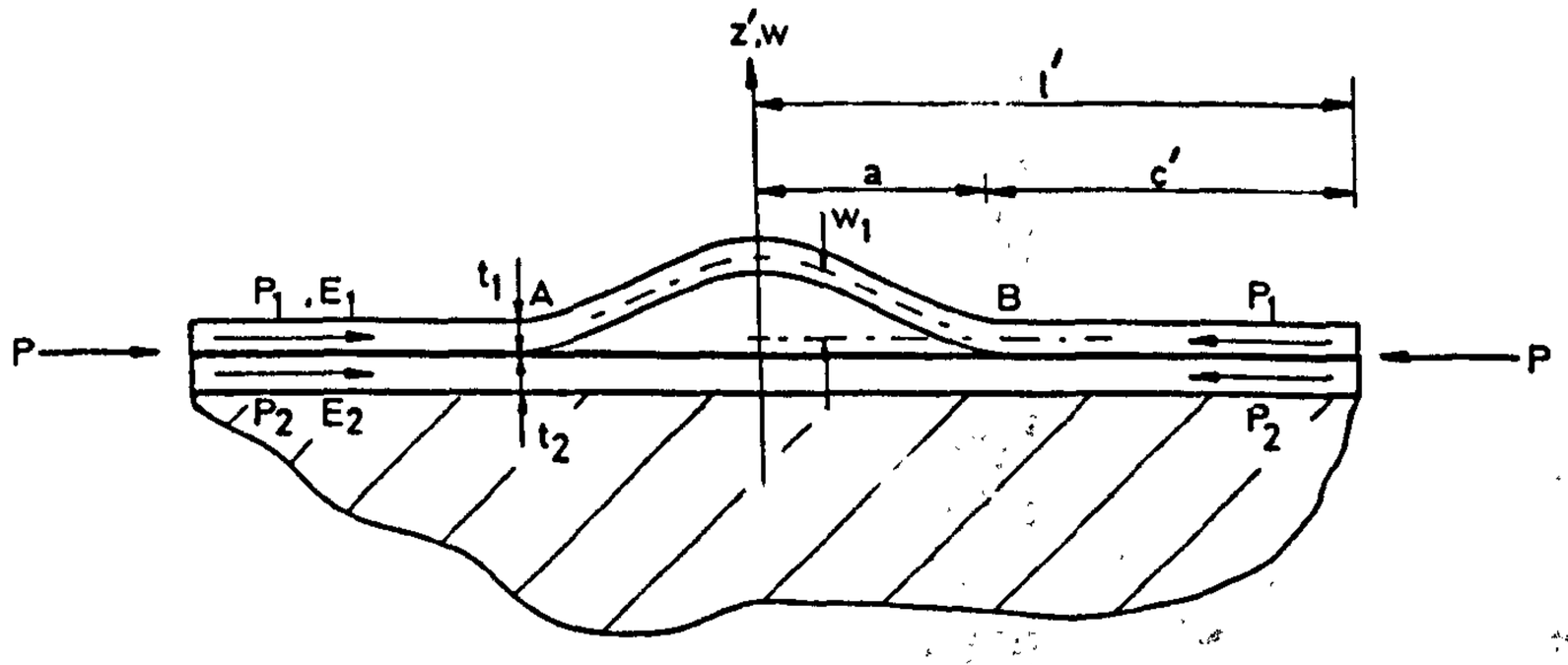

(b) After load has been applied

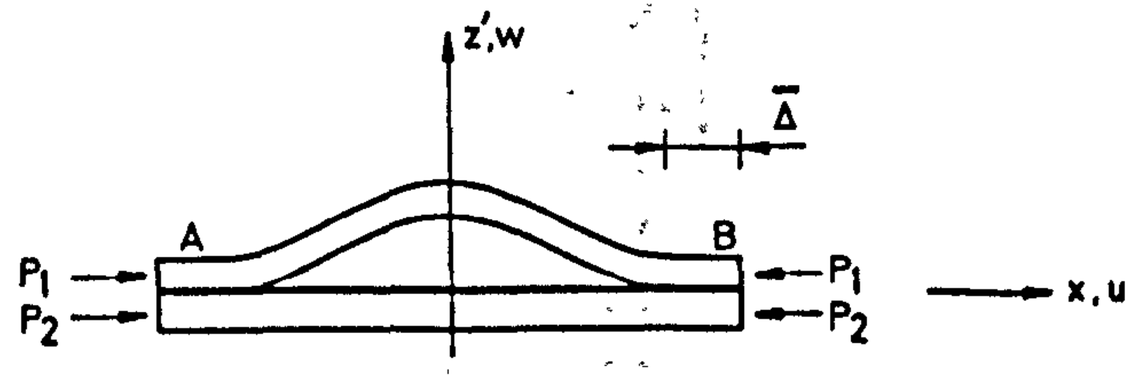

(c) Free body diagram for the delaminated portion

FIG. 4.1 BLISTER MODEL CONFIGURATION AND LOADING

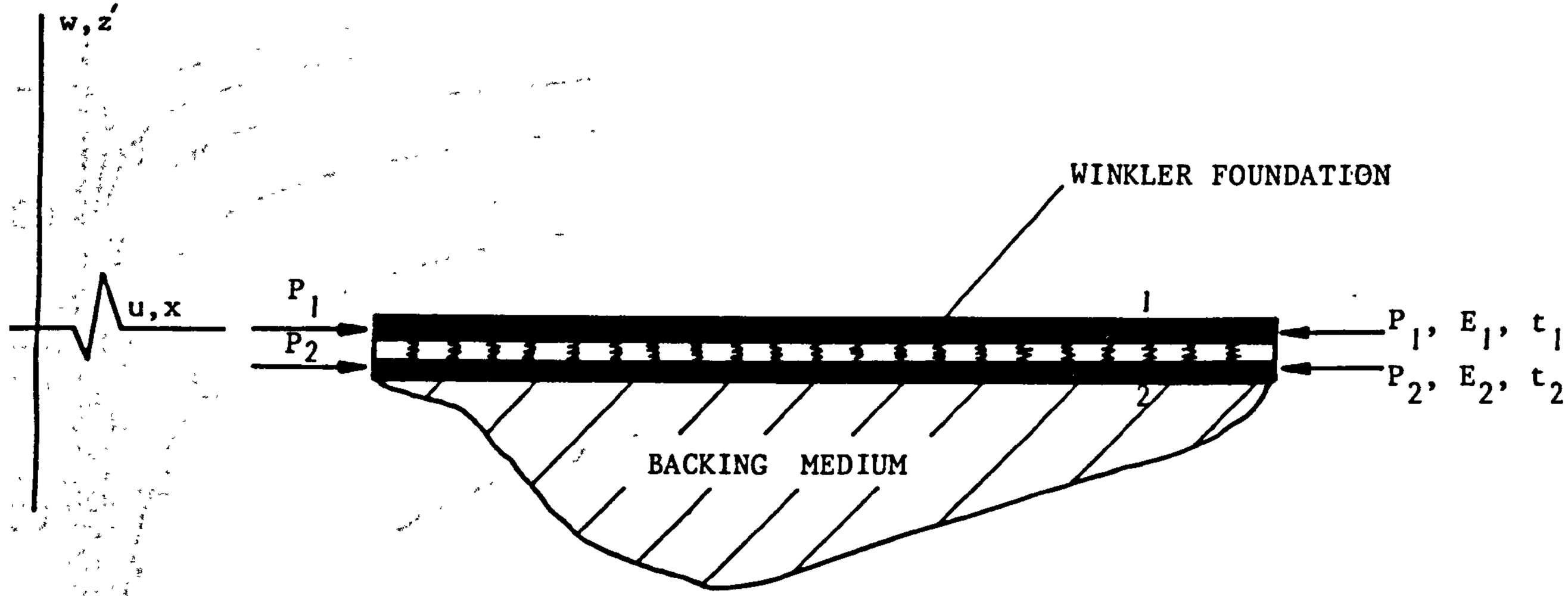

Fig. 4.2 ATTACHED REGION ON WINKLER FOUNDATION

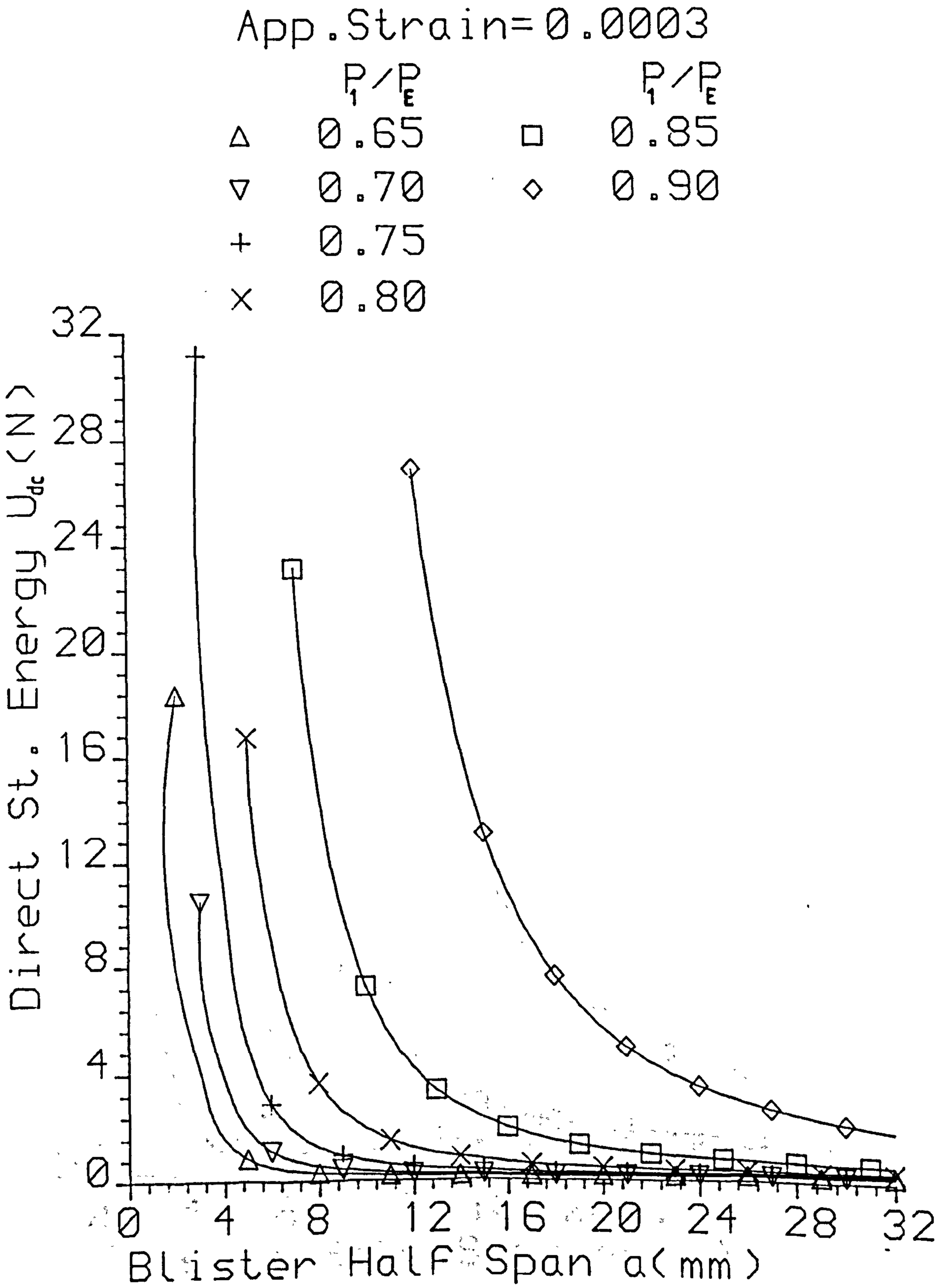

Fig.4.3 Direct St.Energy vs Blister Half Span Length

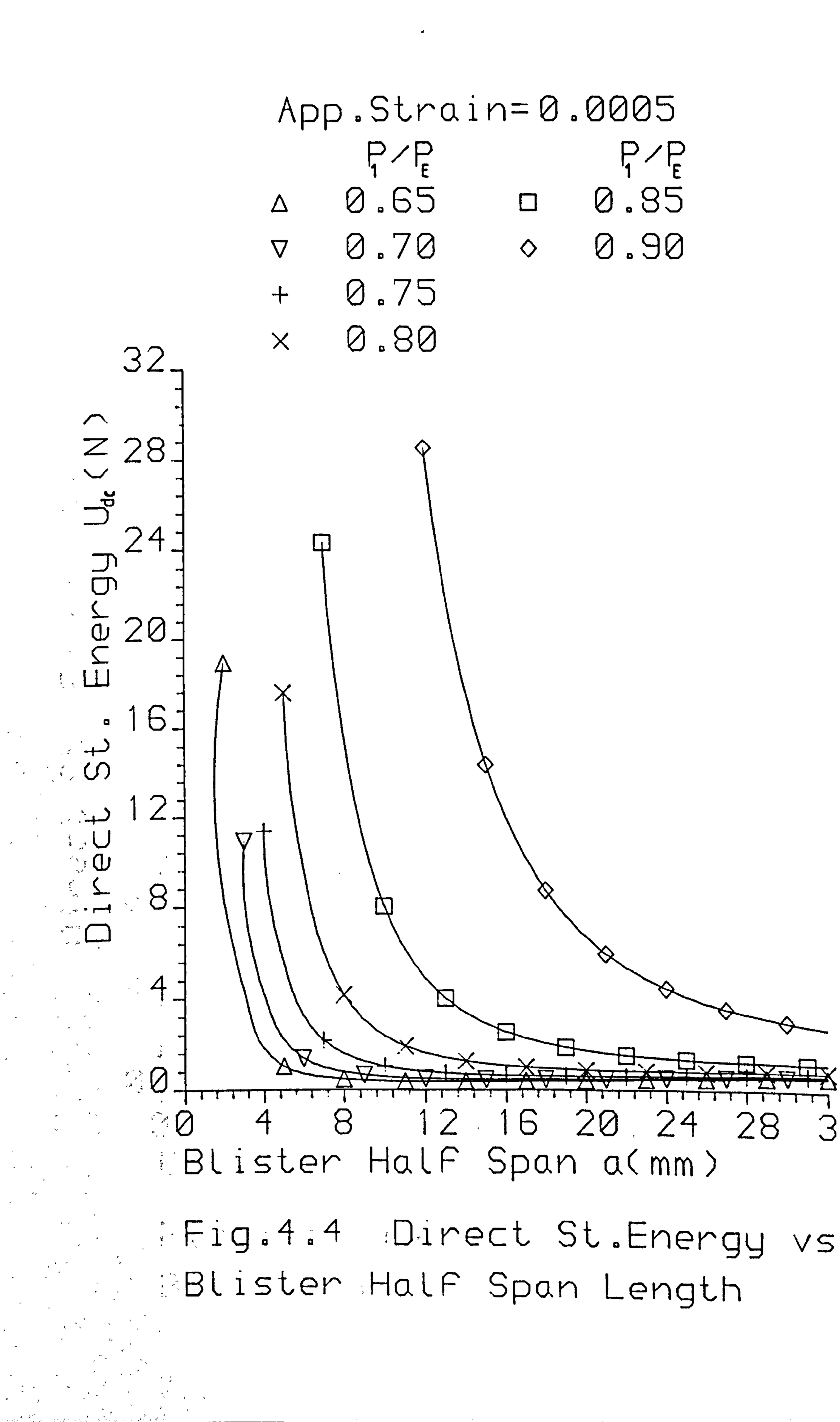

Fig.4.4 Direct St.Energy vs Blister Half Span Length

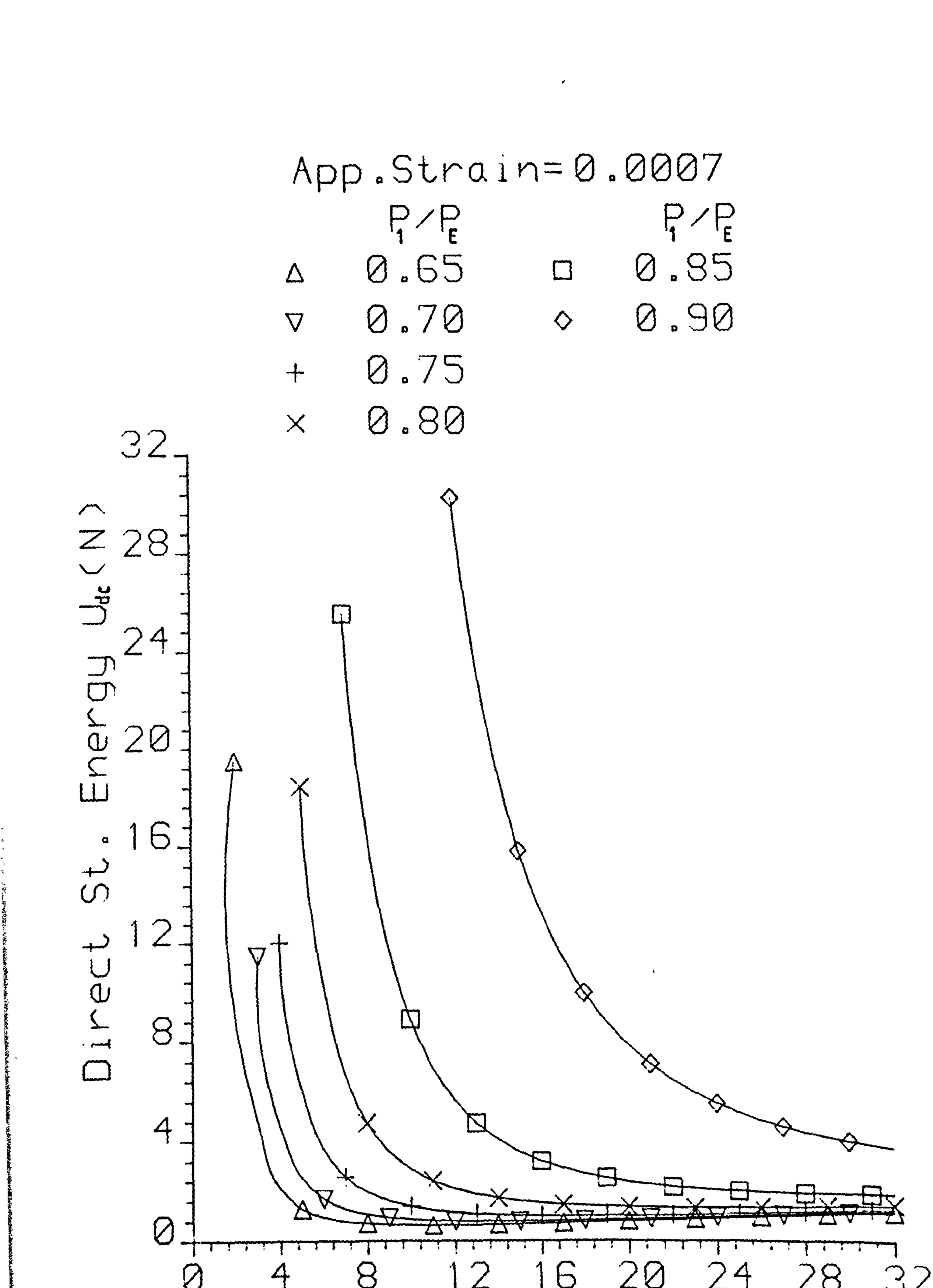

Fig.4.5 Direct St.Energy vs Blister Half Span Length

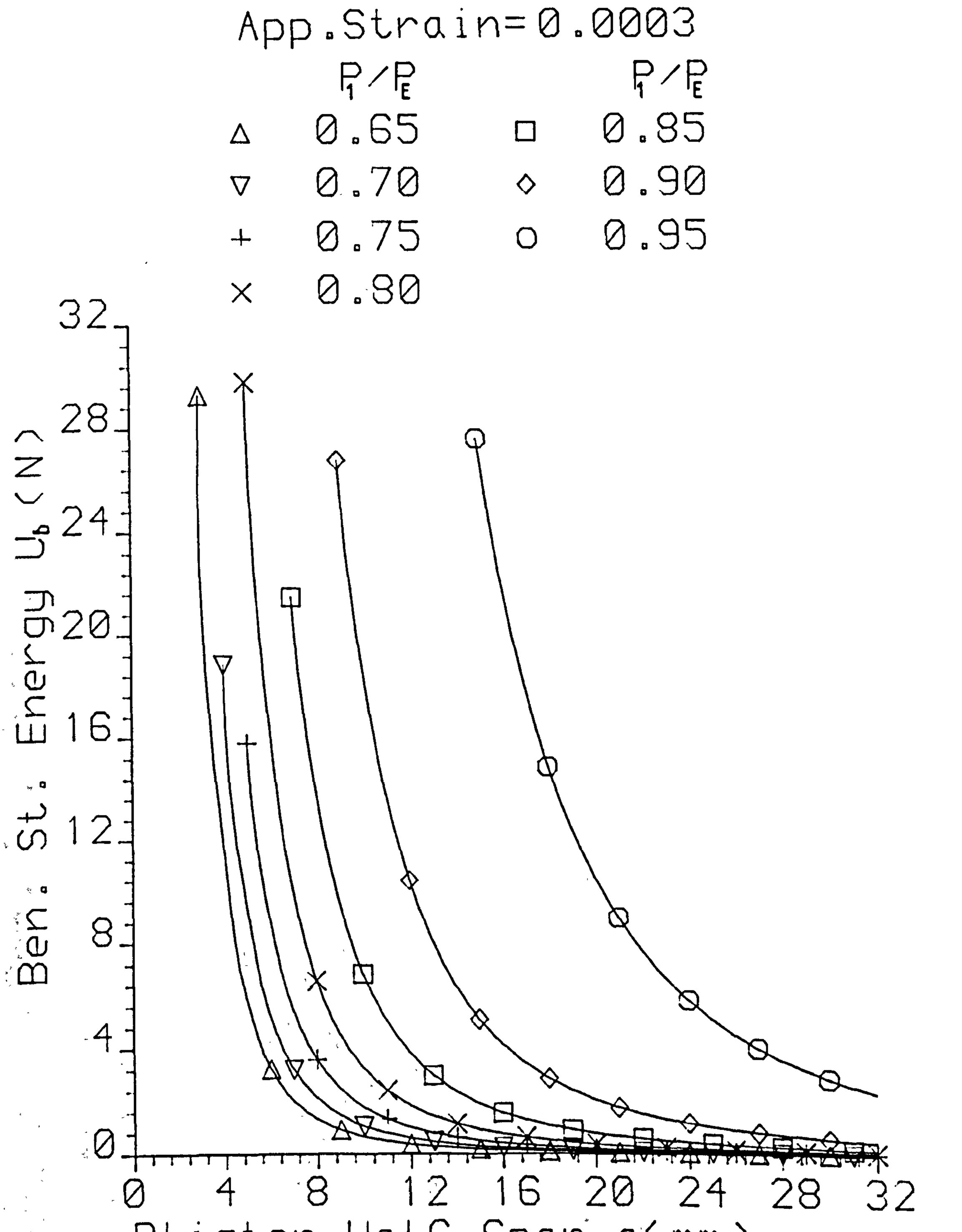

Fig.4.6 Ben. St.Energy vs Blister Half Span Length

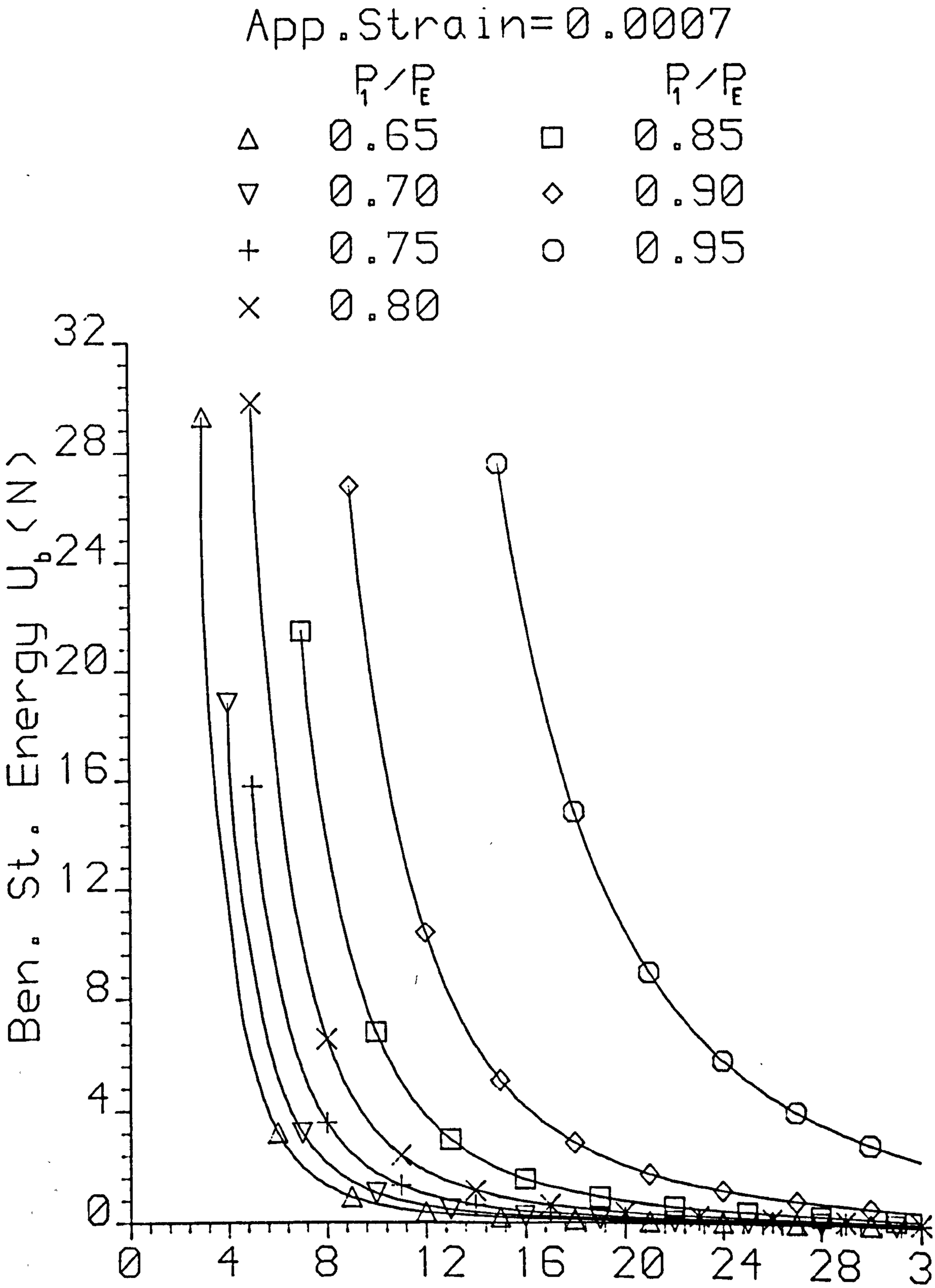

Fig.4.7 Ben. St.Energy vs Blister Half Span Length

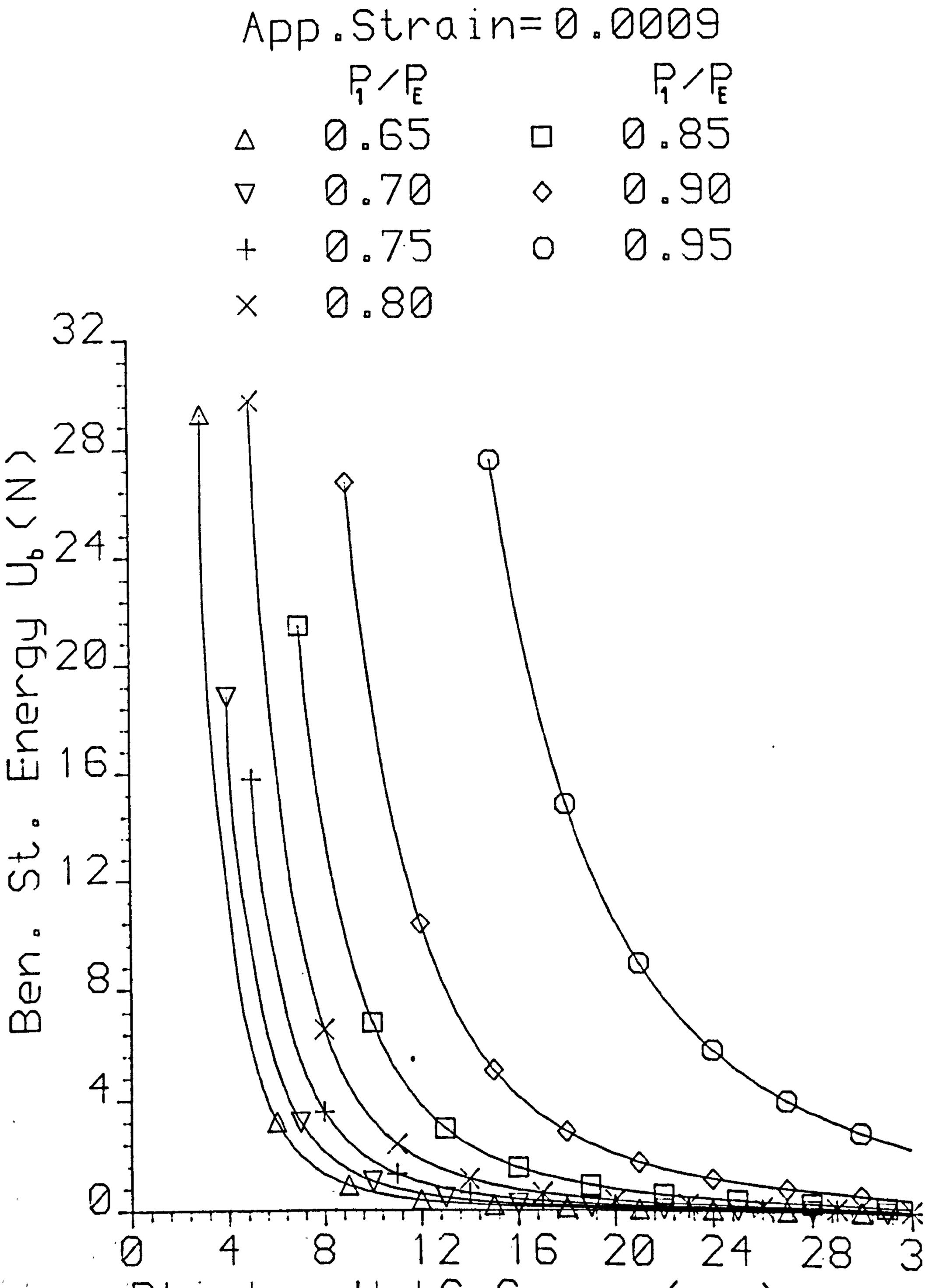

Fig.4.8 Ben. St.Energy vs Blister Half Span Length

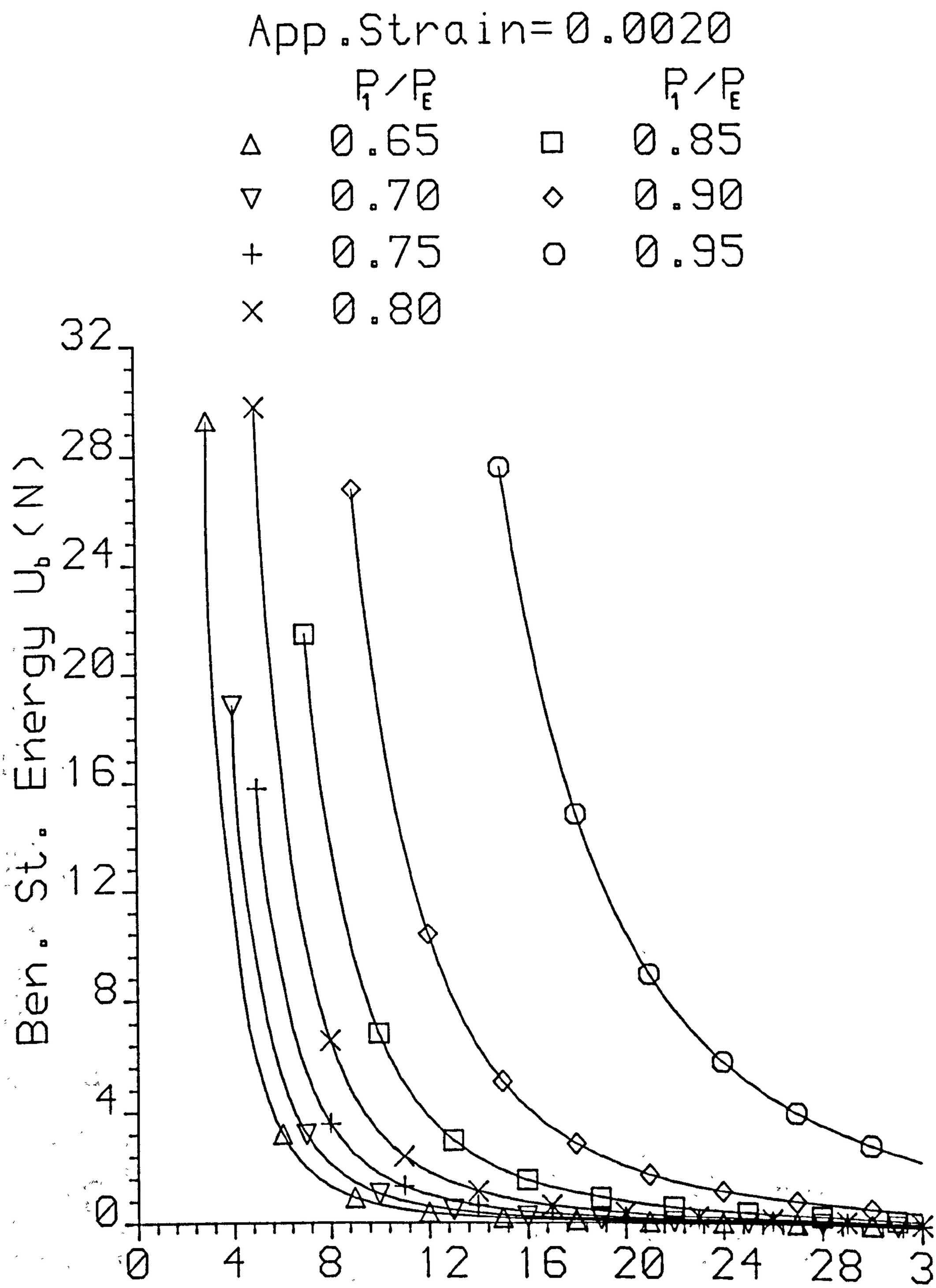

Fig.4.9 Ben. St.Energy vs Blister Half Span Length

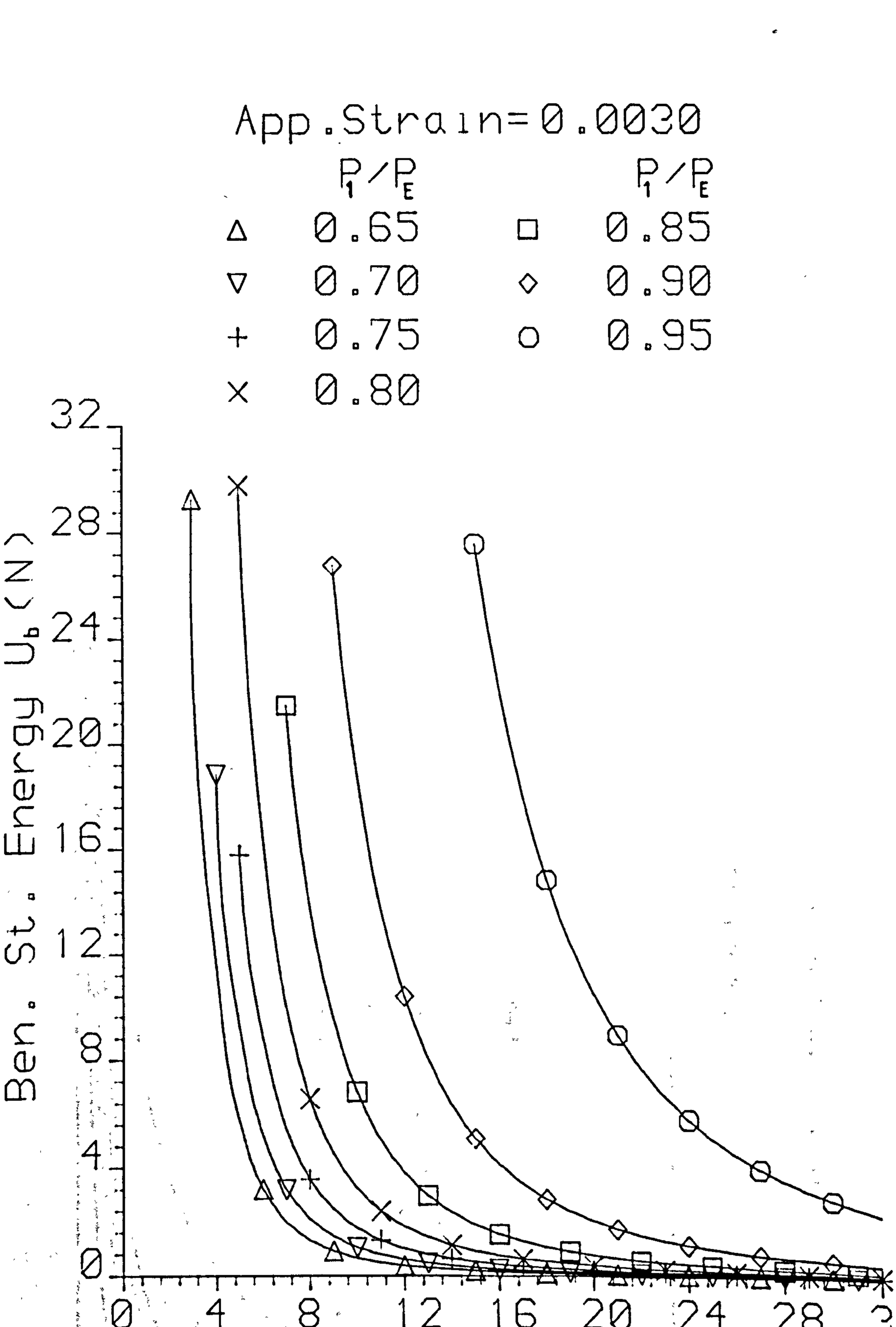

Fig.4.10 Ben. St.Energy vs Blister Half Span Length

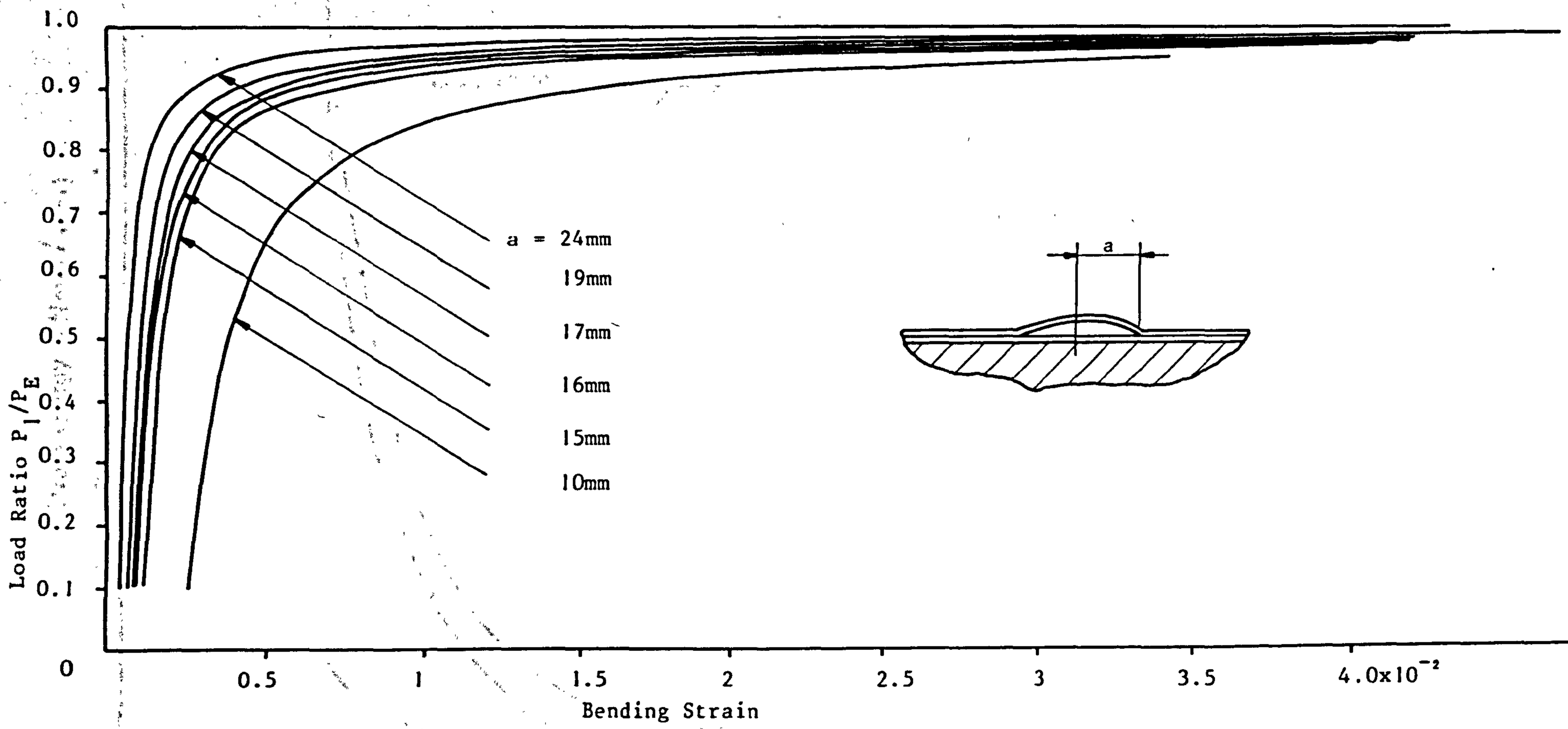

Fig. 4.11 BENDING STRAIN AT THE MIDDLE POINT OF BLISTER VS P_I/P_E

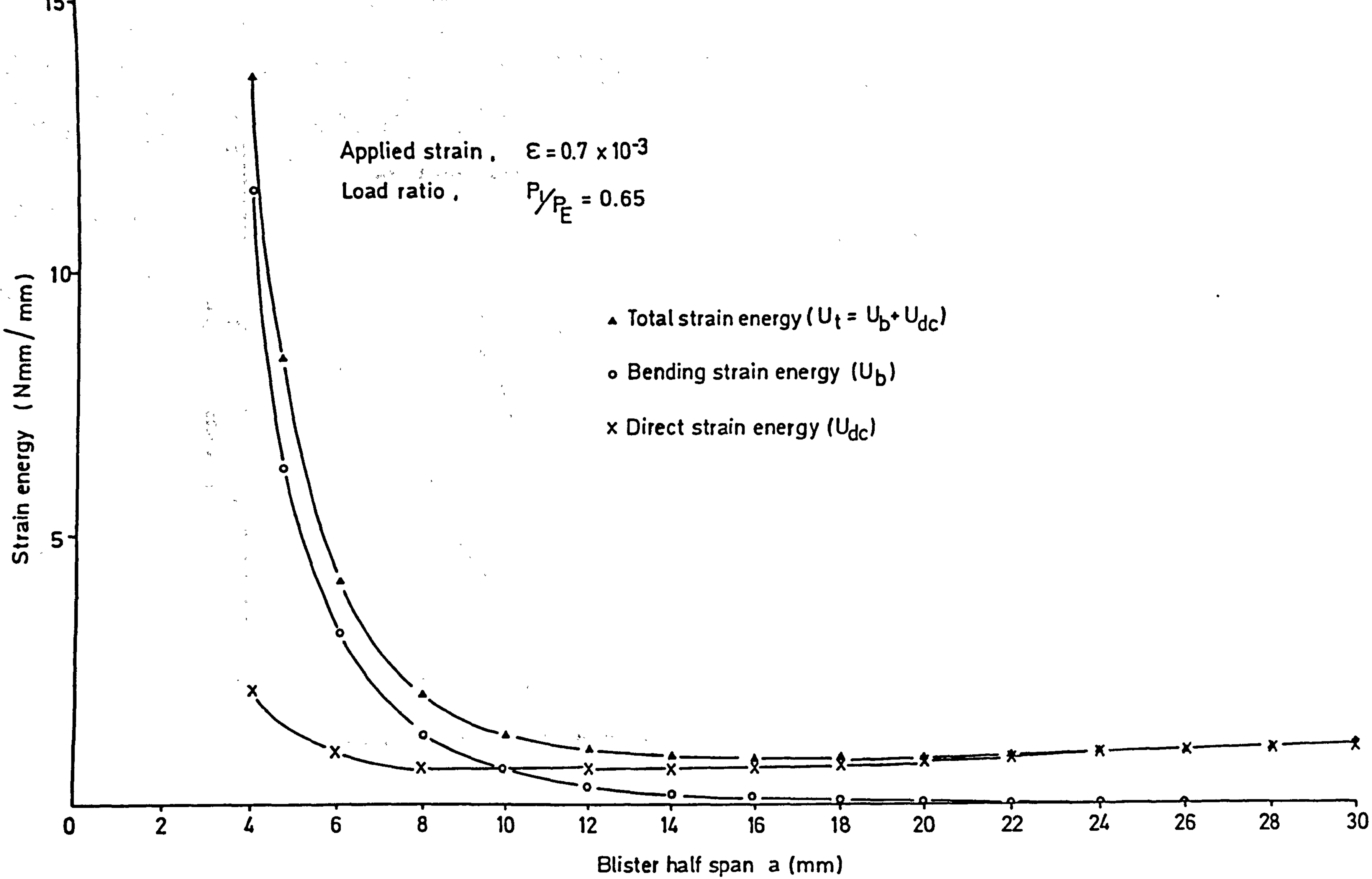

FIG. 4.12 COMPARISON OF STRAIN ENERGY QUANTITIES IN THE BLISTER LAYER

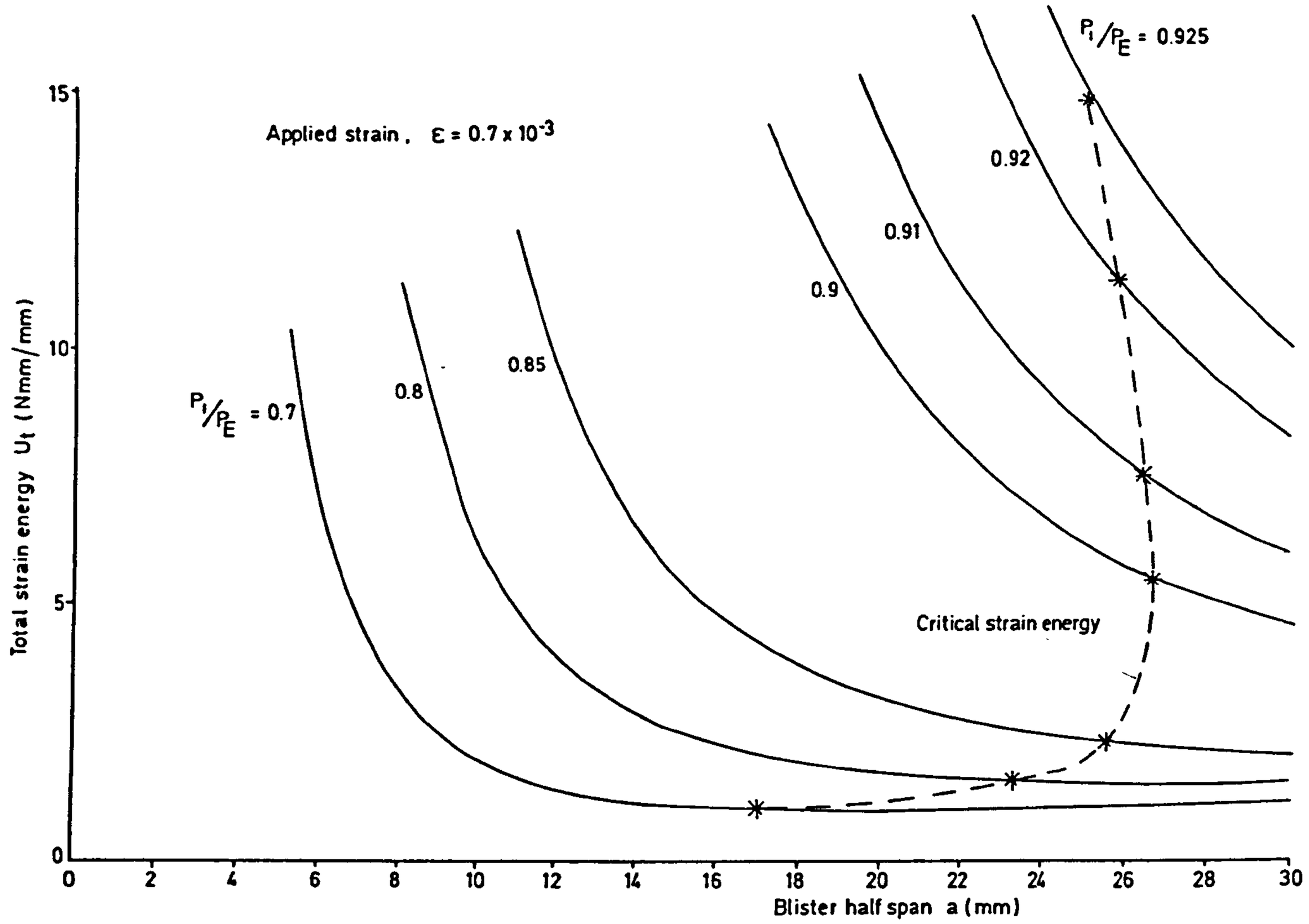

FIG. 4.13 TOTAL STRAIN ENERGY IN BLISTER LAYER vs. BLISTER HALF SPAN FOR VARIOUS LOAD RATIOS

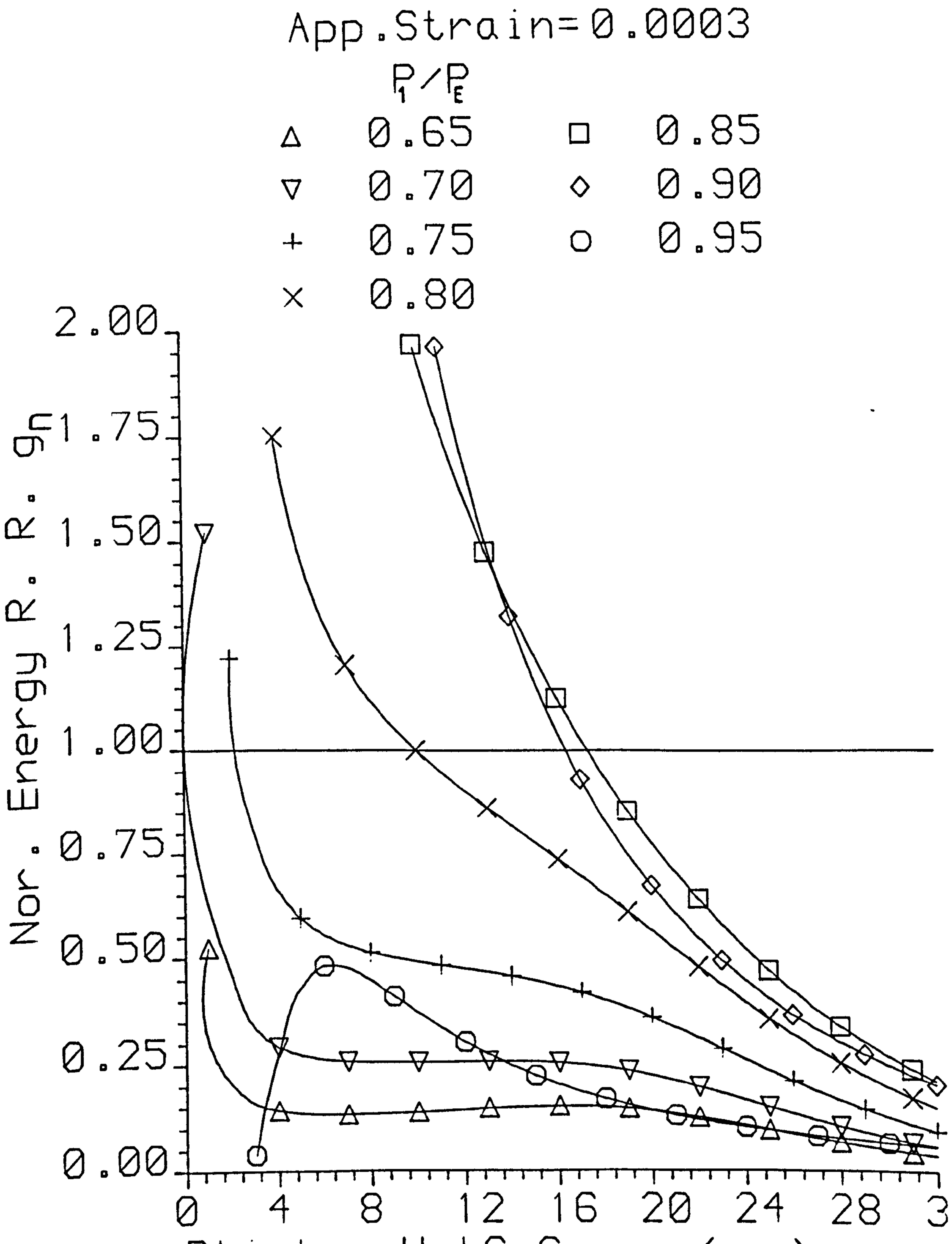

Fig.4.14 Nor.E.R.R. vs Blister Half Span Length

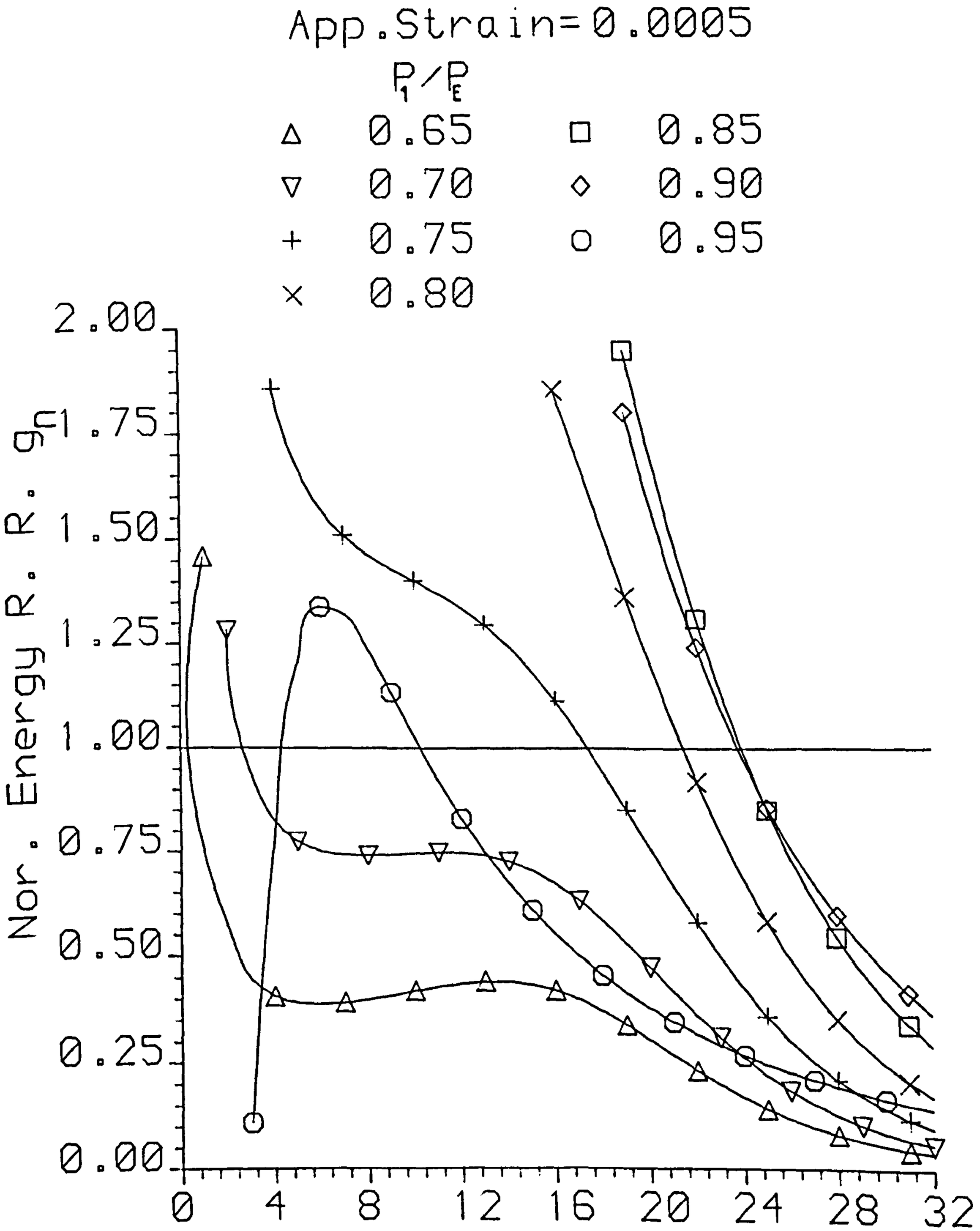

Fig.4.15 Nor.E.R.R. vs Blister Half Span Length

FIG 4.16 NORMALISED ENERGY RELEASE RATE vs. BLISTER HALF SPAN FOR VARIOUS LOAD RATIOS

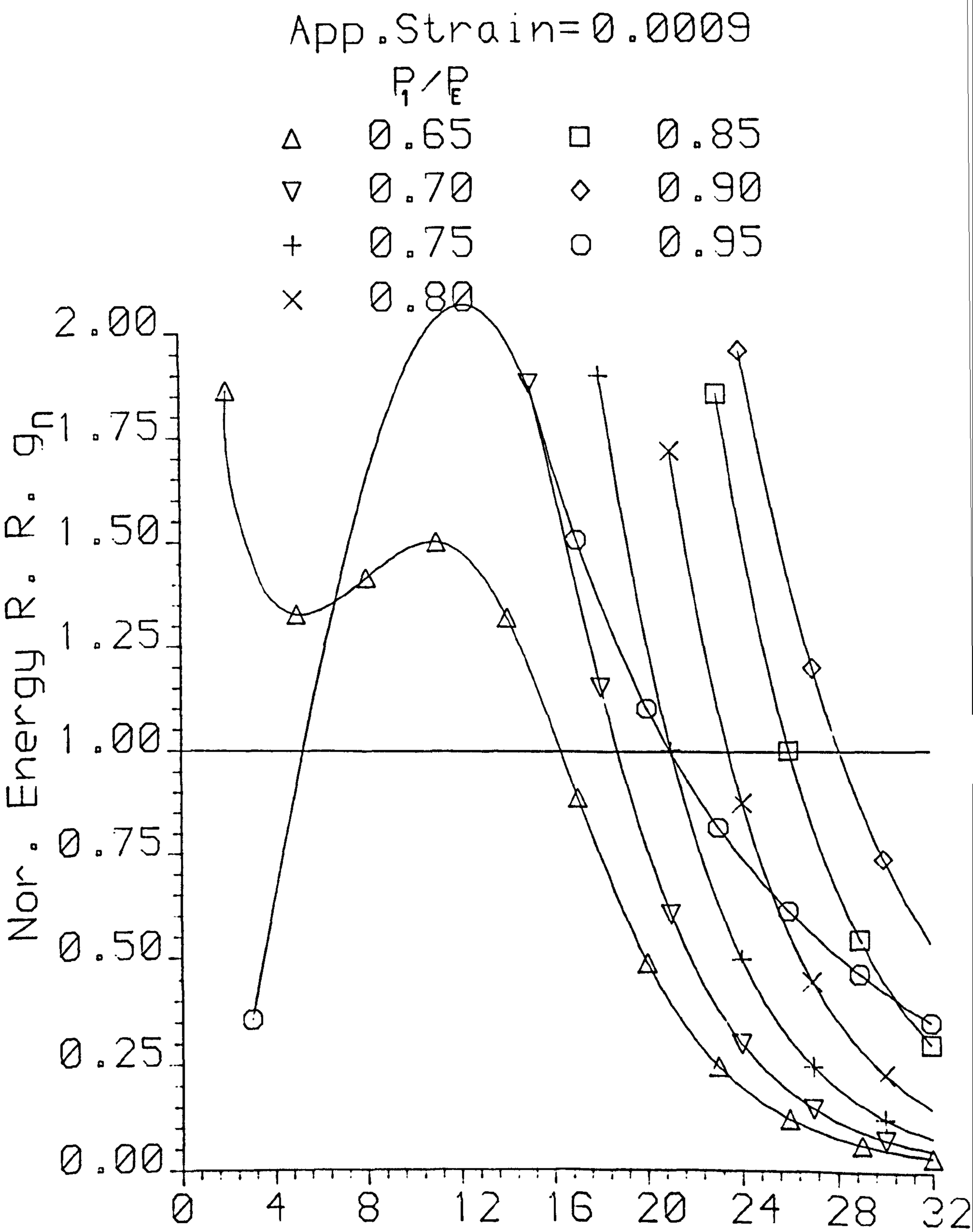

Fig.4.17 Nor.E.R.R. vs Blister Half Span Length

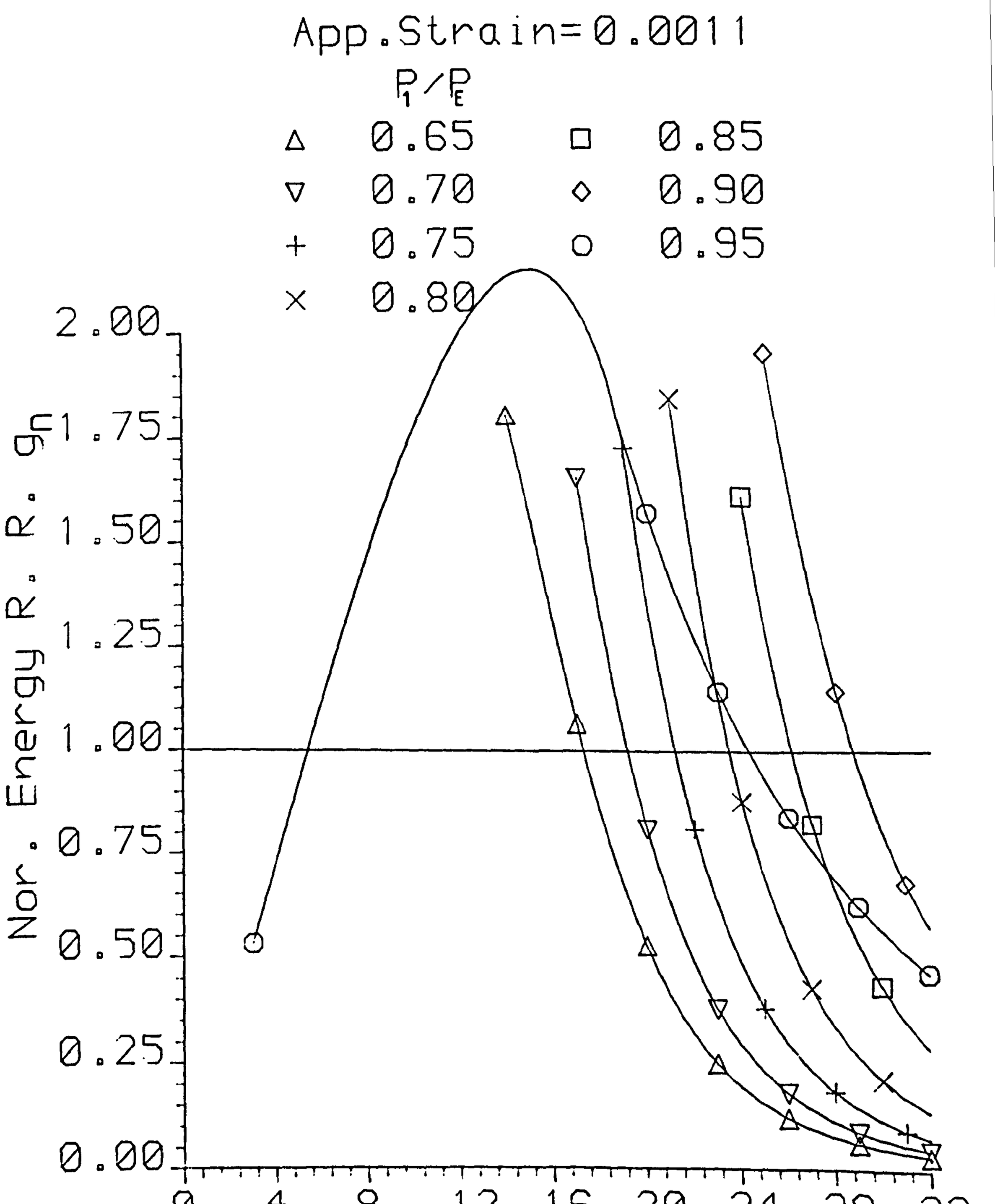

Fig.4.18 Nor.E.R.R. vs Blister Half Span Length

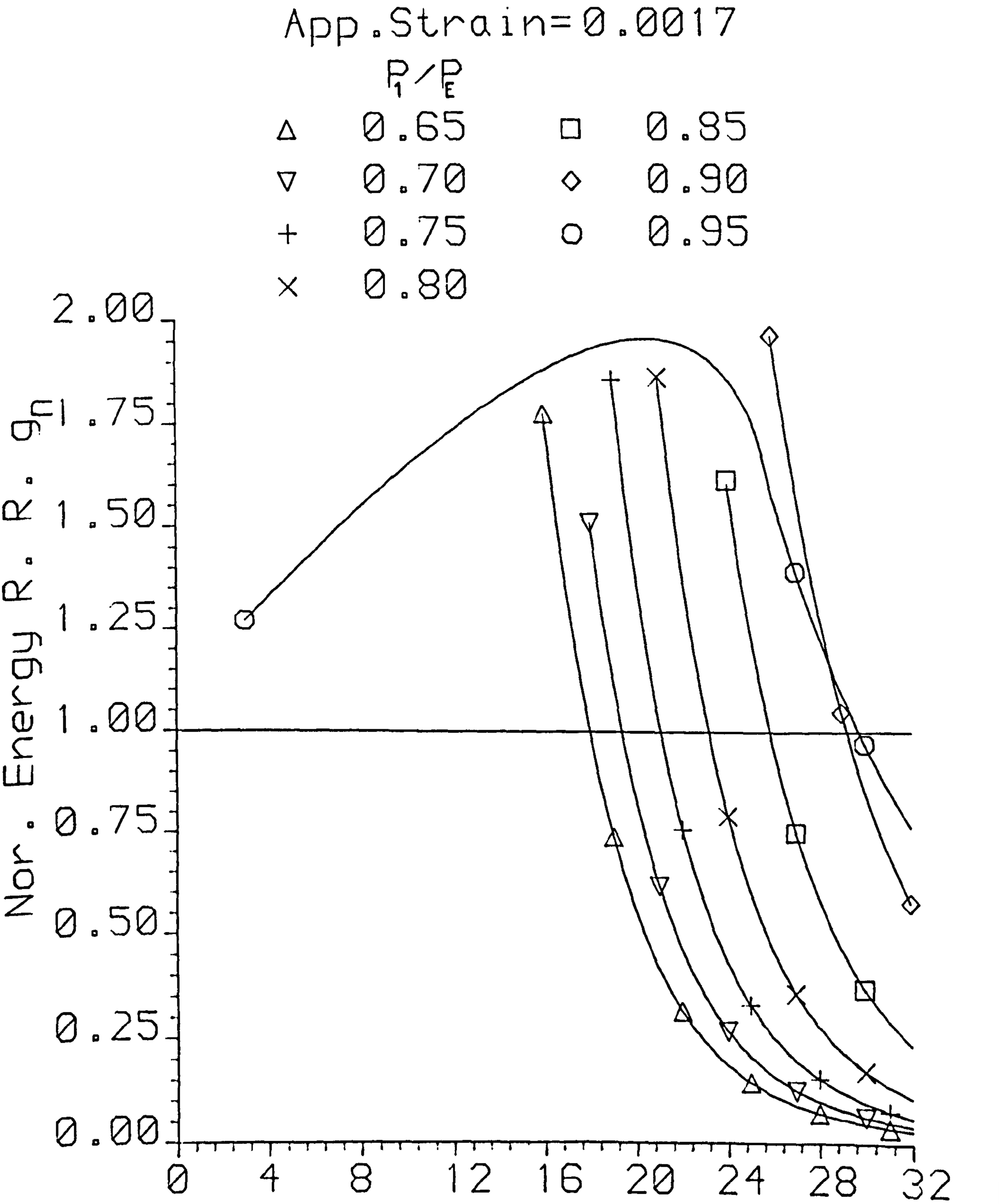

Fig.4.19 Nor.E.R.R. vs Blister Half Span Length

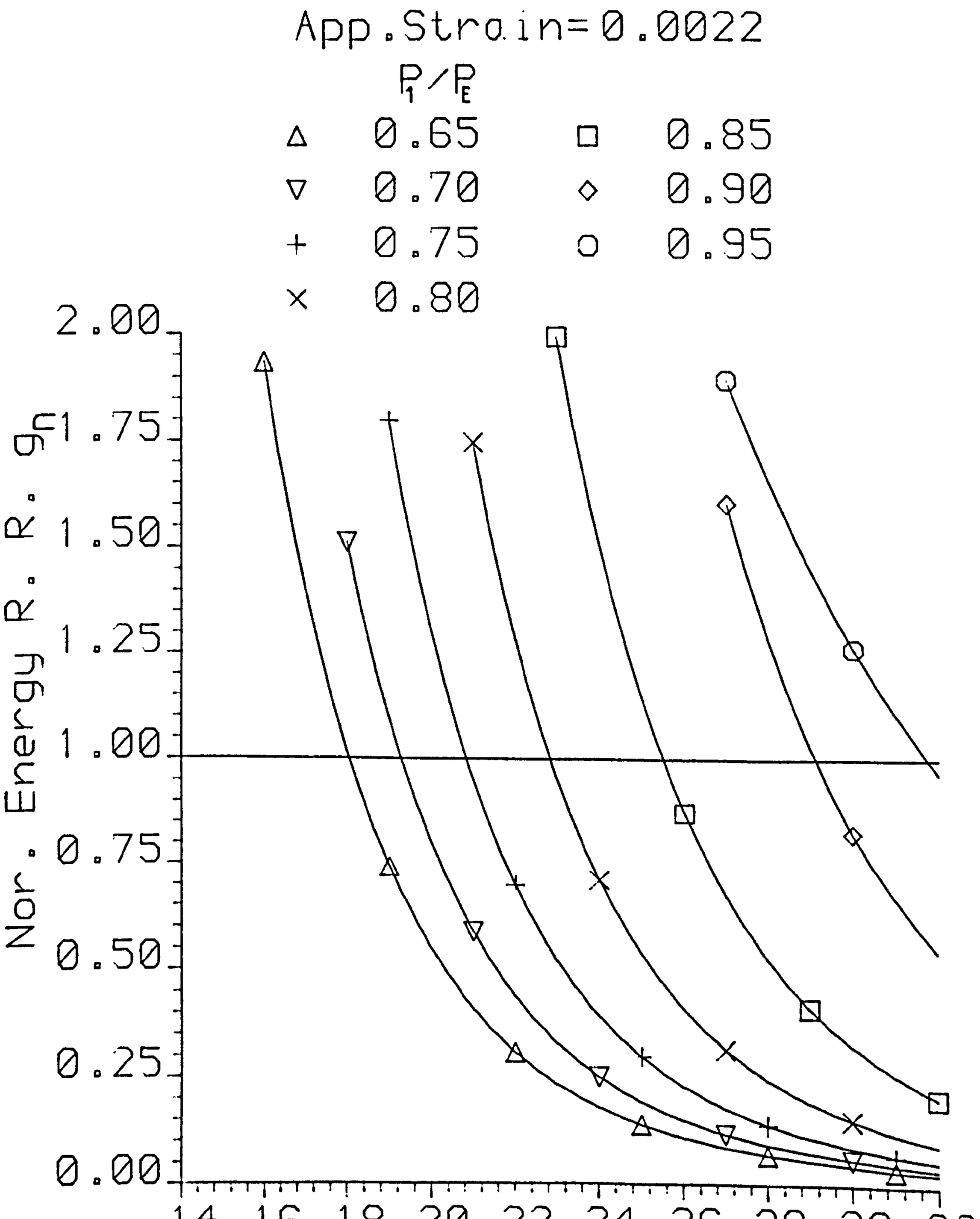

Fig.4.20 Nor.E.R.R. vs Blister Half Span Length

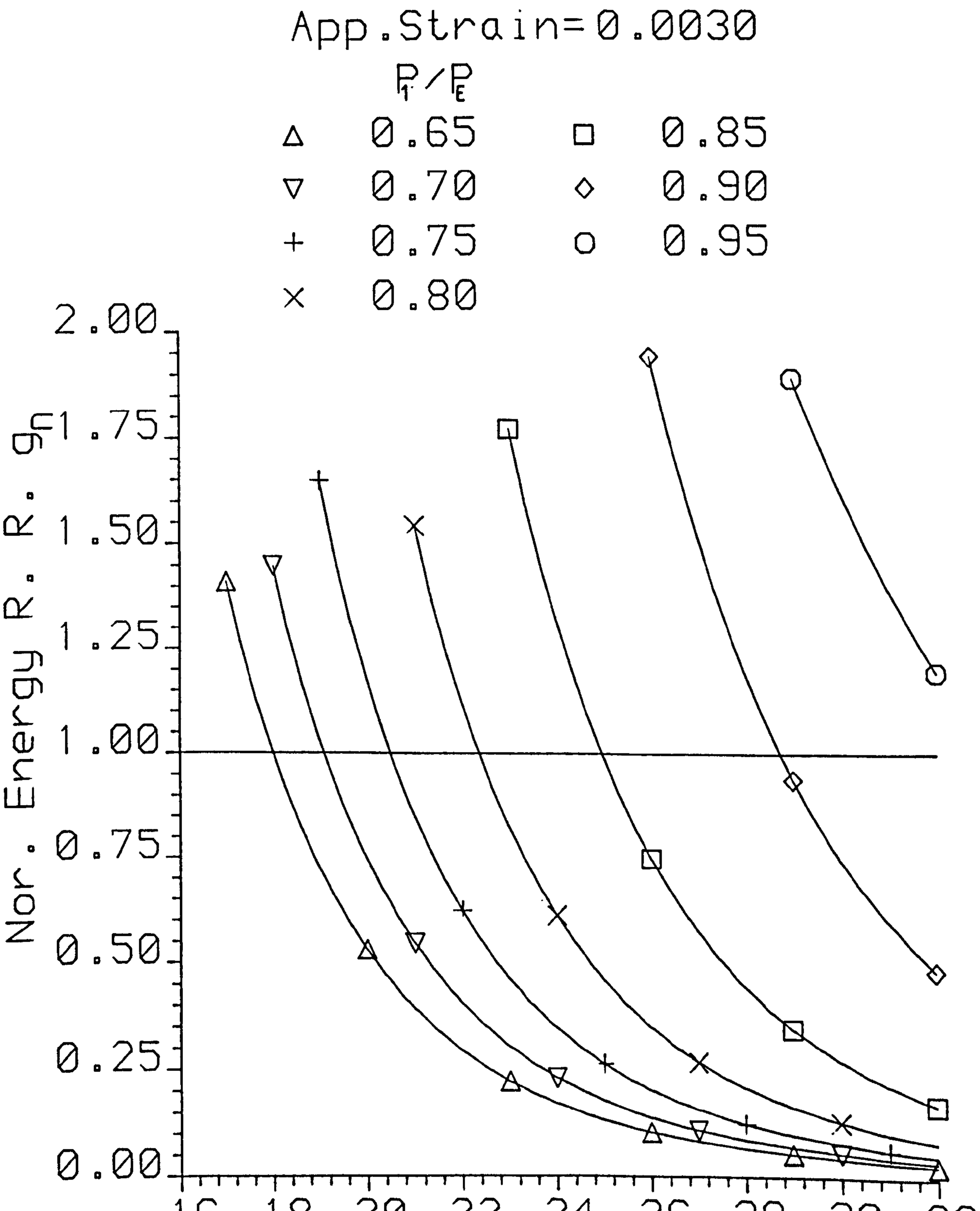

Fig.4.21 Nor.E.R.R. vs Blister Half Span Length

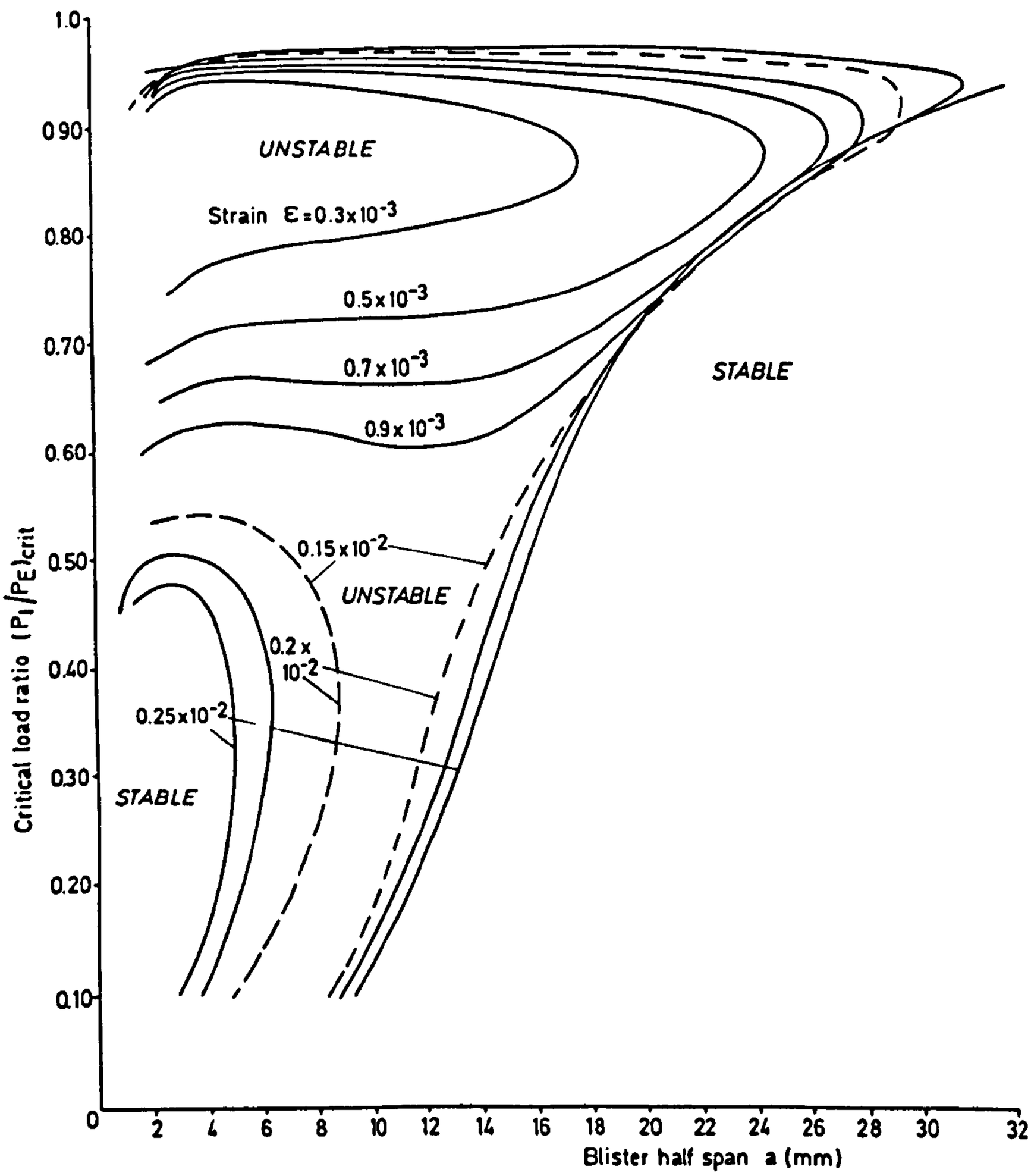

FIG. 4.22 CRITICAL LOAD RATIO vs. BLISTER HALF SPAN FOR VARIOUS APPLIED STRAINS

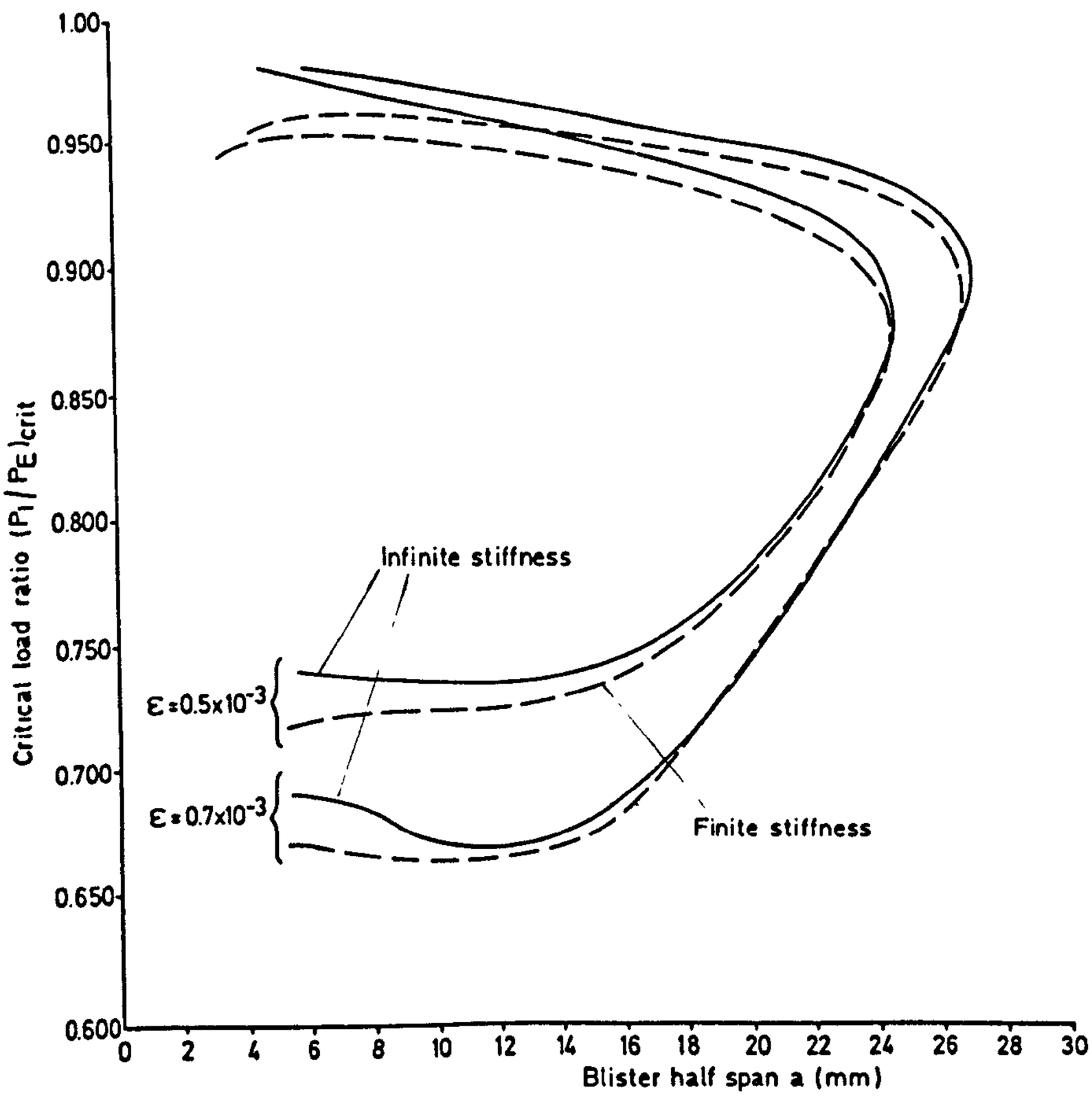

FIG. 4.23 EFFECT OF INFINITELY STIFF FOUNDATION ON CRITICAL LOAD RATIO

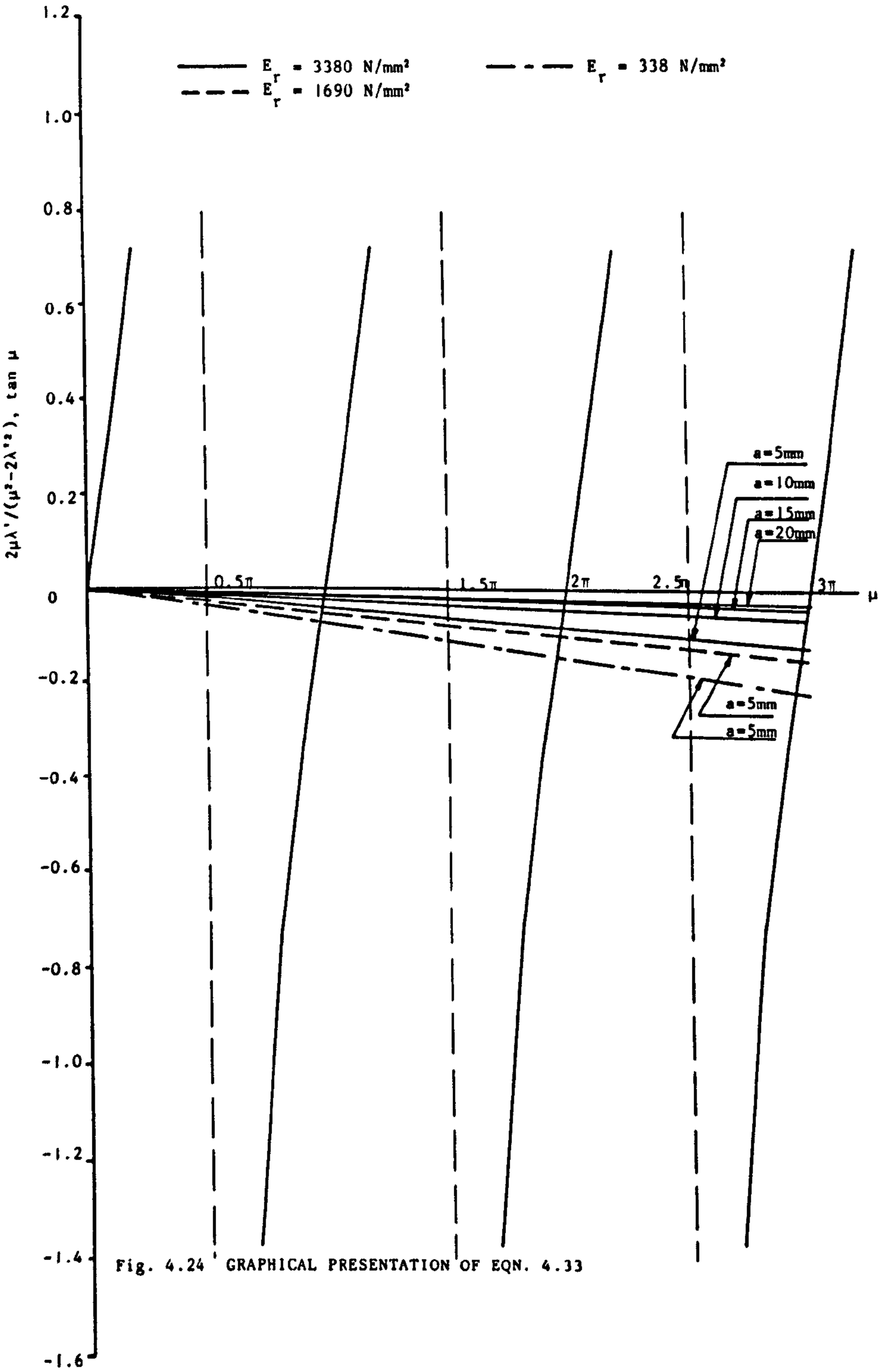

Fig. 4.24 GRAPHICAL PRESENTATION OF EQN. 4.33

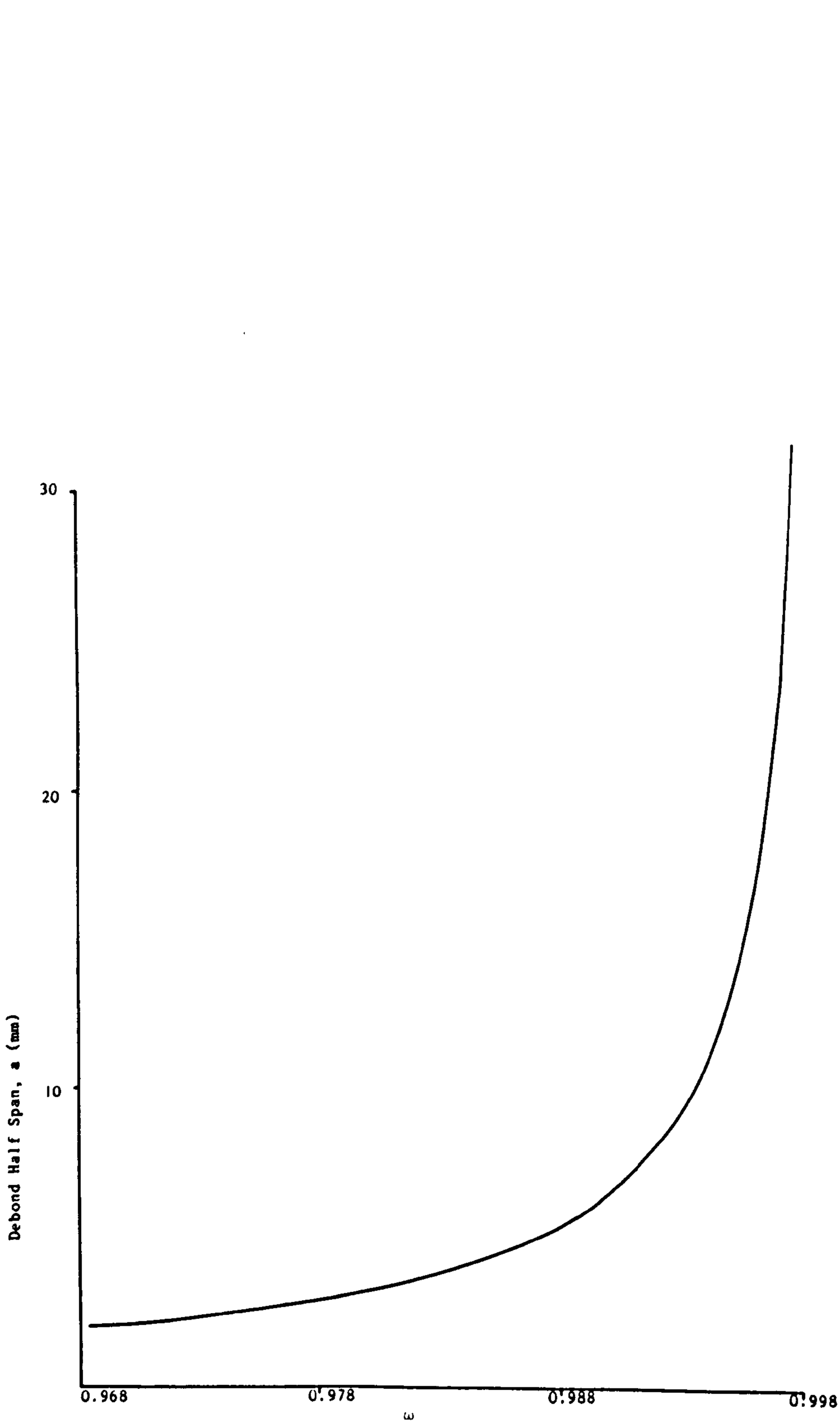

Fig. 4.25 REDUCTION FACTOR ω VS DEBOND HALF SPAN LENGTH a

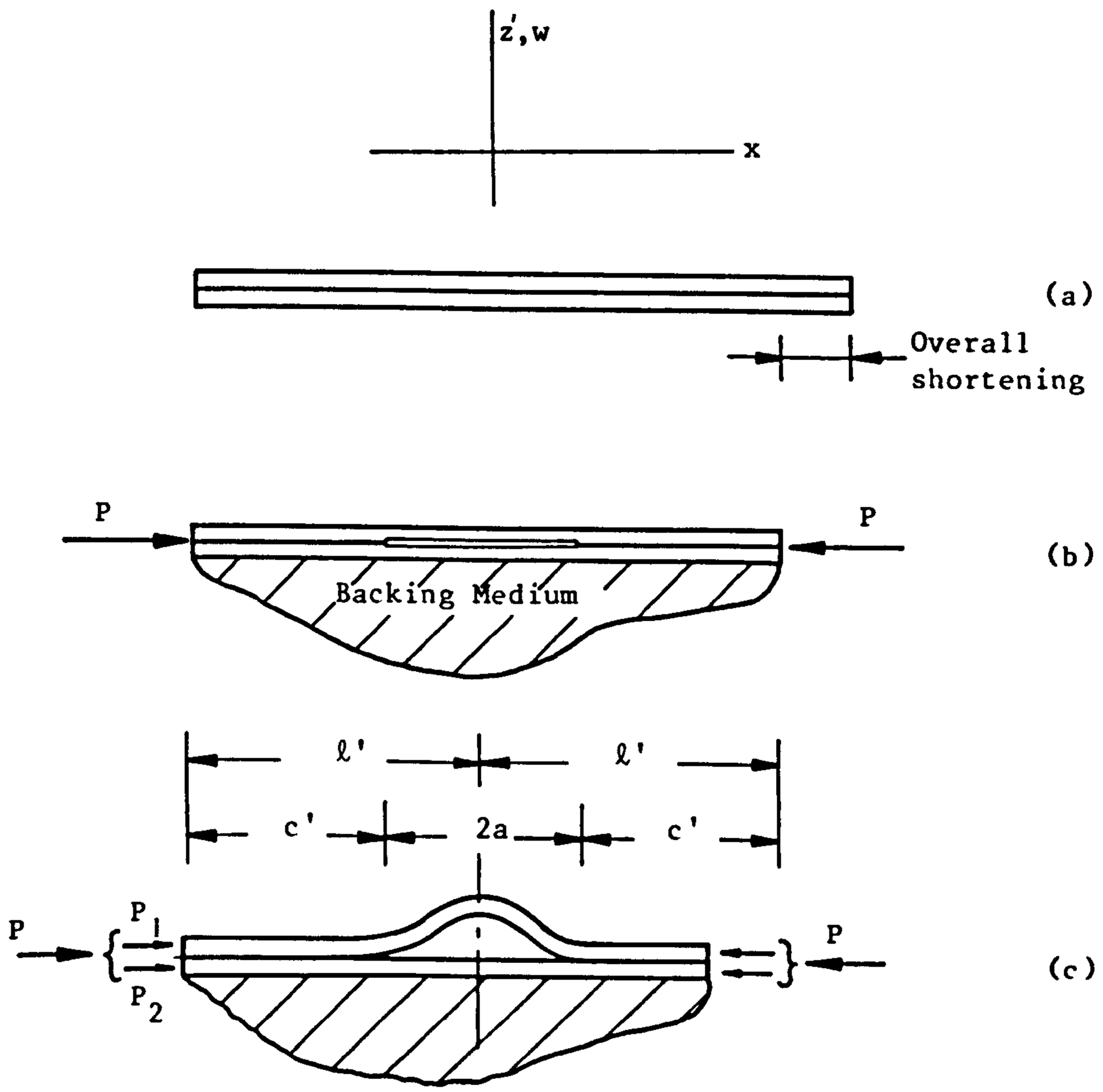

Fig. 4.26 BUCKLING DELAMINATION;

(a) Pre-loading Configuration,
(b) Pre-buckling Loaded Configuration,
(c) Buckled Debonded Layer.

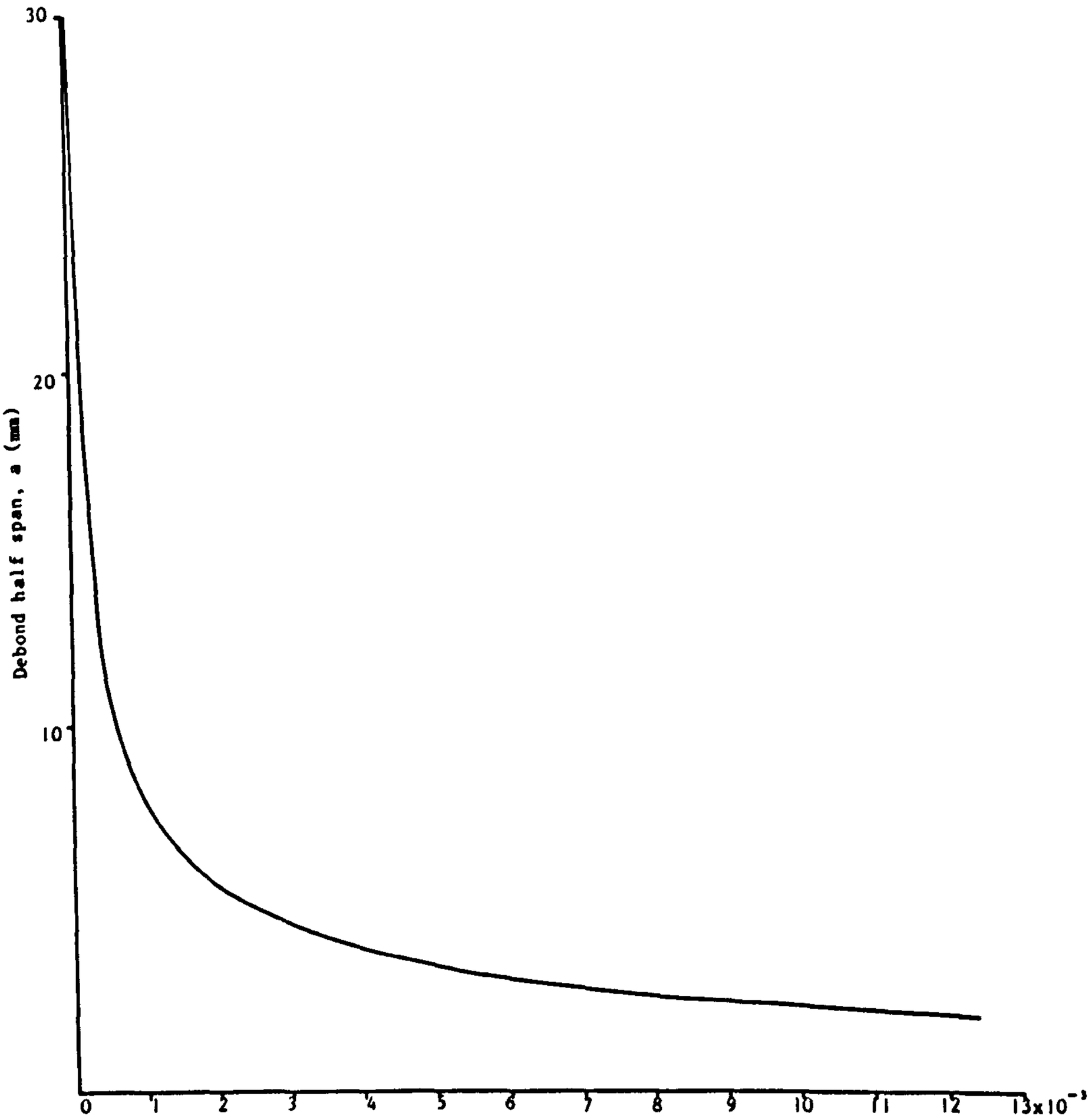

Fig. 4.27 THE RATE OF CHANGE OF THE FACTOR ω WITH DEBOND HALF SPAN LENGTH a

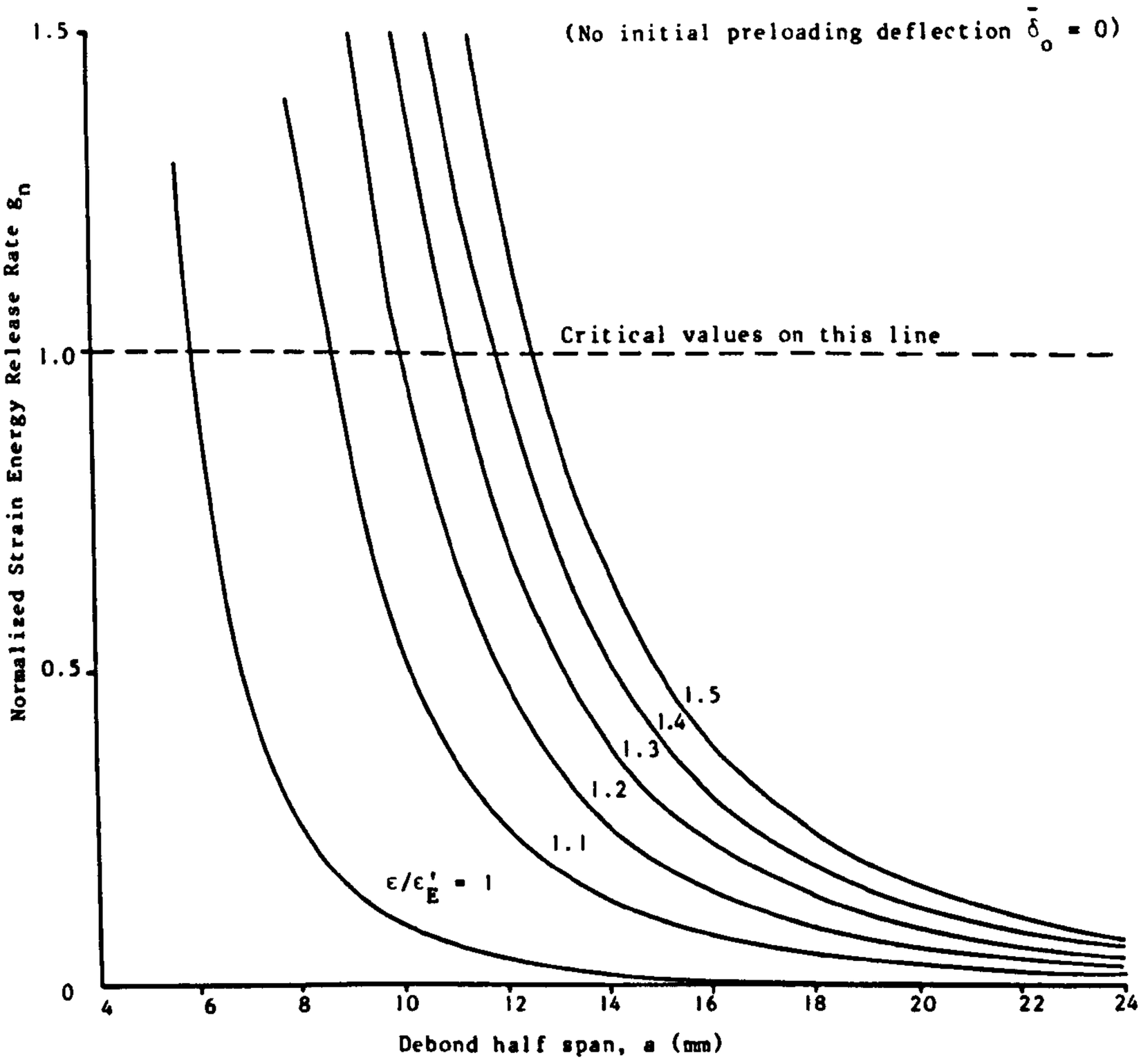

Fig. 4.28 NORMALIZED ENERGY RELEASE RATE VS DEBOND HALF SPAN FOR VARIOUS LOAD RATIOS

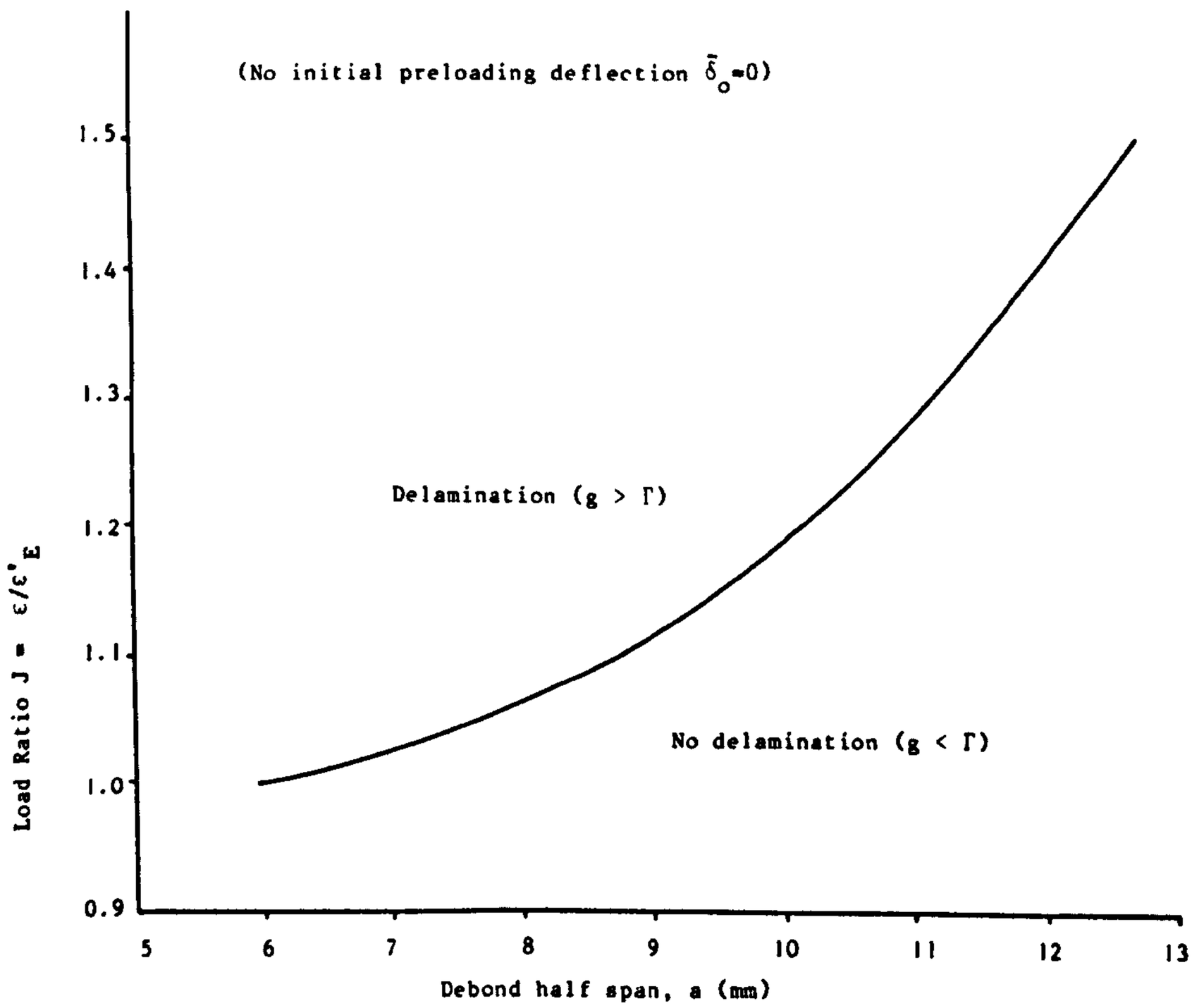

Fig. 4.29 CRITICAL LOAD RATIOS VS CRITICAL DEBOND HALF SPAN

C H A P T E R F I V E

EXPERIMENTAL STUDY OF DELAMINATION IN CFRP BLISTERED STRIPS UNDER IN-PLANE DIRECT COMPRESSION LOADING

5.1 INTRODUCTION

Delamination is one of the major obstacles in the way of exploiting the whole benefits from composite laminated plates. It has been a matter of major concern in engineering applications especially in the aircraft industry where safety is of paramount importance. Delamination is not associated with a particular type of loading but may occur under a myriad of load combinations including environmental effects. One of the most serious aspects of delamination is the interlaminar separation emanating from an initially debonded area as a result of direct in-plane loading. The seriousness of this problem (especially for an originally flat debond) originates from the fact that delamination may occur suddenly, and this may trigger off a sequence of events leading to the loss of the load carrying capacity and collapse of the laminated component. The aforementioned problem has attracted the attention of many researchers in recent years and already considerable theoretical work has been done. However, experimental verification of the problem especially in fatigue is very limited indeed. Whitcomb (Ref. 30) reports some static and fatigue data for a carbon fibre laminated layer bonded to 2024-T3 Al with EA 934 adhesive. The data in this work are not representative of interlaminar splitting because delamination was made to grow along the interface of the carbon fibre layer and the aluminium substrate. In an earlier work by Konishi and Johnston (Ref. 31), experimental data are

given for the growth of a buried circular delamination under static and compression-compression fatigue loading. The authors (Ref. 31) employed a specimen with a relatively small gauge length and used aluminium plates which were clamped to the central portion of the specimen to reduce column buckling. This arrangement may not reflect the actual behaviour of interlaminar delamination as pointed out in Ref. 80. However, Refs. (30) and (31) are the only sources known to the author which treat the delamination problem under in-plane compression-compression fatigue loading. Chai et al. (Ref. 91) have examined the damage behaviour in compressively loaded composite laminates subjected to low-velocity impact and report that the impacted region may buckle under the compressive load and unstable delamination ensue. Another experimental study is reported by Gillespie in (Ref. 87). It consists of a four-point static loading of a sandwich beam with carbon-epoxy laminated faces. The compression face contained a through-width delamination starter between the inner supports. The splitting characteristics from the above specimen are subject to the effects of the overall deflection of the sandwich and the influence of the inner supports.

From the aforesaid, it emerges that there is a need for a test specimen which is reliable, economical and most of all closely representative of the problem of delamination under in-plane direct compression. Part of this aim is hoped to be achieved in the work contained in this chapter. A test specimen, which is conformable to the theoretical model described in Chapter 4, is used here for the study of the delamination problem in static compression and compression-compression fatigue under constant amplitude loading. It consists of two CFRP strips, each with a through-width blister, glued on to each side of a honeycomb to form a sandwich. The ends of the

twin blister (TB) test specimen are resin moulded into mild steel loading fixtures.

5.2 TWIN BLISTER TEST SPECIMENS

5.2.1 Materials

The CFRP blistered faceplates were manufactured from Fibredux 914C prepreg, which is supplied by Ciba-Geigy Ltd., and has been used in earlier work presented in this thesis.

The honeycomb core material was an Aeroweb Type A1 non-metallic (Nomex) core, supplied by Ciba-Geigy. The core has a density of 64kg/m^3 with hexagonal small size cells having a distance across the sides of 3.2mm. It is desirable to select a core with small size cells because it gives uniform support to the facesheets and minimizes crushing during loading.

A Redux BSL 403 cold curing structural adhesive, supplied by Ciba-Geigy, was prepared, following the instructions of the manufacturer, and used for bonding the CFRP blister specimens to the honeycomb core.

5.2.2 Manufacture of Blister Plates, Honeycomb Cores and Loading End-fittings

Three unidirectional CFRP plates, each with a shaped central bulge stretching across the fibres, were fabricated using the vacuum/pressure bag method described in Appendix B, Section 1. Each plate measured a nominal 300mm x 250mm x 1mm, with a nominal cured fibre content of 60% by volume. The plates were laid up from eight 0° layers with the fibres running across the largest plate dimension. Eight strips of different widths were cut from a PTFE film (0.0125mm thick), stacked up, interlayered symmetrically along the central line across the fibres

halfway through the laminate thickness and cured with the laminate to give the desired initial blister shape as shown in Appendix C, Fig. C.1. This shape was calculated using the preloading deflection, $w_o = (\bar{\delta}_o/2)[1 + \cos(\pi x/a)]$, as shown in Appendix C. The caul plate, used in the cure process, was contoured over the hump made by the top four layers in bridging the stepped stack of PTFE sheets (see Appendix C). The three plates had different initial blister spans (2a = 20mm, 32mm and 48mm), therefore, different caul plates were used with each curing operation.

The CFRP plates were first trimmed off by about 10mm along the edges parallel to the fibre direction to rid the laminates of the likely poor material quality along these edges. There was no need for trimming along the sides perpendicular to the fibre direction because these sides were to be moulded into the loading end fixtures. Next, the laminates were cut into strips using a circular diamond saw to form the blistered faces of the sandwich specimens. Each strip measured 250mm in length by 30mm in width. The strips were cleaned from dust, degreased first with Acetone then in a Trichloroethylene solution, dried in blowing air and sealed ready for the gluing up operation.

The core for a twin blister sandwich was cut from the Aeroweb Type A1 honeycomb described in Section 5.2.1. It measured 250mm in length (=length of blister strip) by 40mm in width (in the direction of the cells) by 30mm in depth (=width of blister strip). At the end of the cutting operation, the core was blown with compressed air to remove dust and possible particles hanging along the end perimeters of the cells.

The loading end fittings were machined from mild steel and consisted of hollow cylinders (moulds) with flat sections for gripping purposes (Fig. 5.1). The internal surfaces of the cylinders were

roughed up to give good interlocking binding between the steel walls and the cured resin blocks. Although loading was compressive throughout, the latter step was necessary for the load controlled fatigue tests since each specimen was a part of the servoloop. At the end of testing, a combination of heat and mechanical means were employed to clean the end fittings ready for the next moulding operation.

5.2.3 Assembly of Test Specimens

A twin blister sandwich test specimen was assembled at two stages. In the first stage, CFRP blister strips were glued to the selected honeycomb. The second stage consisted of moulding the ends of the sandwich into the cylindrical load fixtures.

Stage 1: A certain amount of Redux BSL 403 adhesive was prepared according to the instructions of the manufacturer. One side of the sandwich was glued at a time. The adhesive was applied evenly on both the CFRP strip and the corresponding side of the honeycomb using a plastic spatula. The honeycomb bond face was kept inclined to prevent the adhesive paste from flowing down the cells. Next, the bond surfaces were brought together. Then the part was placed CFRP strip down over a flat foam board covered with a release sheet of PTFE coated fabric. As many specimens as required could be glued up at one time from one side of the honeycomb core and compactly arranged parallel to each other on the base foam board, separated by straight foam cushions to keep the glued parts aligned and prevent relative sliding before setting of the adhesive. The array of the newly glued parts was constrained along the outer components by steel bars, covered with another foam board and on top of the latter, weights were distributed to give a uniform pressure over the whole array. This was then left

undisturbed for 24 hours at room temperature before the weights were removed and the gluing up operation duplicated for the other sides of the cores. Enough time was allowed for the adhesive to achieve most of its strength before the sandwich specimens were cleaned ready for the moulding stage.

Stage 2: The sandwich specimen was held vertical with one of its ends centrally positioned inside the loading end fitting using a specially assembled rig with the help of a spirit level. An adhesive system (Epicote 162/Epicure 113) was mixed in the right proportions, taken to a thicker consistency by adding filler powder, left to settle in container for 15 minutes then was poured slowly into the cylindrical cavity of the end-fitting. The mould was left undisturbed for 12 hours. At the end of this period the specimen was removed from the rig and positioned upside down for moulding the other end as described above. A finished twin blister specimen is shown in Fig. 5.1. Two electrical resistance 6mm-strain gauges were glued on each side of the specimen as shown in Fig. 5.1, for measuring the direct strain, along one of the straight portions, and at the central point of the blister bulge. These strain gauges were coupled with dummy ones glued on to small pieces of a CFRP plate for compensation of temperature change. Two main features in the design of the twin blister test specimen were taken into account during manufacture. Firstly, no overall buckling should occur, and secondly the attached portions were made long enough to comply with an earlier assumption adopted during the solution of the differential equation of the beam on elastic foundation as described in Chapter 4. Long portions of the attached regions were also desirable in order to keep the delamination characteristics free from the influence of end constraints.

The initial blister delamination for each CFRP strip was marked

along the edges. These were then painted using a thin Snopake correction liquid so that easy and accurate delamination growth measurements could be obtained.

The four active strain gauges on the TB test specimen were wired together with the corresponding dummies to a digital Strain Indicator type 1526, manufactured by Bruel and Kjaer, to form two complete Wheatstone bridge circuits.

5.3 DELAMINATION STATIC TESTS

5.3.1 General Behavioural Aspects of TB Specimens During Tests

In all, four TB test specimens (Fig. 5.1) TB-S1, TB-S2, TB-S3 and TB-S4, with initial blister spans 2a=32mm, 48mm, 20mm and 20mm, respectively, were tested in static direct compression. The test specimen TB-S4 was made identical to TB-S3 after insufficient data were obtained from the latter. TB-S1 and TB-S2 had the same sandwich span ($2\ell'$=150mm). The other two specimens (TB-S3 and TB-S4) had instead a different span ($2\ell'$=120mm) because the CFRP strips were mistakenly cut shorter. However, this should have hardly any effect on the expected delamination data given that the earlier mentioned assumption was observed by allowing enough lengths for the attached portions of the outer layer.

The specimen shown in Fig. 5.1 was loaded in a 500kN Avery testing machine through flat Aluminium plates with their inner sides slotted for a partial insertion of the loading fixtures as shown in Plate 5.1. Two metric dial gauges attached to the machine bottom platen through magnetic based stands were set to measure the bulge-out displacements at the mid-spans of the debonded layers (Plate 5.1). The axiality of the applied load was checked by comparing the compressive strains in the straight portions from both sides of the specimen. Eventually,

sheets of Aluminium foil or blotting paper were distributed on top of the upper Aluminium plate to bring the above strains close to each other. Delamination growth was measured from both front and back of the specimen using an x20 Stereo Microscope.

The load was applied progressively in a predetermined sequence of intervals. At the end of each interval measurements were taken of the overall applied load, lateral deflections and the various strains (two applied strains in the attached portions and two strains in the middle of the bulge-out layers). The above sequence was continued until the occurrence of delamination which usually took place from one side at a time. The delamination growth was measured and the loading was increased until the next side delaminated and a new growth measurement was taken. From here, the loading sequence was reversed and a record of release data was obtained. The above described loading sequence and specimen response were typical for all the TB test specimens. Often there was observed a drop in the overall applied load level accompanying the onset of crack extension. This drop, however, was never substantial because the loss of stiffness at the delaminated face was immediately compensated by a load transfer to the inner layer of the face and also, to the opposite side of the specimen as was observed from a simultaneous increase in the applied strain of the latter. Perfect alignment remained undisturbed by the event of delamination, not surprisingly, overall instability never occurred with any TB specimen.

The mechanism of splitting growth tended to alternate between top and bottom of the original blister layer and between one face and the other of the sandwich. Only on a few occasions, where the extent of separation and consequently the bulge-out deflection were relatively large, did delamination extend simultaneously from top and bottom of

the same side. Often, the amount of crack extension at the front of the specimen was not matched exactly at the back side which pointed to an oblique crack front with respect to the edges of the CFRP strip. This latter behaviour is typical for relatively wide blister specimens, and can cause slightly varying through-width split deflection. Delamination, especially in the early loading envelopes was accompanied by the initial debond being snapped open with the crack running along the expected path.

Numerical results from Chapter 4 combined with other new analytical curves introduced here were compared with the experimental data described in this chapter.

5.3.2 Collection and Presentation of Data

In the previous subsection, the general behaviour of the TB specimens during loading was described. Apart from this, each specimen had its own characteristic set of results spread over the corresponding delamination growth range. The experimental results from each specimen are described and discussed here below.

(I) Specimen TB-S1. Four loading/unloading envelopes were performed on this specimen. The amount of delamination(s), order of occurrence, and site of delamination(s) corresponding to each load envelope are sketched in Fig. 5.2. The CFRP blister strips have been labelled with the letters "A" and "B" for easy identification and reference. For convenience, each load envelope has been indicated by a number and the primes represent the order in which the delamination occurred. For example, 3" refers to a crack extension which came second (the first occurred at the opposite side of the sandwich) during load envelope number 3, etc. This convention was also adopted for the

other test specimens.

The crack extension during testing of the TB-S1 specimen alternated between sides 'A' and 'B', and between top and bottom for the same side of the specimen where it tended to keep symmetry about the original blister centre line as shown by Fig. 5.2. Plates 5.2 and 5.3 show advanced stages of delamination for specimen TB-S1.

Figs. 5.3 through to 5.5 show the total compressive load versus the compressive strain (applied strain) in the straight portions of the CFRP strips during the four loading envelopes. Fig. 5.3, 5.4 and 5.5 represent the typical behaviour of the specimen where linearity is predominant up to the onset of delamination.

Both sides of the sandwich carry approximately the same proportion of the overall applied load, P_{ov}, especially along the loading lines as judged by comparing the two responses during loading and releasing. The central part of Fig. 5.3 portrays parallel loading/unloading lines which underlines equal load rates in both sides of the TB specimen. This latter behaviour however is not reversible as shown in the loading cycle which follows on immediately (Fig. 5.4). It is seen from Fig. 5.3 that, as far as the loading response is concerned, the load rate from side 'A' of the specimen is not affected by the delamination at the opposite side (side 'B'), suggesting that load transfer was mainly restricted to the delaminated strip from the outer to the inner layers. However, in most of the times, a small drop in the applied strain which accompanied delamination growth gave rise to a slight increase in the corresponding strain at the opposite side. Occasionally, the load rate in one face of the sandwich changed in favour of the other face as shown in Fig. 5.3. This behaviour was attributed to changes in the mechanism of load distribution inside the end-fixtures. It was found that the loss of specimen stiffness

resulting from delamination growth was only temporary, because the overall load regained its previous level at the onset of crack propagation after a slight retardation due to the clamping effect at the ends of the sandwich.

The tensile strains in the delaminated layers, as yielded by the centrally positioned strain gauges, are plotted versus the overall applied load in Fig. 5.6 for the first load envelope. These strains showed sharp drops, at the onset of crack propagation, proportional to the respective delamination growths. The lateral deflections, corresponding to the measuring points of the tensile strains, are plotted in Fig. 5.7 versus the total load, P_{ov}, for the same load envelope. It is seen from Figs. 5.6 and 5.7 that the instantaneous decrease in the tensile strain is accompanied by a corresponding increase in the lateral deflection. The graph in Fig. 5.7 shows a rather peculiar behaviour towards the end of the closing lines. The exact reason behind this is not clear, but it is thought it must be due to extraneous displacements. In fact, the measurements of the lateral deflections as given by the dial gauges were not satisfactory because these incorporated errors from various sources, mainly deformations from the end fixtures and backlash displacements in the stands of the dial gauges. Unfortunately, the latter were the only means available to the author for side deflection measurement. More accurate lateral deflection measurements may be obtained by a specially designed dial gauge fixture attached to the sandwich and no where else so that undesirable displacement components may be eliminated. Not attempt was made to design this dial gauge fixture because the main concern was the study of delamination versus loading. It was observed that at complete load release, the blister layer showed a slight residual deflection (Fig. 5.7). This deflection, however, accumulated over the loading

envelopes and could be clearly distinguished at the late stages of delamination.

Early splitting growths were characterized by unstable crack initiation and a loud cracking noise of about half a second duration. This behaviour subsided when the corresponding outer layer approached complete separation. In fact, by the end of the third load cycle, delamination was extensive, particularly, from side 'A' (Fig. 5.2 and Plate 5.3). This side came second in the order of crack initiation, where growth took place from the bottom and was extensive, slow (21mm extension in ∿10 seconds) and not audible. As a result, the delaminated region from side 'A' shifted its centre line of symmetry downwards by ∿9mm while symmetry was maintained at 'B' when the load cycle was completed. The same pattern of crack growth characterized the fourth load envelope. At this stage, permanent in-plane deformations were observed as the load was released as shown in Fig. 5.8 for the last load envelope. It is clearly seen from this figure that the gap between loading and unloading lines from either side of the specimen has widened compared with the previous load cycles. The above difference was thought to be partially due to the fact that the strain gauges were gradually being affected by the closing in of the delamination fronts.

The experimental delamination strain for each side of the sandwich is plotted versus the blister half span 'a' in Fig. 5.9 together with the corresponding theoretical prediction. The experimental 'a' values shown in Fig. 5.9 are average debonded extents from front and back of the CFRP strips. The calculated curves were obtained as follows:

(i) The set of curves, shown in Fig. 4.22, which represents the load ratio P_1/P_E versus the blister half span 'a' for various applied strains, is used with a similar set (Fig. 5.10) to construct

the set of curves shown in Fig. 5.11 in the form of the load ratio P_1/P_E versus the applied strain 'ε' for various values of 'a'.

(ii) Given the applied strain 'ε' and the blister half span, Fig. 5.11 may be used to find P_1/P_E, therefore P_1 is now known.

(iii) P_1, from above, is added to P_2, which can be calculated from the last formula in Eqn. (4.17), with $E_1 = E_2$, to yield the total applied load P as given by Eqn. (4.16).

(iv) With P at hand, and with the knowledge of the cross sectional area of the CFRP strip along the straight portions, and by simply taking the overall Young's modulus as E_1, an approximate applied strain can be calculated. It is said approximate, because the overall Young's modulus E_d given by Eqn. (4.21) should be used instead of E_1 to attain the exact predicted applied strain. However, this would have entailed the setting up of an iterative procedure, using a different set of curves for the total strain energy in the blister layer (U_t) versus a, each time a new pair ε and P_1 was selected for a particular 'a' value. This amount of calculation is beyond the real aim of the present chapter. Therefore, a straightforward approximate procedure, as described in the above steps, was chosen to evaluate ε. Better approximations, can be achieved provided the ratio a/ℓ' (refer to Fig. 4.1, Chapter 4) is small compared with the ratio c'/ℓ'. Certainly, the above problem should not have arisen if certain means had been available for measuring the in-plane load P_1 in the blister layer at the onset of crack propagation.

The predicted applied strains, as percentages of the respective experimental values, varied between 65% and 57% corresponding, respectively, to the first and third load cycles with an average value of 62%. With the previous approximation in mind, the average agreement may be judged as fair. The gap between experiment and calculation

widens as delamination grows bigger. This is thought to be due to the tacit approximation: accumulative effect in the initial deflection has been ignored in calculating the predicted values of the applied strain ($\bar{\delta}_o$=0.1mm has been used throughout the theory). Therefore, whilst early delamination growths could be better predicted the late growths were in error to some extent. Thus, in order to obtain the best from a twin blister specimen, more design curves are needed which include the effect of varying initial blister deflection.

The smooth curve to the right in Fig. 5.9 represents a stability front and has been constructed from the thresholds corresponding to the maximum values of 'a' at the maximum swing to right of the curves shown in Fig. 5.10 and similar others. It was experimentally observed that delamination growths to the right of the above curve were very stable as predicted by the theory. Moreover, this late delamination growth was not audible which is characteristic of stable crack propagation. The above mentioned smooth curve is actually a part of an orthogonal plane trace of a three dimensional surface with the third dimension represented by the load ratio P_1/P_E. However, the shown part of the complete curve does not depend on the load ratio P_1/P_E and represents an absolute boundary between unstable and stable crack growth regions.

By the end of the fourth load cycle TB-S1 had its side 'A' at the edge of complete delamination from the bottom. Moreover, it was evident, the strain gauges could be affected by the extensive separation of the outer layers. Therefore, no more data were taken from the specimen which was later loaded until the overall failure of the column. The sequence of events in which this way accomplished was as follows:

A steady load rate was applied to the specimen, at an overall load

of 19.4kN delamination started at the bottom of side 'B' and continued to grow slowly in this direction, under slightly increasing load, until complete separation of the bottom of side 'B' at 19.75kN. The overall load dropped to 19.3kN followed immediately by complete delamination of the top of side 'A'. The load was increased steadily until the column failed through direct fracture from the bottom of side 'A'. The load dropped from the failure level 21.73kN to 12.25kN. The final fracture was accompanied by a sharp 'bang' and left the column in the configuration shown by Plate 5.4. This type of failure was attributed to elastic buckling and fracture of the fibres combined with matrix shearing as described in Ref. 92. The bulge-out shapes remained at complete load release indicating that significant plastic deformations preceded the final failure.

The use of theoretical curves, calculation of the predicted applied strains and the modality of data presentation have been detailed in the course of the above discussion, and are tacitly adhered to throughout the remainder of the section.

(II) Specimen TB-S2. The delamination data for this specimen were collected from five load envelopes. The sequential crack accumulation is quoted along the sandwich span and shown in Fig. 5.12 by the front and back views of the specimen. Here the pattern of splitting growth is different in certain aspects from that seen for specimen TB-S1. For instance, the pattern of crack growth alternation between top and bottom of the same side and between the two sides of the specimen was broken. This, however, may be explained in that, the initial debonded areas were relatively large, a fact which was translated into large bulge-out deflections and, as mentioned earlier, favoured simultaneous top and bottom crack growths. One aspect shown in Fig. 5.12, which was not much in evidence for specimen TB-S1 until the last load envelope,

is that the delamination growth is more extensive from the front than the back of the specimen. Excluding load eccentricity because the column was perfectly aligned and twisting (because this was unlikely given the axiality of the overall load) the answer points to preferential sites for the delamination growth caused by different interlaminar strengths.

The audibility of cracking for the first two load cycles was attenuated compared with the previous case for specimen TB-S1. As for the rest of the load envelopes, crack audibility got weaker and weaker as the corresponding debond increased in length. Delamination was more stable than the TB-S1 case, and that stability increased as the crack grew longer. In fact, during the last three load envelopes, the splitting increased slowly in proportion to the applied load. In the course of crack growth no load drop (only hesitation) was noticed throughout the testing session of the specimen. The uneven delamination growth as shown in Fig. 5.12 might have contributed to the stable tendency of split growth. Simultaneous debond extensions from both sides of the sandwich took place in load envelopes 2 and 3. This behaviour was likely enhanced by very good load axiality combined with relatively large bulge-out deflections and blister spans, as will be evident soon from the related load-strain responses. Plate 5.5 shows as interesting feature of the interlaminar interface from side 'A'. The central dark region across the separated outer and inner layers is the original debond (2a=48mm). This is followed outwards by a shiny grey region which represents the delamination growth over the five load envelopes. The extreme small areas are distinguished from the delamination region and were the only attached portions when the two layers were separated for inspection. Benbow (Ref. 37) argues that freshly cracked specimens of plastics exhibit colour effects on

surfaces of stable cracks. He explains that these second-order colours are seen when the surface is viewed by reflected light and are probably caused by interference. In fact, Plate 5.5 was produced by a tentative combination of the right illumination and angle of view. The above effect was not so noticeable for the other test specimens described in this section which backs the explanation that stable crack propagation is at the root of the colour feature.

Figs. 5.13 through to 5.17 represent the load-applied strain response for the five load envelopes. These figures are characterized by a good linear behaviour up to the onset of delamination growth. Also, the rates of load and load release, wherever shown, are almost the same, which demonstrate the axiality and balanced distribution of the overall applied load.

The tensile strains in the middle of the blister layers are shown in Fig. 5.18, for the first load cycle, where delamination during this cycle was allowed to grow only from side 'B' before the load was released. Consequently, most of the load line from side 'A' was traced back by the release line as seen in the figure. A slow starting response was revealed by side 'A'. This behaviour was also noticed for both sides of the specimen TB-S1 (Fig. 5.6), and is thought to be related to the adhesive links offered by the interposed PTFE sheets. In fact, for all the test specimens, it was observed that such behaviour marked the start of the first load envelope and attenuated when the corresponding blister layer popped out open giving rise to a sharp increase of the corresponding lateral deflection as depicted in Fig. 5.19.

The experimental and calculated critical applied strains are plotted in Fig. 5.20 versus the blister half span. Fig. 5.21, which represents the critical load ratio P_1/P_E versus the applied strain for various

'a' values was used, in exactly the same way as for TB-S1, to produce the prediction graphs given in Fig. 5.20. The experimental strain increases steadily with the increasing of the blister half span (Fig. 5.20) and tends to be constant at around 1900με. The calculated strains varied between 62% and 55% of the experimental values corresponding, respectively, to the first and fourth load cycles. These percentages, compared with the 65% and 57% for specimen TB-S1, show a reduction in the predicted values when larger blister half spans are considered. Accumulative initial deflections have also here the effect of widening the gap between experiment and calculations.

Fig. 5.22 shows the load strain response for side 'A' while the specimen was loaded to failure. The figure is characterized by a good linear behaviour up to the final failure of the column, where almost complete delamination from both sides of the specimen was immediately followed by a direct fracture from one side as was previously observed for specimen TB-S1. The state of delamination and lateral deflection just before the final collapse is displayed by Plate 5.6. It is noted that the uneven delamination extent from both sides of the specimen, the outer layers being completely separated from top, has shifted the maximum lateral deflections upwards.

(III) Specimens TB-S3 and TB-S4. Relatively limited delamination data were obtained from each one of these two specimens because of problems with load eccentricity, brought about by relatively short extremities (~15mm) being moulded into the loading end-fittings. This was imposed by the use of shorter strip faces for the sandwich, as a result of a mistake in cutting the CFRP board. Consequently, often difficulties were encountered in stabilizing the applied load because it transferred in turn between the two sides of the specimen before the

column settled and a stable loading regime was reached. This was achieved sometimes at the expense of the specimen overall axiality. In fact, while the sandwich was perfectly straight it tilted noticeably sideways as a result of deformations in the end-fittings. The overall lateral deformations for the two specimens are reflected in Figs. 5.23 and 5.24 of the lateral deflections, measured in the middle of the blister layers, versus the total applied loads. The same pattern of behaviour is echoed in Figs. 5.25 and 5.26 where the strains in the middle of the bulge-outs are plotted versus the overall applied loads. It is seen from the latter figures (Figs. 5.25 and 5.26), that the strains in the middle of the bulge-out portions often take on compressive values at the start of the load cycles. This is partially because the initial blister spans are relatively small, apart from contributions from overall lateral deformations, as shown in Fig. 5.26.

The extent of delaminations for specimens TB-S3 (over two load cycles) and TB-S4 (over four load cycles) are sketched, respectively, in Figs. 5.27 and 5.28. The figures show generally non-uniform splitting growth from the same side (e.g. side 'B' in Figs. 5.27 and 5.28). Moreover, the specimens tended to split more from one side than the other or even from one side only as in the case of specimen TB-S3 (Fig. 5.27). The above behaviour is thought to be caused mainly by the eccentricity of the overall applied load.

The applied compressive strain versus the overall load is plotted in Figs. 5.29 through to 5.34 for each of the six load envelopes (two, from TB-S3, and four, from TB-S4), where delamination loads and average blister spans are also quoted in the figures. The central regions of the graphs are characterized by a good linear behaviour while the start and the end are generally marked by unsettled behaviour due to load transfer from one side to the other side within a certain

specimen. This load transfer, as was mentioned earlier, is enhanced by deformations in the end fixtures. However, the two specimens combined provided overall good delamination results as described in the following paragraph.

The experimental applied strain together with the corresponding predicted value, at the onset of crack propagation, are plotted versus the blister half span in Fig. 5.35. The calculated curve was produced through the use of the load ratio P_1/P_E versus the blister half span 'a' (Figs. 5.36 and 5.37) to construct the graphs shown in Fig. 5.38 of P_1/P_E versus ε for several 'a' values. These latter curves were then used to calculate the applied strains as described for the other specimens.

The calculated applied strains, as percentages of the corresponding values on the experimental curve, varied between a very good 85% for the first delamination growth (Fig. 5.35) to a fair 60% for the last crack propagation. Again the trend of widening gap between calculation and experiment as the delamination grew longer is clearly shown in Fig. 5.35. This, as explained earlier, was thought to be mainly due to accumulative effects in the initial blister shape. However, other causes, such as fibre bridging, might have been equally responsible.

Splitting, especially in the early stages, was characterized by a jumpy and audible unstable growth. In fact, these relatively small initial 'a' values are found well inside the unstable zone predicted by the theory (e.g. Figs. 5.36 and 5.37) and may give rise to a sudden and extensive damage once the critical conditions are met. However, the unstable behaviour gradually attenuated towards the late crack extensions where a quasi-stable delamiantion was observed.

The final specimen failures were similar to those for the previous cases. Specimen TB-S3 failed by direct fracture from side 'B' when

this was almost completely delaminated. Specimen TB-S4 was loaded while the extent of splitting was as shown in Fig. 5.28. When the load reached 19.4kN delamination took place from the bottom of side 'B' and continued to grow as the load was increased progressively. At 19.75kN, side 'B' was completely separated followed by total delamination from the top of side 'A'. Finally, the column collapsed at 21.725kN (Plate 5.7) through a combination of overall separation of the outer layers, and fracture at the lower end fixture by what was thought to be due to the developing of high bending stresses at the lower end of the specimen, created by load eccentricity.

The critical applied strain from experiment and prediction, for the first delamination growth in all the test specimens, is plotted versus the initial blister half span in Fig. 5.39. It is clearly seen that once the accumulative effects in the initial blister bulge-out are excluded, a reasonable agreement between theory and experiment is achieved.

5.4 DELAMINATION FATIGUE RESULTS AND DISCUSSION

5.4.1. Specimens and Pretesting Set up

It was seen from the previous section that twin blister (TB) test specimens proved to be a suitable means for the study of static delamination under direct compression loading. In the present section, the splitting growth in other TB specimens subjected to repeated compressive loads (fatigue) will be described. It must be understood that whenever a reference is made simply to a maximum or a minimum the word 'compressive' is tacitly implied.

Four test specimens TB-F1, TB-F2, TB-F3 and TB-F4 with, respectively, an initial blister span (2a=20, 32, 32, and 48mm), were made for the fatigue study in this section. The columns had the same

length ($2\ell'$=150mm) except TB-F1 which had ($2\ell'$=100mm). The other dimensions are shown in Fig. 5.1 and are common to all the specimens. In a similar fashion to the static case, each sandwich had its sides designated by the letters "A" and "B" for reference and identification.

The fatigue TB test specimen was loaded in the Instron servo-hydraulic testing machine as displayed in Plate 5.8. Prior to the start of the test, the column was vertically aligned with the help of a spirit level. The two strain gauges on both sides of the specimen were connected to two Strain Indicators type 1526, and the x20 Stereo Microscope was set for measuring delamination growth from the front of the specimen (a magnifying glass was used for back measurements). At regular intervals, the alternating load signal was disconnected and the overall load taken up to its maximum limit. At this stage, lateral deflections from both front and back were measured at the centre of the original debond span for each side of the specimen using a dial caliper. At the same time, the total bulge-out of both sides combined of the sandwich was also measured. This latter information was added so that secondary lateral deformations other than those directly associated with delamination could be appreciated.

A sinusoidal compression-compression constant amplitude loading, at a frequency of 6Hz, at a mean load level of 5kN was selected for all the specimens. Temperature related time-dependent effects were neglected, given that the frequency was reasonably small. The cycling amplitude, minimum and maximum of the alternating compressive load and maximum of the compressive load at the onset of static crack extension, are presented in Table 5.1. Plate 5.9 depicts a typical fatigue delamination growth. Despite the extensive splitting, as seen from the plate, the lateral deflections were not as large as in the static case. However, the bulge-out from both sides increased and

decreased in phase with the loading frequency.

A rather curious behaviour was observed, with all test specimens, when comparing the maximum strain during cycling, and the corresponding maximum for the same total load while the alternating signal was disconnected (these two strains will be referred to, respectively, as maximum dynamic and maximum static). In fact, for a certain side of the tested specimen, the maximum dynamic strain was lower than the maximum static value. In other words, even though the machine was cycling between the preset upper and lower load limits the sides of the specimen failed to match the respective shares of the load, which would be recorded when the machine was stationary with the specimen under the maximum load condition. The ability of the sandwich to respond to the full extent of the load amplitude was influenced by the frequency, the load amplitude and the damping effect of the end fixtures. Therefore, in order to appreciate the maximum amount of load, carried by each side of the sandwich while cycling, the maximum compressive strains were frequently monitored (Tables 5.2, 5.3 and 5.4). The effect of frequency on the dynamic strain response is represented by the typical behaviour shown in Fig. 5.40, drawn for specimen TB-F1. These linear graphs show how the increase in frequency is proportionally responded to by a decrease in dynamic strain value. Both sides of the specimen exhibit a similar response as seen from the parallelism of their respective graphs which points to the overall damping of the end-fixtures as the main cause behind this behaviour. This truncated response occurred because before the strain reached its maximum value the load had already been relieved as the machine ram went down towards the bottom of its stroke.

5.4.2 Presentation of Fatigue Data and Discussion

(I) Specimen TB-F1. The data presentation given here in the course of discussing the results for this specimen is common to all other cases.

The above specimen totalled 1050345 cycles, during which only side 'B' accumulated delamination growth with side 'A' remaining intact. This was thought to be a direct result of more load taken by side 'B' than side 'A'. In fact, at the start of the test the former had a maximum dynamic 710 μ-strain compared with 385 μ-strain for the latter. These values increased after 600000 cycles to, respectively, 728 and 425 μ-strain, and were matched by similar increases in the respective minimums and mean load levels. However, this behaviour could not be associated with a certain trend because it lacked consistency as the strains increased at times and decreased at other times as will be shown for the other specimens. One possible explanation was that the shaking effect of cycling could have continuously altered the state of stress and consequently the strain distribution across the faces of the sandwich, although some other causes might have been responsible as well. Nevertheless, the aforementioned strain variations were relatively small, therefore, an average strain value was accepted, with good approximation, to represent the true in-plane load of a certain side of the tested specimen, provided the material response was still elastic and linear. This should be the case given that similar specimens were characterized by an overall good linear elastic behaviour up to the onset of static delamination.

A semi-log plot of the blister span versus the number of cycles is shown in Fig. 5.41 for side 'B' of specimen TB-F1. These graphs are characterized by an overall linear behaviour between 100,000 and one million cycles. Delamination growth started from the back of side 'B'

and was followed later by the front where this was marked by a higher rate of crack growth until it equalized the splitting extent from the back at around 100,000 cycles. Beyond this point a nearly uniform and quasi-linear delamination growth was achieved. The crack propagated in almost equal amounts above and below the centre line across the original blister layer for both the front and the back of the bulge-out. The rate of debonding growth was higher at the start of the test and gradually attenuated before it stabilized at around 100,000 cycles. Crack extension was very stable, slow with no jumping and not audible. If the explanation for the colour on the fracture surface is accepted as a sign of stable crack growth then the fracture surface, shown in Plate 5.10 for side 'B' of specimen TB-F1, can be regarded as a typical example. The progressive crack propagation is clearly indicated by relatively bright beach markings following outwards from the initial split distinguished by the central dark area. The fatigue markings, which are separated from the static fracture regions by the crescent shaped lines, give information about the shape of fatigue crack fronts at various stages of growth. The fatigue delamination surface was found to be smoother when compared with the outer regions which were split by hand.

Figs. 5.42 and 5.43 display, respectively, the specimen overall blister bulge-out and side 'B' front and back lateral maximum deflections, versus the number of cycles, while the specimen was under the total maximum compressive load (8kN) with the fatigue signal disconnected. These figures, however, are relative to the point of zero load at the start of test. Therefore, in order to assess the effect of cycling on the lateral deformations, it is advisable to take measurements relative to the starting point on each curve. The same convention will be adopted also for the other specimens. It is seen

that the curves, especially those in Fig. 5.43, are reflecting the image of the graphs shown in Fig. 5.41 for the blister span versus the number of cycles. In comparing Figs. 5.42 and 5.43 an increase of the total bulge-out (Fig 5.42) over the corresponding values in Fig. 5.43 is noticed beyond 500000 cycles. Otherwise, the lateral deformations as given by one figure are approximately representative of those from the other, indicating that lateral secondary displacements, are so small as to be contained within the precision of the measuring device (± 0.05mm).

II) Specimens TB-F2, TB-F3 and TB-F4. Fatigue delamination data for these specimens are shown in Figs. 5.44 through to 5.48. For clarity, each figure, except for specimen TB-F2, is associated with a complete set of data from either sides of one of the specimens. An approximate linear behaviour is observed beyond 100000 cycles, where the rate of crack increase with the number of cycles increases as the overall compressive applied load increases. Another common feature which was observed earlier for TB-F1, is the nearly equal rates of crack extension from the front and back of the same side of a certain specimen. Occasional sharp jump in crack propagation took place as observed, for example in Fig. 5.44 for the front of side 'A'. This behaviour might have been due to a batch of weak interlaminar bonds, therefore, it can be ignored when calculating the rate of crack extension.

Plate 5.11 displays the fatigue delamination surface for side 'A' of specimen TB-F2, with the inner edges representing the back of this side. It is interesting to see that the beach markings started from the front and worked their way inwards and logitudinally, however, without reaching the inner edges (back of side 'A'). This is confirmed

by the rate of crack growth shown in Fig. 5.44, where splitting was continuously accumulating from the front of the specimen while its back remained virtually undelaminated save an initial slight growth.

Another interesting fatigue fracture surface is offered by Plate 5.12 for side 'B' of specimen TB-F3. This specimen accumulated the largest number of cycles which is reflected by many beach markings. These were initially horizontal then became gradually oblique showing more growth rate from the front than from the back of the specimen. Again the above observation is echoed in Fig. 5.45 where equal crack growths were measured from the front and the back of the specimen up to 100000 cycles then the rate of growth changed being slightly larger from the front. The beach markings on side 'A' of specimen TB-F3 were observed to be mainly perpendicular to the fibre direction which is a sign of uniform crack extension as seen from Fig. 5.46. Similar behaviour was found for specimen TB-F4 as seen from Plate 5.13 and confirmed by Figs. 5.47 and 5.48. As was observed for specimen TB-F1, the delamination fatigue surfaces were smooth when compared with the static case. The lateral deformations for the above discussed specimens are given versus, N, in Figs. 5.49 through to 5.56.

III) General to all Fatigue Specimens

In general, the influence of N on the behaviour of the lateral deflection is mainly through the increase of crack length with load cycling. This fact is often highlighted by the shape of the various deflection curves when compared with that for 'a' versus 'N'. The graphs for the lateral deformations and blister spans can be used to correlate their rates of growth with respect to 'N' over a certain range of the latter.

A common characteristic to all the fatigue fracture areas

displayed, is the tendency of the aforementioned beach markings to concave outwards in the direction of crack growth, especially in those cases where the crack propagated uniformly (e.g. Plate 5.10). This behaviour has a simple explanation: fatigue delamination growth starts first at the edges then it gradually propagates inwards towards the centre of the specimen.

The side 'A' and 'B' average slopes of the linear portions of 2a versus N graphs represent the crack growth rates for the same regions. These are plotted versus the fatigue maximum total compressive load in Fig. 5.57. It is clearly seen from this figure that the net effect consists of higher crack growth rates corresponding to higher compressive maximum loads and therefore higher load amplitudes. This same conclusion is generally evident from Fig. 5.58 of log ε versus log [d(2a)/dN]. The two points not laying on the curve are those for specimen TB-F3. In fact, this case was characterized by the highest maximum applied strain difference between its two sides among the rest of specimens with delamination on both sides. However, when viewed in the net damage context the above mentioned points will be represented by one, consistent with the rest of the data shown in Fig. 5.58 and consequently with the net behaviour as depicted in Fig. 5.57.

5.5 CONCLUSIONS

Twin blister specimens and test procedures have been given for the study of delamination characteristics under static and fatigue in-plane compressive loading. The TB specimens offered several advantages, e.g. they were self supporting in that no compression guides were needed with subsequent elimination of unwanted effects. They are economical and time saving because sufficient data could be obtained

from a small number of such specimens and they were found to be reliable with relatively stable delaminations. The main conclusions from the test programme described in this chapter are summarized below.

(a) Static tests

(i) Four TB specimens were tested in static direct compression. Shorter initial blister spans were marked by unstable and audible crack growth, while relatively long spans yielded stable or quasi-stable delamination extension.

(ii) Splitting growth tended to alternate between top and bottom of the original blister layer and between one side and the other of the same sandwich.

(iii) Often, the crack extension from one edge was not matched exactly at the opposite edge of the same face which resulted in an oblique crack front with the longitudinal direction.

(iv) Graphs representing load-strain and load-original blister mid-span lateral deflection were given and discussed for each specimen.

(v) The compressive applied strain was mainly linear up to the onset of crack propagation.

(vi) Experimental delamination strain was plotted versus blister half span and compared with a theoretical prediction for each individual specimen side.

(vii) The predicted delamination strain varied between 62% and 85% of the experimental value for the first delaminations and the agreement decreased for subsequent splitting as a result of the effect of an accumulation in the initial deflection of the debonded layer.

(viii) The average agreement between theoretical and experimental applied compressive strains has been found to be around 70% for the first crack growths.

(ix) The delamination surfaces showed colour reflection for

stable crack growth which showed that splitting was resin dominated.

(b) Fatigue tests

(i) Four TB specimens were tested in fatigue direct compression at the same mean load level but with various load amplitudes. Delamination growths and lateral deformations have been given versus the number of cycles and discussed for each specimen.

(ii) Splitting exhibited very stable crack growth and showed mainly linear behaviour beyond 100000 cycles when plotted versus the number of cycles on a semi-log scale. These linear regions were used for measuring the rate of delamination growth for the same regions.

(iii) Fatigue crack growth was characterized by beach markings on the fracture surfaces.

(iv) The beach markings tended to concave outwards in the direction of crack growth. This was because fatigue splitting started first at the edges and propagated gradually inwards with load cycling.

(v) The maximum value of the overall fatigue load has been given versus the average rate of crack growth for each specimen. It is shown that the higher the maximum value of fatigue load (and consequently the load amplitude) the higher is the overall rate of damage growth.

(vi) The maximum value of dynamic strain in each side has been plotted versus the corresponding delamination growth rate. This result compared favourably with that in (v).

TABLE 5.1 TEST PARAMETERS FOR TB FATIGUE SPECIMENS

Specimen	Initial blister half span a (mm)	Static overall applied load at delamination (kN)*	Mean load level (kN)	Overall compressive alternating load (kN) Max. load	Min. load	Load Amplitude Max.load Min. load (kN)
TB-F1	10	14.30	5.0	8.0 (56%)**	2.0	6.0
TB-F2	16	14.60	5.0	7.0 (48%)	3.0	4.0
TB-F3	16	14.60	5.0	8.75(60%)	1.25	7.5
TB-F4	24	11.65	5.0	9.5 (82%)	0.5	9.0

* Average delamination loads from both sides of the specimen.

** ( ) Max. of alternating load as a percentage of the static delamination load.

TABLE 5.2. STRAIN VARIATION WITH THE NUMBER OF CYCLES FOR SPECIMEN TB-F2.

No. of cycles, N	Side 'A' Max. dynamic μ-strain	Side 'A' Mean μ-strain	Side 'B' Max dynamic μ-strain	Side 'B' Mean μ-strain
0	605 (744)	-	663 (822)	-
20000	597	-	657	-
55370	584 (731)	526	641 (807)	578
96090	583 (728)	521	643 (806)	587
328000	592 (731)	529	658 (817)	599
400000	576 (721)	506	646 (808)	573
500000	569 (711)	505	640 (803)	570
568000	572 (713)	505	647 (811)	570
614640	453 (603)	398	838 (1005)	759

(.....) Max. static compressive strain.
Ave. max. dynamic compressive strains for sides 'A' and 'B' are; respectively, 581 μ-strain and 647 μ-strain.
Max., mean and min. compressive loads = 7kN, 5kN and 3kN, respectively.
f = 6Hz.

TABLE 5.3 STRAIN VARIATION WITH THE NUMBER OF CYCLES FOR SPECIMEN TB-F3

No. of cycles, N	Side 'A'		Side 'B'	
	Max. dynamic μ-strain	Mean μ-strain	Max dynamic μ-strain	Mean μ-strain
0	642 (884)	504	698 (963)	544
3000	660 (898)	524	715 (977)	566
5000	646 (896)	516	699 (970)	584
10000	644 (897)	524	705 (976)	573
20000	649 (902)	540	705 (983)	579
32000	654 (900)	532	718 (994)	601
44000	653 (904)	534	735 (1018)	613
75000	658 (901)	536	740 (1016)	631
219680	666 (952)	536	777 (1035)	652
300000	607	515	715	616
400000	646	-	762	-
450000	636	544	746	636
700000	648	551	758	652
770000	670	536	788	638
850000	651	544	767	633
892000	658	539	774	636
1200000	667	558	781	654
1395000	645	542	748	650
1765000	674	539	781	641
1900000	687	-	781	-
2250000	687 (957)	610	787 (1091)	697

(....) Max. static compressive strain
After load release the specimen showed 56 and 107 permanent compressive μ-stains, respectively, from sides 'A' and 'B'.
Ave. max. dynamic compressive strains for sides 'A' and 'B' are, respectively, 654 μ-strain and 747 μ-strain.
Max., mean and min. compressive loads = 8.75kN, 5kN and 1.25kN respectively.
f = 6Hz.

TABLE 5.4 STRAIN VARIATION WITH THE NUMBER OF CYCLES FOR SPECIMEN TB-F4.

No. of cycles, N	Side 'A' Max. dynamic μ-strain	Side 'A' Mean μ-strain	Side 'B' Max. dynamic μ-strain	Side 'B' Mean μ-strain
0	743 (1073)	552	715 (1037)	536
2560	741 (1076)	560	725 (1049)	546
5400	747 (1072)	572	737 (1057)	553
10000	740 (1078)	566	733 (1073)	562
23000	742 (1083)	569	727 (1067)	558
41000	740 (1076)	569	729 (1066)	554
63000	742 (1084)	-	729 (1071)	-
100000	753 (1071)	569	746 (1066)	558
150000	713 (1049)	557	709 (1052)	546
200000	712 (1038)	557	713 (1049)	544
265000	711 (1027)	547	709 (1035)	539
488000	687 (997)	536	687 (1004)	533
550000	676 (978)	523	675 (990)	516
660000	666 (982)	518	659 (970)	503
729000	653 (939)	515	655 (961)	506
973000	605 (855)	535	637 (918)	528
1074000	555 (825)	468	616 (893)	474
1200000	635 (854)	578	601 (855)	463
1502040	1052 (1380)	1007	444 (654)	317 **

(.....) Max. static compressive strain.

** Results affected by extensive delamination.
Ave. max. dynamic compressive strains for sides 'A' and 'B' are, respectively, 697 μ-strain and 694 μ strain.
Max., mean and min. compressive loads = 9.5kN, 5kN and 0.5kN, respectively.
f = 6Hz.

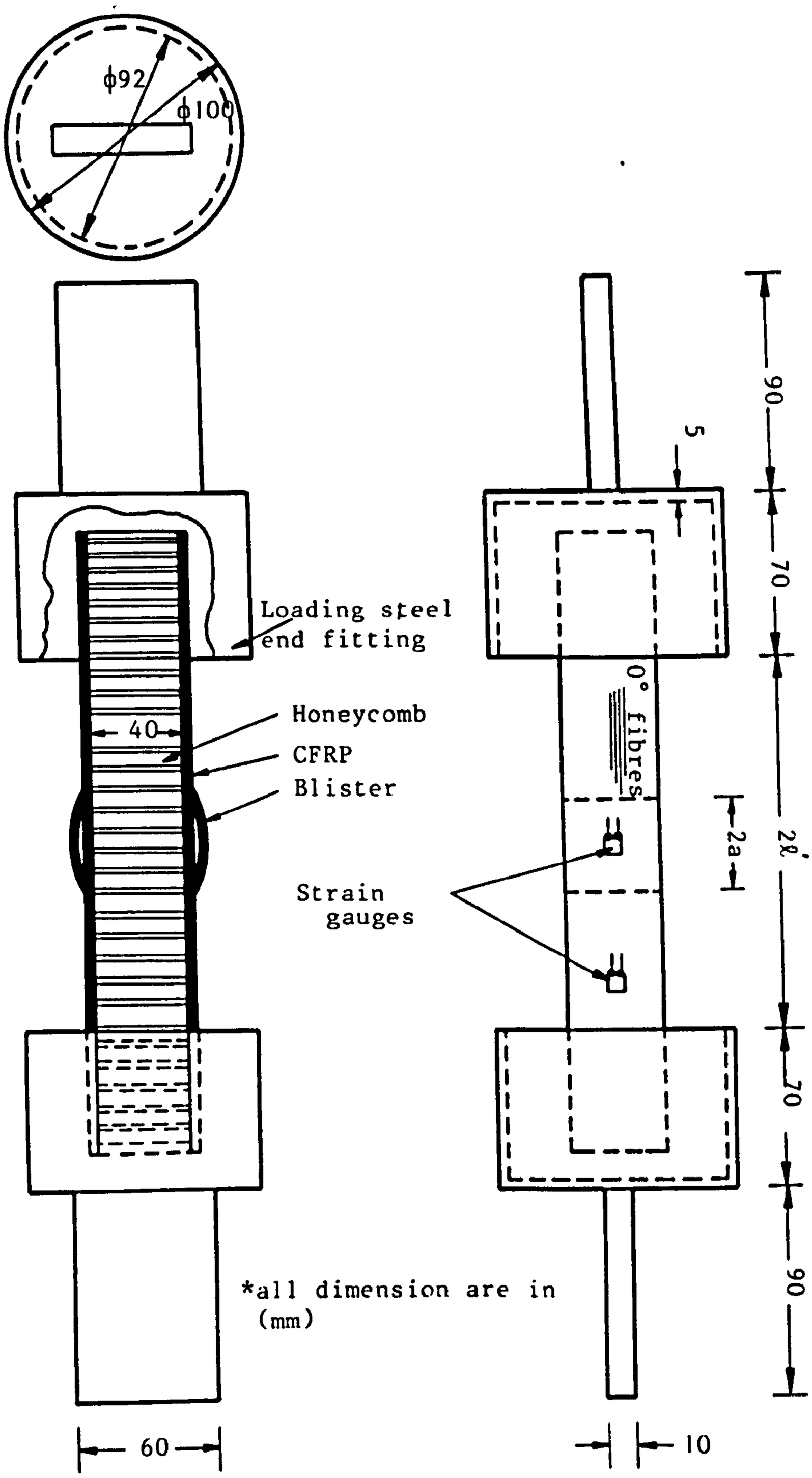

Fig. 5.1 TWIN BLISTER TEST SPECIMEN CONFIGURATION AND BASIC DIMENSIONS

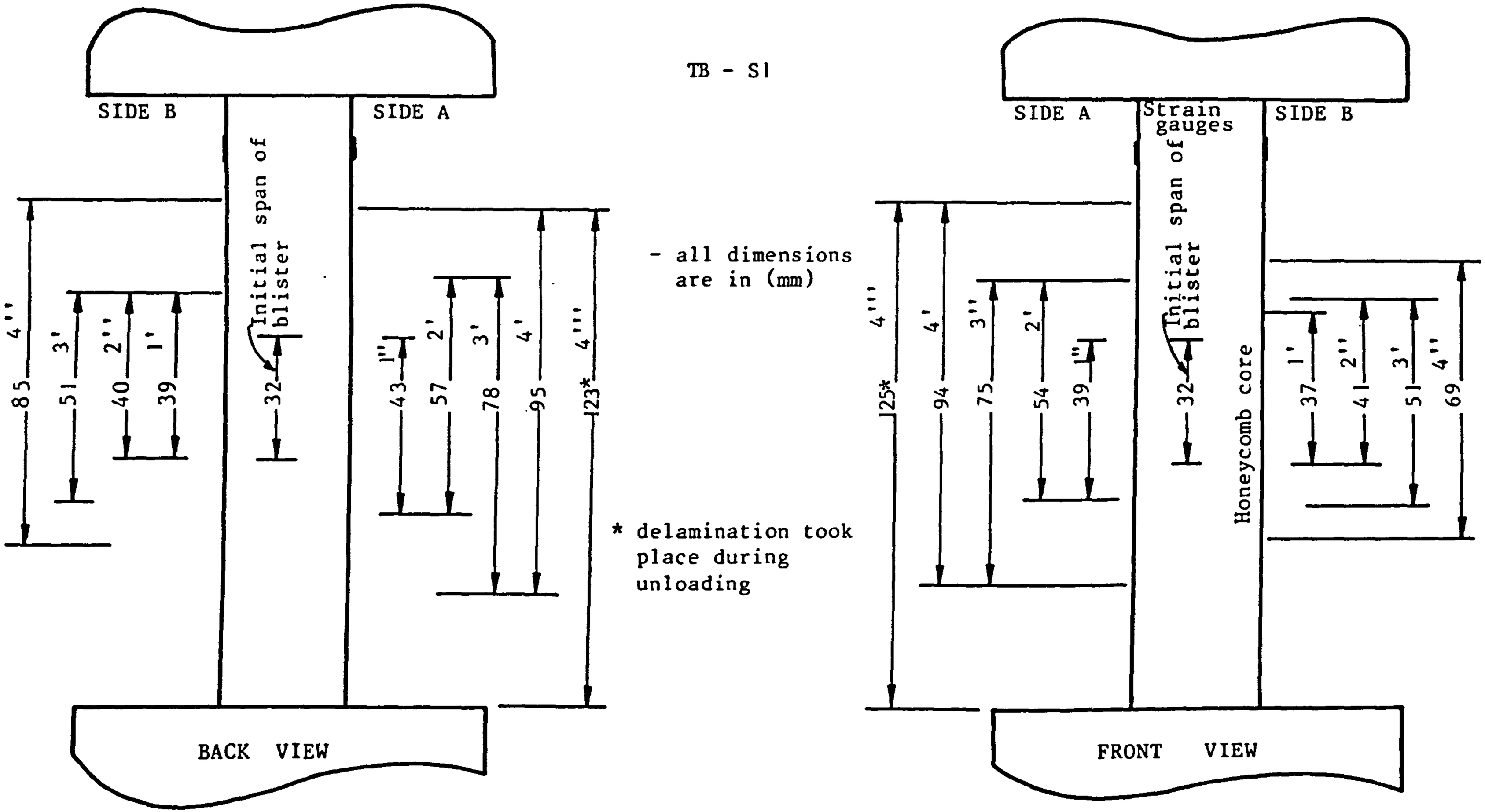

Fig. 5.2 ACCUMULATIVE PICTURE OF CONSECUTIVE CRACK PROPAGATION FOR SPECIMEN TB-S1

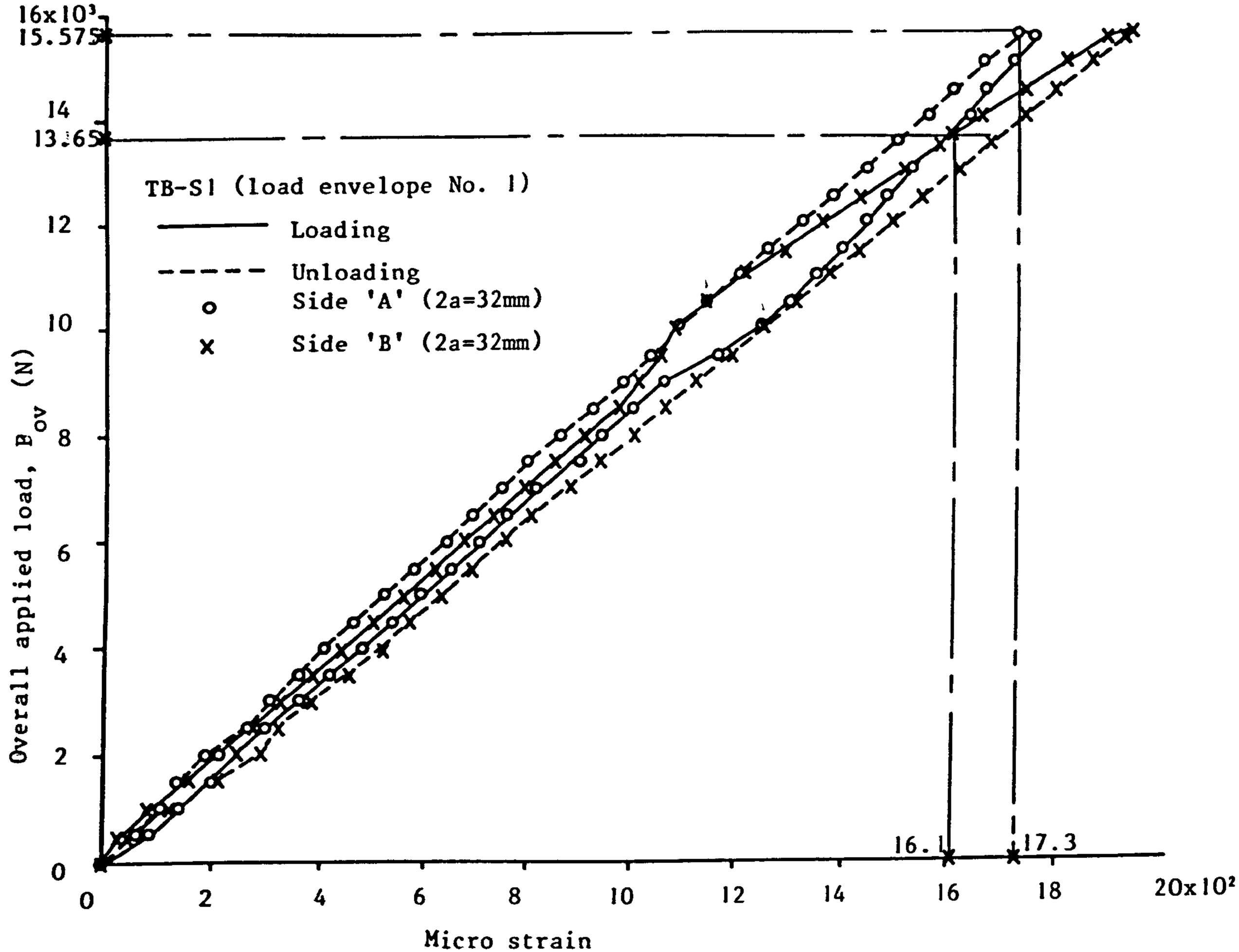

FIg. 5.3 LOAD-STRAIN RESPONSE FOR SPECIMEN TB-S1 (LOAD ENVELOPE No.1)

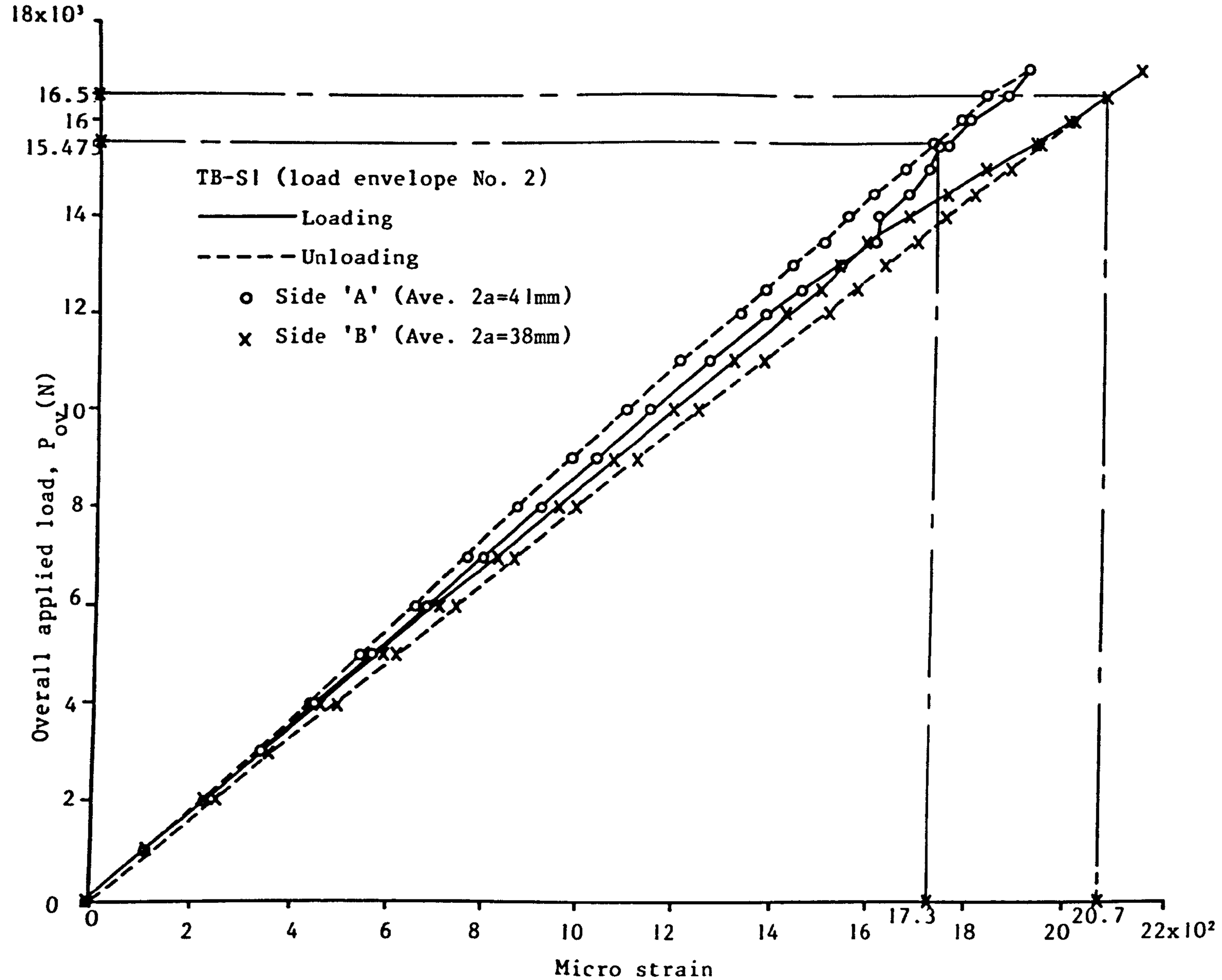

Fig. 5.4 LOAD-STRAIN RESPONSE FOR SPECIMEN TB-S1 (LOAD ENVELOPE No. 2)

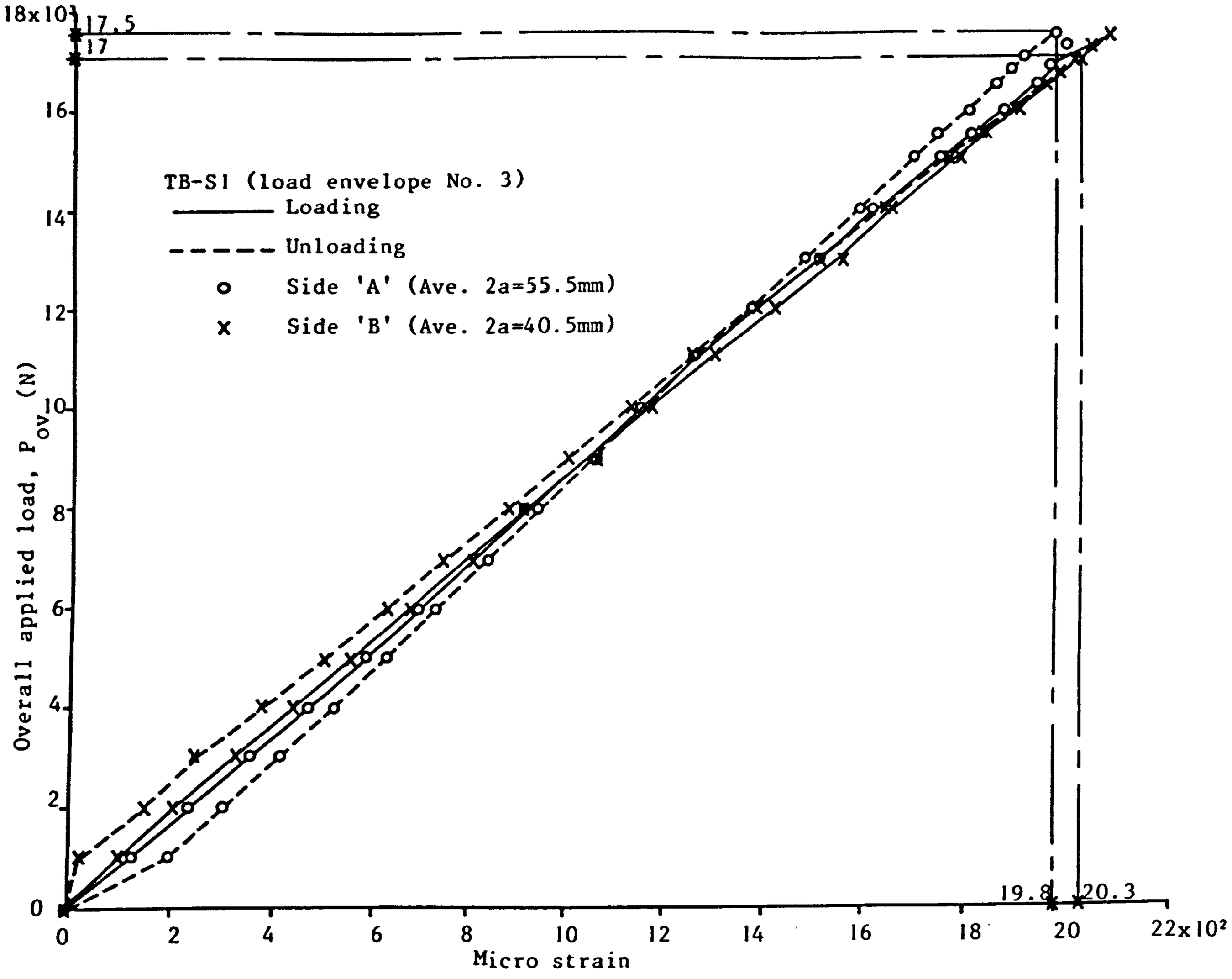

Fig. 5.5 LOAD-STRAIN RESPONSE FOR SPECIMEN TB-S1 (LOAD ENVELOPE No. 3)

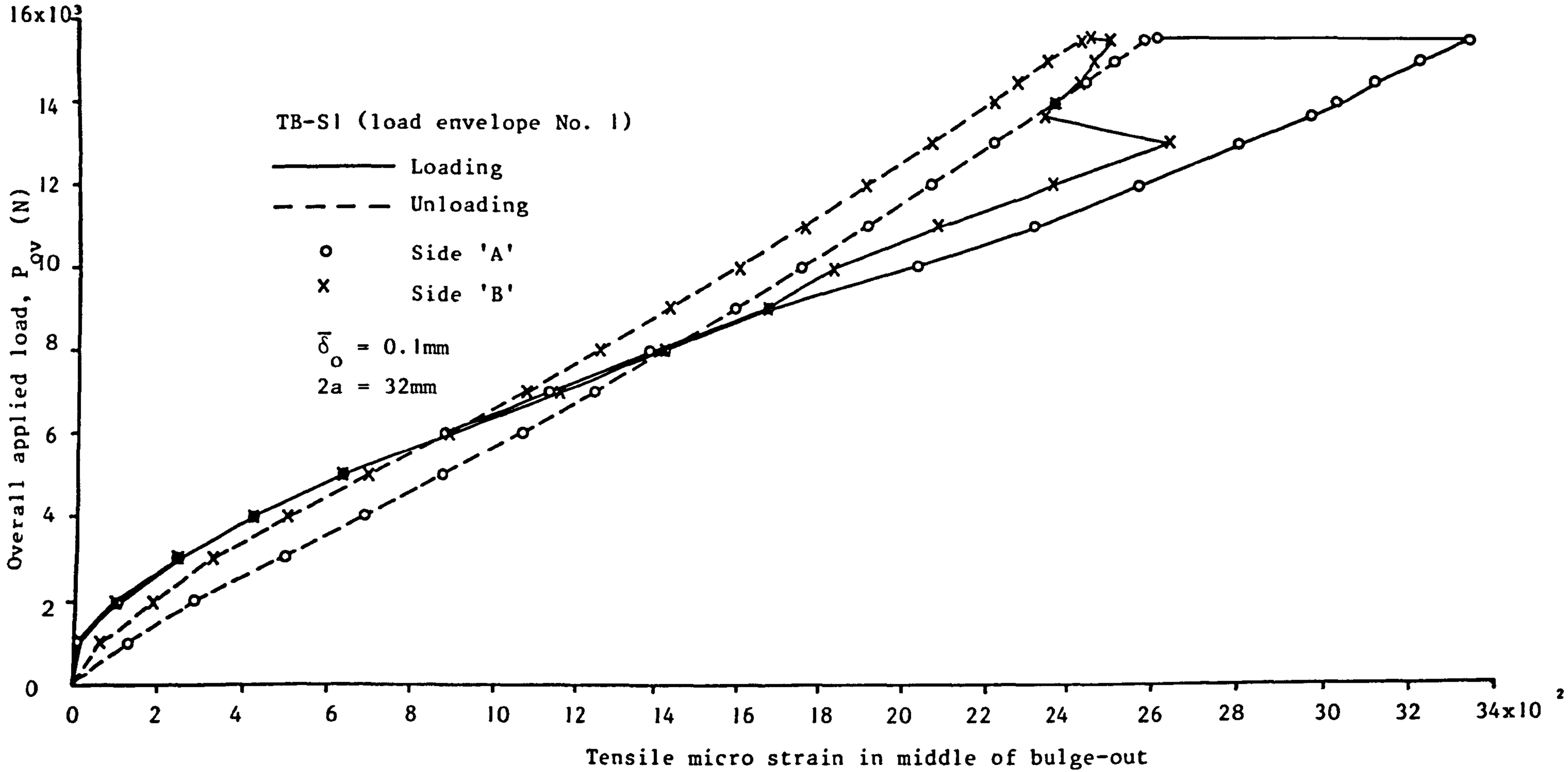

Fig. 5.6 TENSILE STRAIN IN BLISTER LAYERS VS. OVERALL APPLIED LOAD FOR SPECIMEN TB-S1

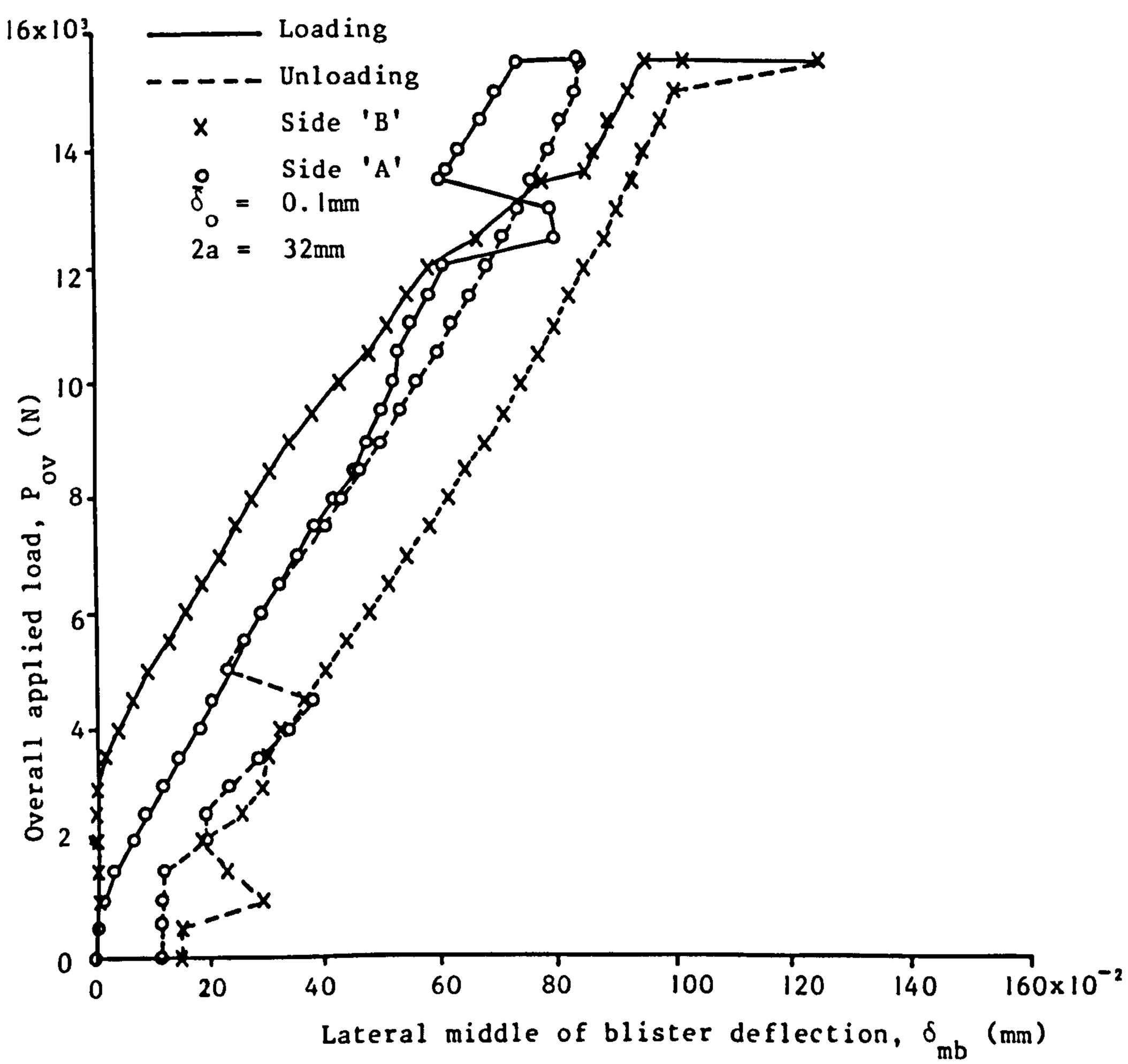

Fig. 5.7 LATERAL DEFLECTION IN THE MIDDLE OF BLISTER LAYER VS. OVERALL APPLIED LAOD FOR SPECIMEN TB-S1

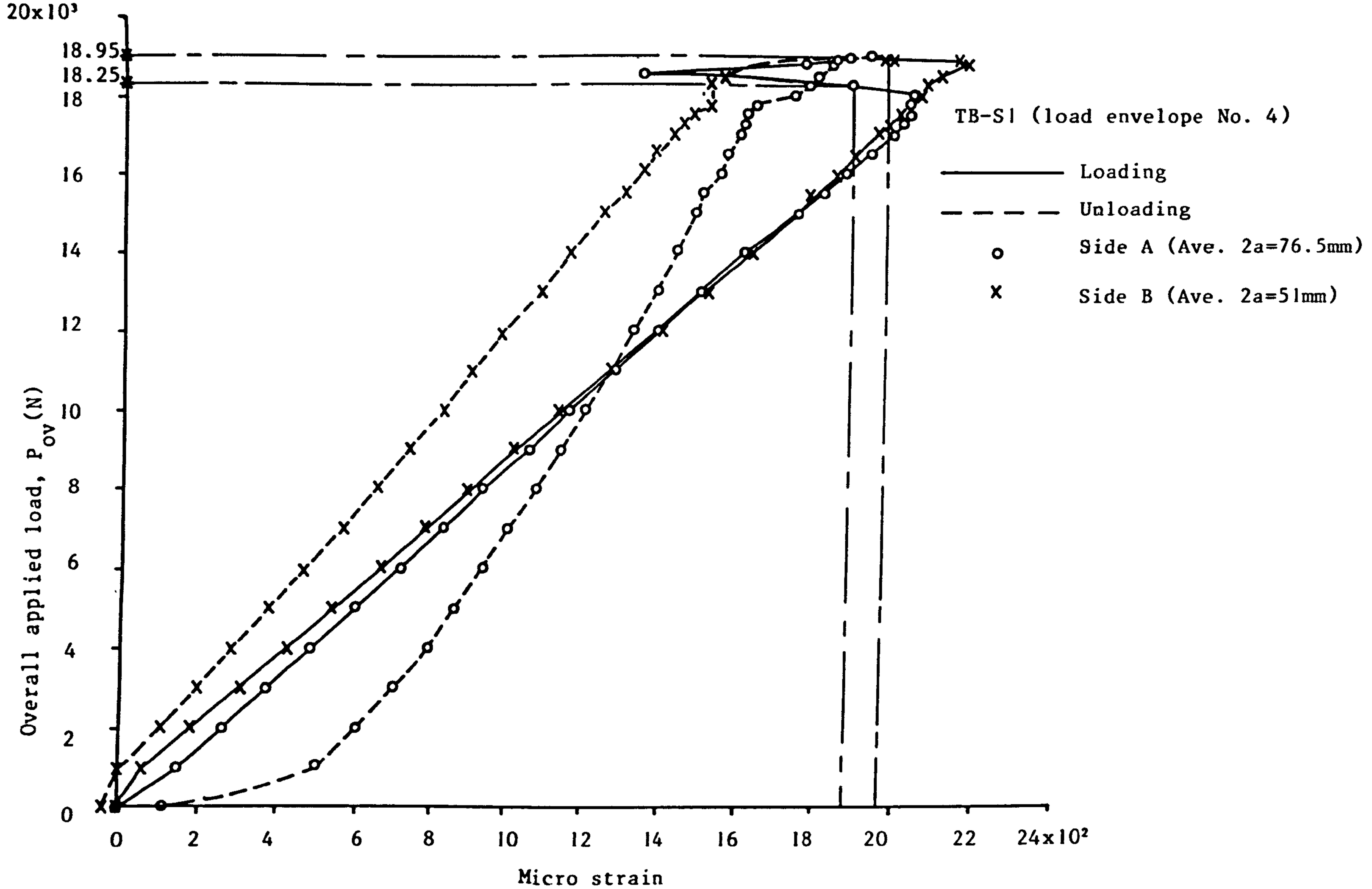

Fig. 5.8 LOAD-STRAIN RESPONSE FOR SPECIMEN TB-S1 (LOAD ENVELOPE No.4)

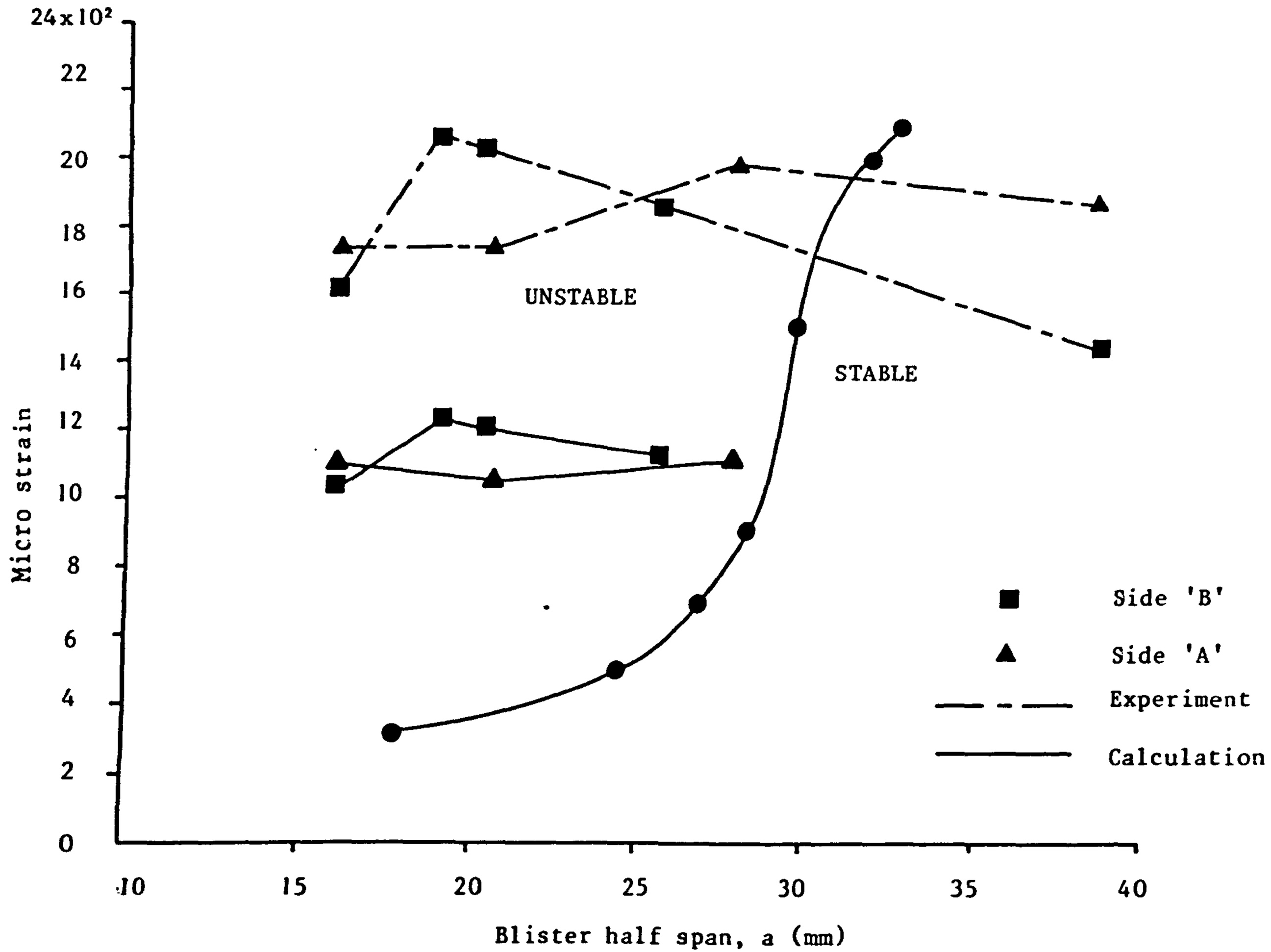

Fig. 5.9 CRITICAL APPLIED STRAIN VS. BLISTER HALF SPAN FOR SPECIMEN TB-S1

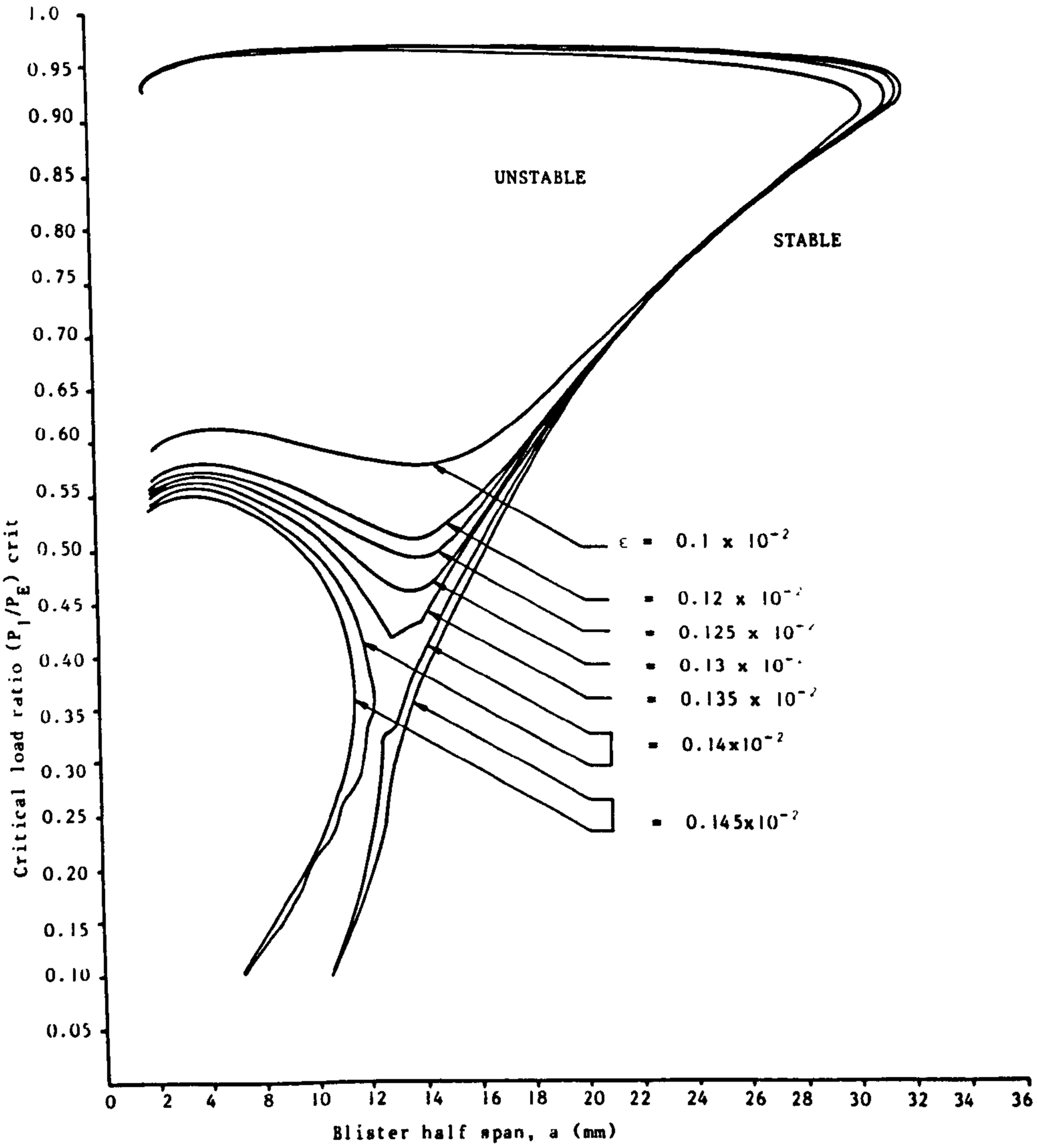

Fig. 5.10 CRITICAL LOAD RATIO VS. BLISTER HALF SPAN FOR VARIOUS APPLIED STRAINS

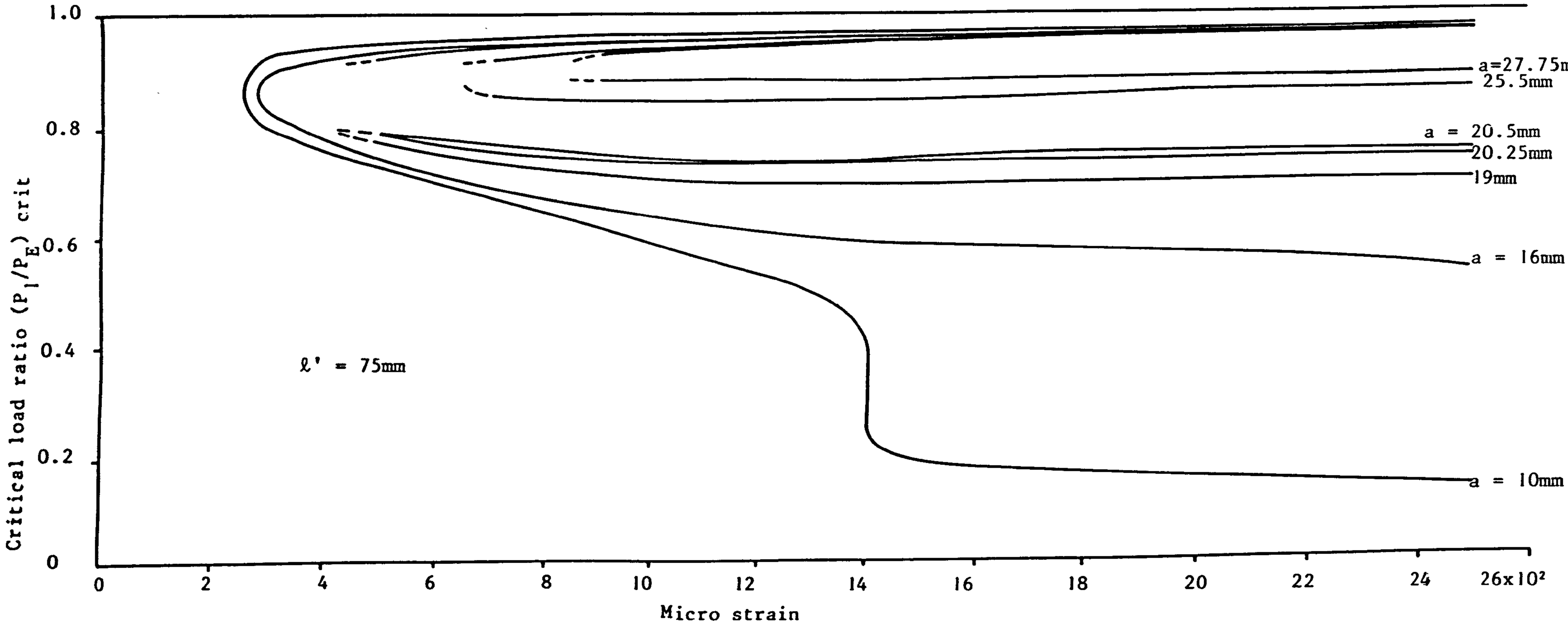

Fig. 5.11 CRITICAL LOAD RATIO VS. APPLIED STRAIN FOR VARIOUS BLISTER HALF SPANS

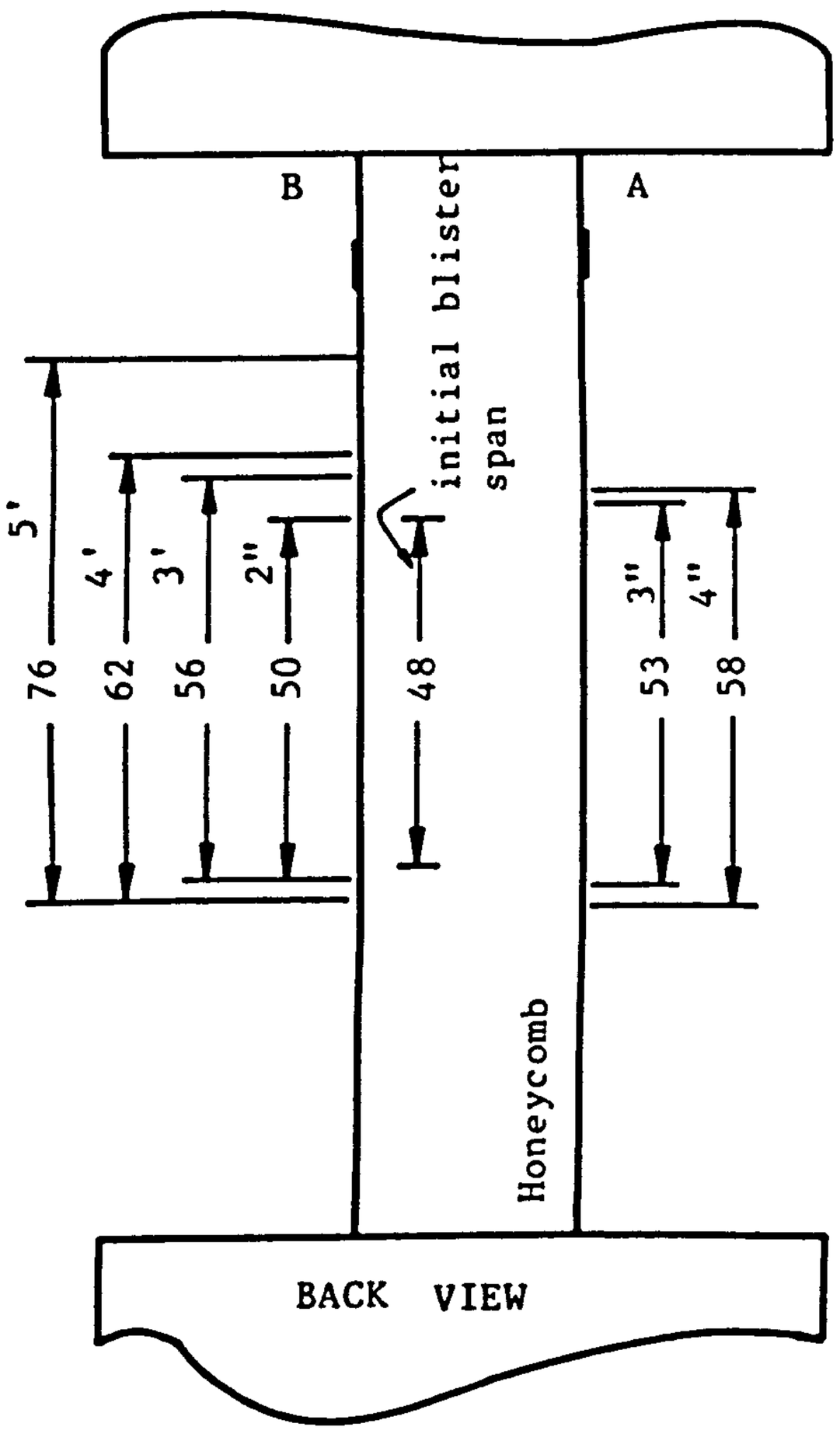

All dimensions are in (mm)

TB - S2

*Where the (') is absent, there is no second to that delamination within the same load envelope

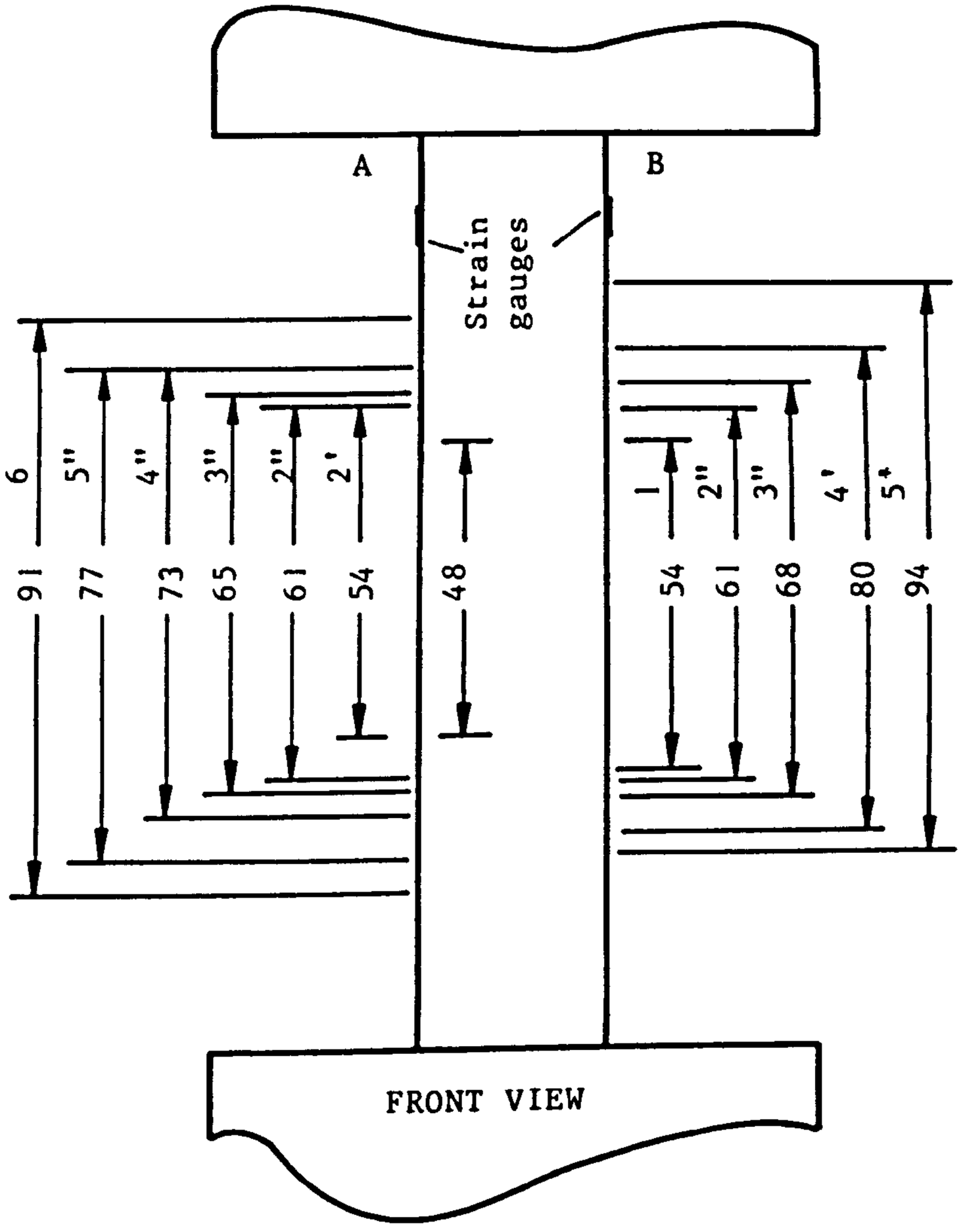

FIg. 5.12 ACCUMULATIVE PICTURE OF CONSECUTIVE CRACK PROPAGATION FOR SPECIMEN TB-S2

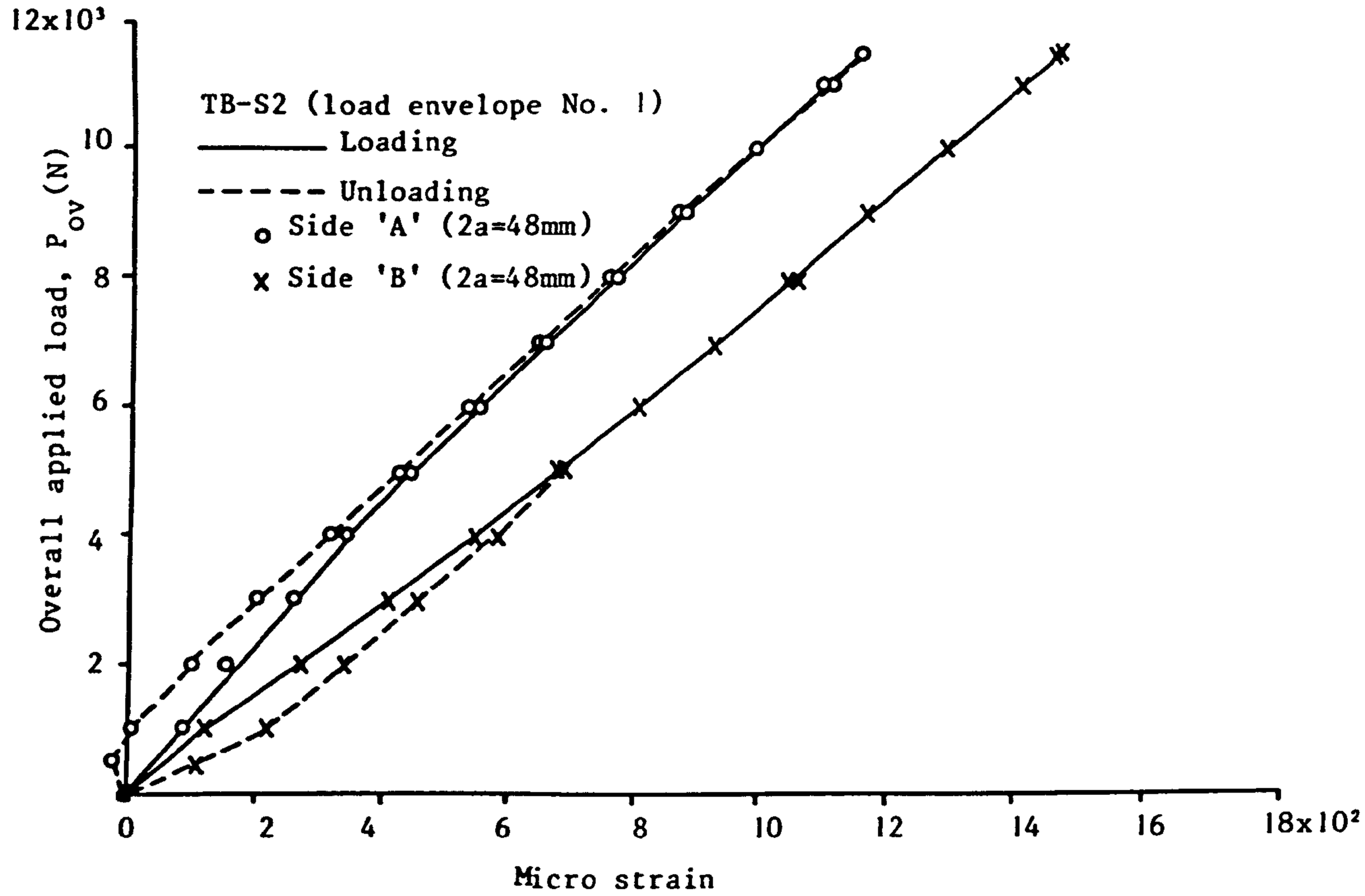

5.13 LOAD-STRAIN RESPONSE FOR SPECIMEN TB-S2 (Load envelope No. 1)

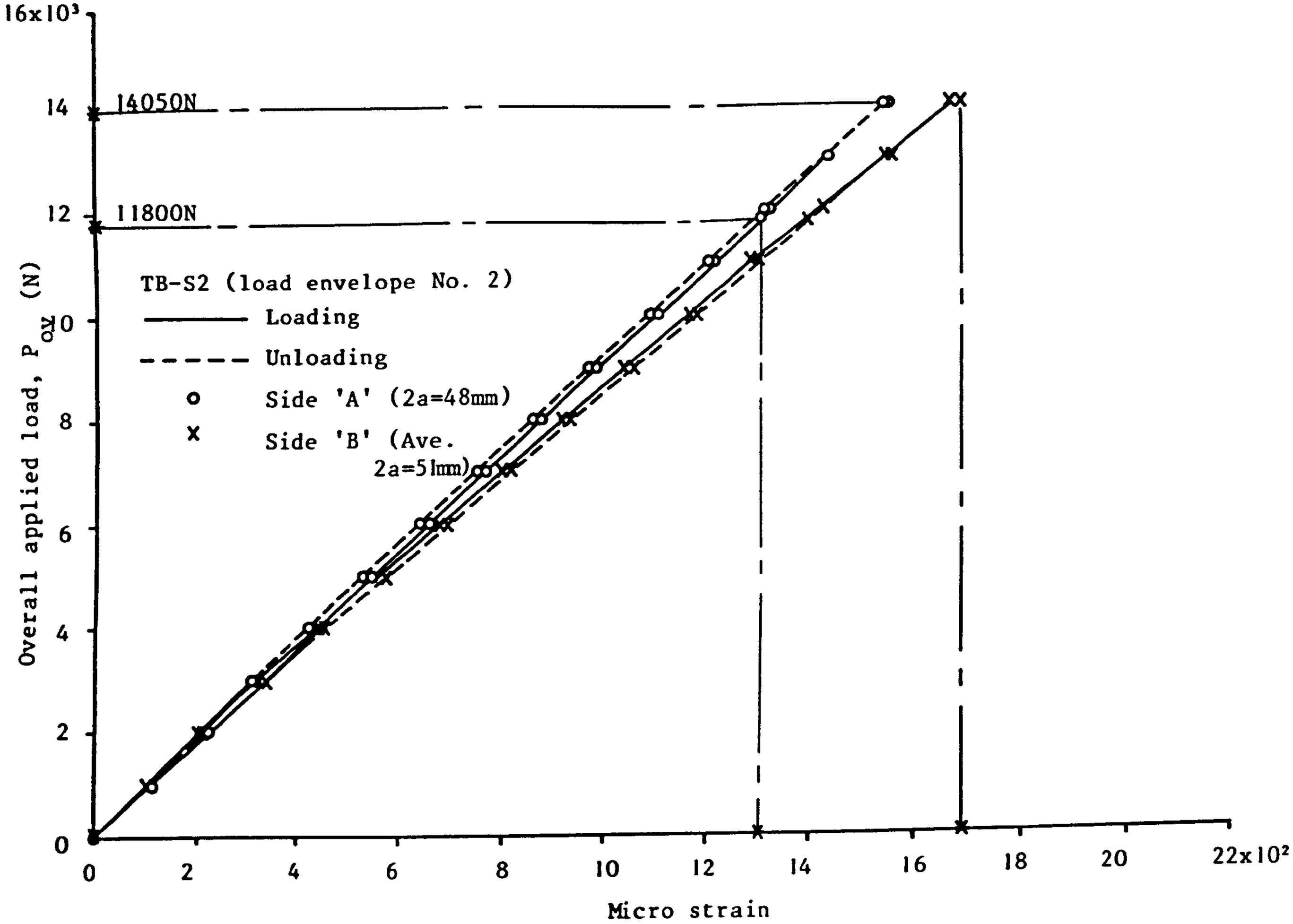

Fig. 5.14 LOAD-STRAIN RESPONSE FOR SPECIMEN TB-S2 (Load envelope No. 2)

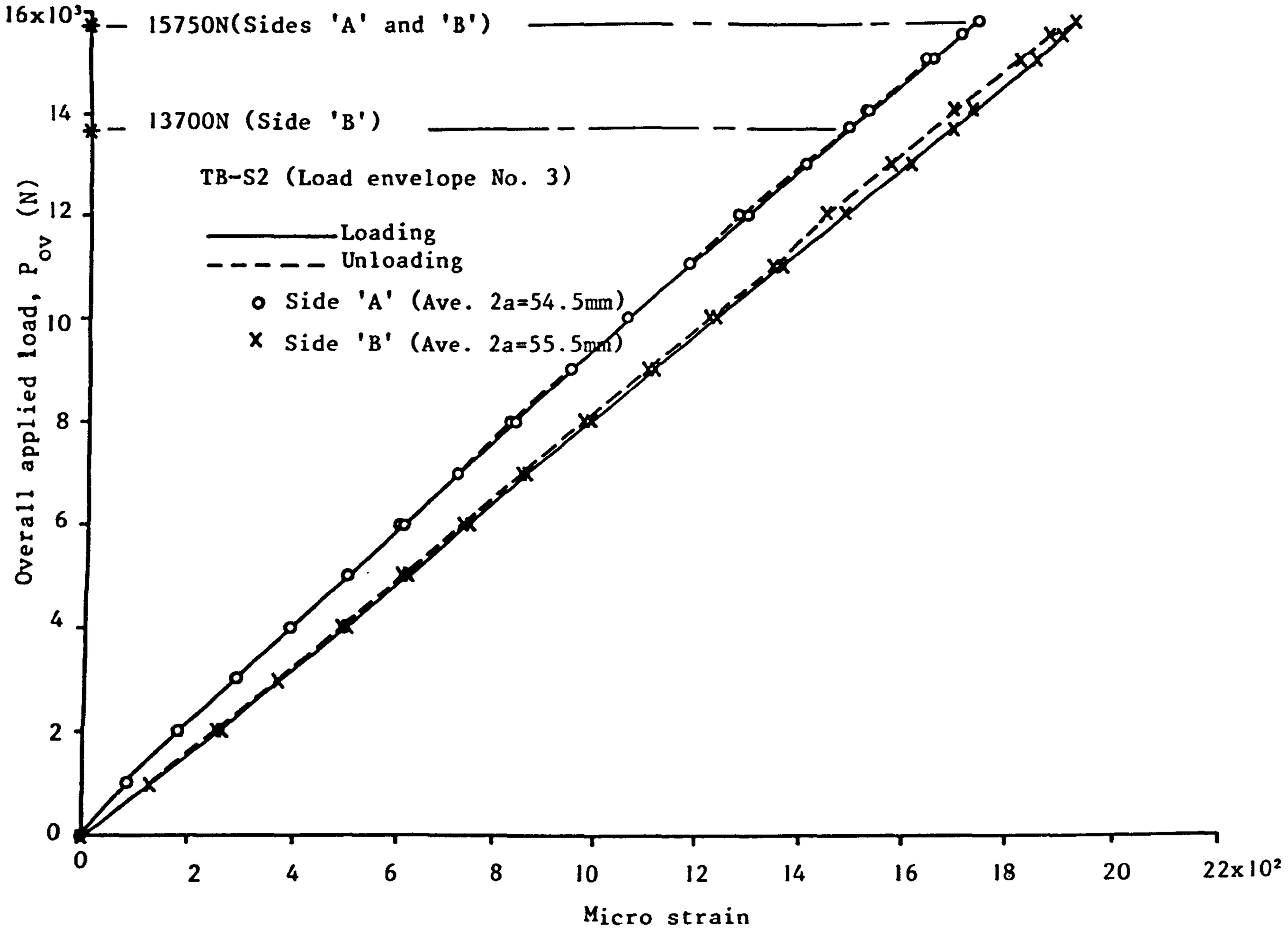

Fig. 5.15 LOAD-STRAIN RESPONSE FOR SPECIMEN TB-S2 (Load envelope No. 3)

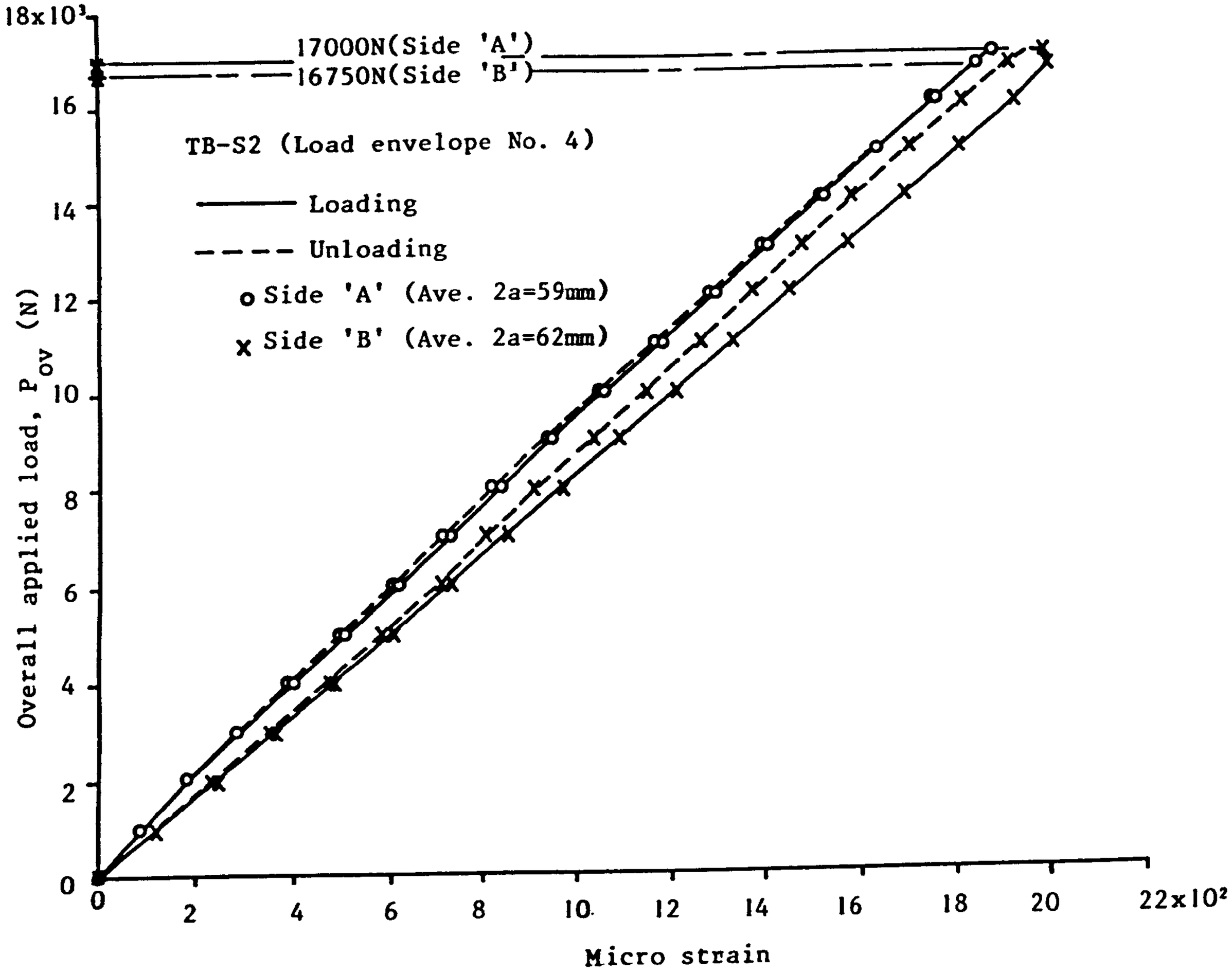

Fig. 5.16 LOAD-STRAIN RESPONSE FOR SPECIMEN TB-S2 (load envelope No. 4)

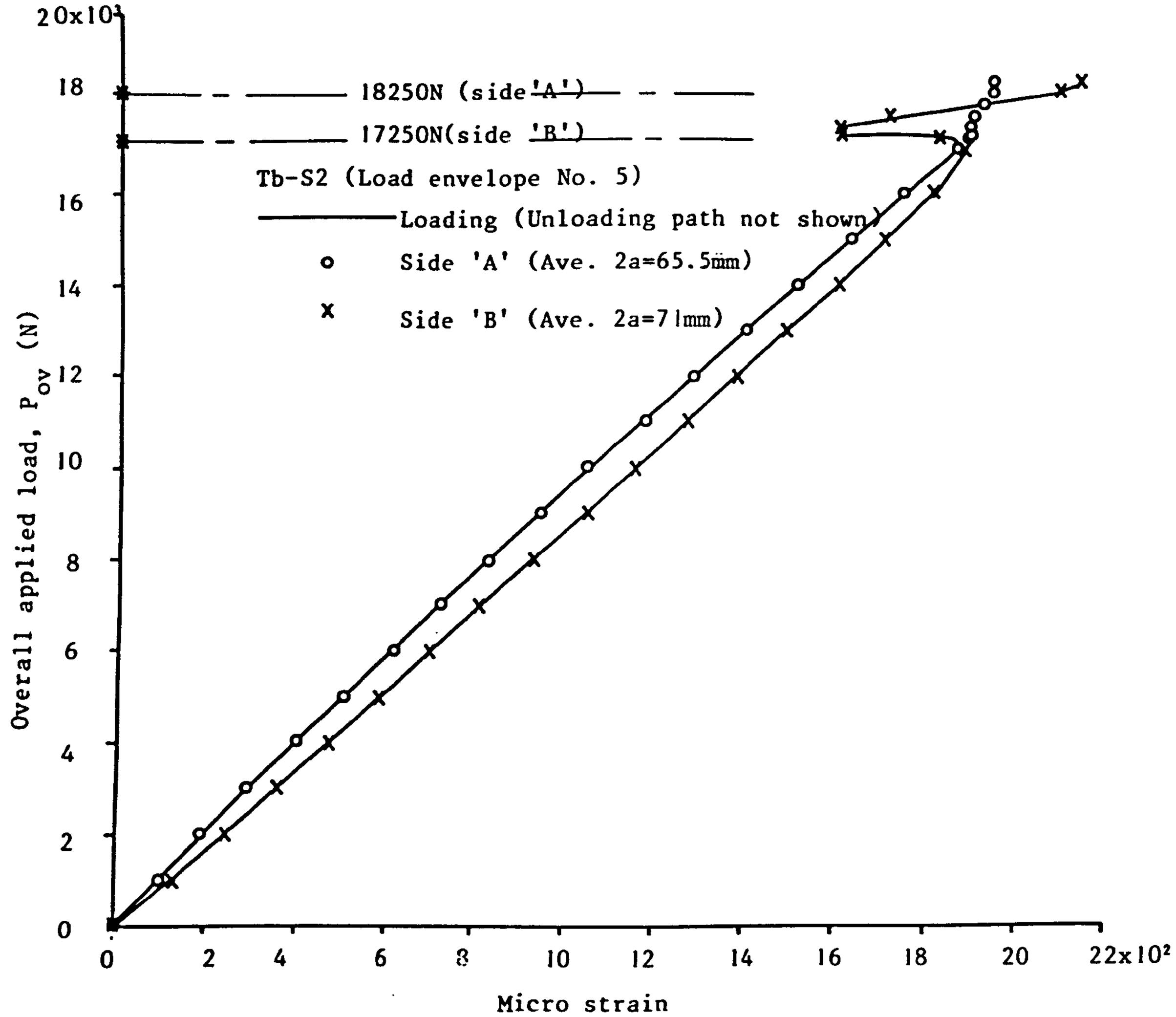

Fig. 5.17 LOAD-STRAIN RESPONSE FOR SPECIMEN TB-S2 (load envelope No.5)

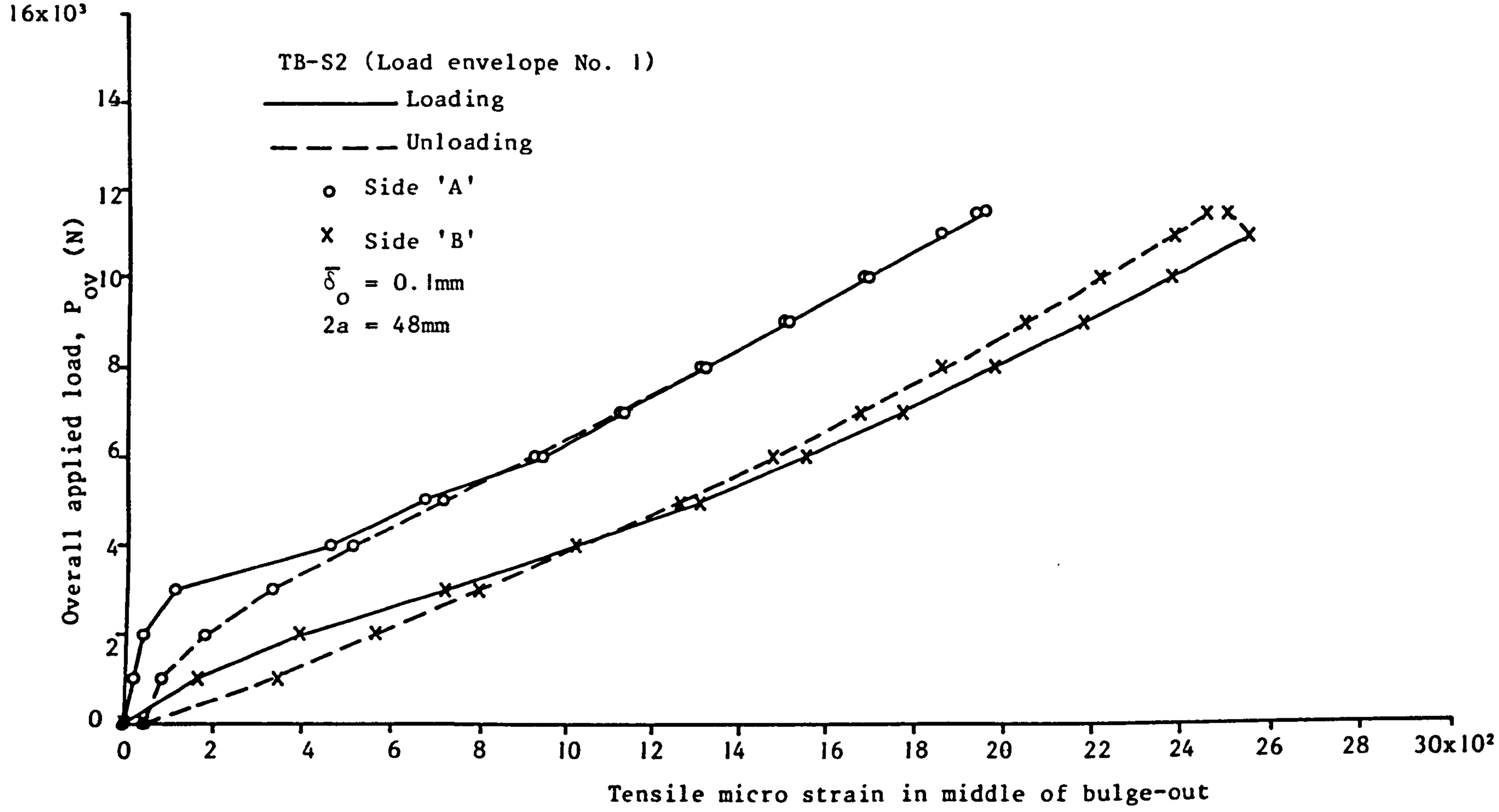

Fig. 5.18 TENSILE STRAIN IN BLISTER LAYERS VS. OVERALL APPLIED LOAD FOR SPECIMEN TB-S2

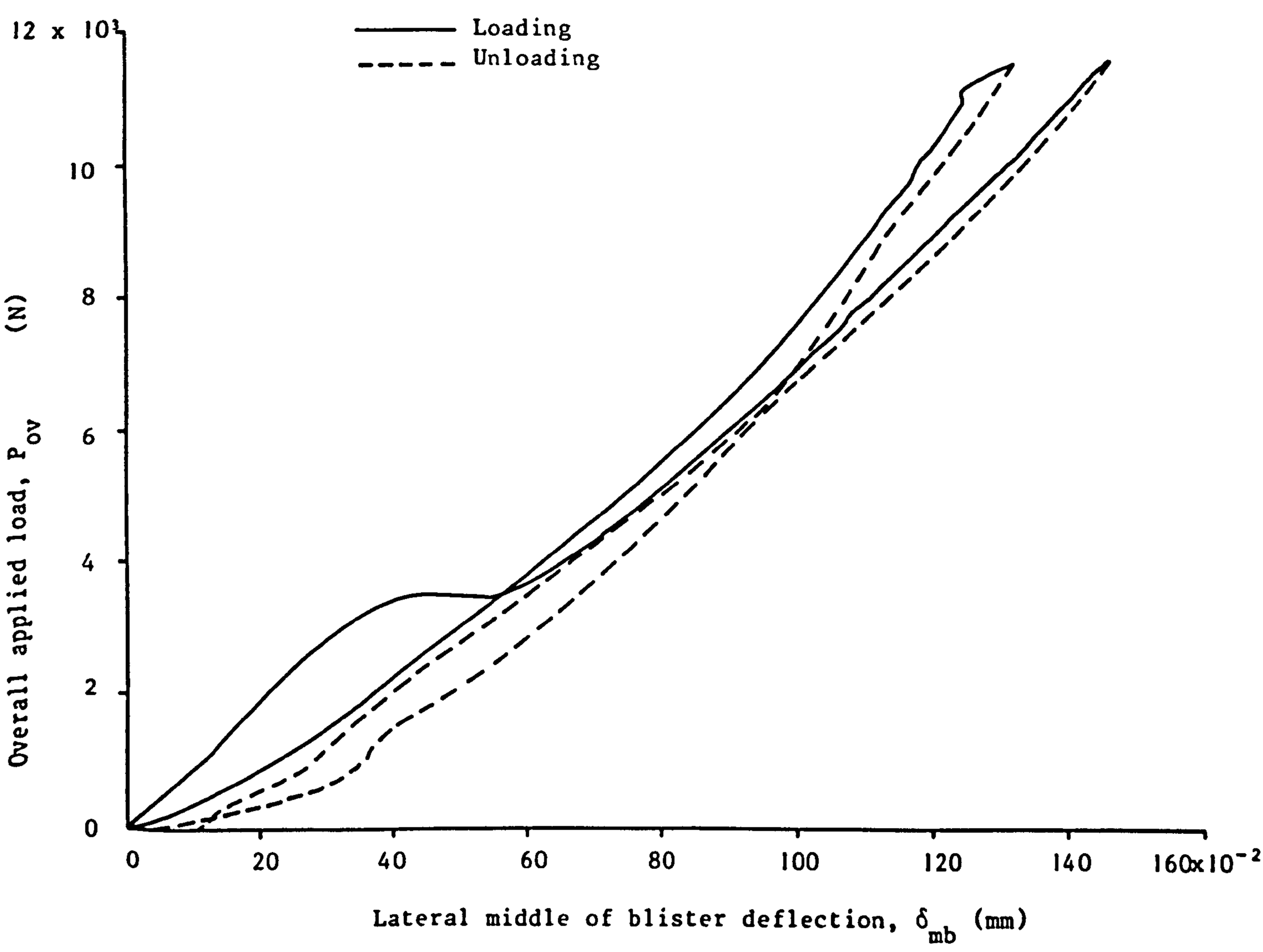

Fig. 5.19 LATERAL DEFLECTION IN THE MIDDLE OF BLISTER LAYER VS. OVERALL APPLIED LOAD FOR SPECIMEN TB-S2

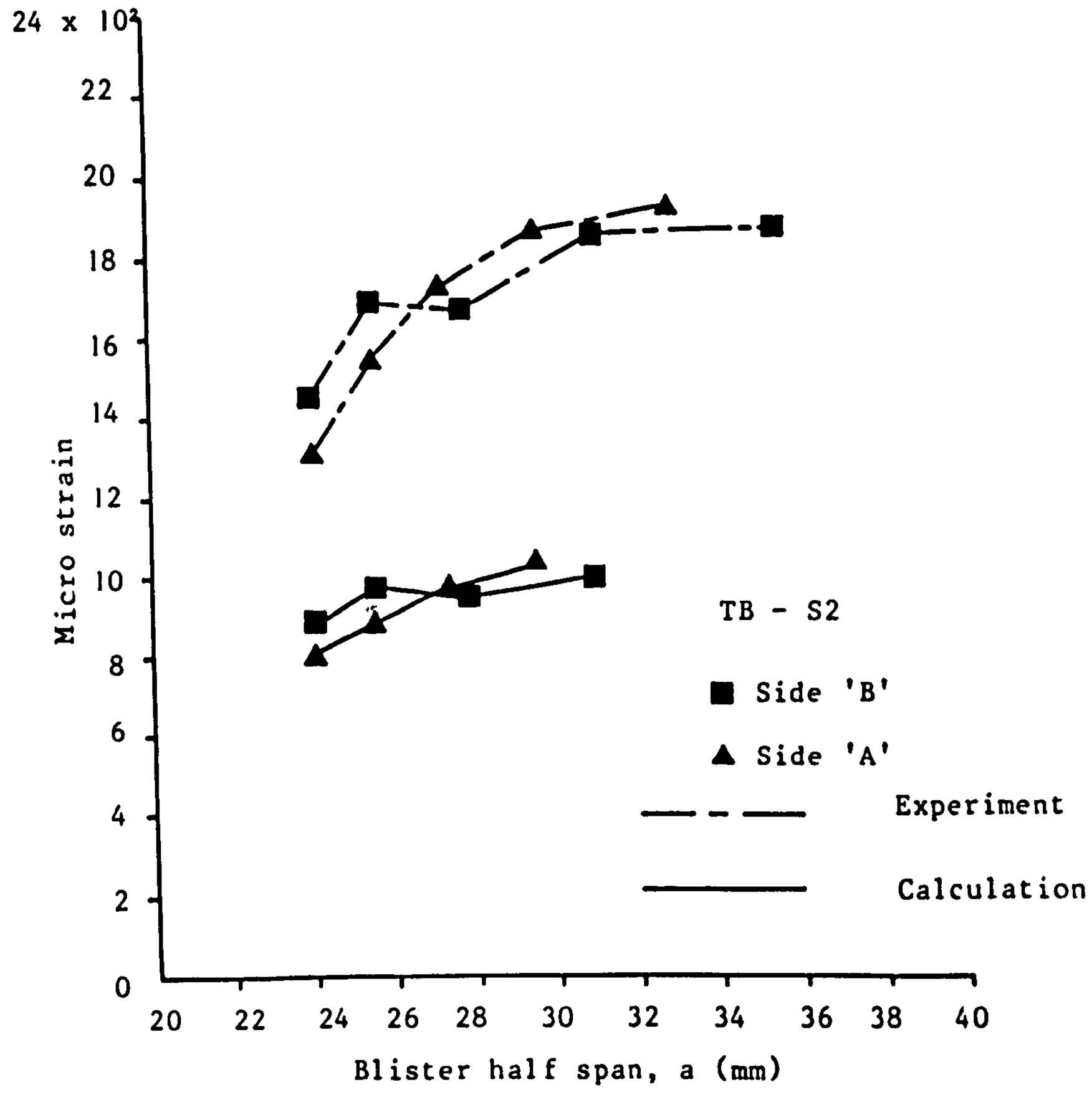

Fig. 5.20 CRITICAL APPLIED STRAIN VS. BLISTER HALF SPAN FOR SPECIMEN TB-S2

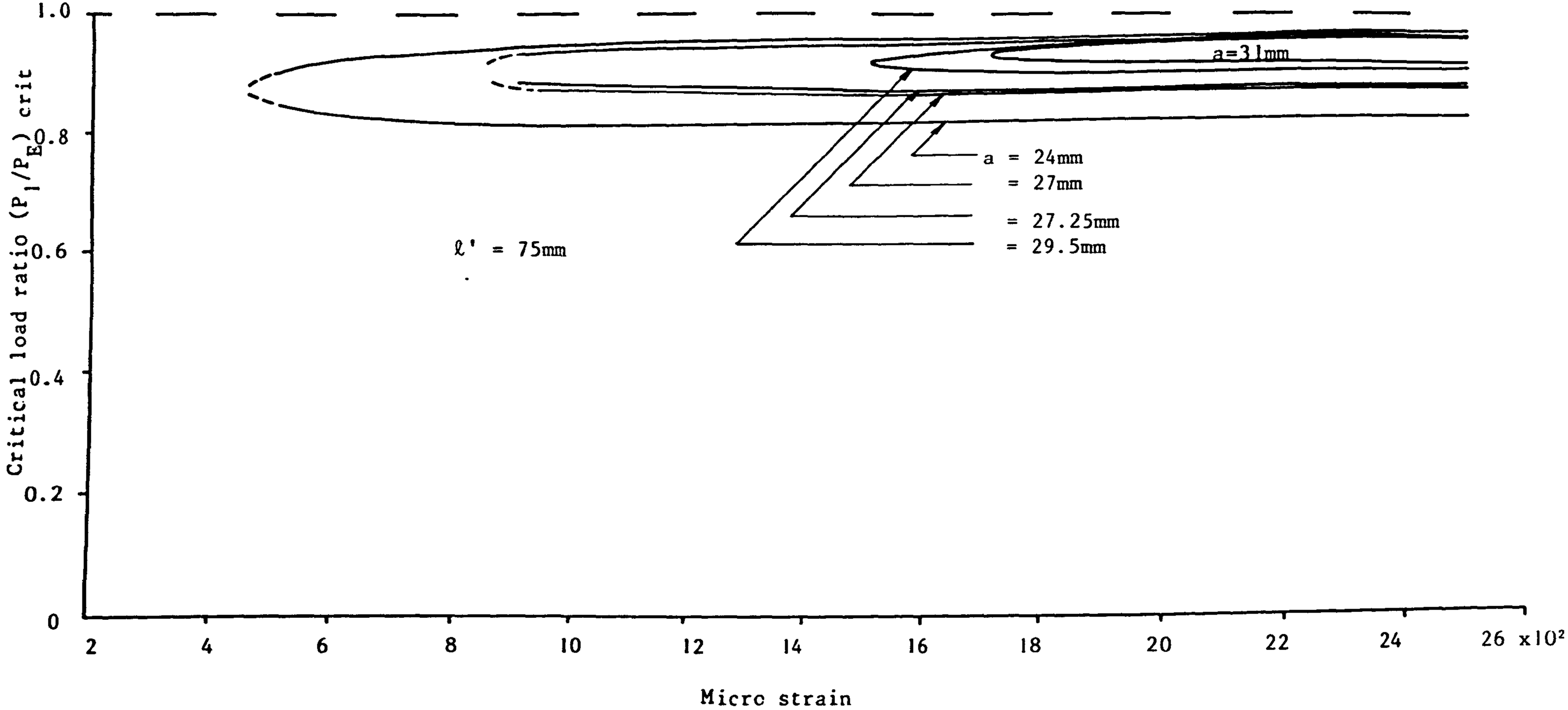

FIg. 5.21 CRITICAL LOAD RATIO VS. APPLIED STRAIN FOR VARIOUS BLISTER HALF SPANS

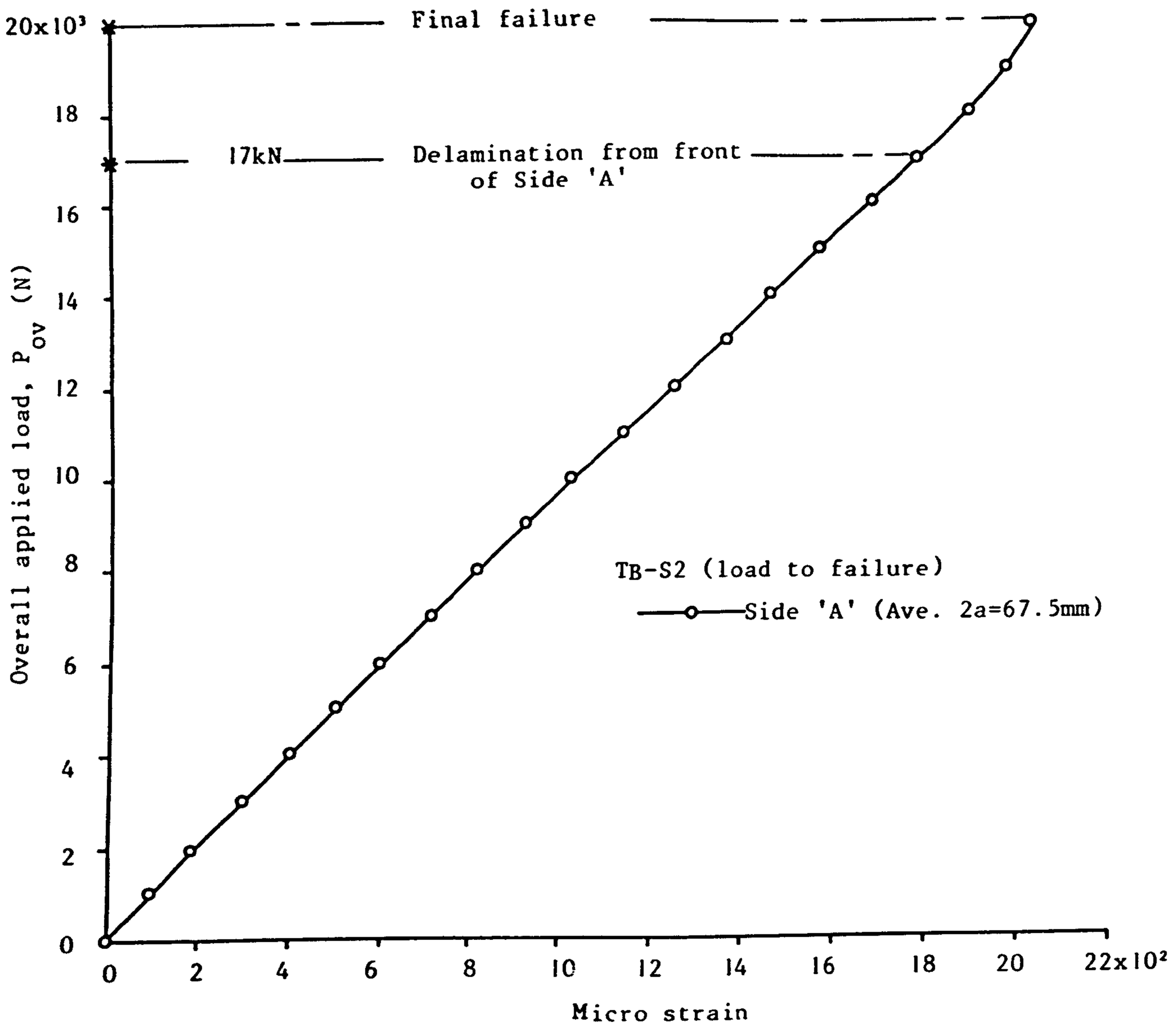

Fig. 5.22 LOAD-STRAIN RESPONSE FOR SIDE 'A' AND FINAL FAILURE OF SPECIMEN TB-S2

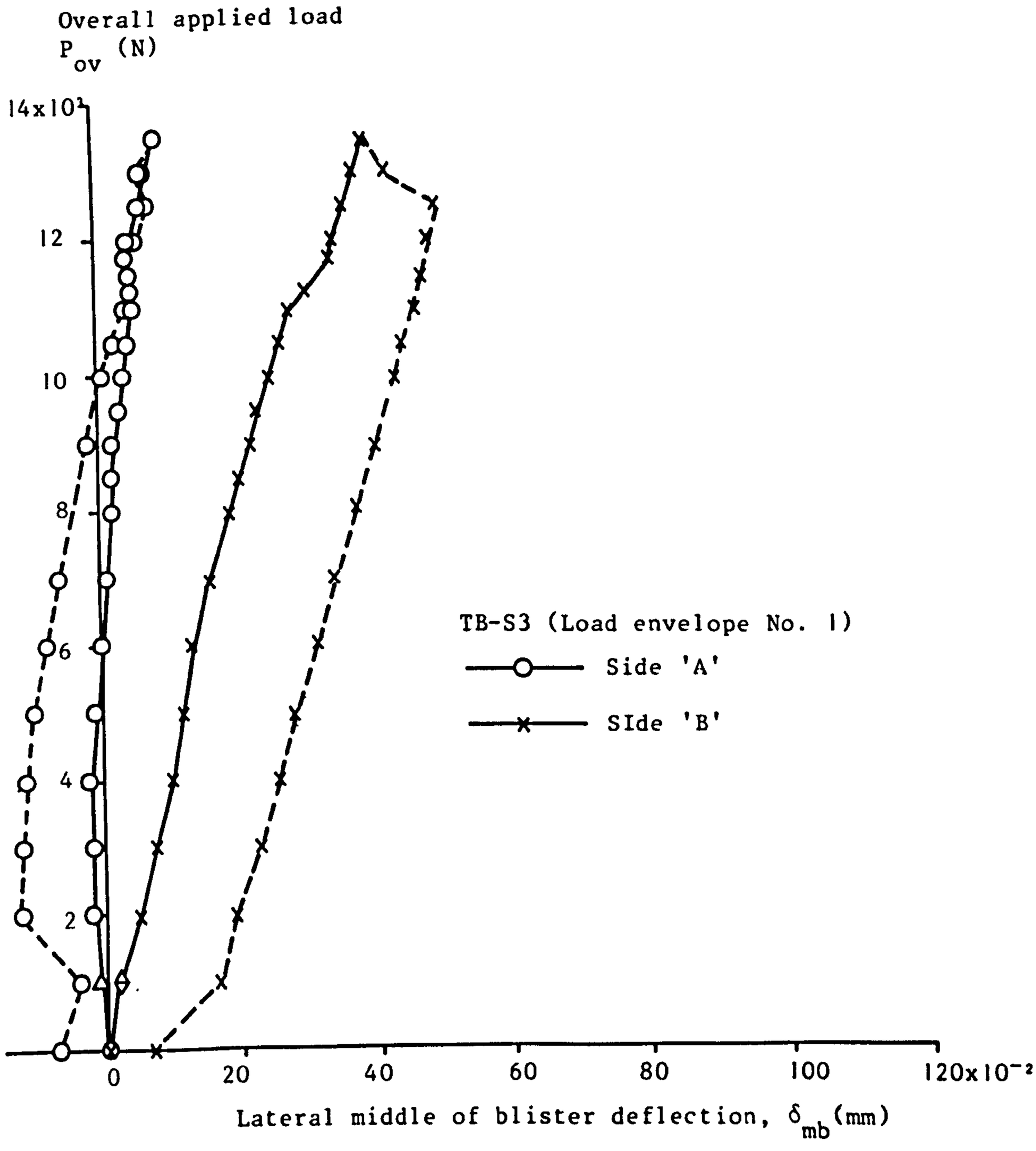

Fig. 5.23 LATERAL DEFLECTION IN THE MIDDLE OF BLISTER LAYER VS. OVERALL APPLIED LOAD FOR SPECIMEN TB-S3

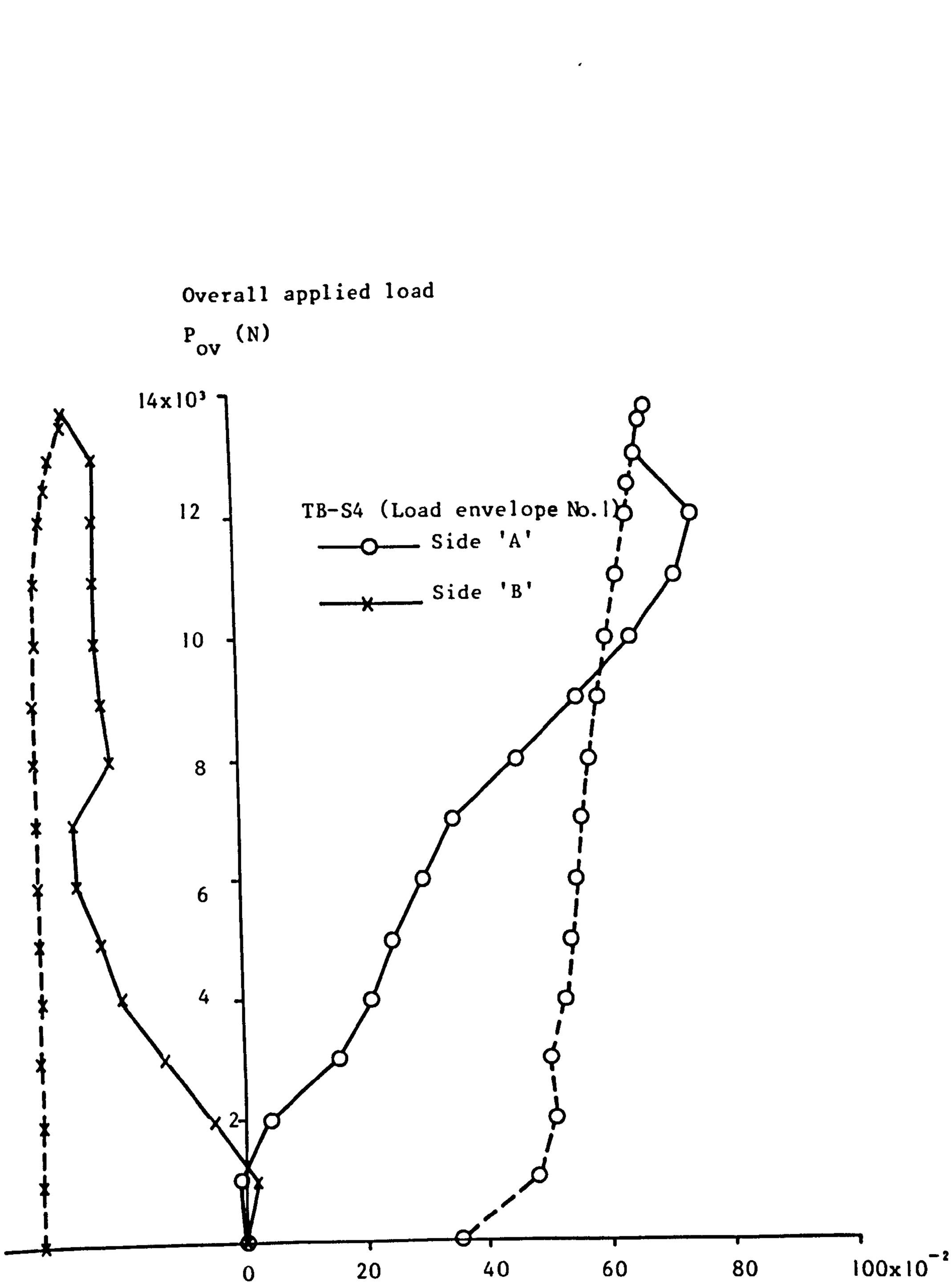

Fig. 5.24 LATERAL DEFLECTION IN THE MIDDLE OF BLISTER LAYER VS. OVERALL APPLIED LOAD FOR SPECIMEN TB-S4

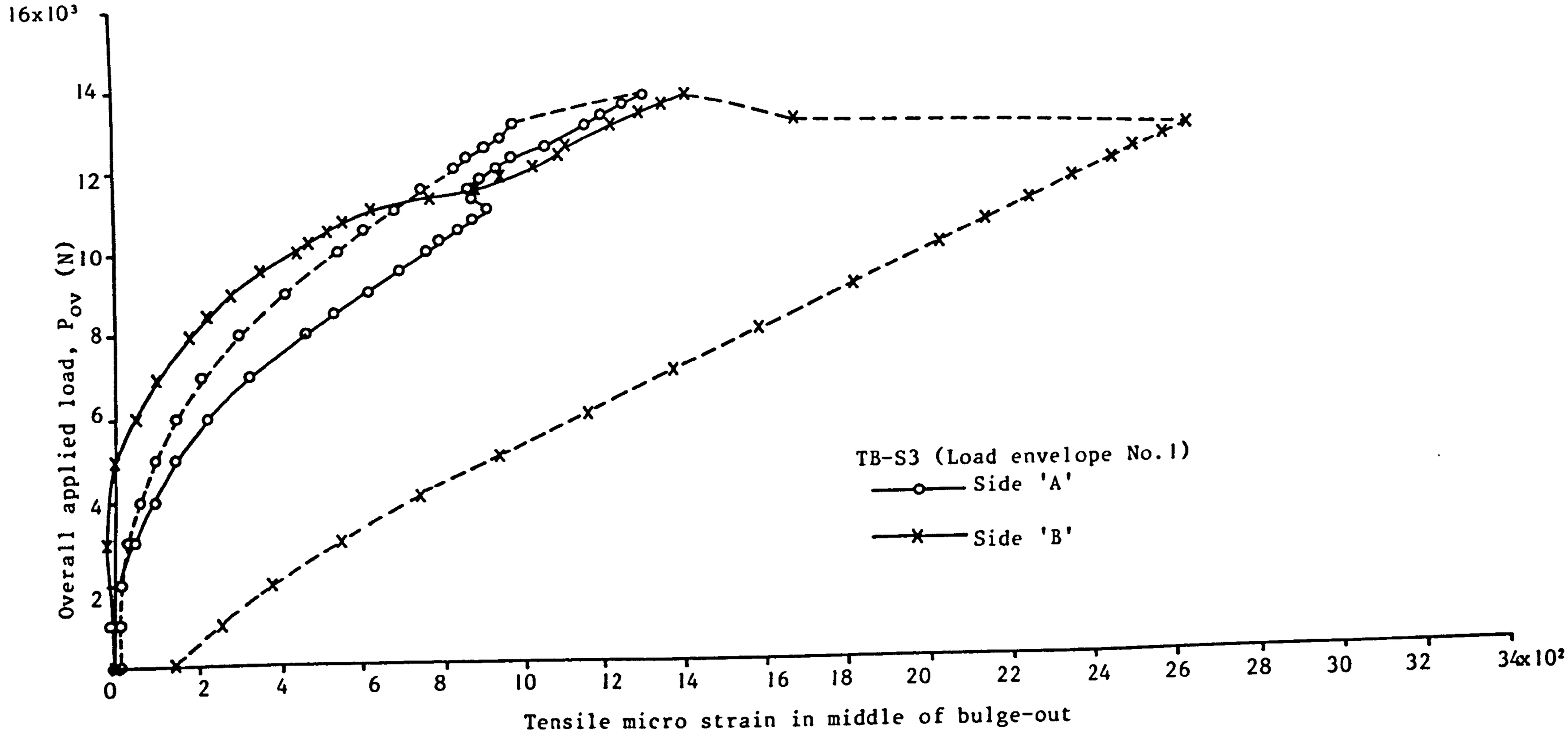

Fig. 5.25 TENSILE STRAIN IN BLISTER LAYERS VS. OVERALL APPLIED LOAD FOR SPECIMEN TB-S3

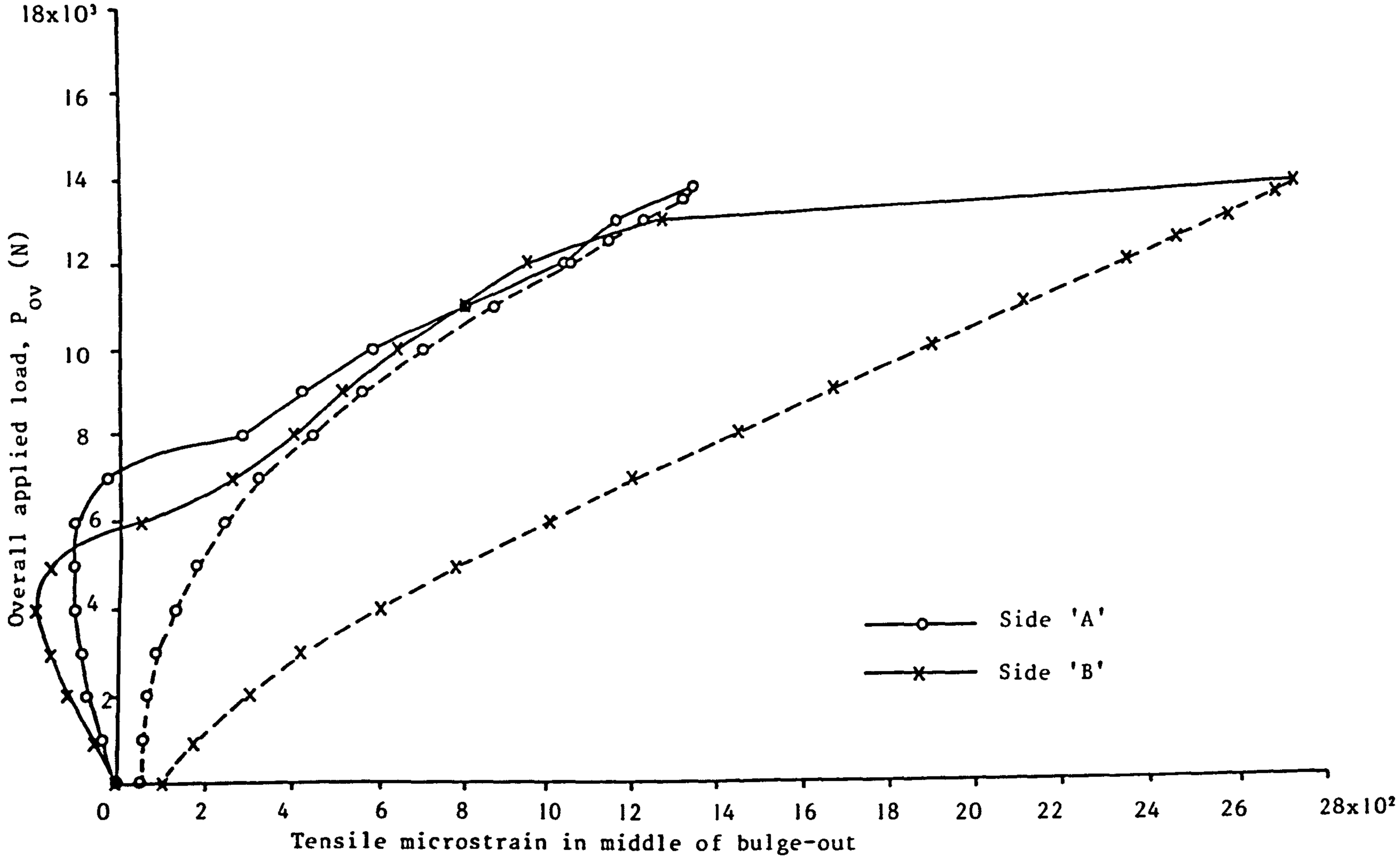

Fig. 5.26 TENSILE STRAIN IN BLISTER LAYERS VS. OVERALL APPLIED LOAD FOR SPECIMEN TB-S4

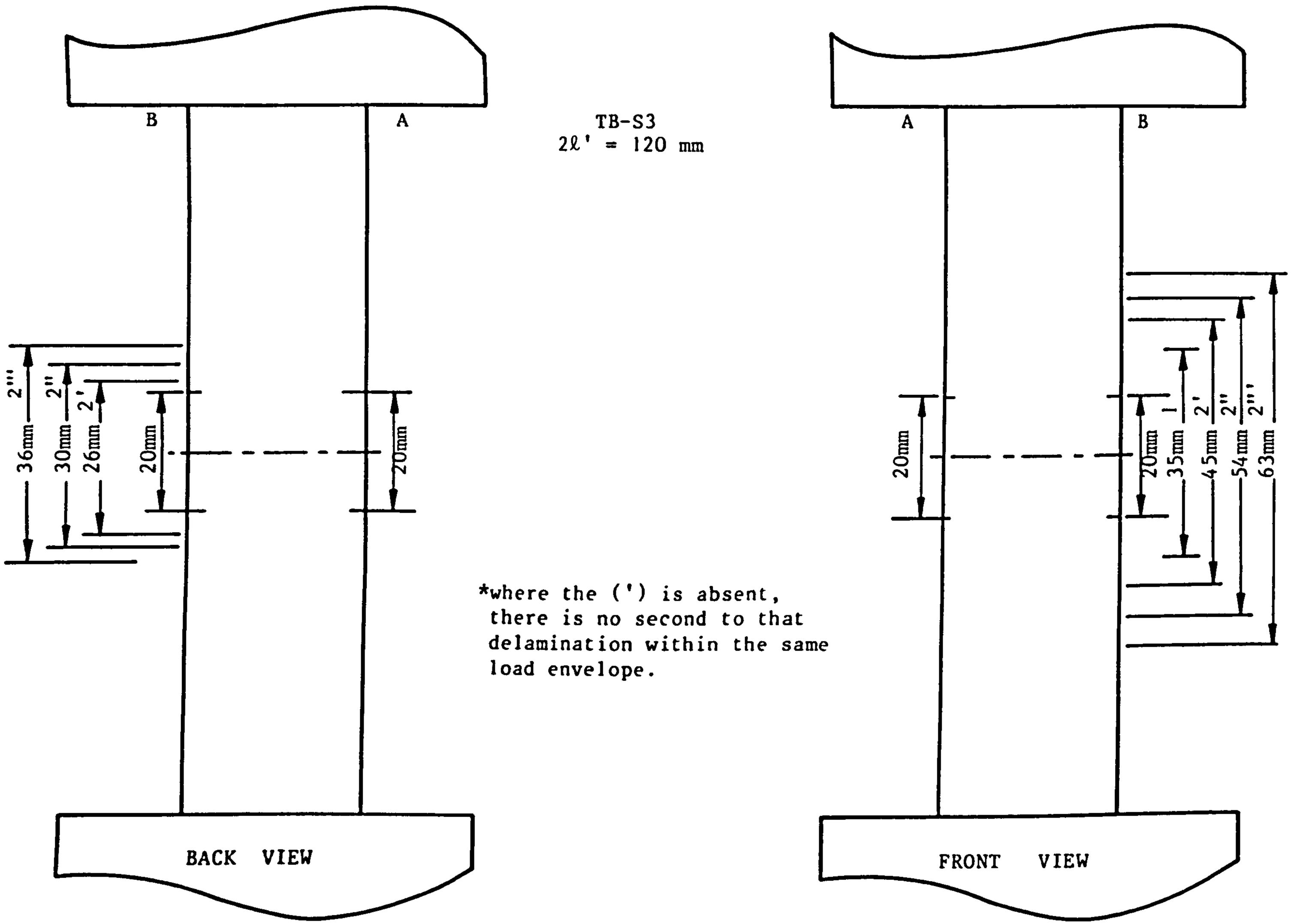

Fig. 5.27 ACCUMULATIVE PICTURE OF CONSECUTIVE CRACK PROPAGATION FOR SPECIMEN TB-S3

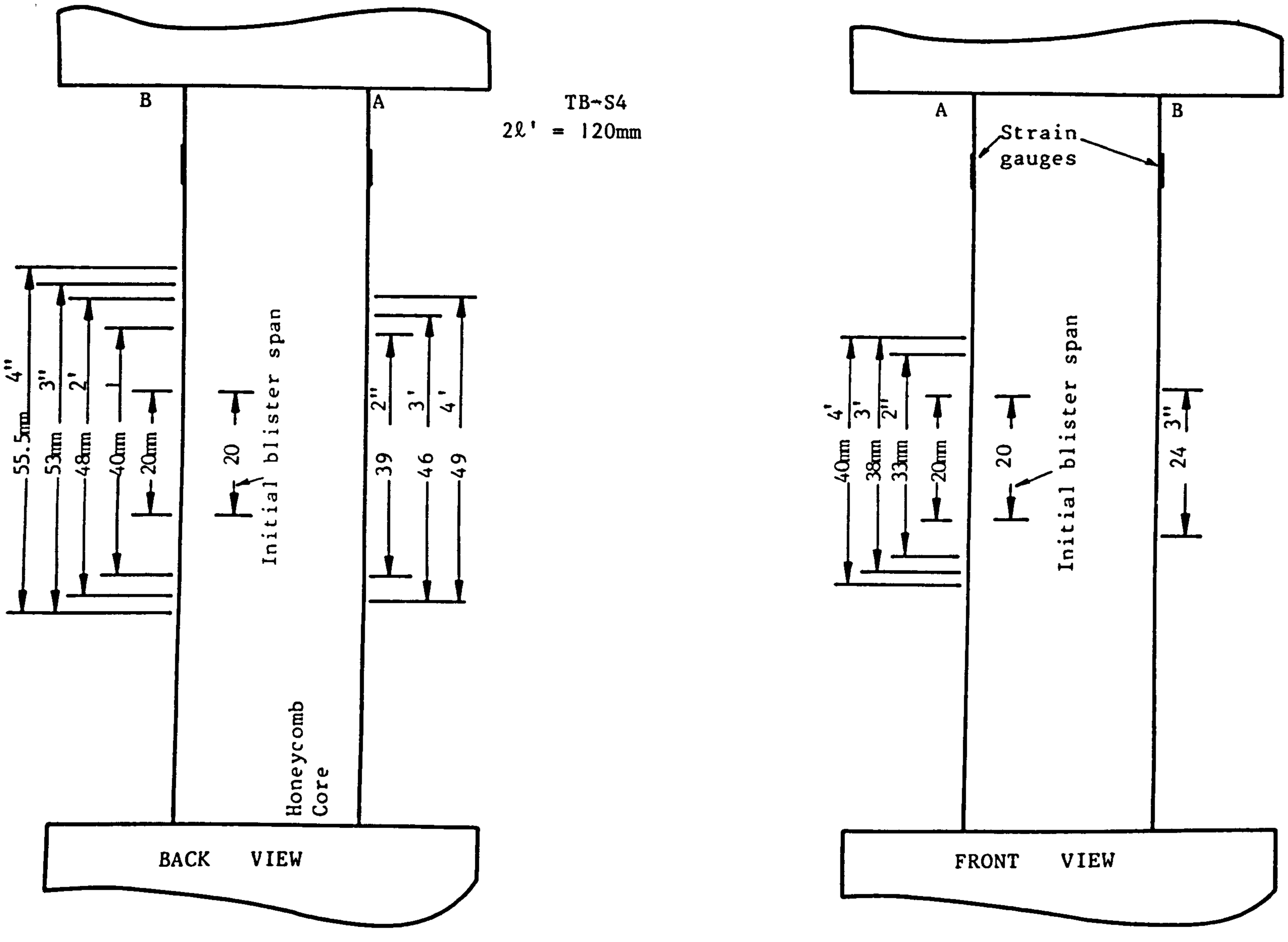

Fig. 5.28 ACCUMULATIVE PICTURE OF CONSECUTIVE CRACK PROPAGATION FOR SPECIMEN TB-S4

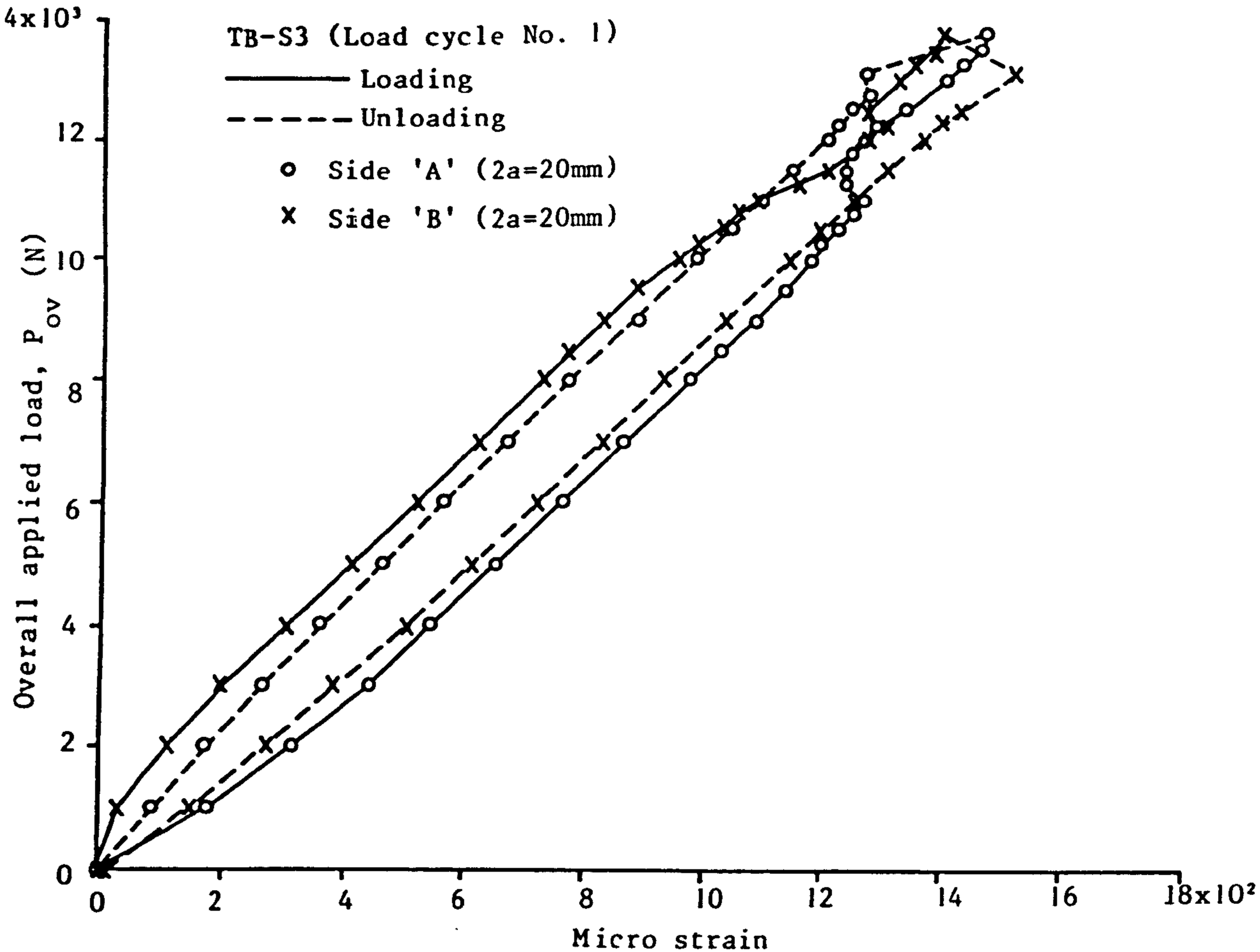

Fig. 5.29 LOAD-STRAIN RESPONSE FOR SPECIMEN TB-S3 (load cycle No. 1)

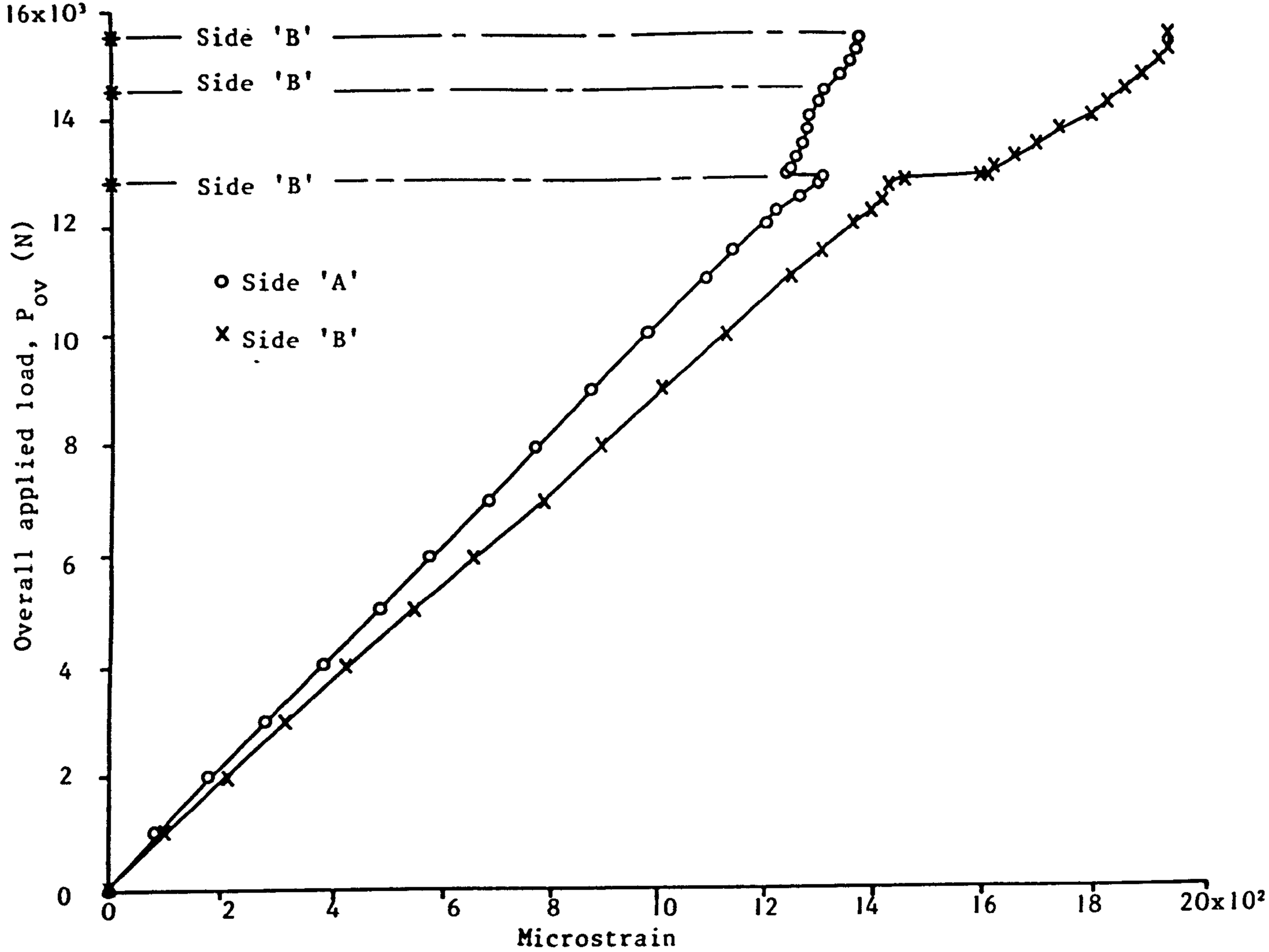

Fig. 5.30 FINAL LOAD-STRAIN RESPONSE FOR SPECIMEN TB-S3

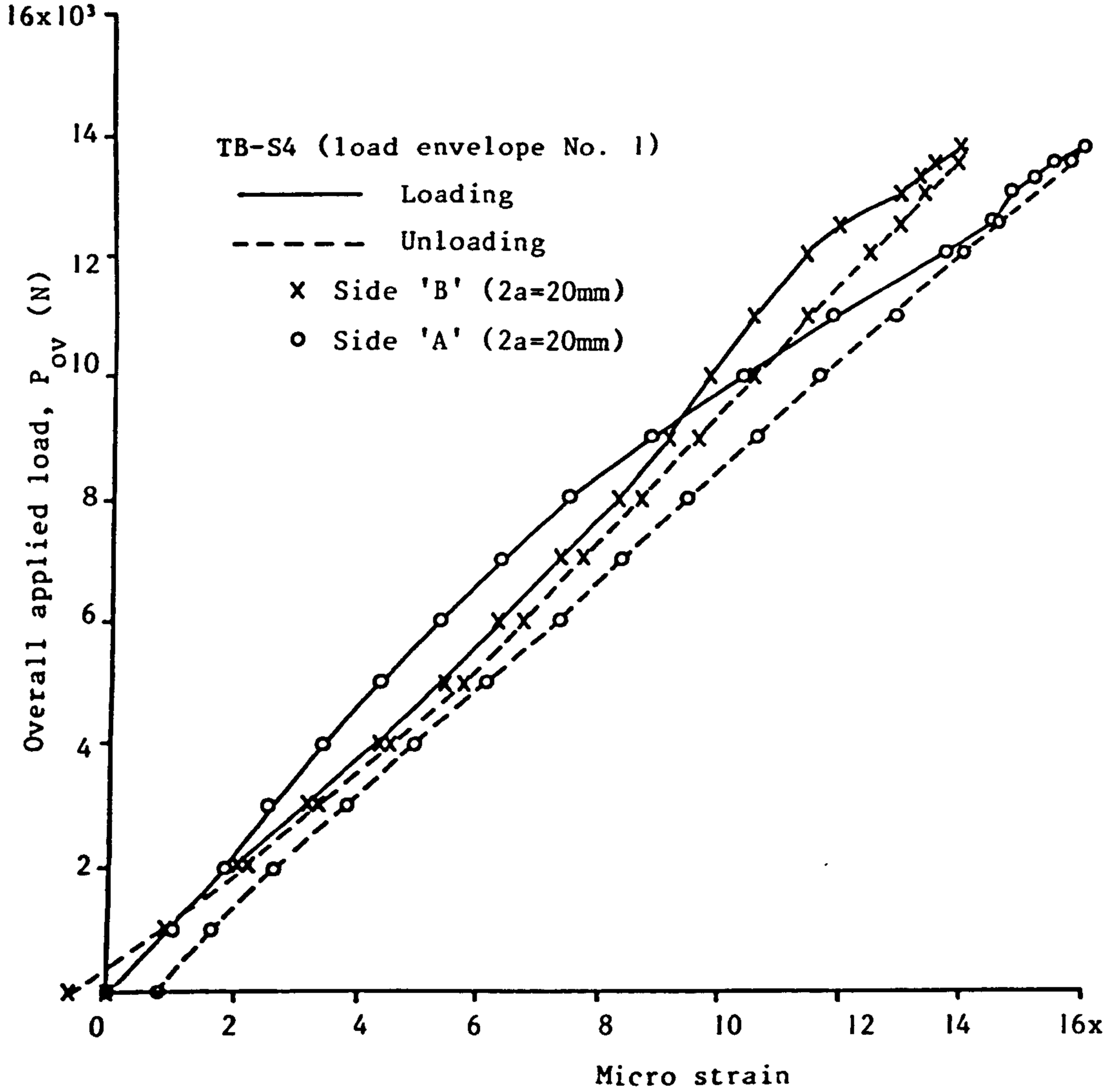

Fig. 5.31 LOAD-STRAIN RESPONSE FOR SPECIMEN TB-S4 (load envelope No. 1)

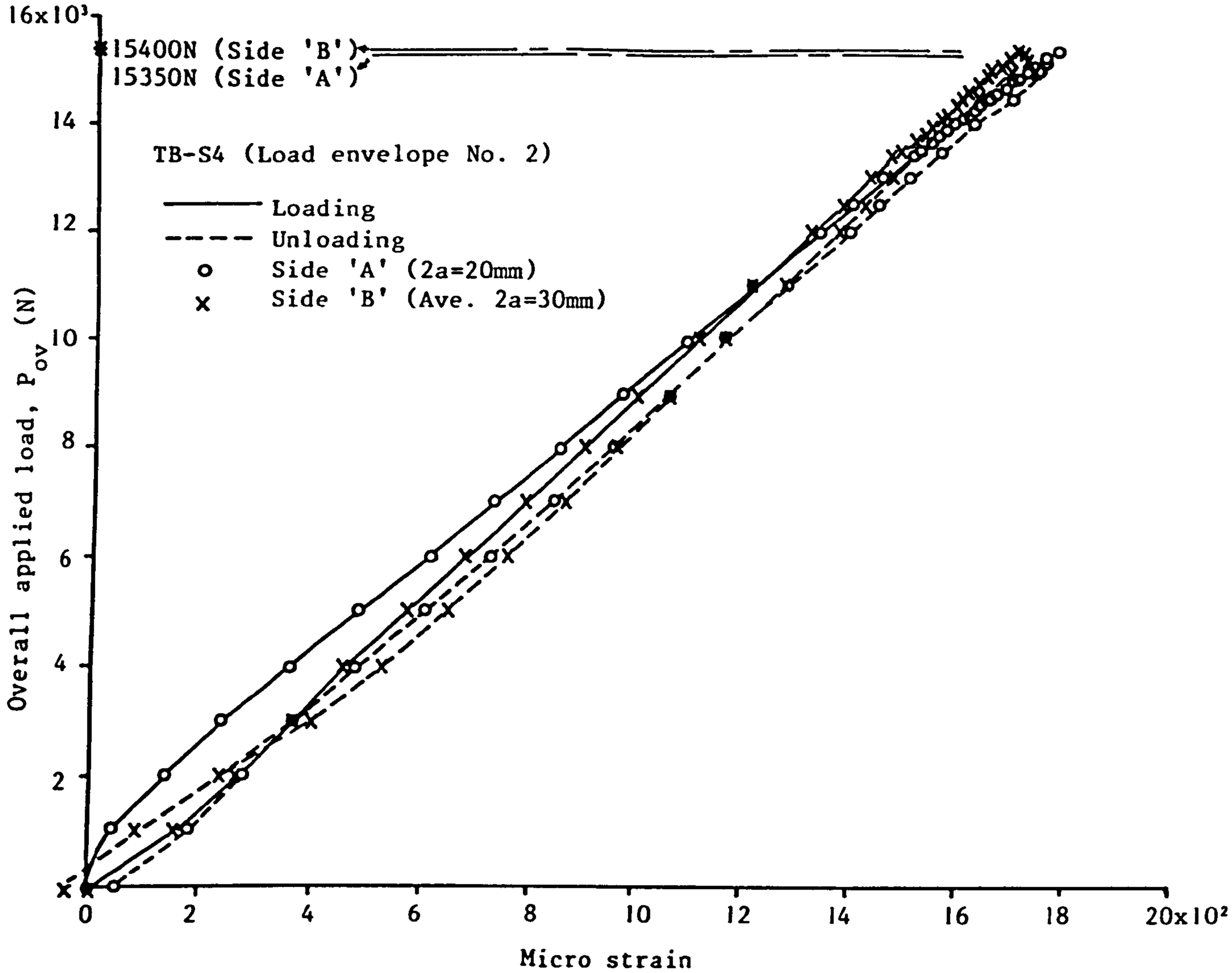

5.32 LOAD-STRAIN RESPONSE FOR SPECIMEN TB-S4 (LOAD ENVELOPE No.2)

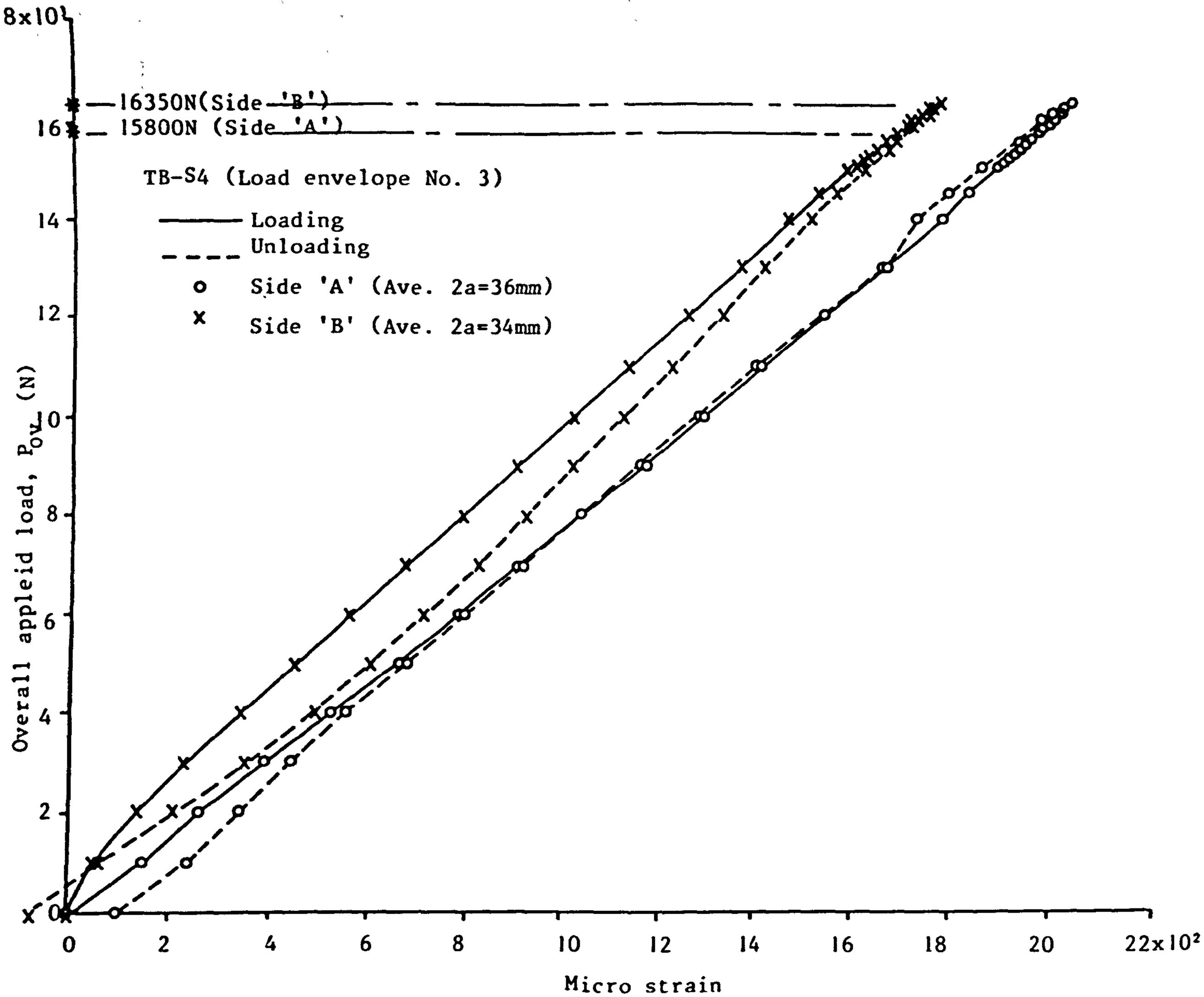

Fig. 5.33 LOAD-STRAIN RESPONSE FOR SPECIMEN TB-S4 (LOAD ENVELOPE No. 3)

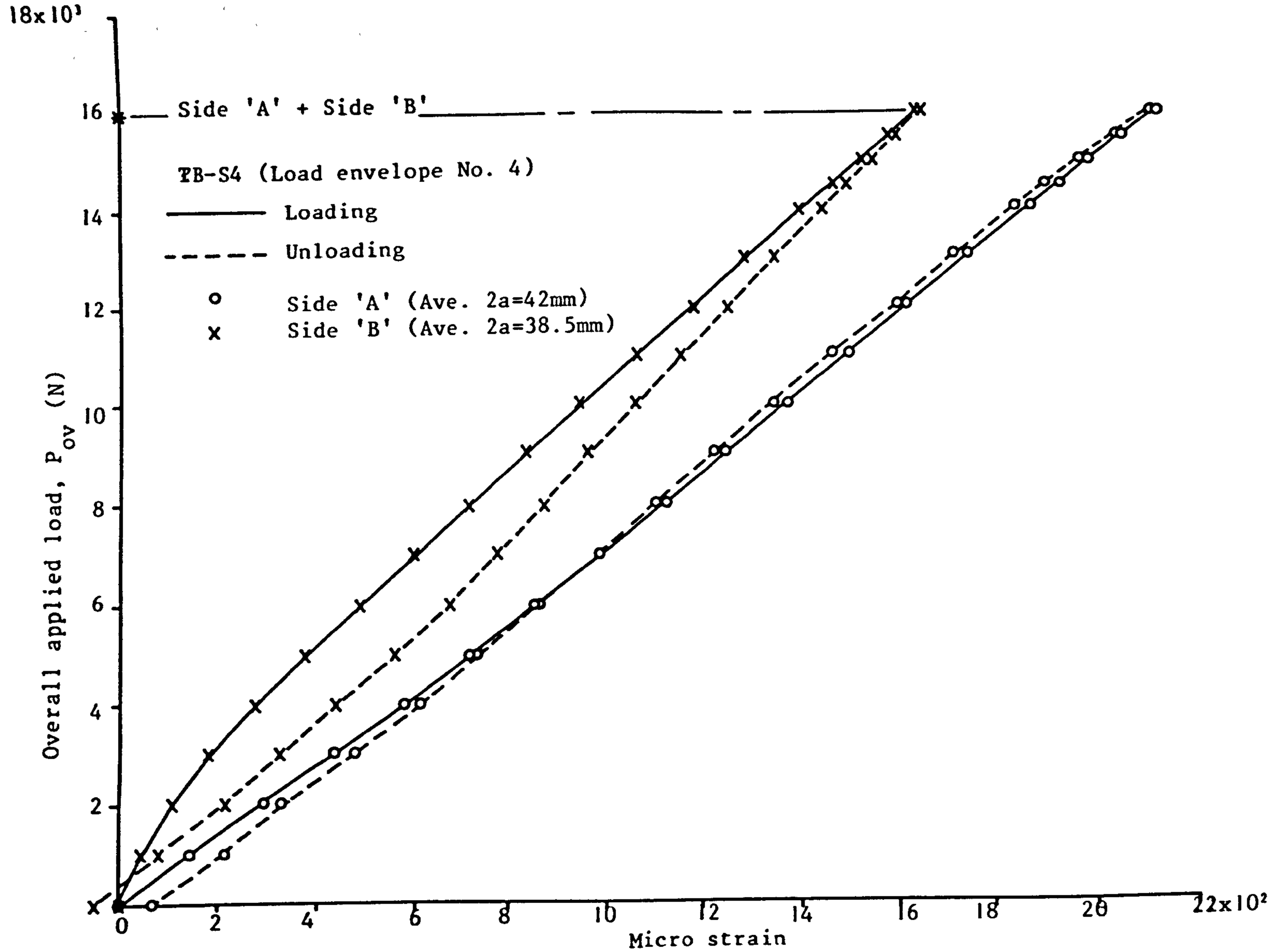

Fig. 5.34 LOAD-STRAIN RESPONSE FOR SPECIMEN TB-S4 (LOAD ENVELOPE No. 4)

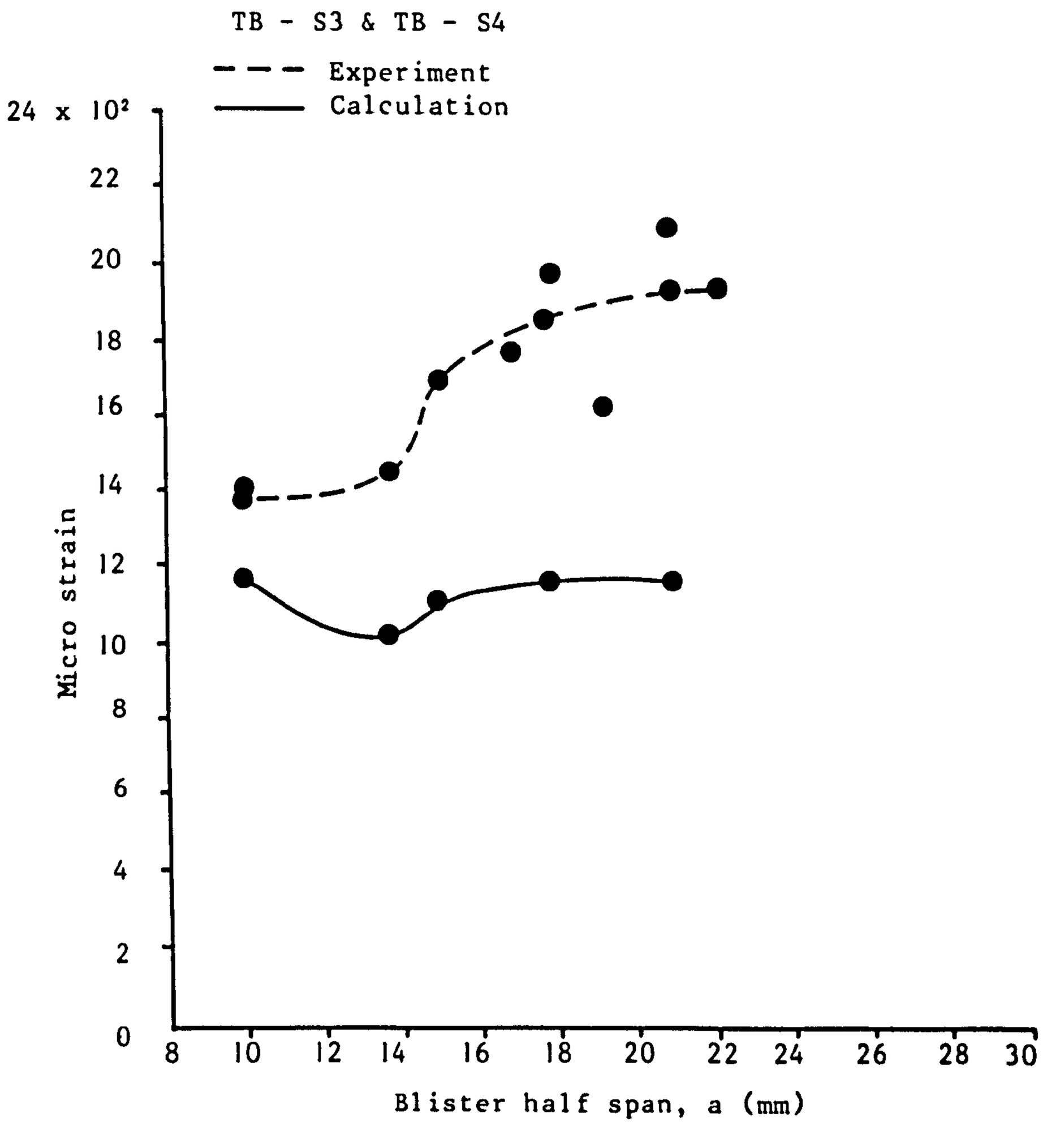

Fig. 5.35 CRITICAL APPLIED STRAIN VS. BLISTER HALF SPAN FOR SPECIMENS TB-S3 AND TB-S4

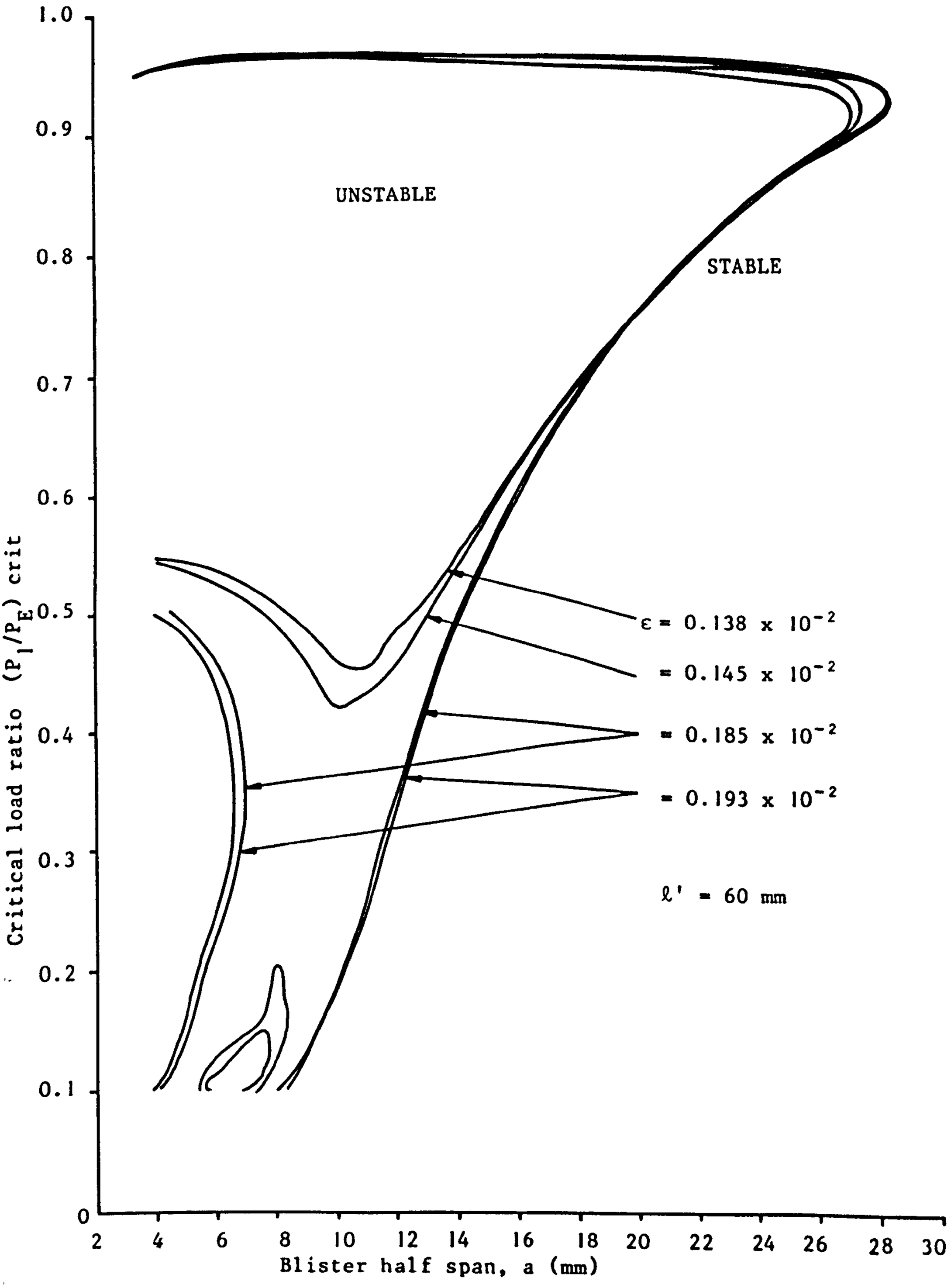

Fig. 5.36 CRITICAL LOAD RATIO VS. BLISTER HALF SPAN FOR VARIOUS APPLIED STRAINS

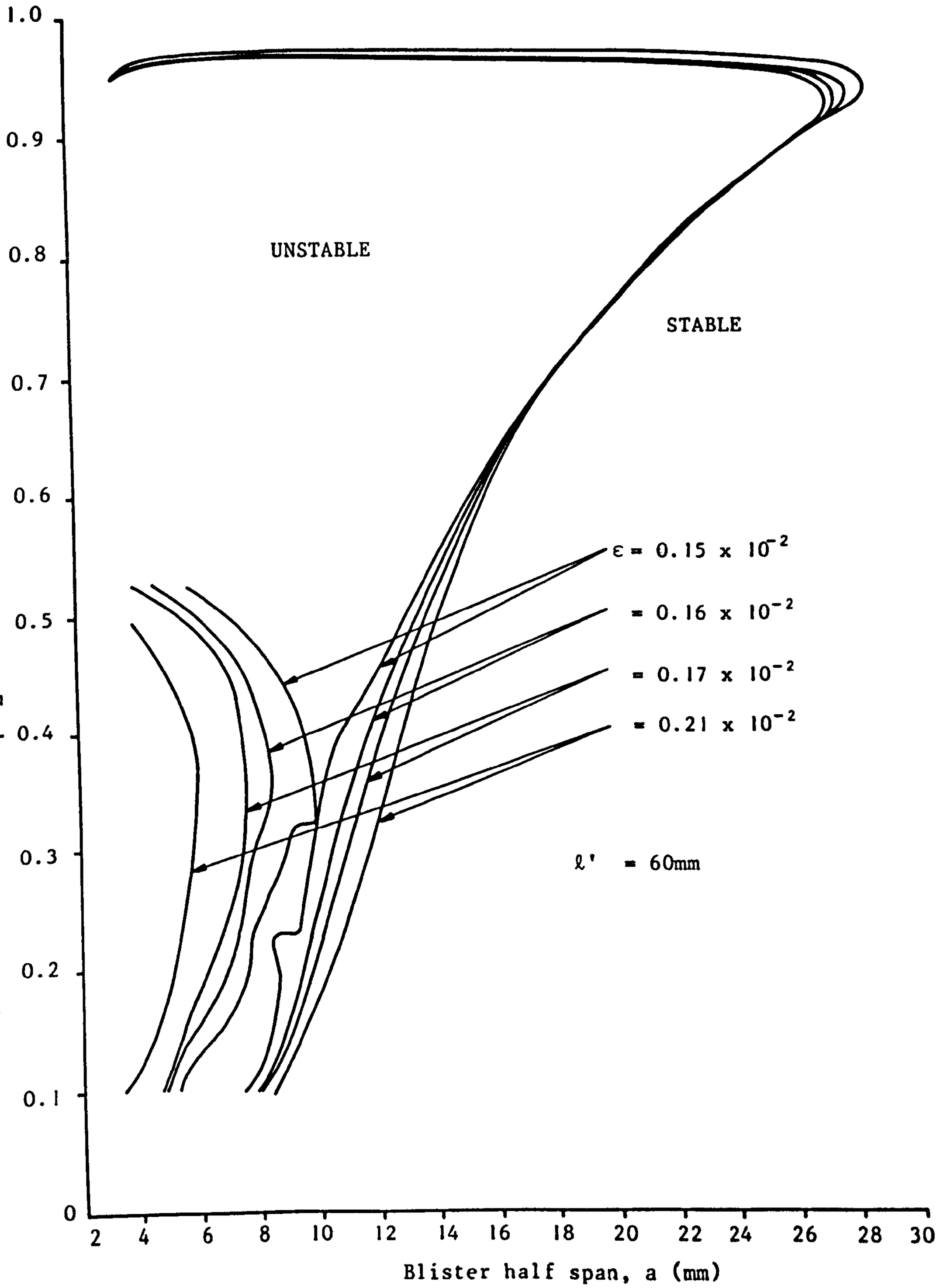

Fig. 5.37 CRITICAL LOAD RATIO VS. BLISTER HALF SPAN FOR VARIOUS APPLIED STRAINS

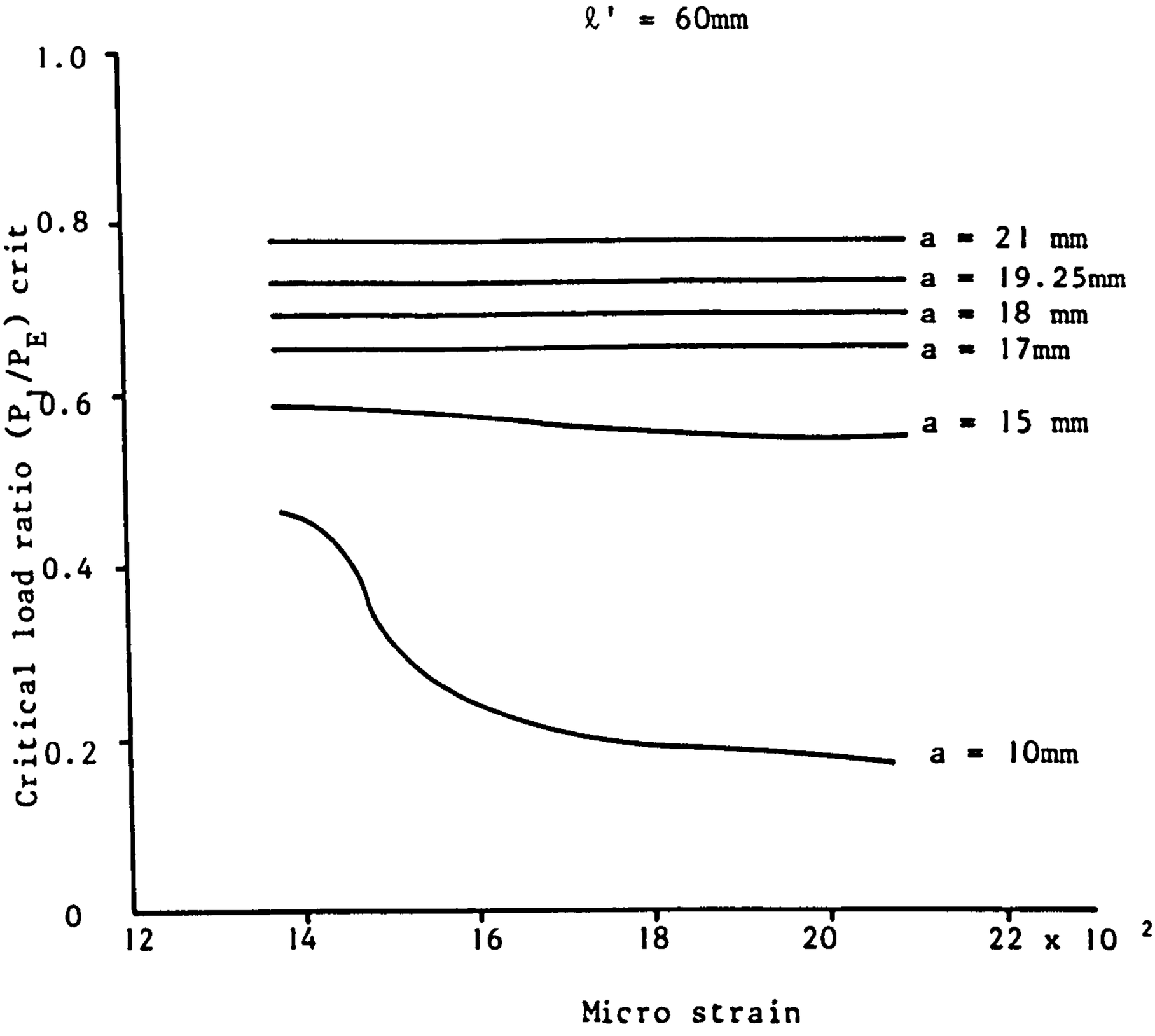

Fig. 5.38 CRITICAL LOAD RATIO VS. APPLIED STRAIN FOR VARIOUS BLISTER HALF SPANS

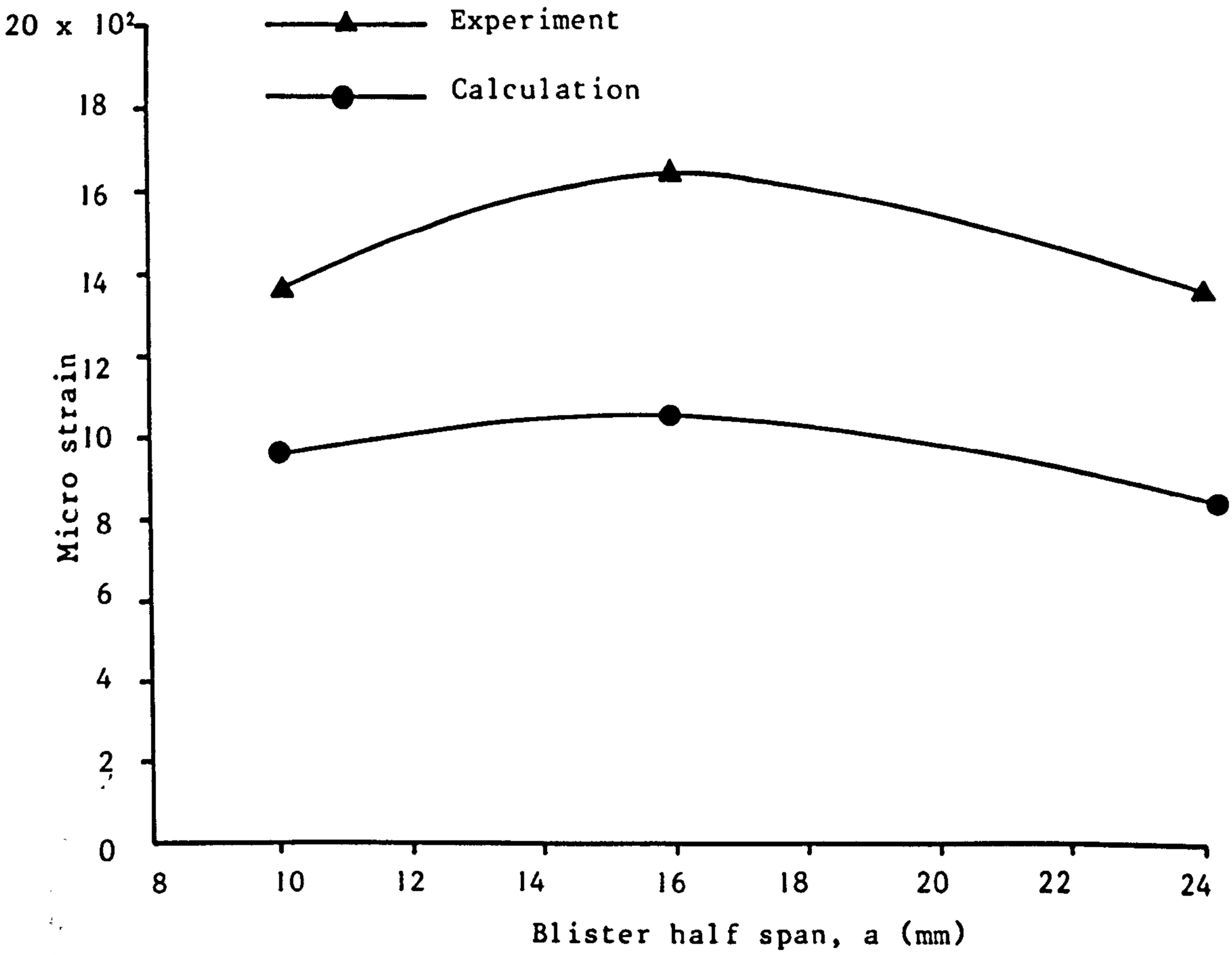

Fig. 5.39 CRITICAL APPLIED STRAIN VS. BLISTER HALF SPAN FOR THE FIRST DELAMINATION IN ALL TEST SPECIMENS

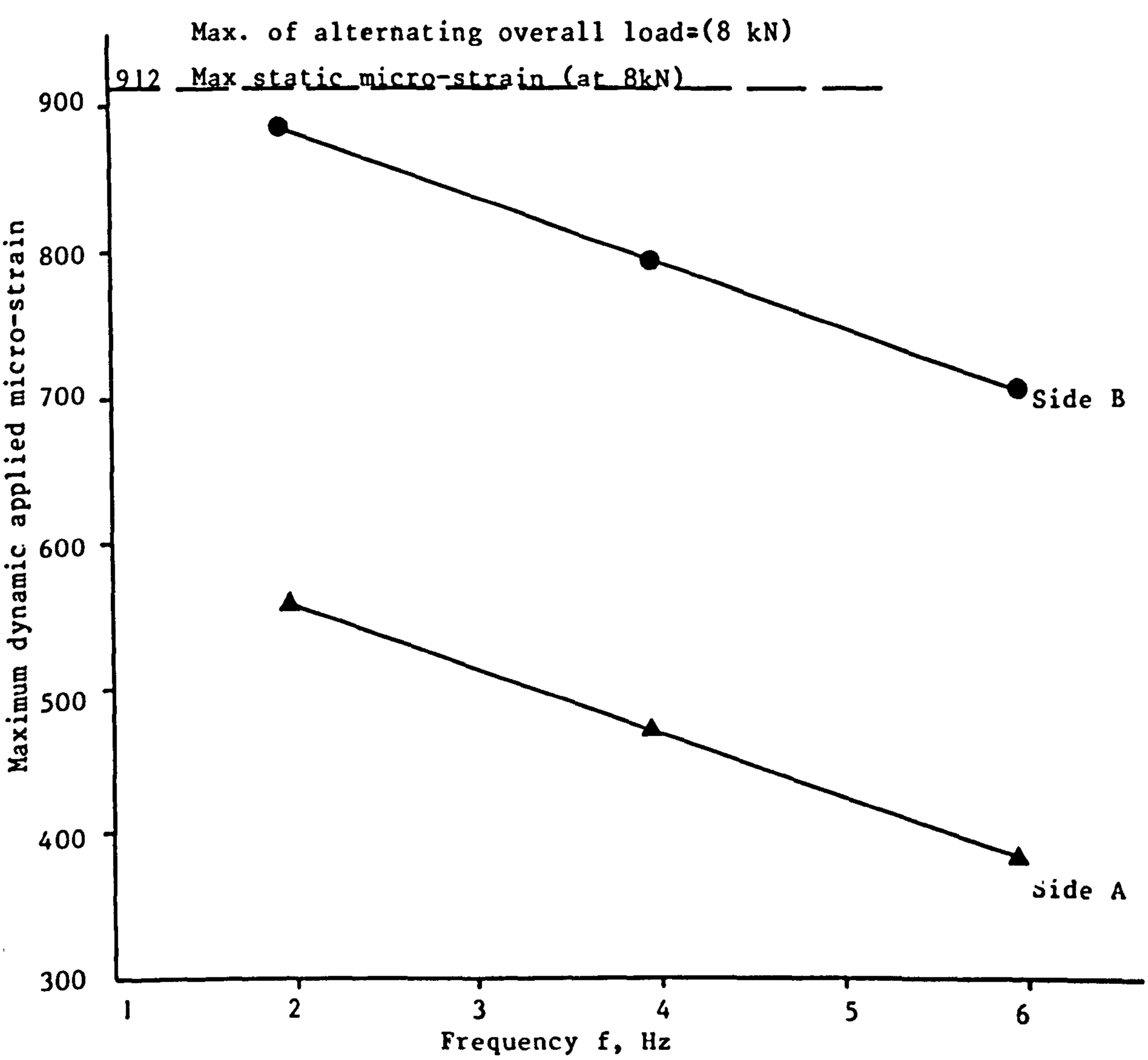

Fig. 5.40 TYPICAL BEHAVIOUR OF FREQUENCY VS. MAX DYNAMIC APPLIED STRAIN (FROM TEST OF SPECIMEN TB - F1)

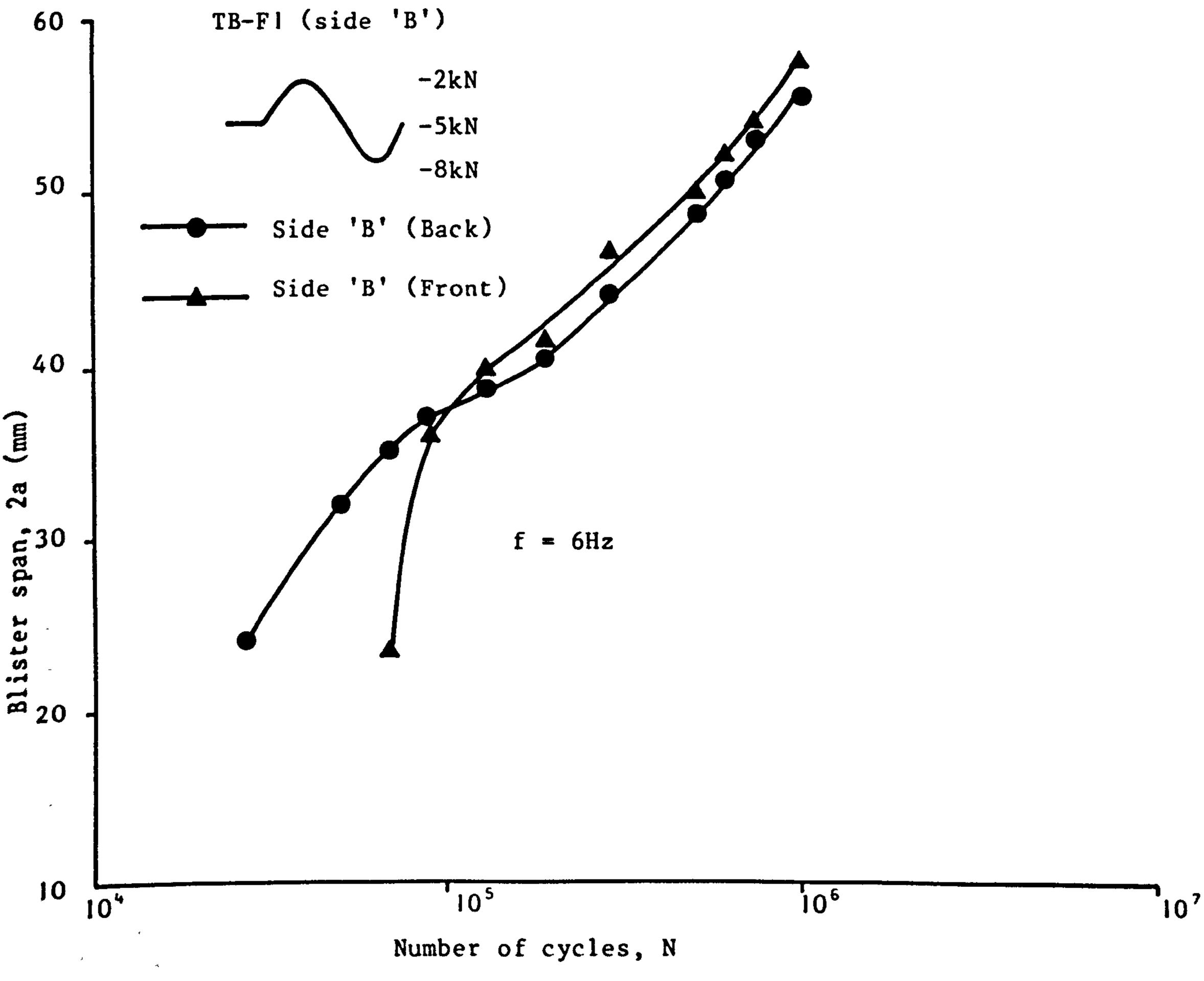

Fig. 5.41 FATIGUE CRACK PROPAGATION DATA FOR SPECIMEN TB-F1 (Side 'B')

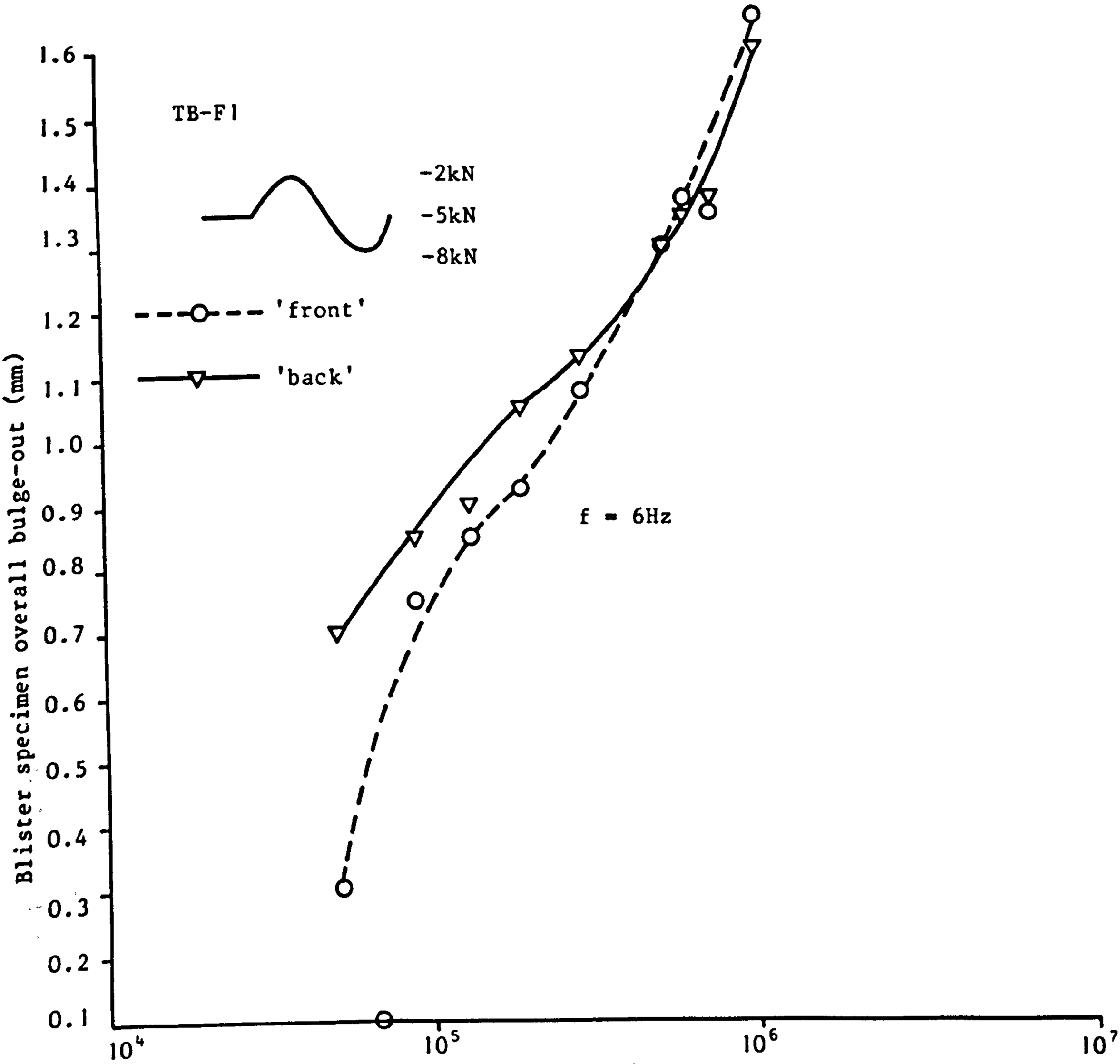

Fig. 5.42 OVERALL BULGE-OUT VS. NUMBER OF CYCLES FOR SPECIMEN TB-F1

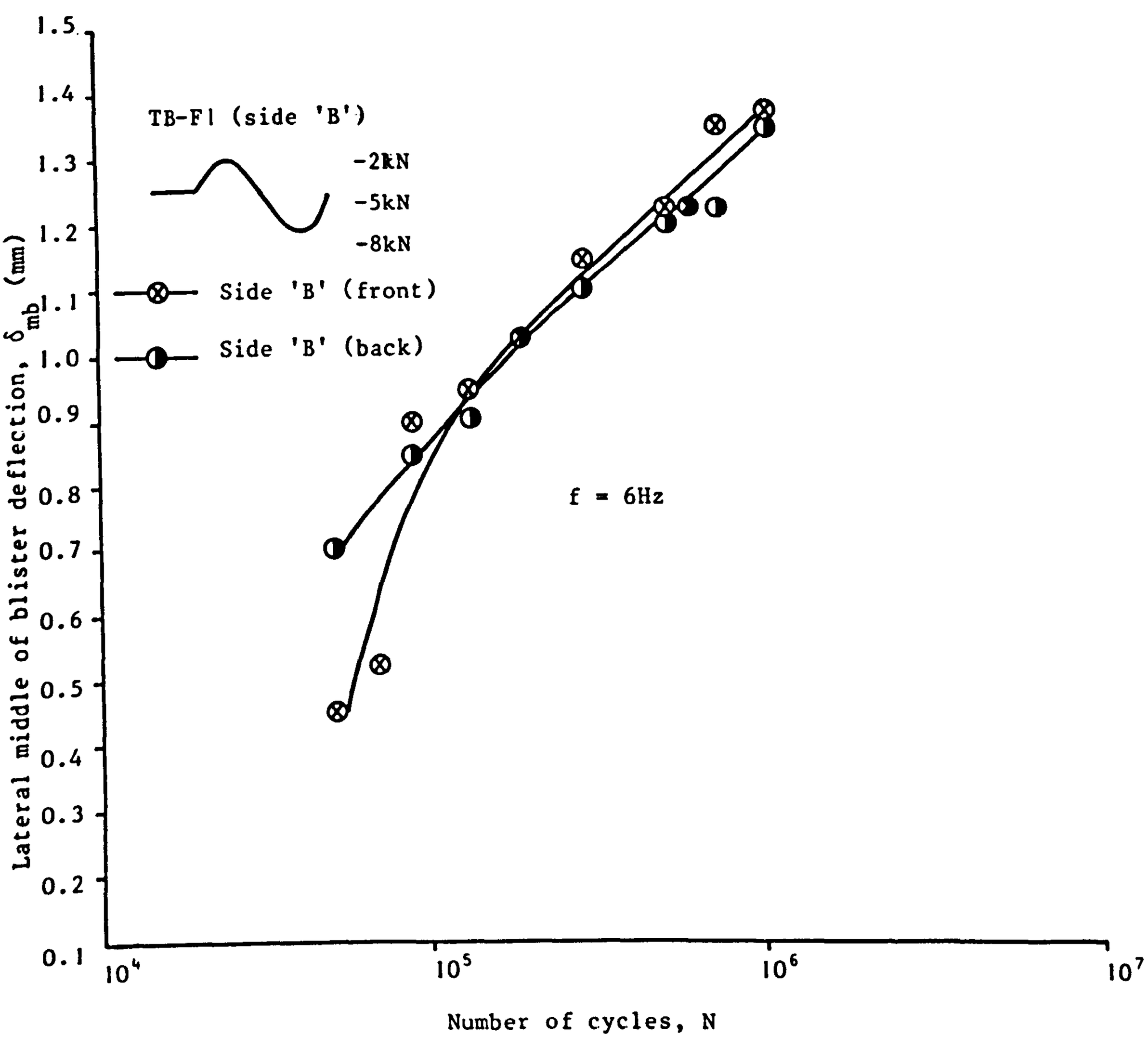

Fig. 5.43 MIDDLE OF BLISTER DEFLECTION VS. NUMBER OF CYCLES FOR SEPCIMEN TB-F1 (Side 'B')

TB-F2

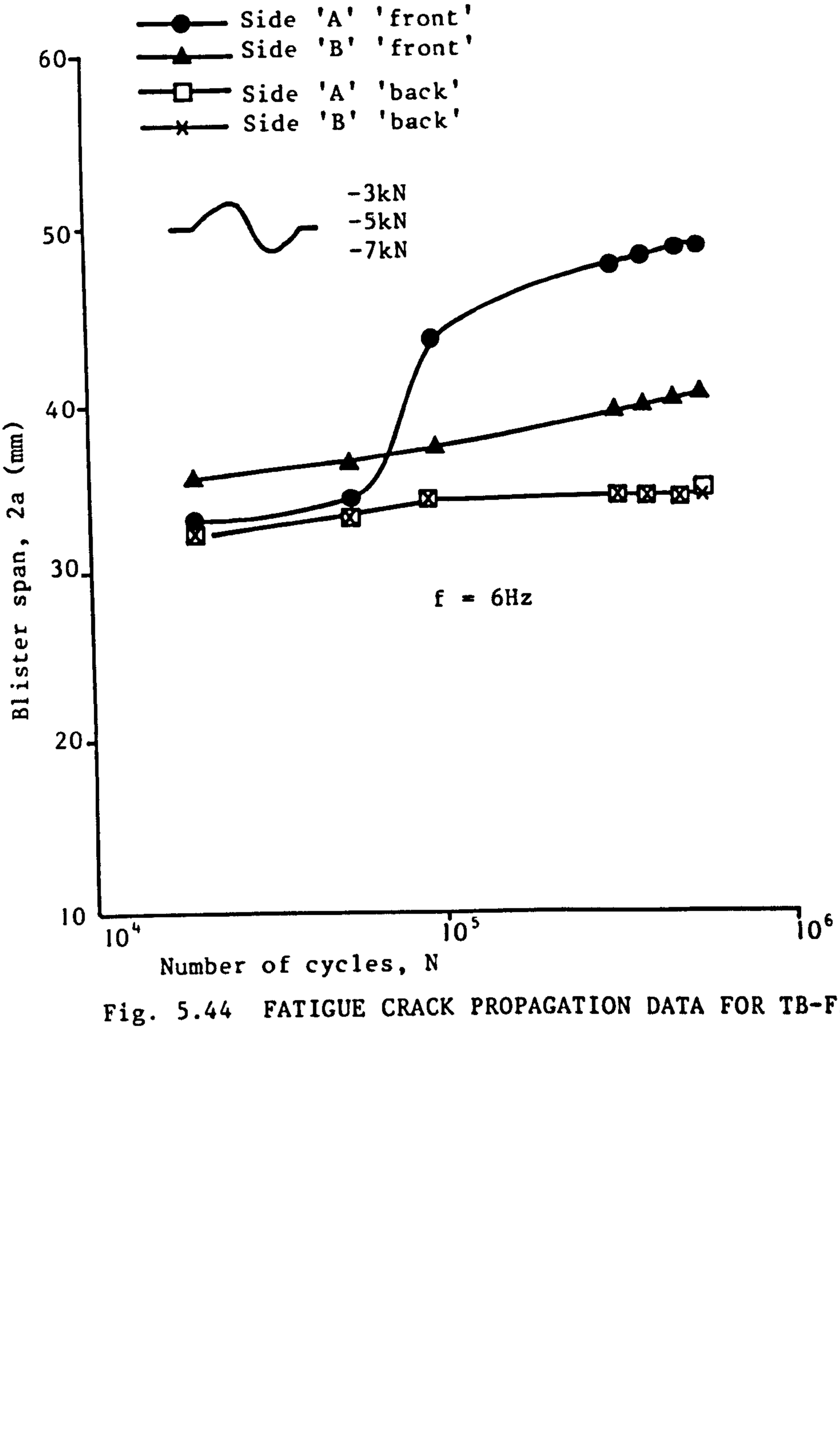

Fig. 5.44 FATIGUE CRACK PROPAGATION DATA FOR TB-F2

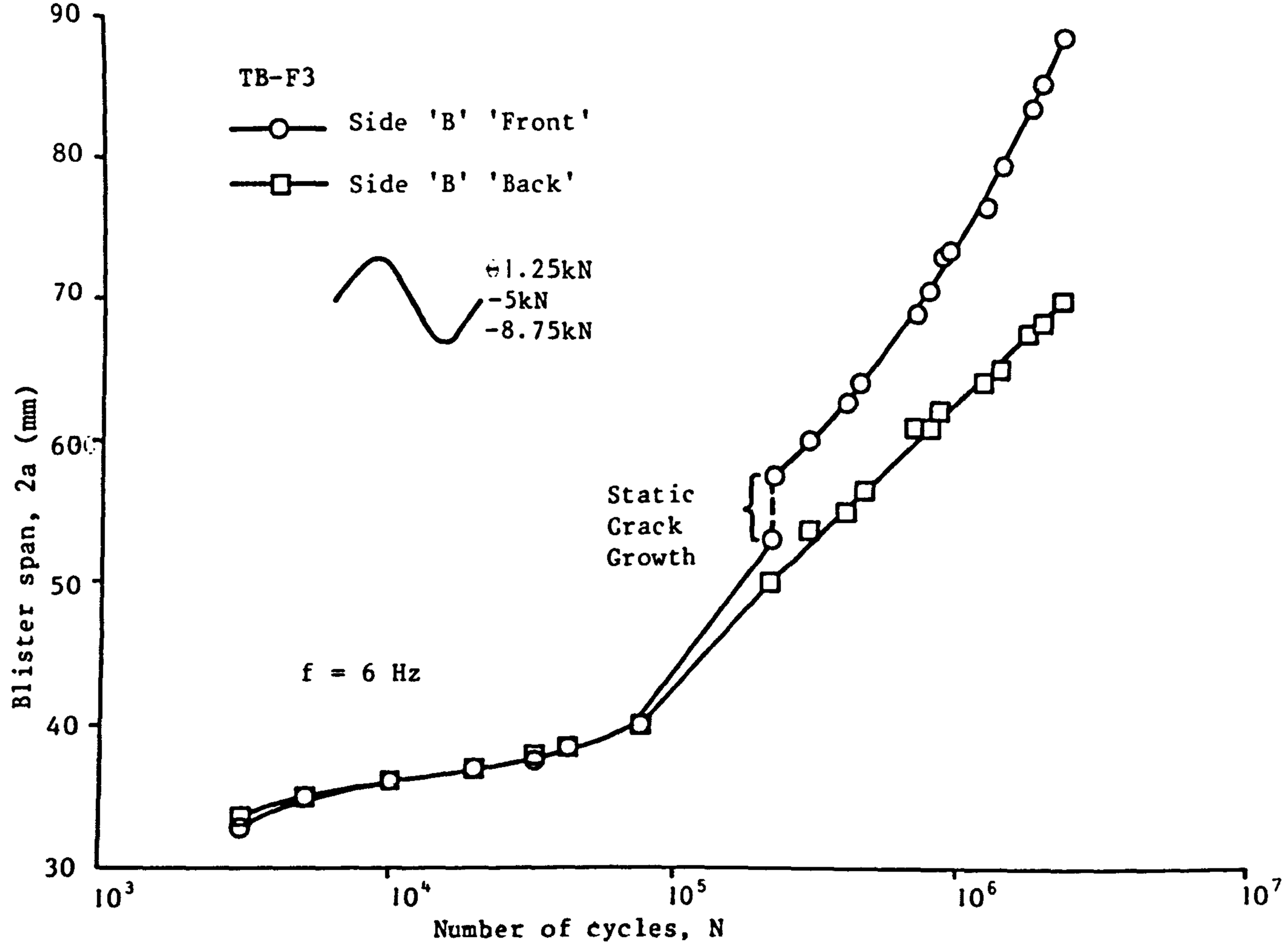

Fig. 5.45 FATIGUE CRACK PROPAGATION DATA FOR SPECIMEN TB-F3 (Side 'B')

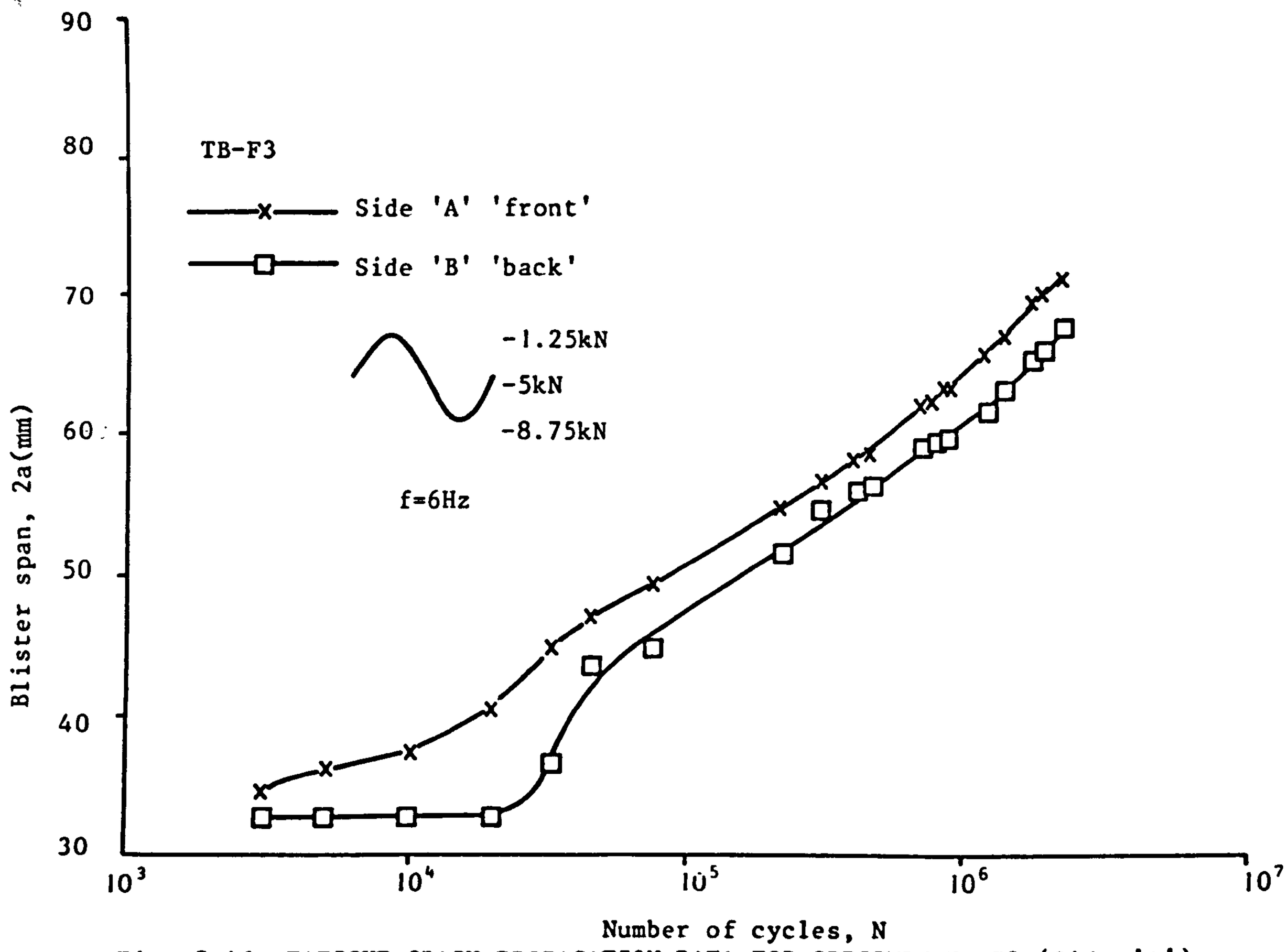

Fig. 5.46 FATIGUE CRACK PROPAGATION DATA FOR SPECIMEN TB-F3 (Side 'A')

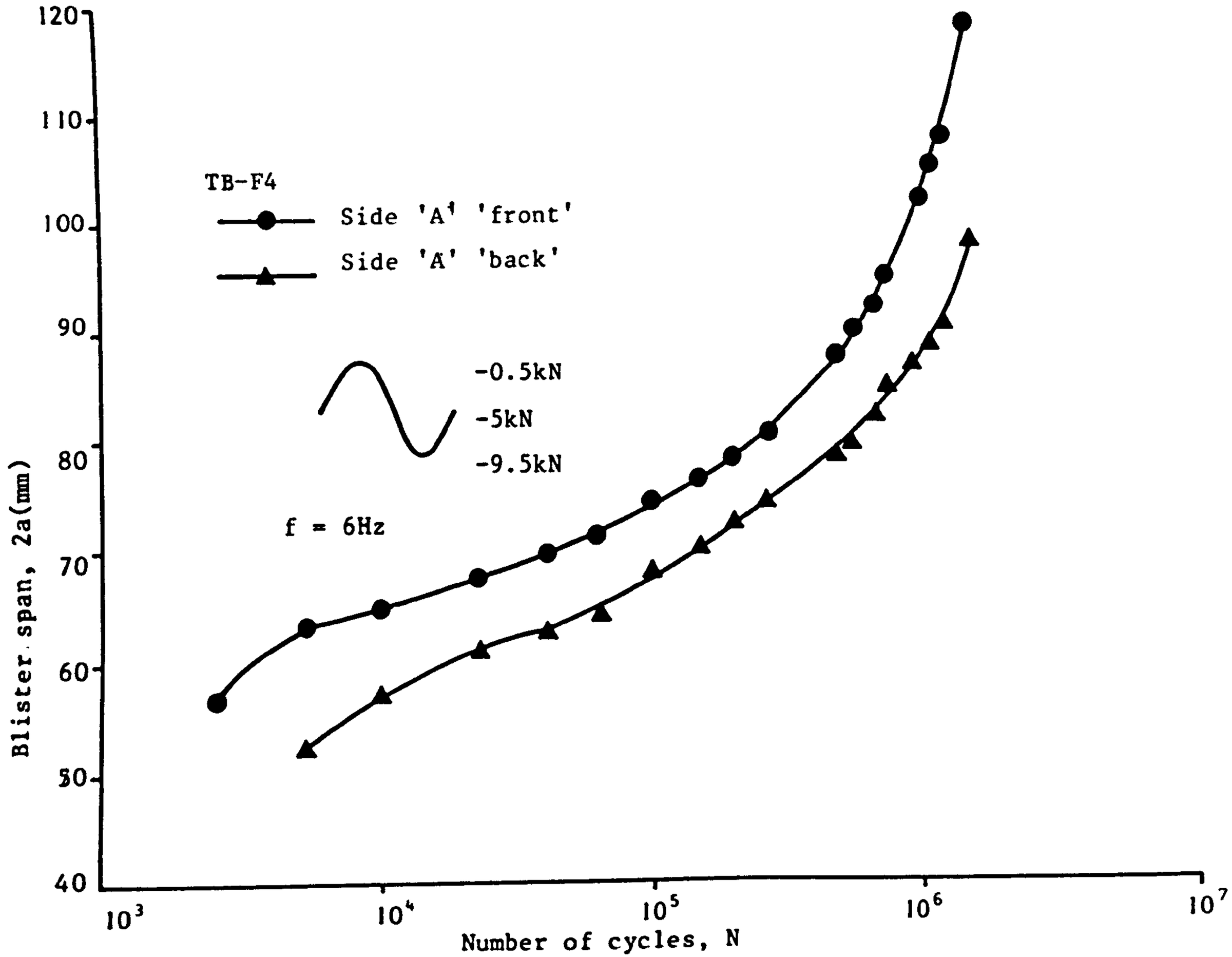

Fig. 5.47 FATIGUE CRACK PROPAGATION DATA FOR SPECIMEN TB-F4 (side 'A')

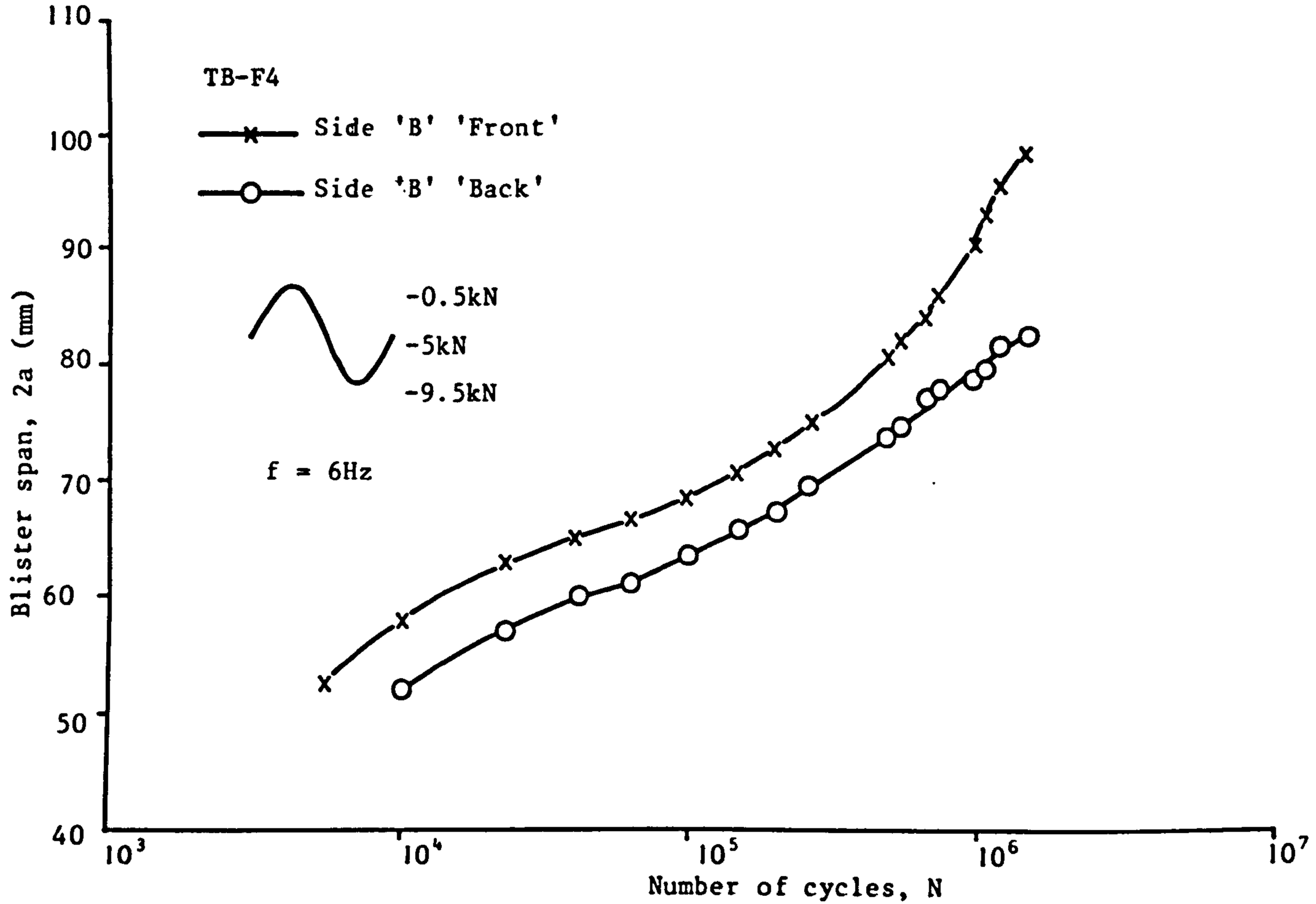

Fig. 5.48 FATIGUE CRACK PROPAGATION DATA FOR SPECIMEN TB-F4 (Side 'B')

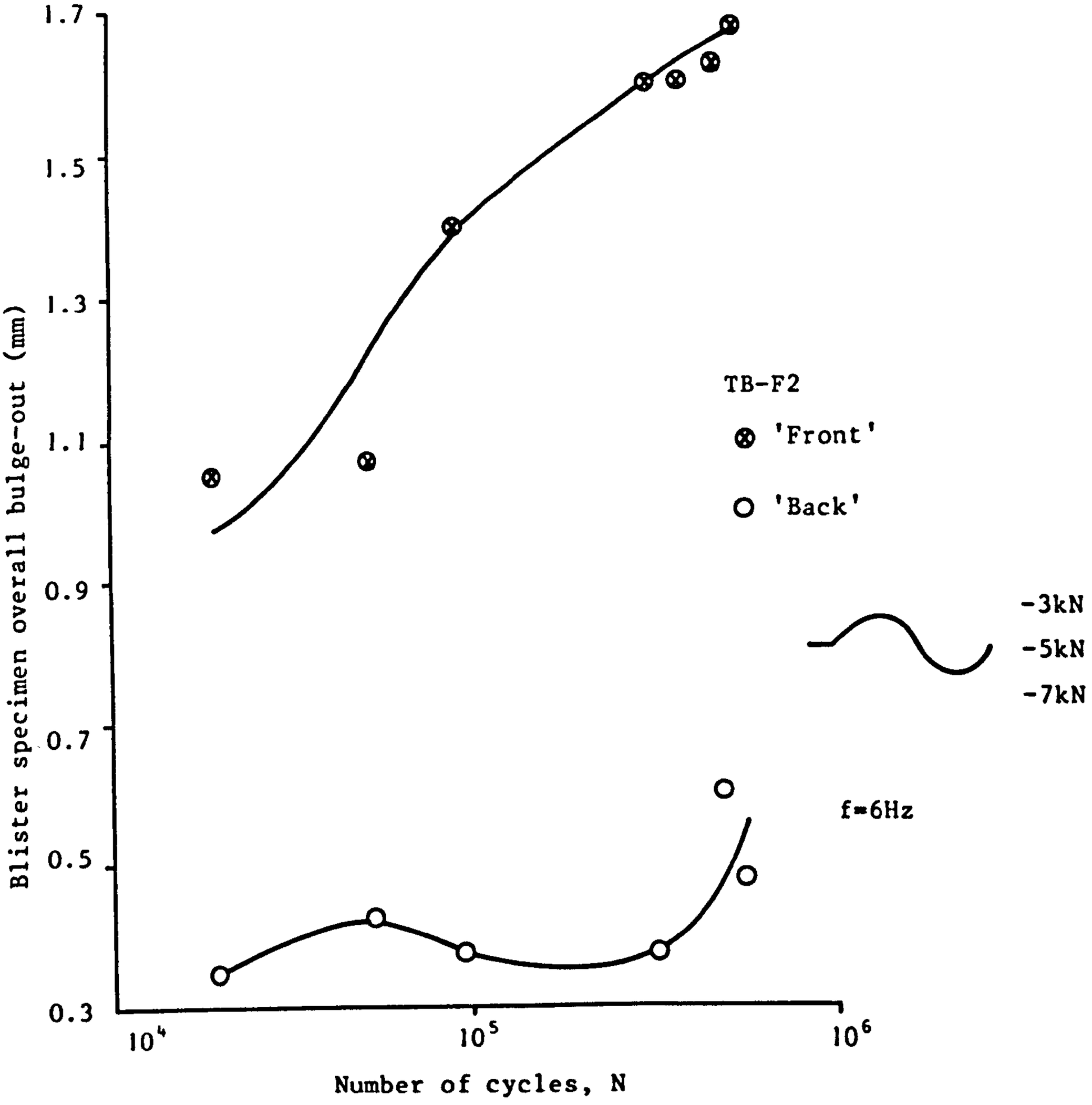

Fig. 5.49 OVERALL BULGE-OUT VS. NUMBER OF CYCLES FOR SPECIMEN TB-F2

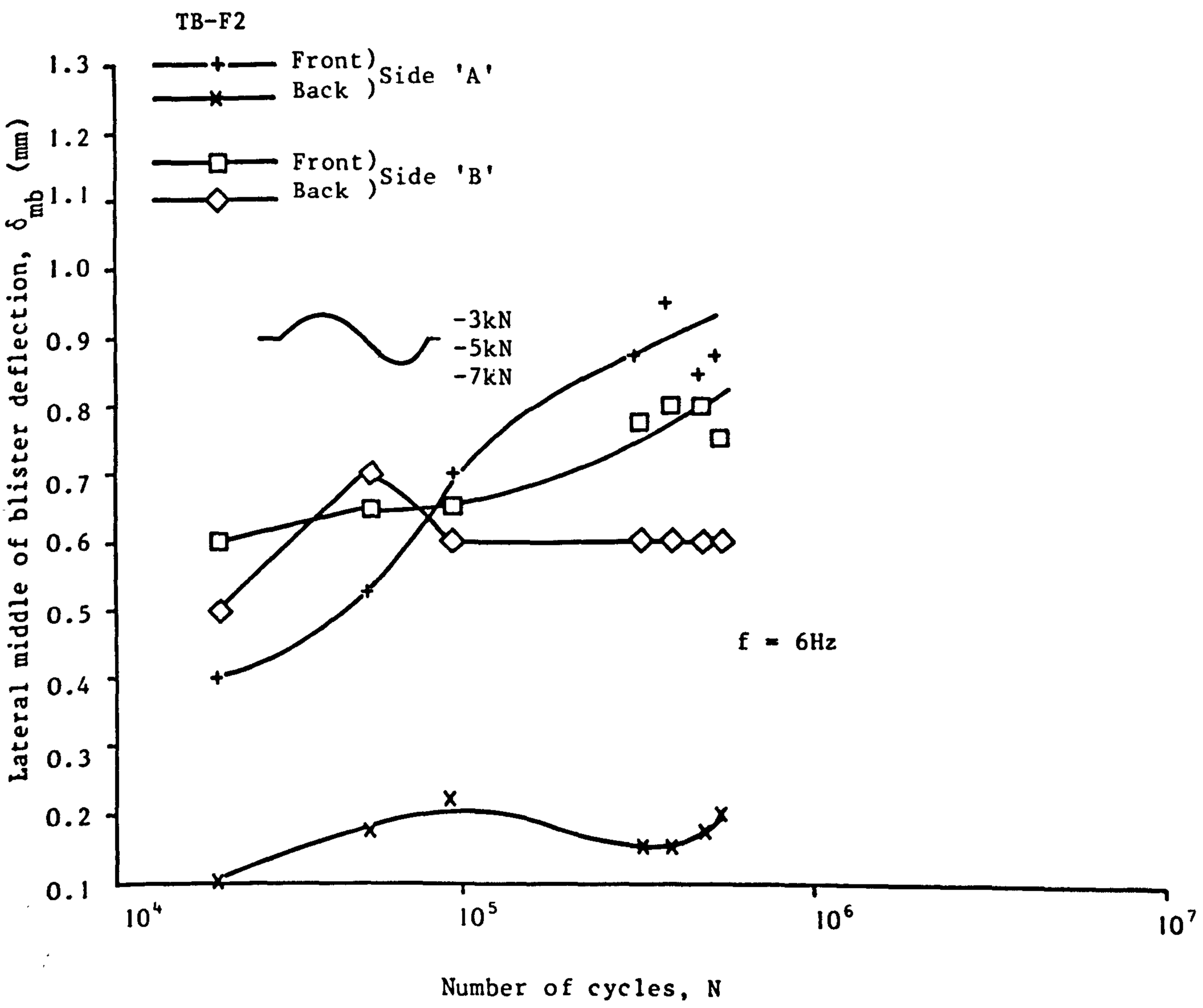

Fig. 5.50 MIDDLE OF BLISTER DEFLECTION VS. NUMBER OF CYCLES FOR SPECIMEN TB-F2

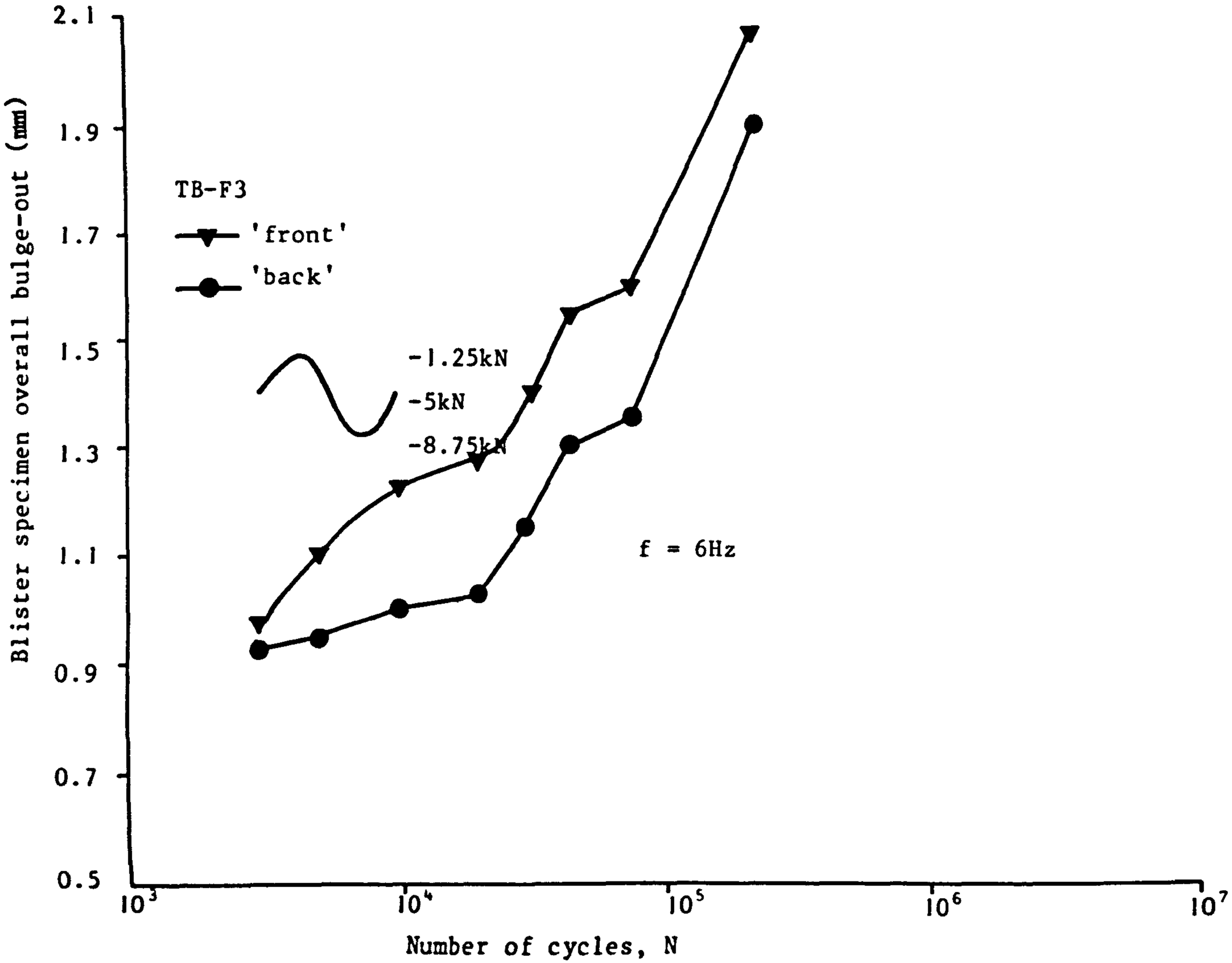

Fig. 5.51 OVERALL BULGE-OUT VS. NUMBER OF CYCLES FOR SPECIMEN TB-F3

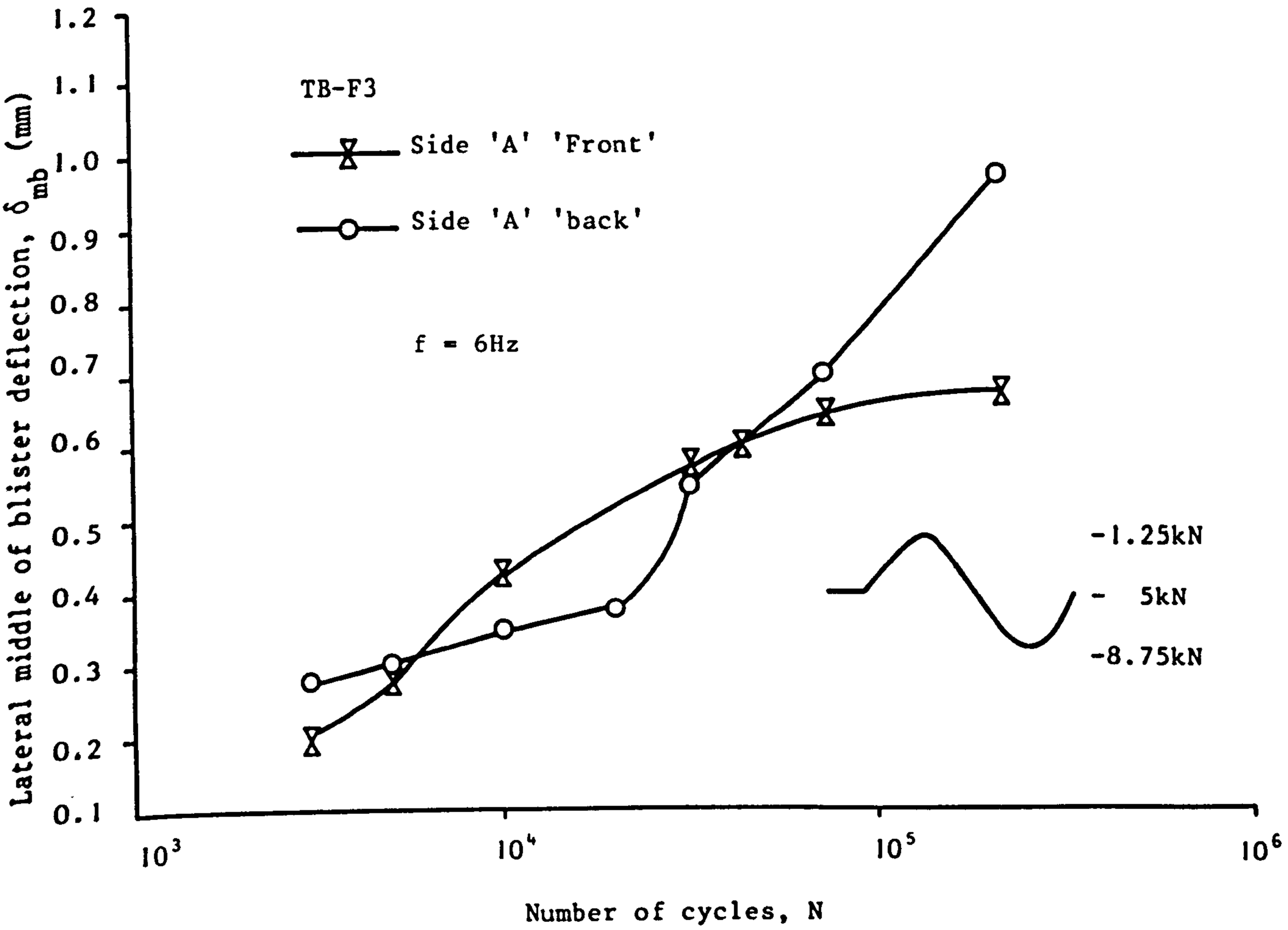

Fig. 5.52 MIDDLE OF BLISTER DEFLECTION VS. NUMBER OF CYCLES FOR SPECIMEN TB-F3 (Side 'A')

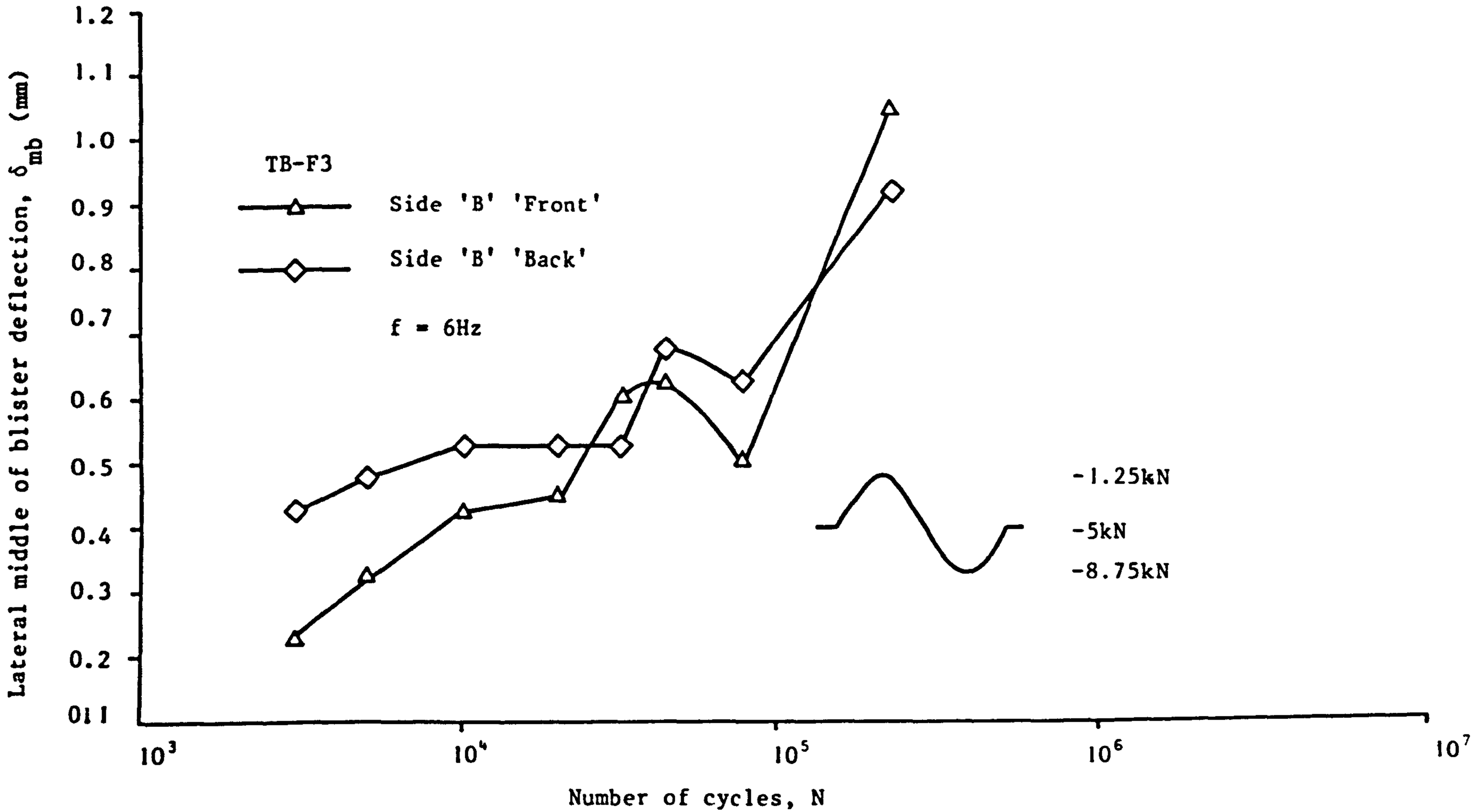

Fig. 5.53 MIDDLE OF BLISTER DEFLECTION VS. NUMBER OF CYCLES FOR SPECIMEN TB-F3 (Side 'B')

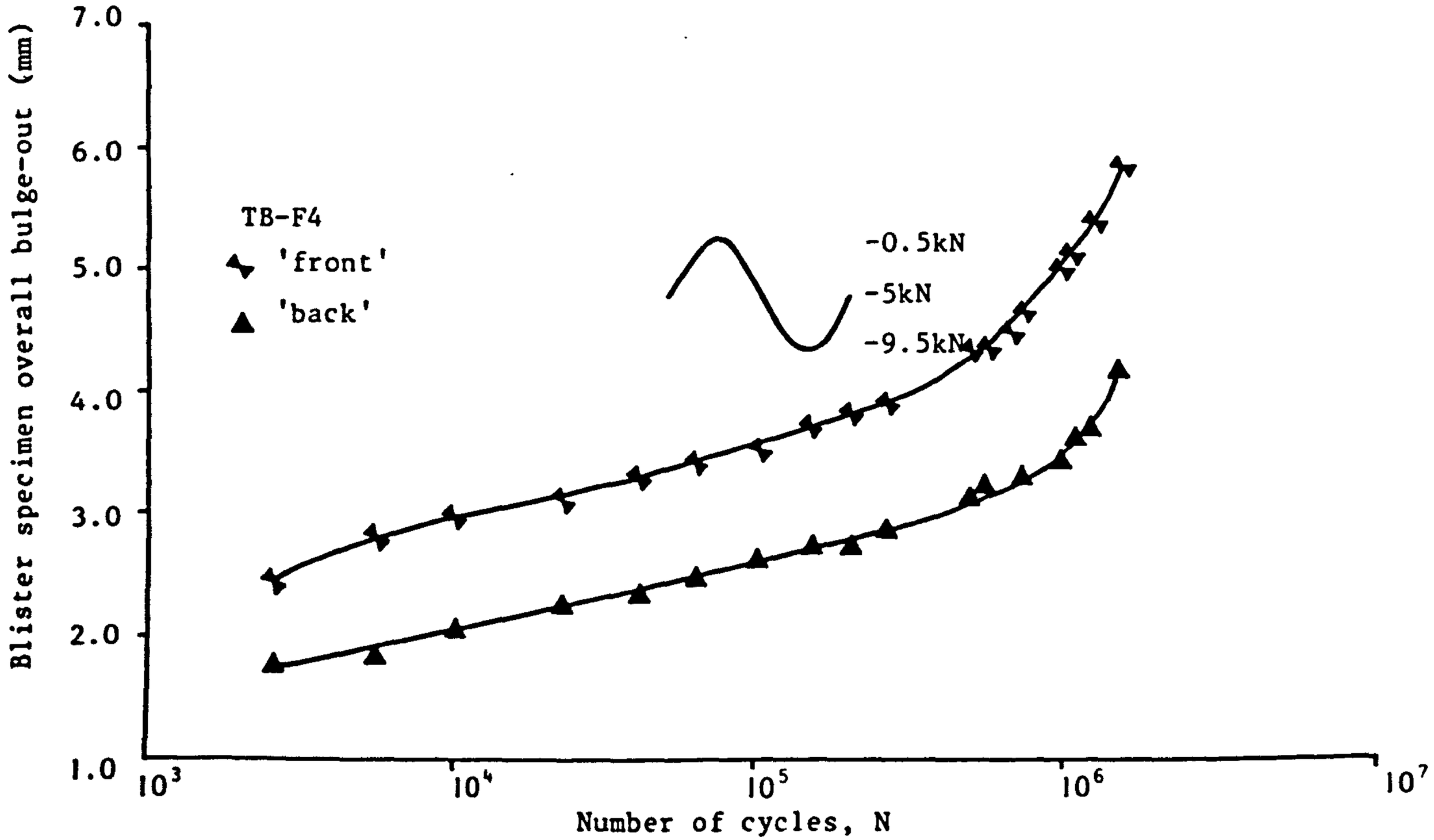

Fig. 5.54 OVERALL BULGE-OUT VS. NUMBER OF CYCLES FOR SPECIMEN TB-F4

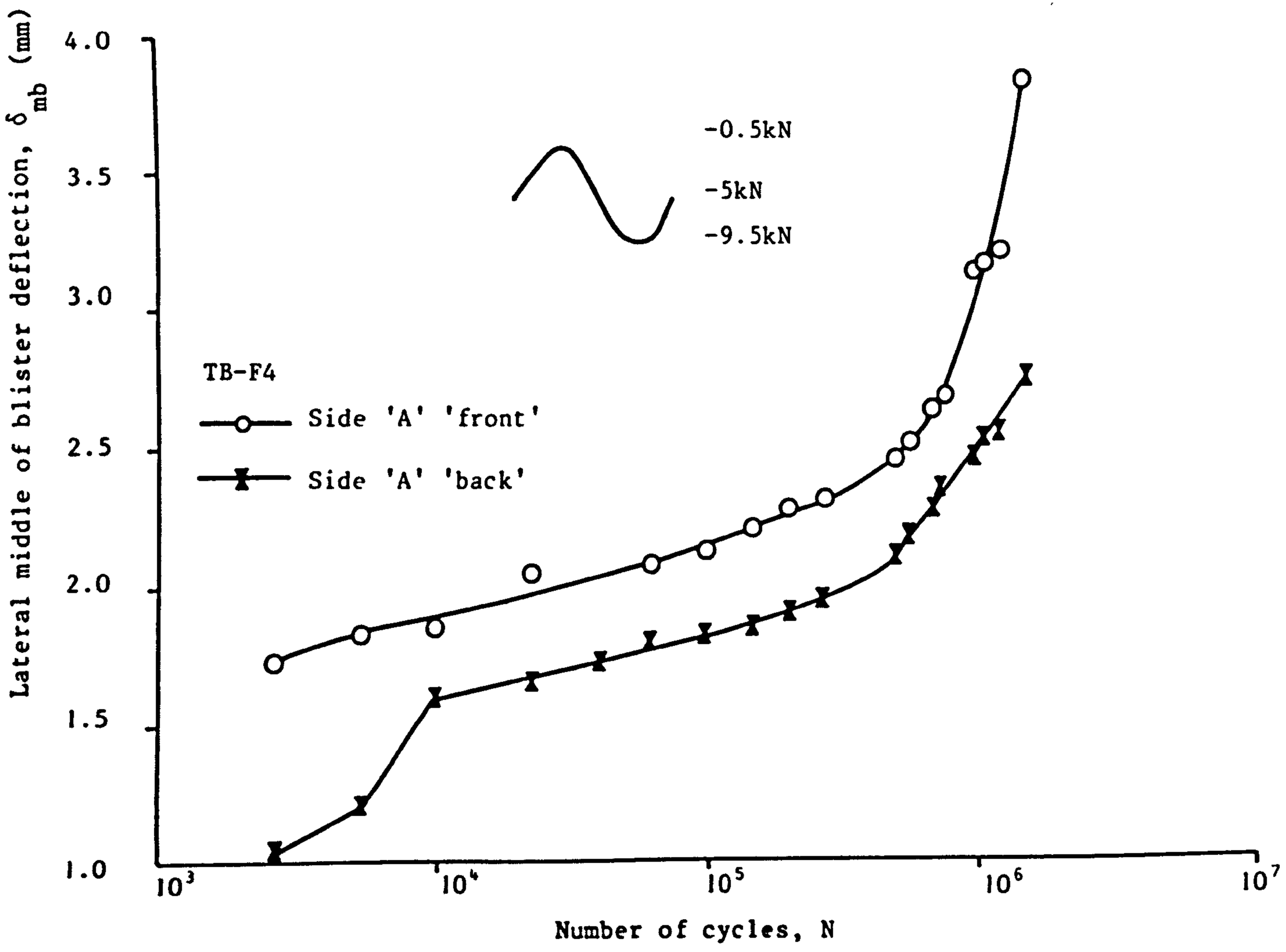

Fig. 5.55 MIDDLE OF BLISTER DEFLECTION VS. NUMBER OF CYCLES FOR SPECIMEN TB-F4 (side 'A')

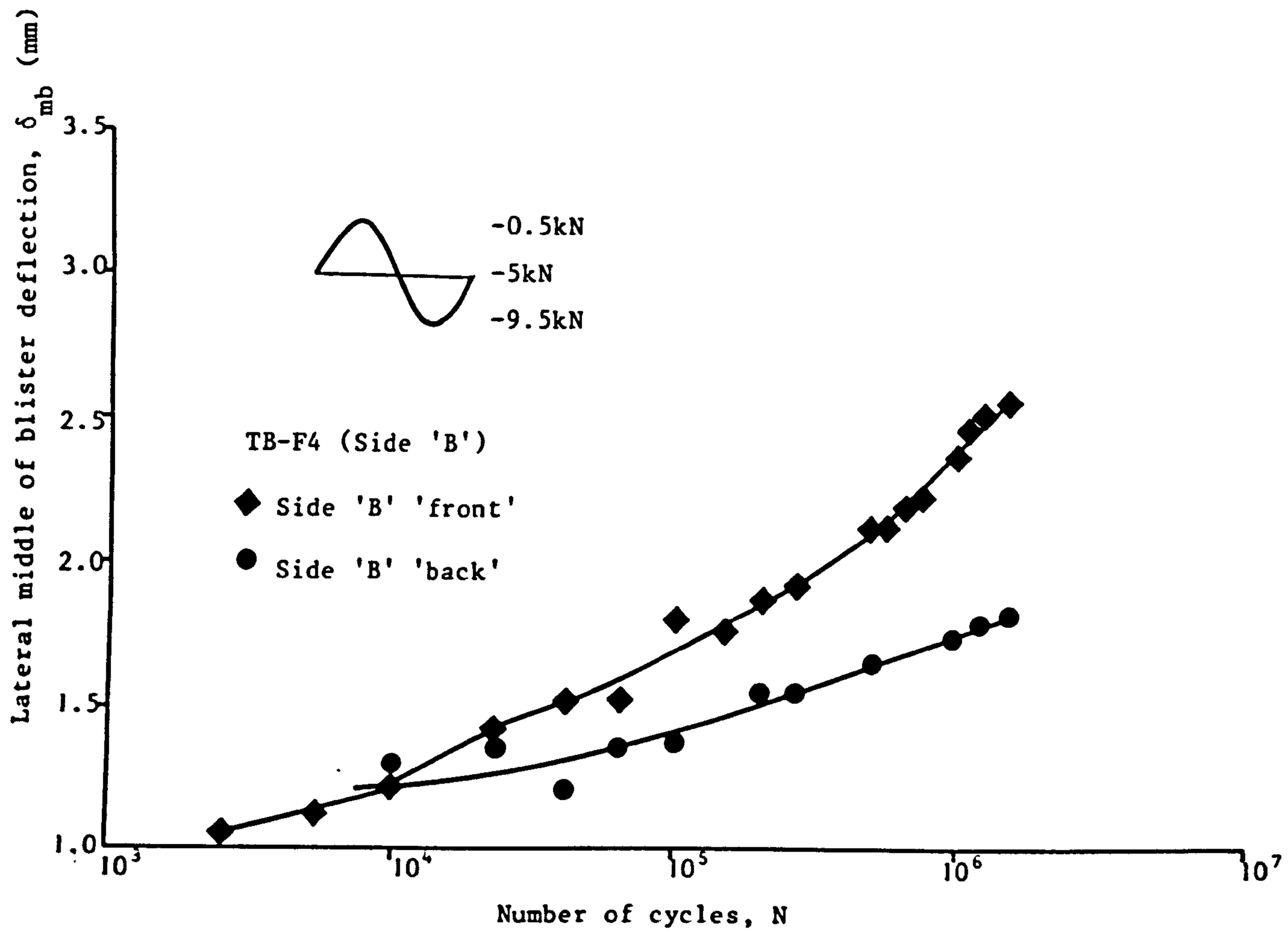

Fig. 5.56 MIDDLE OF BLISTER DEFLECTION VS. NUMBER OF CYCLES FOR SPECIMEN TB-F4 (Side 'B')

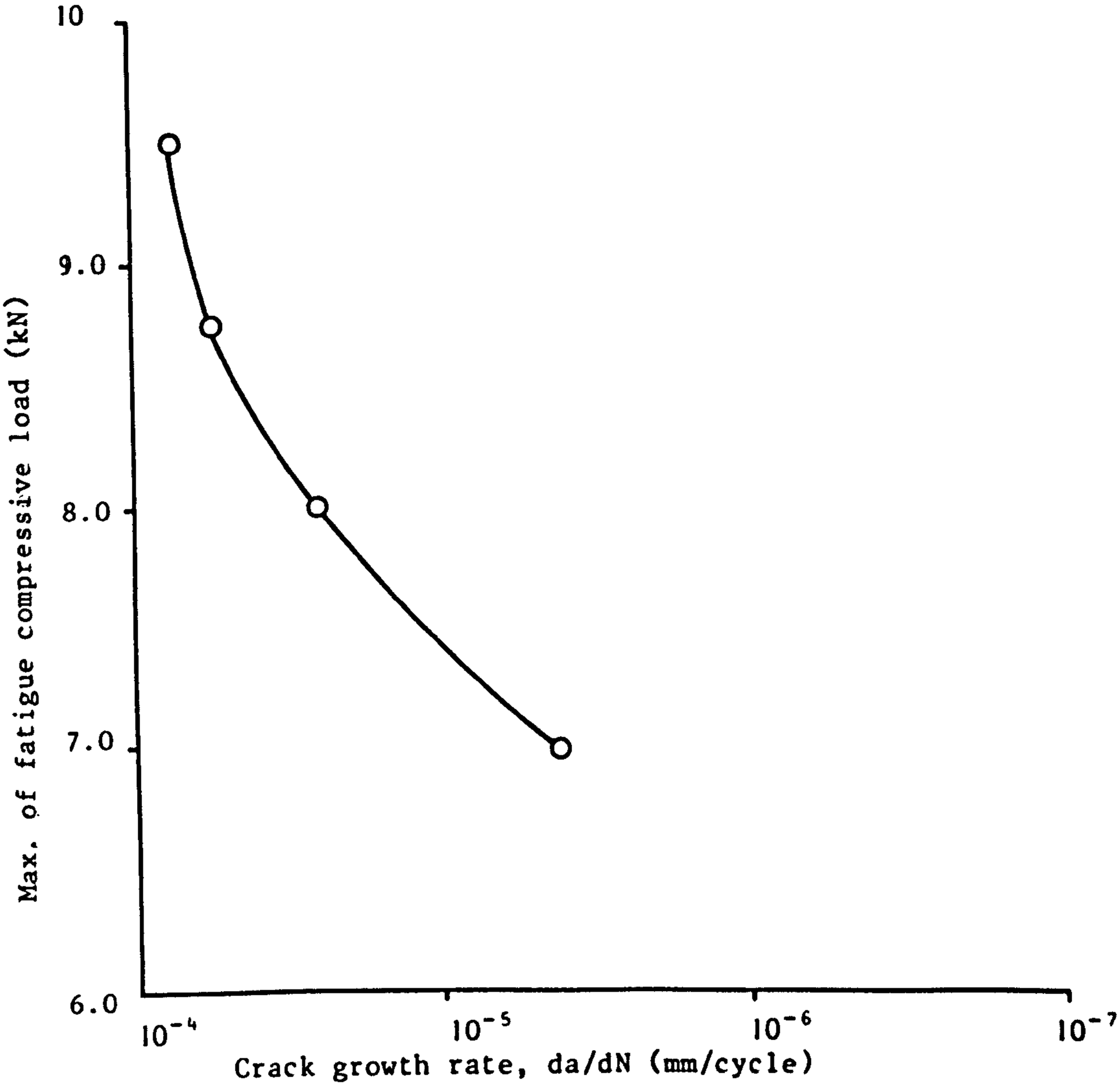

Fig. 5.57 MAXIMUM OF FATIGUE COMPRESSIVE LOAD VS. SIDE 'A' AND 'B' AVERAGE RATE OF CRACK GROWTH

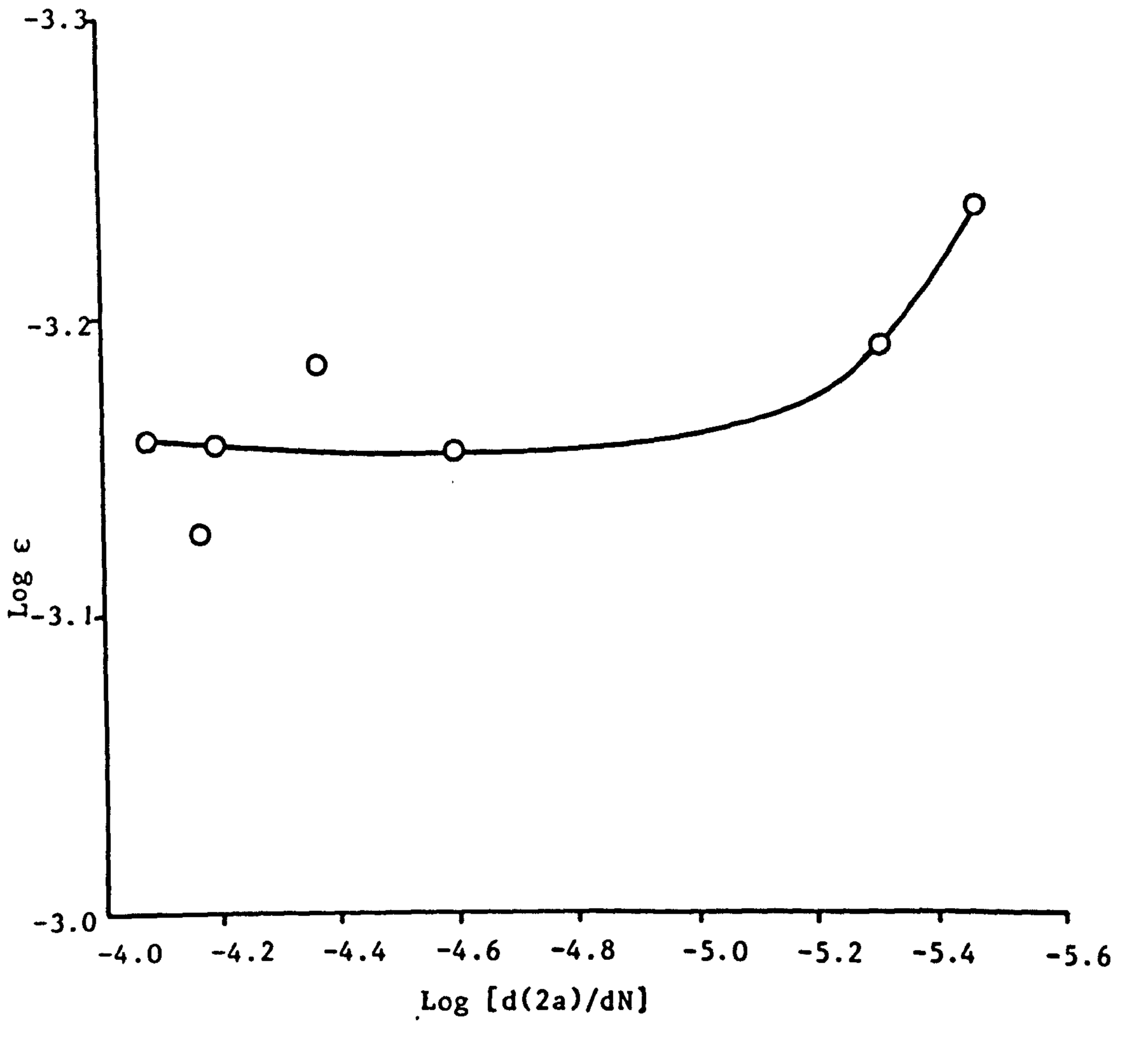

Fig. 5.58 DYNAMIC COMPRESSIVE MAXIMUM APPLIED STRAIN VS. RATE OF CRACK GROWTH

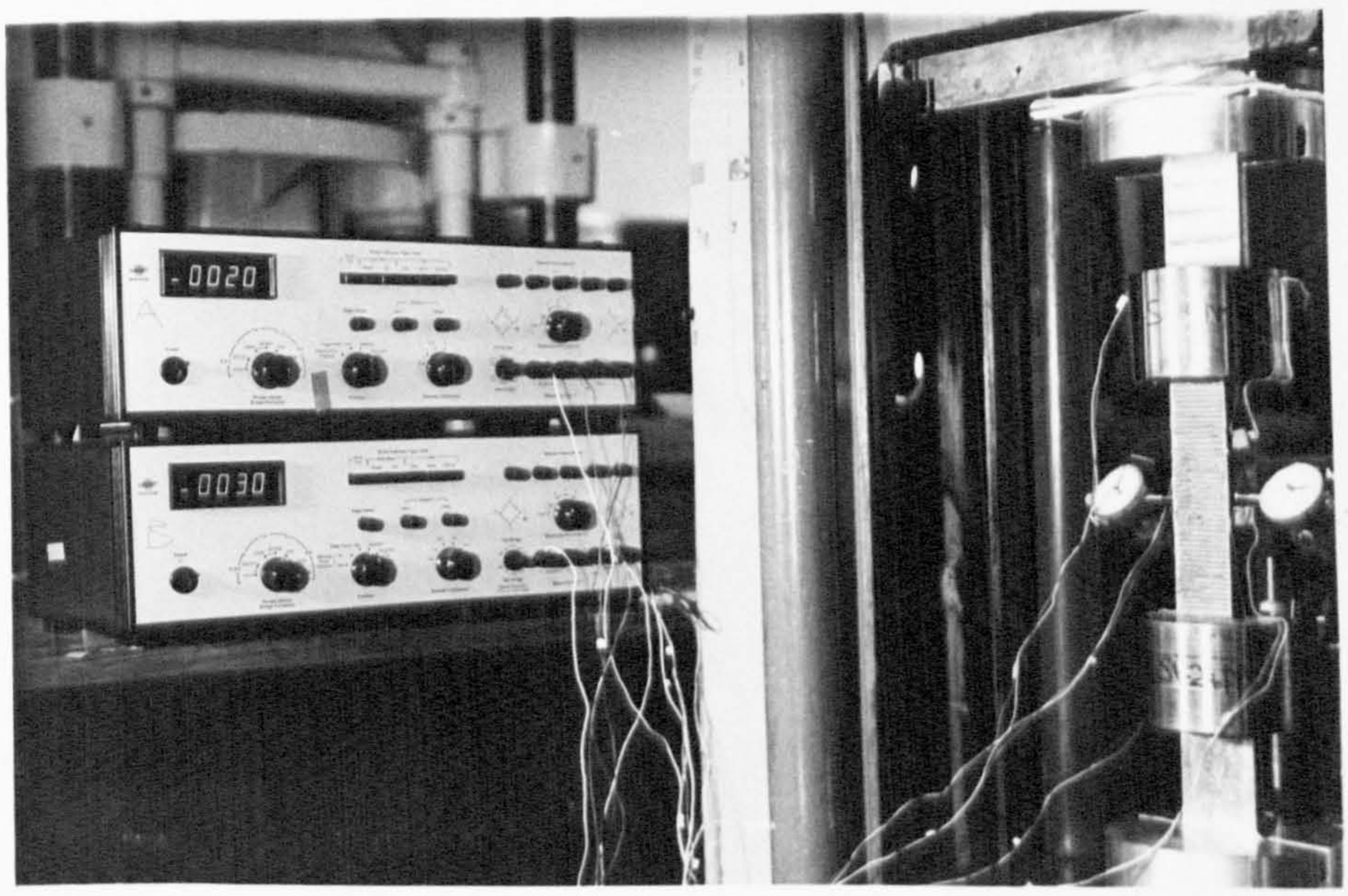

PLATE 5.1

TB SPECIMEN TEST SET UP

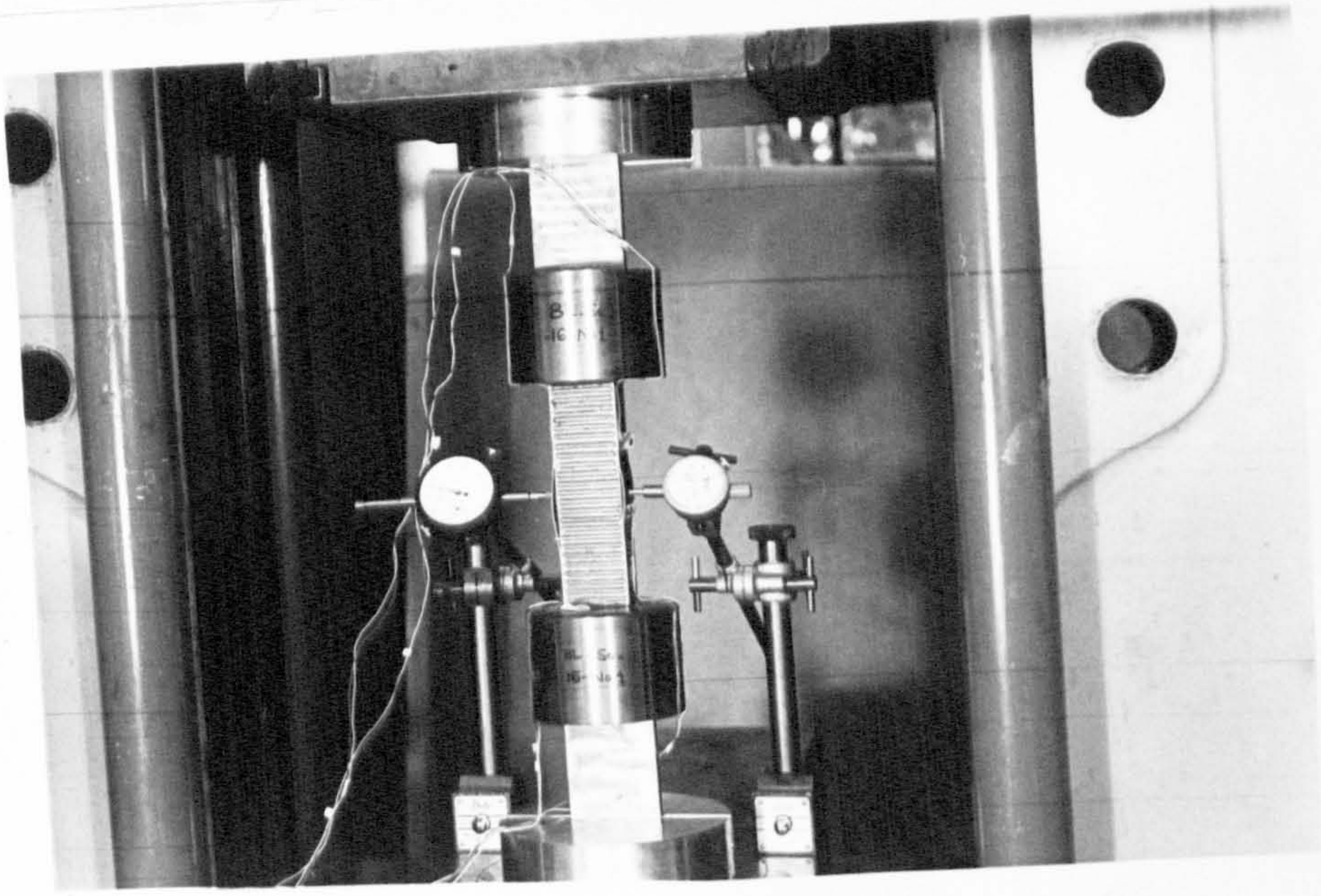

PLATE 5.2

DELAMINATION GROWTH IN SPECIMEN TB-S1

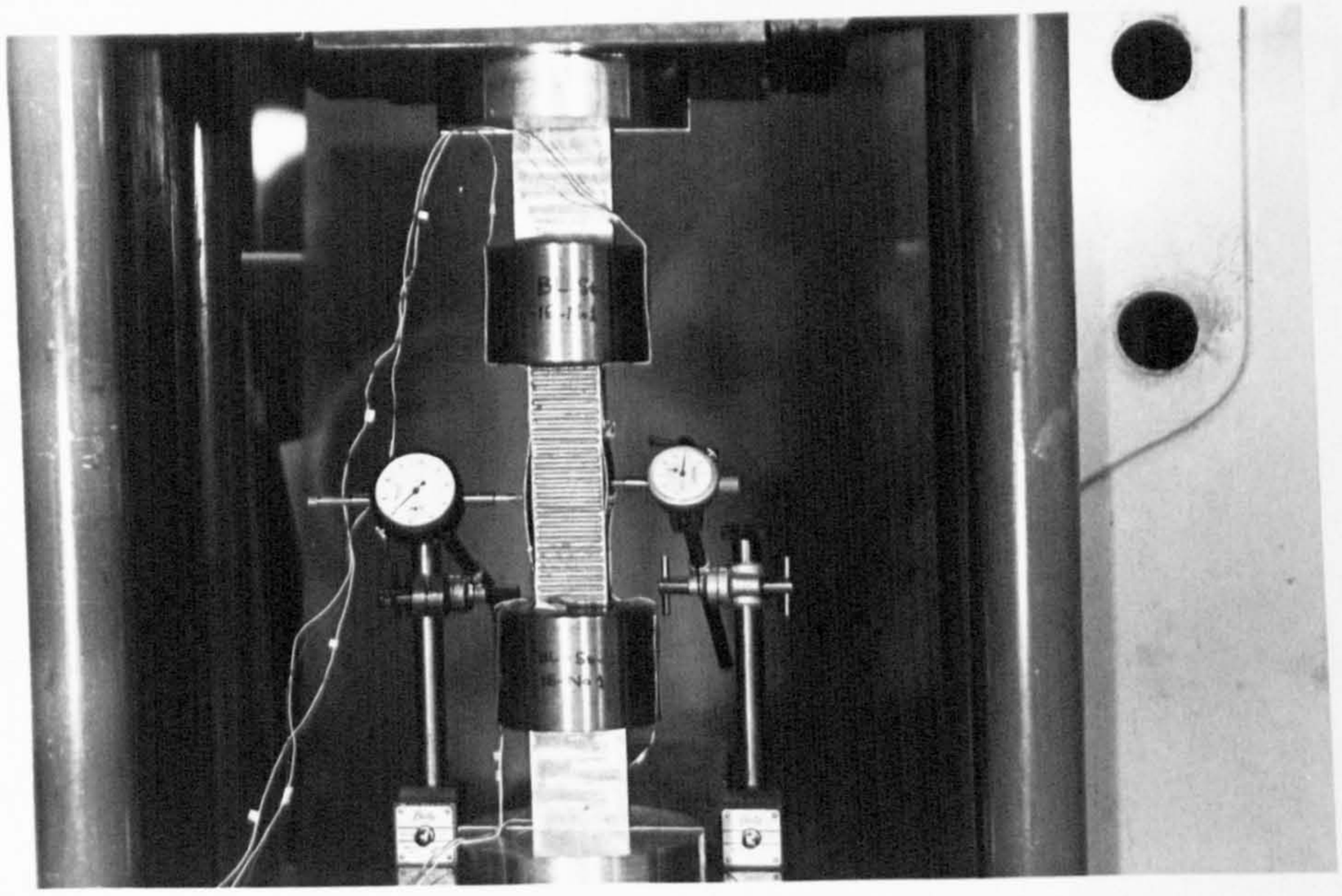

PLATE 5.3

EXTENSIVE DELAMINATION GROWTH IN SPECIMEN TB-S1

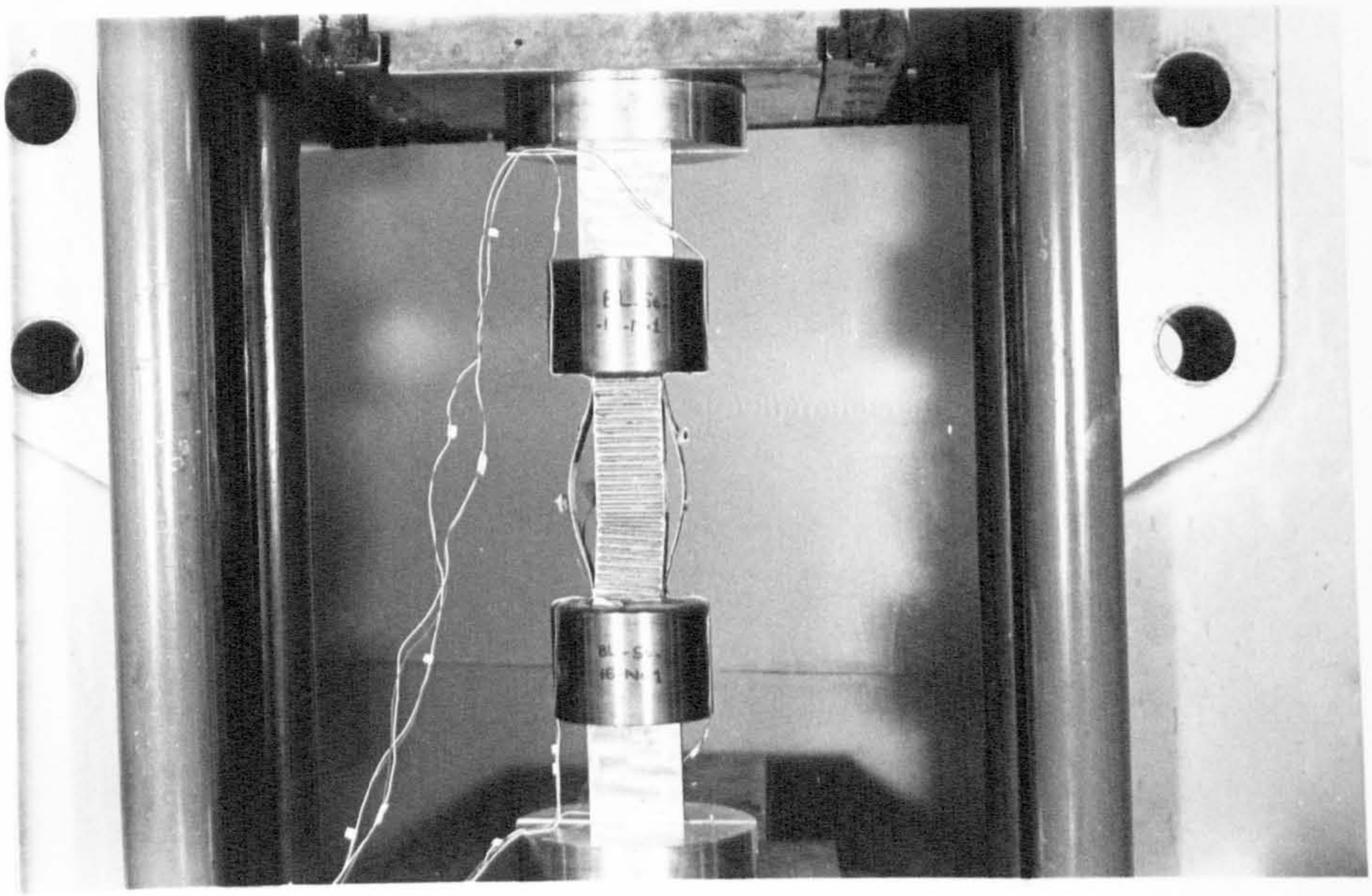

PLATE 5.4

COMPLETE DELAMINATION AND FINAL FAILURE OF SPECIMEN TB-S1

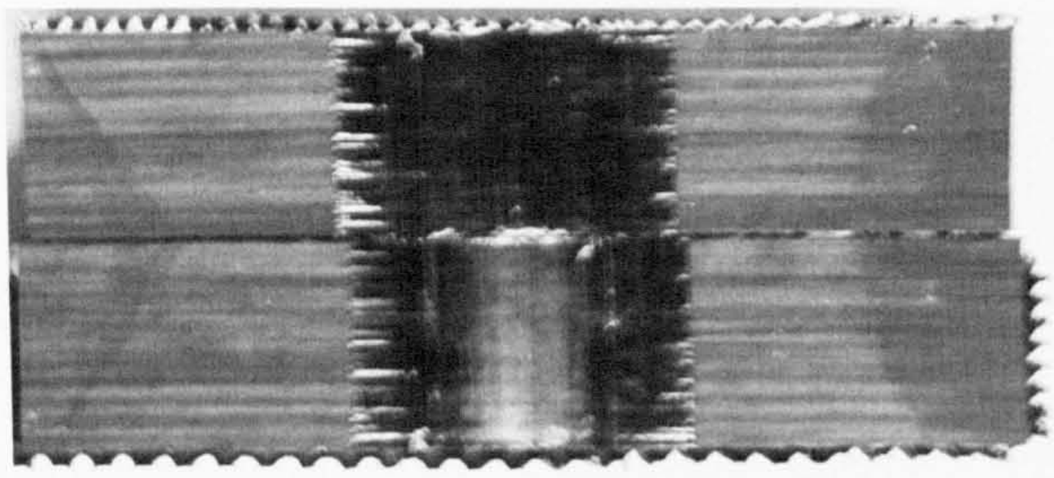

PLATE 5.5

INTERLAMINAR INTERFACE SHOWING EXTENT OF

DELAMINATION FOR SIDE 'A' FROM FRONT AND BACK OF SPECIMEN TB-S2

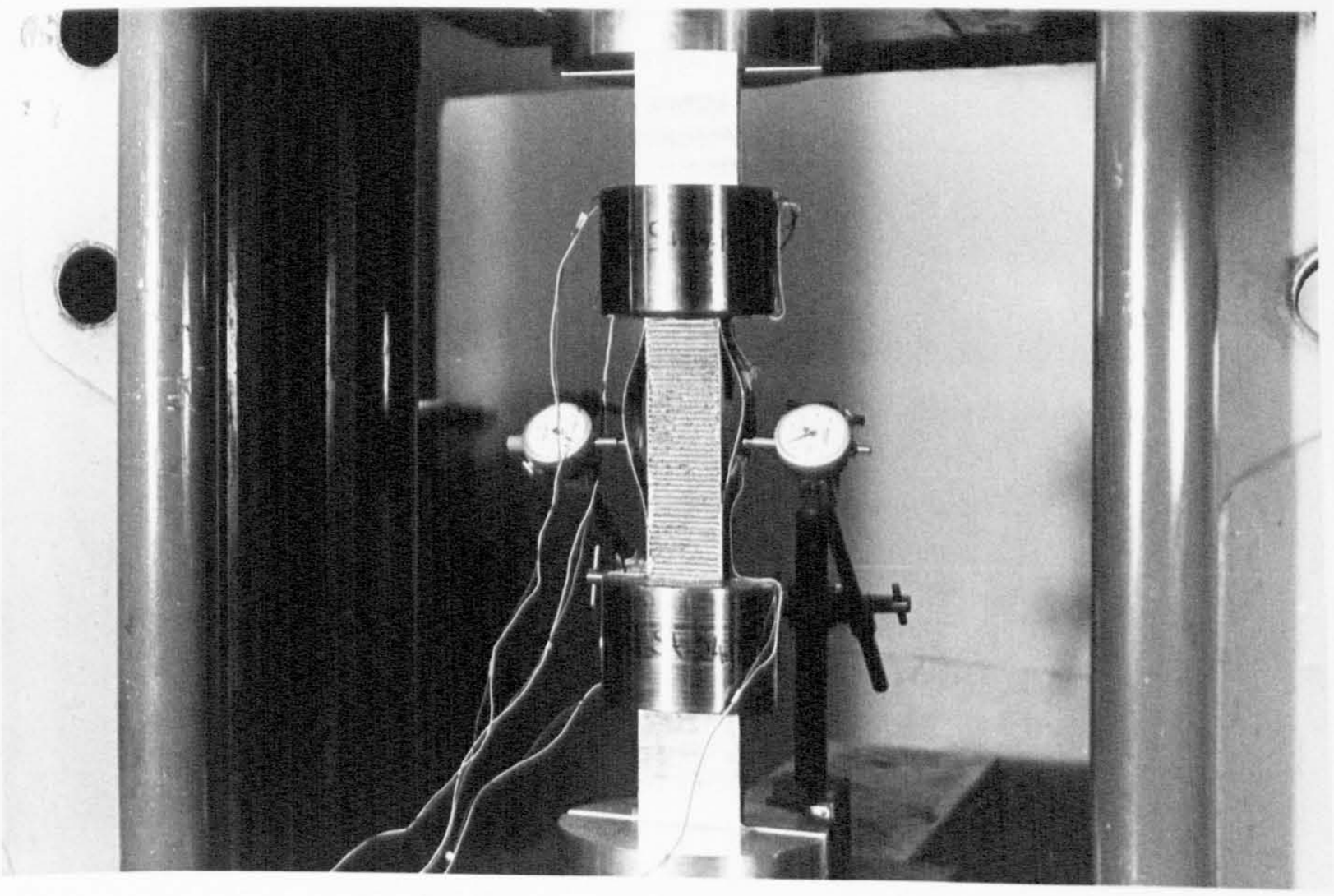

PLATE 5.6

DELAMINATION EXTENT AND LATERAL DEFLECTION

CONFIGURATIONS JUST BEFORE THE FINAL FAILURE

OF SPECIMEN TB-S2

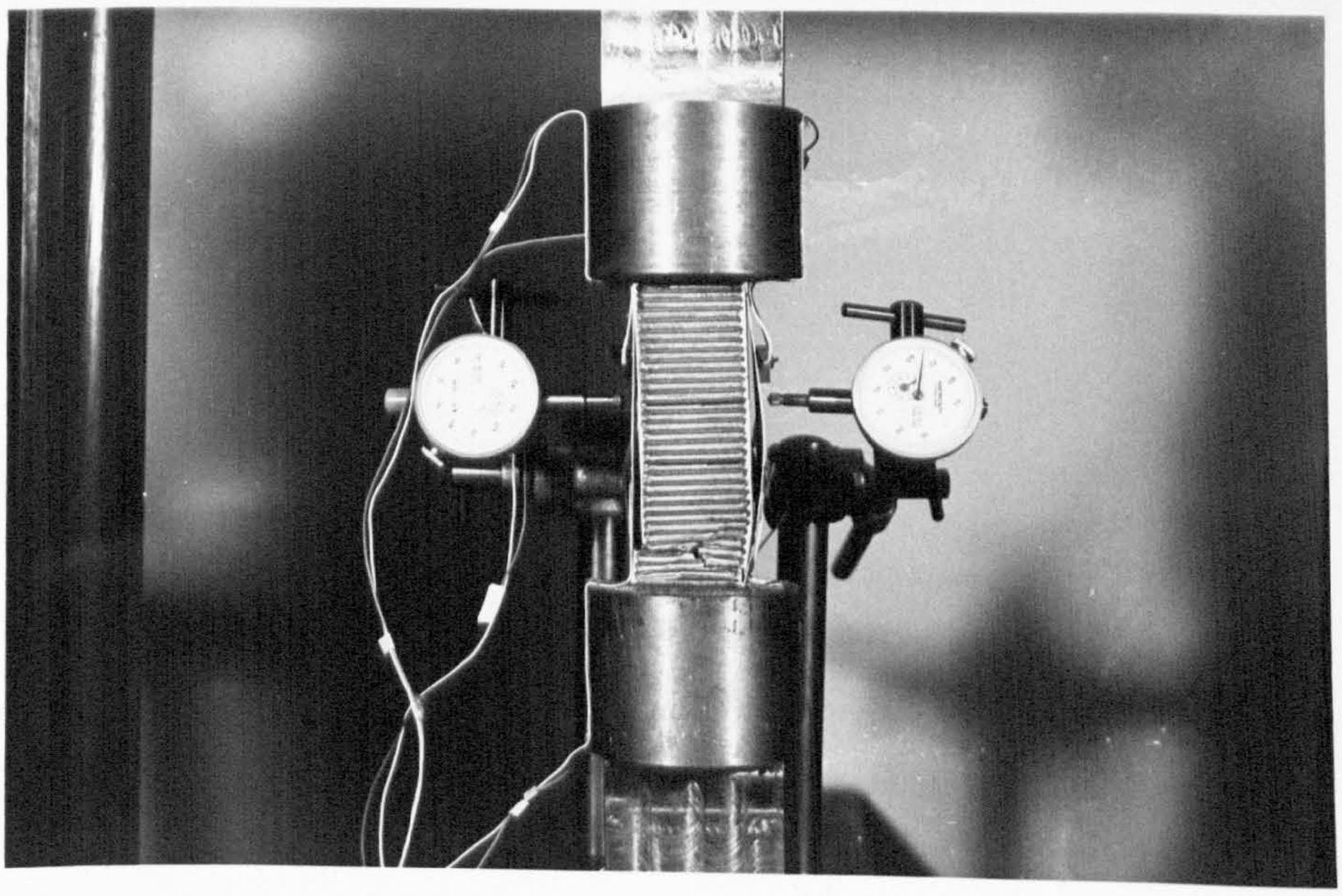

PLATE 5.7

SPECIMEN TB-S4 FINAL FAILURE

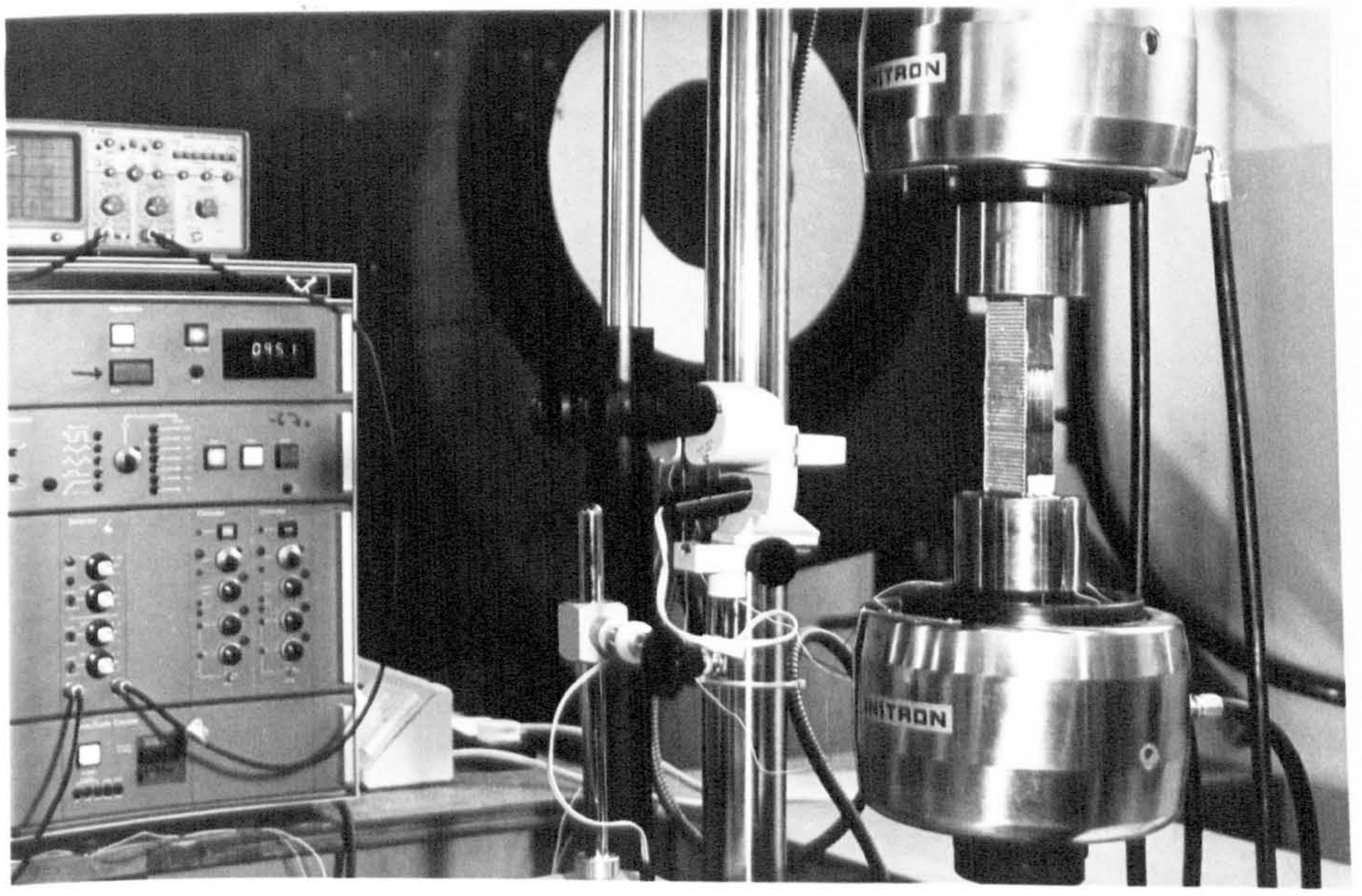

PLATE 5.8

TEST SETUP FOR TB FATIGUE SPECIMEN

PLATE 5.9

TYPICAL FATIGUE DELAMINATION GROWTH

(FROM SPECIMEN TB-F4)

PLATE 5.10

FATIGUE DELAMINATION SURFACE FEATURES FOR SPECIMEN TB-F1

(SIDE 'B') (TOTAL N = 1,050,345 CYCLES)

PLATE 5.11

FATIGUE DELAMINATION SURFACE FEATURES FOR SPECIMEN TB-F2

(SIDE 'A') (TOTAL N = 685,650 CYCLES)

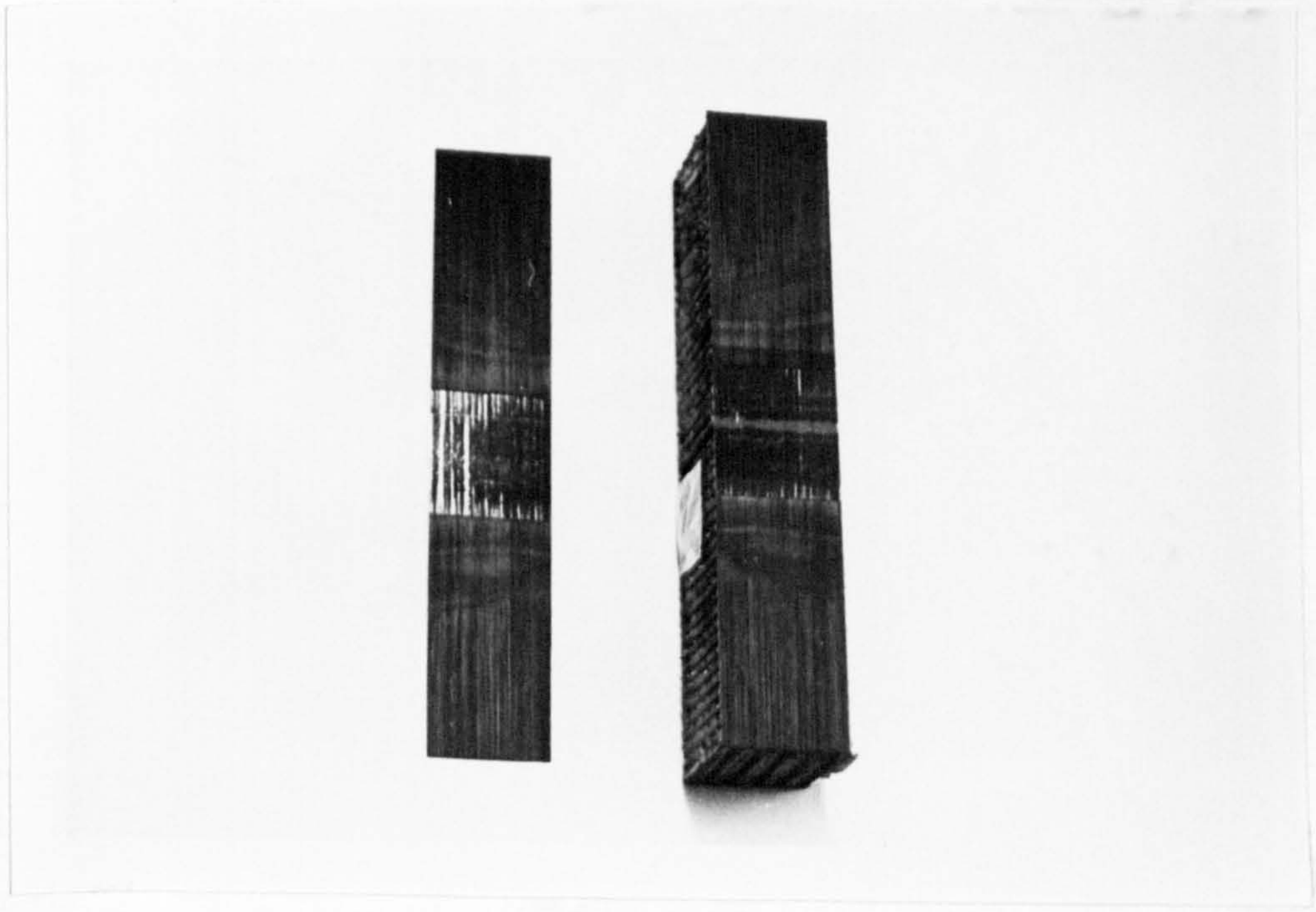

PLATE 5.12

FATIGUE DELAMINATION SURFACE FEATURES FOR SPECIMEN TB-F3

(SIDE 'B') (TOTAL N=2,250,000 CYCLES)

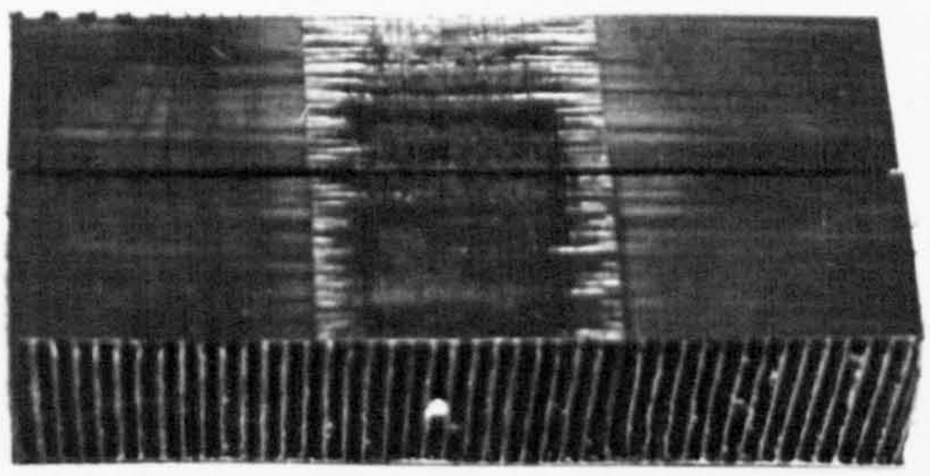

PLATE 5.13

FATIGUE DELAMINATION SURFACE FEATURES FOR SPECIMEN TB-F4

(SIDE 'A') (INNER EDGES REPRESENT THE 'FRONT')

(TOTAL N=1,502,040 CYCLES)

CHAPTER SIX

GENERAL CONCLUSIONS AND SUGGESTIONS FOR FURTHER WORK

6.1 GENERAL CONCLUSIONS

The interlaminar delamination problem in CFRP has been the subject of the present investigation. It is the relative ease with which debonding may ensue and propagate, especially under direct compressive loading, with consequent loss by the composite of its stiffness and load carrying capacity that has made the aforementioned problem a primary design consideration. Reliable and relatively simple theoretical models to assess the delamination problem have been developed and these have been supported by experiments on a number of representative specimens.

A simple theoretical analysis based on a realistic model has been established of the load-deflection relationship for the DCB specimens. It accounts for the strains beyond the crack tip section. Comparisons of the predicted deflections with the results of a previous elasticity solution and the beam-on-elastic-foundation model have shown reasonable agreement. Further comparisons with some published experimental data revealed good agreement. The strain energy of bending stored in the DCB arms was evaluated and used in formulating expressions for the strain energy release rate which can be employed reliably to predict the fracture toughness of a certain material. Calculated stress intensity factors showed excellent agreement with results from two elasticity solutions and

from the elastic foundation model. TDCB dimensionless fracture strength was compared with established experimental data and found to be in very good agreement for values of ratio between crack length and effective specimen length (distance between load line and specimen base) ranging up to 0.7. The stability criterion for crack propagation has been established for the TDCB specimen with respect to both load and deflection controlled cases.

DCB type test specimens, made of partially delaminated CFRP strips glued to steel adherends, and test procedures have been given for measuring the critical energy release rate in the opening delaminating mode between 0° layers. TDCB type-specimens, capable of raising the critical delamination load and therefore suitable for controlled stable tests on a servo-hydraulic machine were selected in the study of both static and fatigue splitting in the opening mode. The critical energy release rates, from Irwin-Kies compliance and Gurney's irreversible work methods, have been given versus the crack length alongside the corresponding analytical prediction. Fatigue data for various maximums of the alternating load have been presented in the form of crack length versus the number of cycles and a Paris type formula has been found for the prediction of fatigue delamination growth rate in the linear region of 'crack length versus number cycles'.

A theoretical analysis based on beam-column theory and an energy release rate criterion has been presented for the crack propagation of a layered fibre reinforced plastic strip in direct in-plane compression, in the presence of a blister. Account has been taken of a resin rich layer at the delaminating edge and of an initial deflection in the blister geometry. The total strain energy for the blister layer has been calculated and combined with a law of mixtures to determine an overall Young's modulus for the laminate

which in turn was used in the evaluation of the strain energy release rate. Typical design curves have been given showing the influence of blister span, applied compressive strain and resin stiffness on the critical loads. It has been found that delamination may occur at in-plane load in the blister layer well below the Euler buckling load for a built-in strut. The case with no pre-loading initial deflection has also been developed along the same lines, and the effect of stiffness of the resin rich layer on the post-buckling behaviour of the debonded layer has been discussed. Design curves are given to predict the critical applied strain knowing the initial half debond length. Delamination is not possible unless the split layer buckles.

Twin blister (TB) specimens with various initial spans and test procedures have been described for the study of delamination characteristics under static and constant amplitude compressive fatigue loading. In the static case, four specimens were tested in direct in-plane compression. Delamination was audible and unstable for short blister spans and became gradually stable as the crack grew longer. Several graphs which represent load-strain and load-lateral deflection responses are given and discussed. Also the critical compressive strains are shown versus the blister half span and compared with the analytical predictions. Four additional TB specimens were tested in compressive fatigue. Data for crack growth and lateral deformation are plotted versus the number of cycles and discussed in the light of fatigue beach markings on the fracture surfaces. Other graphs describing, respectively, the maximum of fatigue overall load and the applied strain versus the rate of crack propagation show delamination sensitivity to high maximum fatigue loads and therefore high load amplitudes. Non uniform fatigue crack

growth is shown by the shape of the beach markings. These tended to concave outwards because fatigue delamination first started at the edges and subsequently propagated inwards with load cycling. Fatigue and static fracture surfaces exhibit a colour effect for stable crack growth as demonstrated by the provided plates.

6.2 SUGGESTIONS FOR FURTHER WORK

Further work is needed as a follow up to the experimental and analytical investigations given in Chapters 3,4 and 5. In the light of this, future work may be conducted along the following lines:

(i) TDCB type test specimens may be used to study the delamination characteristics for different CFRP lay-ups in both static and fatigue testing with emphasis on the effect of delamination surface morphology on the strain energy release rate.

(ii) In the blister analysis, it remains to assess the influence of various initial mid-span deflection values and therefore eliminate the accumulative deflection effect on the delamination data when testing TB specimens. Also, the analysis may be extended to include different lay-ups and debonded layer thicknesses.

On the experimental side, TB specimens can be employed in assessing the influence of the various mechanical and geometrical parameters on the delamination behaviour under both static and fatigue loading. In addition, other initial debond shapes such as burried delaminations (e.g. Ref. 31), crack propagation from edge debonds, cut-outs, edge slots, etc. may be studied. In particular, sandwich specimens, with zero initial deflection for the debonded layer including impact induced delamination can be used to study buckling related interlaminar splitting behaviour and therefore

provide a backing for the theoretical analysis presented at the end of Chapter 4. To this extent, Ref. 91 could be a valuable start. Furthermore, thermal effects on the behaviours of debonding and buckling of originally flat layers can be assessed through the use of TB sandwich specimens.

A P P E N D I X A

DISTRIBUTION OF DISPLACEMENTS ALONG THE DCB ROOT SECTION

A.1 Calculation of the Displacement Components $u_{1\ell}$, $u_{2\ell}$, u_{2u}, u_{4r} and u_{4u}

A.2 DCB Arm End-Deflection due to Arm Root Rotation, Choosing a Linear Displacement Distribution

A.1 CALCULATION OF THE DISPLACEMENT COMPONENTS

$u_{1\ell}$, $u_{2\ell}$, u_{2u}, u_{4r} and u_{4u}

The vertical displacements resulting from a vertical load distribution over a semi-infinite straight boundary can be evaluated following the method explained in Chapter 2. Similarly, if there are several load distributions, the displacements are calculated for each individual loading, then the various contributions are superimposed to give the resultant displacement at each point along the straight boundary. For the DCB specimen, there are four load triangles along the root cross-section as shown at the top of Fig. A.1. The idea is to calculate the displacement distribution due to each load triangle, say to the left of the centre line, as shown in Fig. A.1(a) through to A.1(e), and then superimpose the different components. It must be remembered that the displacement component $u_{3\ell}$ due to the load triangle No. 3, has already been evaluated in Chapter 2. Therefore, there remains to calculate the displacement components $u_{1\ell}$, $u_{2\ell}$, u_{2u}, u_{4r} and u_{4u}. For simplicity, each load triangle is associated with a local coordinate along the root cross-section. These local coordinates are converted, after the integration operation, to a common coordinate as explained in Chapter 2.

The above displacements are evaluated applying Eqn. (2.1) of Chapter 2, i.e.,

$$u = \frac{2}{\pi E}\int_{x}^{\ell+x} q \ln\frac{d}{r}\, dr - \frac{1+\nu}{\pi E}\int_{x}^{\ell+x} q\, dr \qquad (A.1)$$

For the triangular load distributions shown in Fig. A.1 we have, $\ell = h/2$, x = the local coordinate for the load triangle under

consideration, and q represents the linearly varying bending stress. With reference to Fig. A.1(a) the vertical displacement $u_{1\ell}$ produced at an arbitrarily chosen point O distant r from the elementary load qdr is given by the integration of Eqn. (A.1) after replacing, respectively, u, x and ℓ by $u_{1\ell}$, $x_{1\ell}$, h/2 and substituting

$$- \sigma_o \left(1 - \frac{2r}{h} + \frac{2x_{1\ell}}{h}\right)$$ for the value of q (assuming positive compressive stresses), thus,

$$u_{1\ell} = - \left(\frac{2\sigma_o}{\pi E}\right) \int_{x_{1\ell}}^{(h/2)+x_{1\ell}} \left(1 - \frac{2r}{h} + \frac{2x_{1\ell}}{h}\right) \ln\left(\frac{d}{r}\right) + \left(\frac{1+\nu}{\pi E}\right) \int_{x_{1\ell}}^{(h/2)+x_{1\ell}} \sigma_o \left(1 - \frac{2r}{h} + \frac{2x_{1\ell}}{h}\right) dr$$

or

$$\left(\frac{2u_{1\ell}}{h}\right)\left(\frac{\pi E}{\sigma_o}\right) = \left(\frac{h/2 + x_{1\ell}}{h/2}\right)^2 \ln\left(\frac{h/2 + x_{1\ell}}{d}\right) - \frac{4(x_{1\ell}^2 + hx_{1\ell})}{h^2} \ln\left(\frac{x_{1\ell}}{d}\right) - \frac{2(h/2 + x_{1\ell})}{h} + \frac{\nu}{2} \quad \text{(A.2)}$$

Similarly, the other displacement components are derived using Eqn. (A.1) as follows:

* referring to Fig. A.1(b) wherein, $x = x_{2\ell}$, and $q = -2\sigma_o \dfrac{r - x_{2\ell}}{h}$,

we obtain

$$\left(\frac{2u_{2\ell}}{h}\right)\left(\frac{\pi E}{\sigma_o}\right) = \frac{4(h^2/4 - x_{2\ell})}{h^2} \ln\left(\frac{h/2 + x_{2\ell}}{d}\right) + \left(\frac{x_{2\ell}}{h/2}\right)^2 \ln\left(\frac{x_{2\ell}}{d}\right) + \frac{2x_{2\ell}}{h} + \frac{\nu}{2} \quad \text{(A.3)}$$

* referring to Fig. A.1(c) wherein, $x = -x_{2u}$, and $q = -\sigma_o \left(1 - \dfrac{2r}{h} - \dfrac{2x_{2u}}{h}\right)$,

it is found

$$\left(\frac{2u_{2u}}{h}\right)\left(\frac{\pi E}{\sigma_o}\right) = \left(\frac{h/2 - x_{2u}}{h/2}\right)^2 \ln\left(\frac{h/2 - x_{2u}}{d}\right) - \frac{4(x_{2u}^2 - hx_{2u})}{h^2} \ln\left(\frac{x_{2u}}{d}\right) - \frac{2(h/2 - x_{2u})}{h} + \frac{\nu}{2} \qquad (A.4)$$

* referring to Fig. A.1(d) wherein, $x = x_{4r}$, and

$q = \sigma_o(2r/h - 2x_{4r}/h)$, it is shown

$$\left(\frac{2u_{4r}}{h}\right)\left(\frac{\pi E}{\sigma_o}\right) = -\left[\frac{4(h^2/4 - x_{4r}^2)}{h^2} \ln\left(\frac{h/2 + x_{4r}}{d}\right) + \left(\frac{x_{4r}}{h/2}\right)^2 \ln\left(\frac{x_{4r}}{d}\right) + \frac{2x_{4r}}{h} + \frac{\nu}{2}\right] \qquad (A.5)$$

* finally, with reference to Fig. A.1(e) wherein, $x = -x_{4u}$, and

$q = \sigma_o\ (2r/h + 2x_{4u}/h)$, integration of Eqn. A.1 yields

$$\left(\frac{2u_{4u}}{h}\right)\left(\frac{\pi E}{\sigma_o}\right) = -\left[\frac{4(h^2/4 - x_{4u}^2)}{h^2} \ln\left(\frac{h/2 - x_{4u}}{d}\right) + \left(\frac{x_{4u}}{h/2}\right)^2 \ln\left(\frac{x_{4u}}{d}\right) - \frac{2x_{4u}}{h} + \frac{\nu}{2}\right] \qquad (A.6)$$

A.2 DCB ARM END-DEFLECTION DUE TO ARM ROOT ROTATION, CHOOSING A LINEAR DISPLACEMENT DISTRIBUTION

The additional end-deflection, due to the strains beyond the crack tip, of one arm of the DCB specim, can be evaluated using the complementary energy principle in the form shown by Eqn. (2.22); wherein $\sigma_x = \sigma_o\ (2x/h - 1)$, and u is substituted by $(h\sigma_o/\pi E)[4.3(x/h) - 2.5]$ which is the displacement distribution based on the linear central part of the graph shown in Fig. 2.4. Thus,

$$U_c = \lim_{R\to 0} \frac{b}{2} \int_R^{h-R} \sigma_o\left(\frac{2x}{h} - 1\right)\left(\frac{h\sigma_o}{\pi E}\right) \left[4.3\left(\frac{x}{h}\right) - 2.5\right] dx$$

or

$$U_c = \frac{0.7167 b h^2 \sigma_o^2}{2\pi E} \qquad (A.7)$$

From Eqns. (A.7) and (2.21) we obtain ($\sigma_o = 6Pa/bh^2$)

$$\delta_o = \frac{4.3\ a\sigma_o}{\pi E} = \frac{8.212 P a^2}{E b h^3} \qquad (A.8)$$

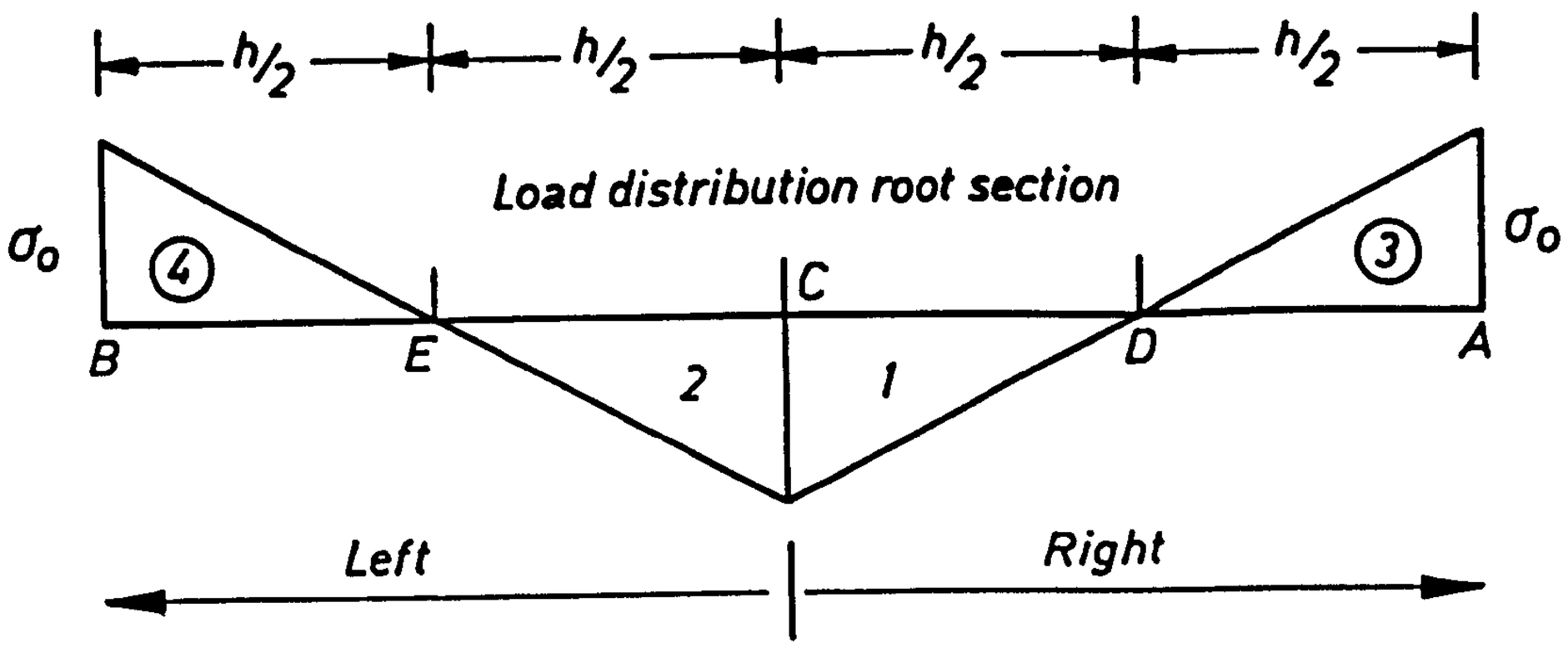

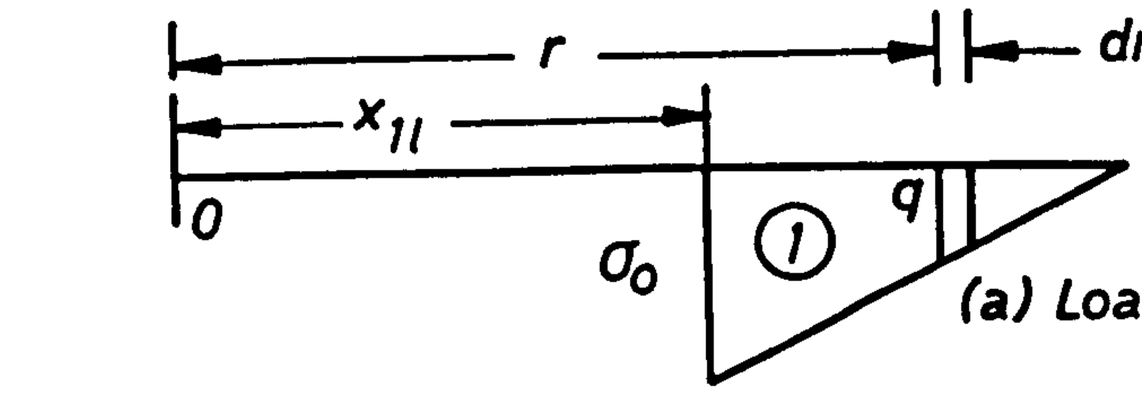

(a) Load triangle No.1

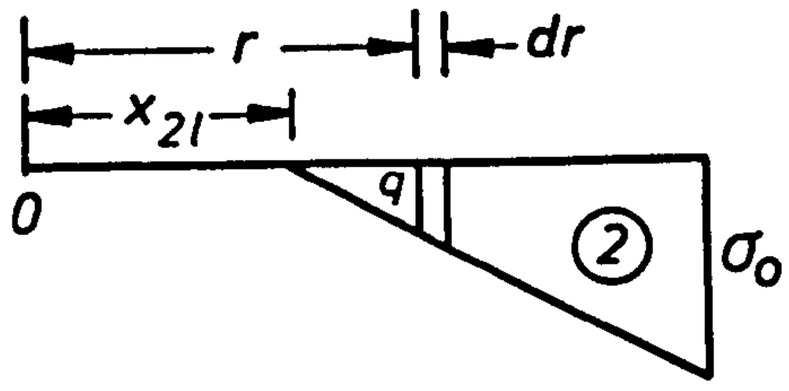

(b) Load triangle No.2

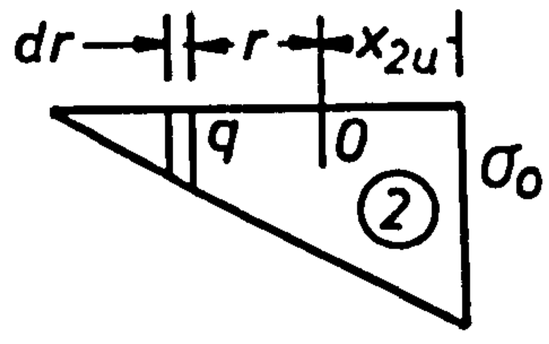

(c) Load triangle No.2

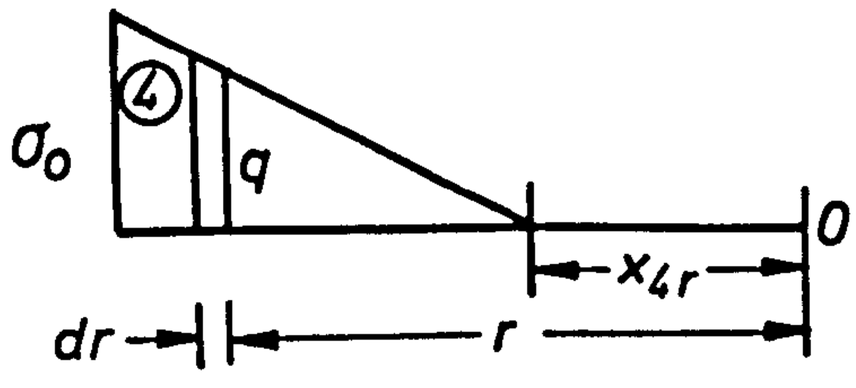

(d) Load triangle No. 4

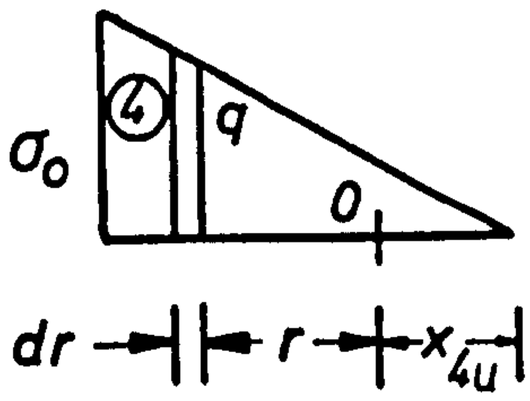

(e) Load triangle No.4

FIG. A.1 TRIANGULAR LOAD DISTRIBUTION ALONG THE DCB ROOT SECTION

A P P E N D I X B

MANUFACTURE OF CFRP AND SELECTION OF ADHESIVE SYSTEM

B.1 Manufacture of CFRP

B.2 Selection of Adhesive system

* Figures

* Plates

B.1 MANUFACTURE OF CFRP

Carbon fibres can be arranged either in fabric or unidirectional tape form in the dry condition and then can be impregnated with wet resin which is partially cured to enable easy handling. These partially cured sheets are commonly called prepreg. The prepreg sheets can be stacked to the required array and cured under a combination of heat and pressure in an autoclave or by other similar means.

The prepreg used in this work was Ciba-Geigy Fibredux 914C-TS-5 with 40% nominal resin content. It contains Courtaulds' high strength surface treated fibres.

A face bleed technique was employed to cure the CFRP wherein the excess of resin content was removed from the upper and lower surfaces of the laminate. The cure cycle involved the application of heat and pressure and aimed at removing the excess resin, the entrapped air and any volatiles. The consolidating pressure was supplied by a combination of vacuum and air pressure to ensure a uniform pressure distribution over the surface of the laminate.

The rig used in the curing process is shown in Fig. B.1. The sequence of operations for the curing process was mainly drawn from Ref. 76 and given here below for completeness:

(i) Remove the prepreg from the deep freeze and allow about 15 minutes to adjust to room temperature before removing from the protecting bag.

(ii) Ensure that the working area and tools are clean.

(iii) Cut the required number of prepreg layers to the desired dimensions and fibre orientation.

(iv) Build up the laminate by stacking the prepreg layers in their correct order starting the contact at one edge and working it

inwards by applying a slight fibre-lengthwise pressure with the hand.

(v) Find the weight of the laminate and calculate the number of thin blotting paper layers, $\bar{N}$, required for the bleed pack. This number should be just sufficient to absorb the excess resin in the prepreg during the cure cycle, leaving the cured laminate with the desired thickness and fibre content by volume. A typical calculation for the number of the blotting paper layers, $\bar{N}$, follows the end of this section.

(vi) Cut out four layers of "peel ply" and place one each side of the prepreg to give an overlap of about 10mm all round. Peel ply is a PTFE coated fabric supplied by Fothergill and Harvey, Tygadure Division, Lancashire, and its trade name is Tygaflor 108C/03T. The fabric acts as a release layer for the cured laminate, and allows excess resin and air flow through from the laminate to the paper layers.

(vii) Cut out $\bar{N}$ thin blotting paper layers to the size of the laminate plus 10mm all round, and place $\bar{N}/2$ layers each side of the layup of (vi) above.

(viii) Complete the layup as shown in Fig. B.1 and place in the curing rig on top of a thin (16swg) Aluminium alloy sheet. This sheet which should be completely flat, serves as a base plate for the layup and should have the same size of the laminate plus about 30mm all round. The caul plate has the laminate size and consists of a mild steel plate 3/16 in or 1/4 in thick, with the sharp edges rounded off to prevent piercing of the vacuum bag. A layer of thick blotting paper is placed over the layup with an overlap of about 40mm all round, to make it easier for the gases to escape through the

vacuum chamber.

(ix) Cover the layup with a high temperature stable nylon membrane, extending to the edges of the perforated base of the rig, and seal around the edges using sealing mastic. As vacuum is drawn underneath, the nylon bag should be a snug fit around the edges of the layup which can be achieved by allowing a certain degree of laxity around the component. This precaution is necessary since the bag material hardens with heat and becomes prone to cracks.

(x) Bring the two parts of the curing rig together and place between two heating platens of a 1000kN (100 ton) press.

(xi) Allow the layup to settle in under vacuum (~ 1 atm) for at least one hour. During this time some of the air which has been trapped between prepreg layers may escape.

(xii) Apply a load of 500kN to the rig. This load is sufficient to keep the rig sealed when the air pressure is applied.

(xiii) Heat the rig up slowly at 2°C/minute to 135°C.

(xiv) Apply air pressure of approximately 0.6N/mm^2 (85psi) and allow the temperature of the rig to rise at a rate of 1°C/minute to 175°C.

(xv) Maintain the temperature at 175°C for one hour.

(xvi) Cool the rig to 60°C by passing cooling water through the heating platens of the press. During cool-down the vacuum and air pressure should be maintained.

(xvii) Release the air pressure and remove the vacuum. Allow the laminate to cool to room temperature before removal from the rig. A typical cure cycle is shown in Fig. B.2.

(xviii) Post cure the laminate in an oven at a temperature of 180°C for 8 hours.

** CALCULATION OF THE NUMBER OF BLOTTING PAPER SHEETS **

Plate size: 190mm x 150mm x 1mm

Density of carbon fibre = 1.76 grs/cm^3

Density of XAS/914 resin = 1.28 grs/cm^3

Resin content of prepreg = 40%

Weight of carbon fibre required in laminate, at 60% by volume

= 0.60 x 0.1 x 19.0 x 15.0 x 1.76

= 30.1 grs

Weight of resin required in laminate at 40% by volume

= 0.40 x 0.1 x 19.0 x 15.0 1.28

= 14.59 grs

Total weight of laminate required

= 44.69 grs

If W_i = initial pre-cure weight of plate in grammes, then weight of resin to be removed =(W_i - 44.69) grs.

Now, one blotting paper layer absorbs 3 times its own weight of resin.

Weight/m^2 of blotting paper = 31.67 grs.

If $\bar{N}$ is the number of blotting paper layers required, we have

$3\bar{N}$ x 31.67 x 0.19 x 0.15 = W_i - 44.69

Thus:

$$\bar{N} = \frac{W_i - 44.69}{2.71}$$

B.2 SELECTION OF ADHESIVE SYSTEM

During the early stages of the series of cleavage quasi-static tests, the TDCB specimens suffered from a pre-mature failure along the interfaces of the steel adherends and the adhesive films (Ordinary Araldite). For this reason, a survey for selecting a suitable adhesive was planned and consisted of finding the strongest binding mean from between a number of adhesive systems. These systems are:

(a) Ordinary pack Araldite (supplied by Ciba-Geigy).

(b) Araldite 2005, high shear and peel strength (two pack epoxy paste, supplied by Ciba-Geigy).

(c) Ordinary pack Araldite with added Acetone.

(d) Thin Araldite; resin LY560 with hardener HY560 (supplied by Ciba-Geigy Ltd.).

(e) HYSOL EA 9330/1 (supplied by British Aerospace).

(f) Ordinary pack Araldite with added Acetone and abraded CFRP.

(g) Araldite 2005 with abraded CFRP.

The selection of the best adhesive system was accomplished using the test specimen shown in Fig. B.3. Two small blocks of mild steel, each having (15mm x 15mm) square cross-section, are joined together by a strip of CFRP laminate with the adhesive under examination acting as a glue between the CFRP and the steel blocks. The block faces were degreased, shot-blasted and degreased again before the gluing operation. The adhesive under test was carefully mixed and then applied to both the surfaces of steel and CFRP. The assembled joint was secured in a jig, left to settle at room temperature for about 4 hours, and then placed in an oven to cure for 6 hours at (40 C-60 C).

Two steel arms were screwed into the joint for loading the specimen as shown in Fig. B.3. A universal tensile testing machine was used to

apply the tensile load with a steady rate up to specimen failure. Three specimens (1, 2 and 3) were tested for each gluing system and the arithmetic average of the three strengths was taken as the comparison parameter with the other choices.

Obviously the bond surfaces of the CFRP strip (16, 0°, plies = 2mm in thickness) had exactly the same dimensions of those for the pair of steel blocks. Care had been taken to ensure flat bonding surfaces, alignment of joint components and uniform adhesive thickness throughout the bonded areas. The threaded joint was left loose to eliminate any torsion stresses which might occur during loading. Each test specimen was arranged completely vertical between the jaws of the machine to ensure axial loading and to minimize the effects of bending and shear forces. The idea behind the adhesive systems (f) and (g) was to assess the effect of abrasion of the CFRP on the adhesive bond.

Six pairs of steel blocks were made to carry out the 21 tests (3 for each resin system). Environmental and operational conditions were maintained for each resin system by preparing it once and gluing the corrsponding joints at the same time. After testing these specimens, the steel blocks were cleaned, shot-blasted and cleaned again ready for the next gluing process. The rate of loading was kept around 40N/sec for all test specimens.

The experimental results are summarized in Table B.1 where a wide scatter of data is evident. This may be because the bond surfaces are small which makes them sensitive to flaws, misalignment, non uniform adhesive film, etc. Also, the effects of CFRP abrasion and also of the Acetone addition are within the scatter boundary, therefore cannot be assessed. However, as the main purpose of this exercise was to compare different adhesive systems, the results obtained here could be taken as indicative for choosing the strongest adhesive system. This is Araldite 2005.

Table B.1 Experimental Data for Adhesives

Adhesive system	Joint strength (N) Specimen 1	Specimen 2	Specimen 3	Strength ave. (N)	Mode of failure
Ordinary Pack Araldite cured at 40°C for 6 hours	3750	4437.5	3850	4012.5	Adhesive failure (between CFRP and steel); Plate B.1
Araldite 2005 cured at 40°C for 6 hours	7175	5812.5	6787.5	6591.7	interlaminar failure (between CFRP plies); plate B.2
Thin Araldite cured at 60°C for 6 hours	190*	3250	-	-	adhesive failure Plate B.1
Ordinary Araldite with added Acetone cured at 82°C for 2 hours	1625	2900	2375	2300	Adhesive failure Plate B.3
Hysol AE 9330/1 cured at 82°C for 2 hours	3037.5	2475	1015*	2178.8	adhesive failure Plate B.1
Ordinary Araldite+ with added acetone cured at 40°C for 12 hours	5600	4412.5	4900	4970.8	mixture of interlaminar and adhesive failures
Araldite 2005+ cured at 40°C for 12 hours	6312.5	5162.5	6200	5891.7	predominent interlaminar failure

* blocks were not exactly aligned

+ where the bond surfaces of CFRP were abraded using an emery paper under running water.

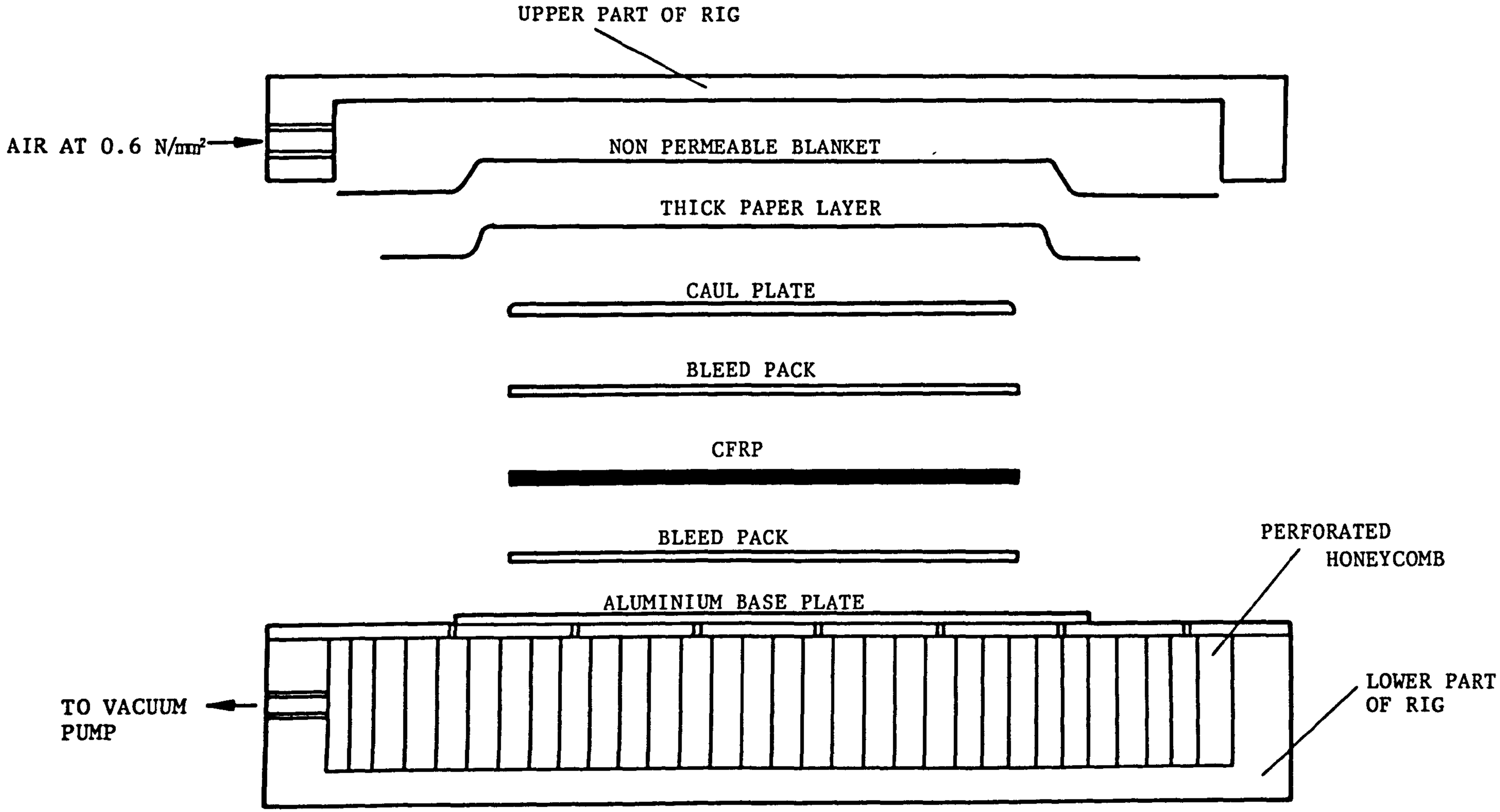

Fig. B.1 CFRP CURING RIG AND LAYUP

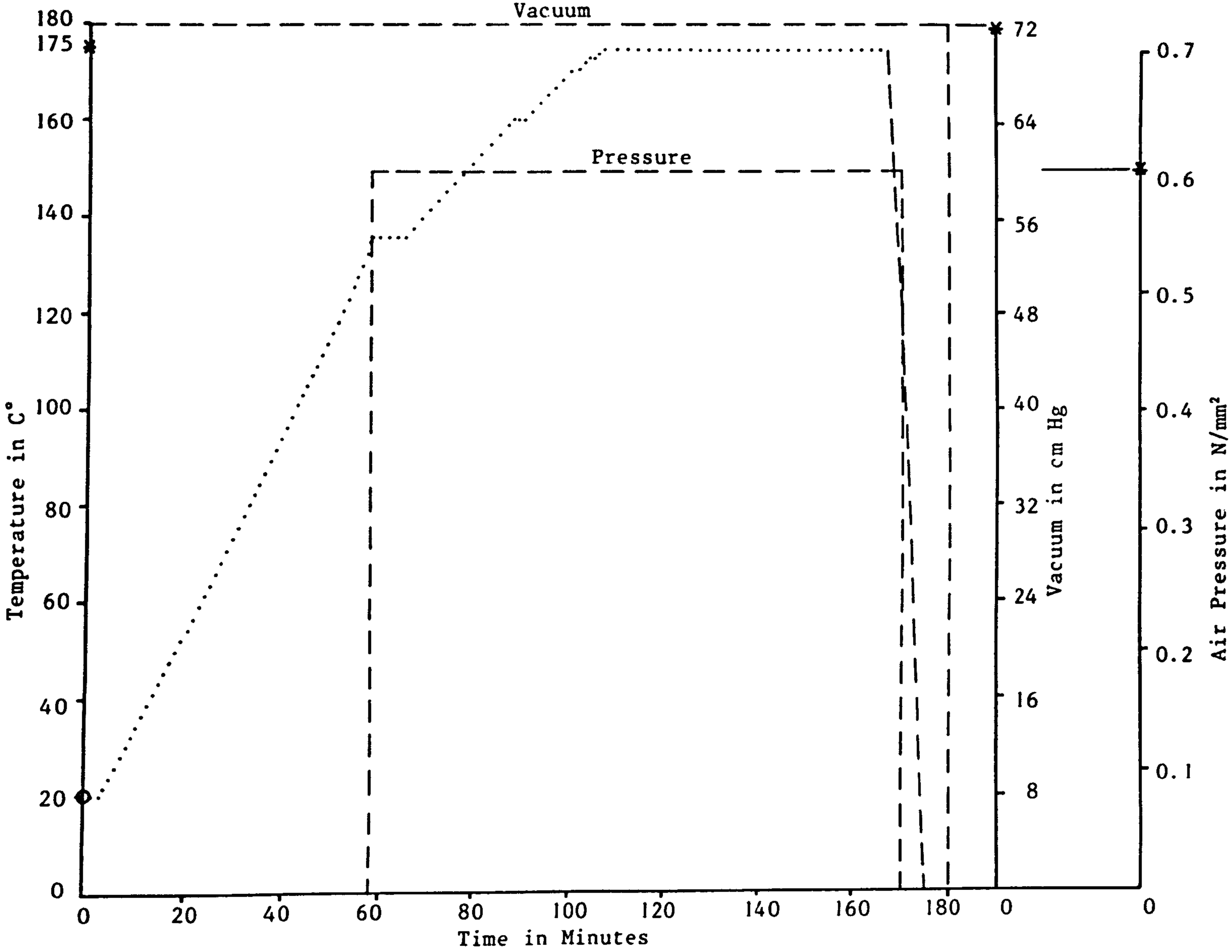

Fig. B.2 CURE CYCLE FOR CFRP PLATES

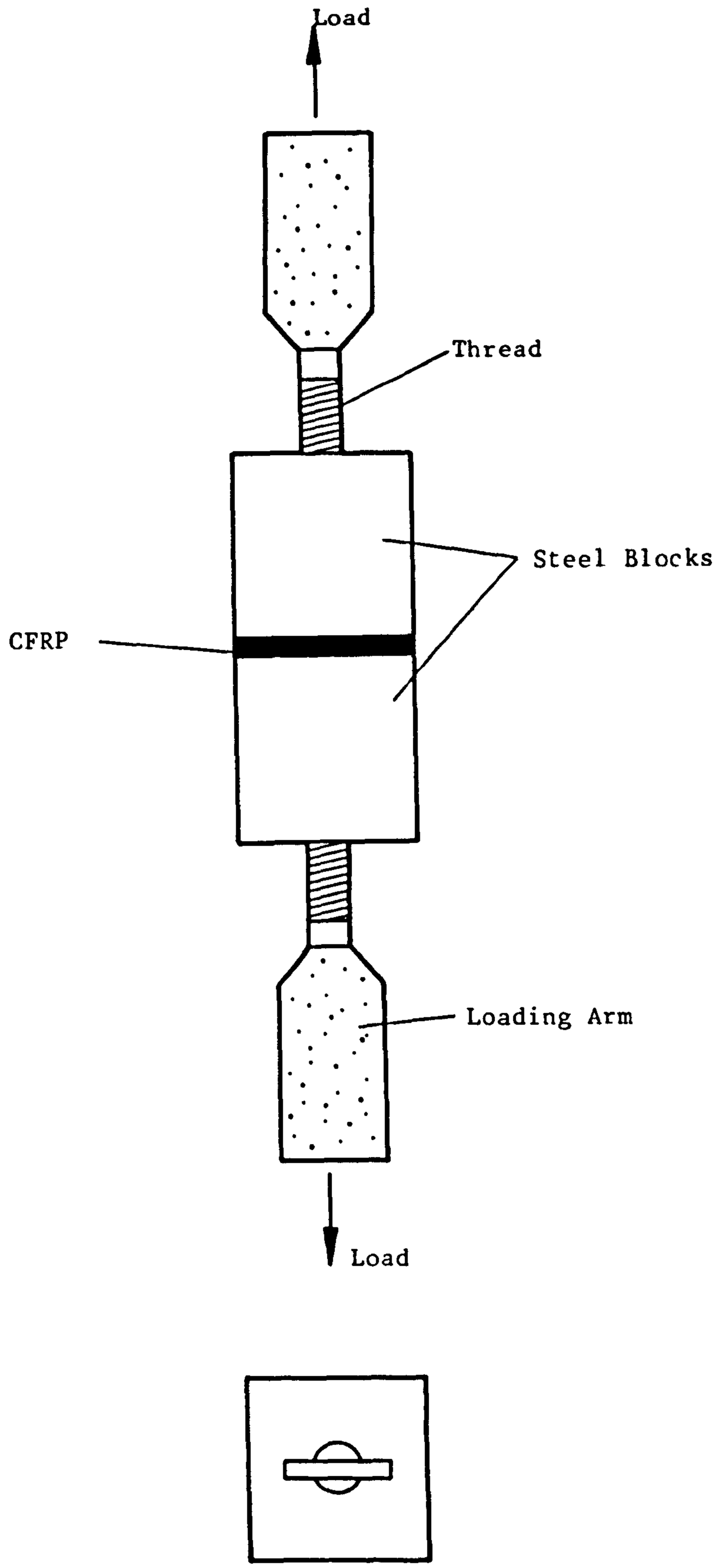

Fig. B.3 BUTT-JOINT TYPE FOR MEASURING THE STRENGTH OF ADHESIVES

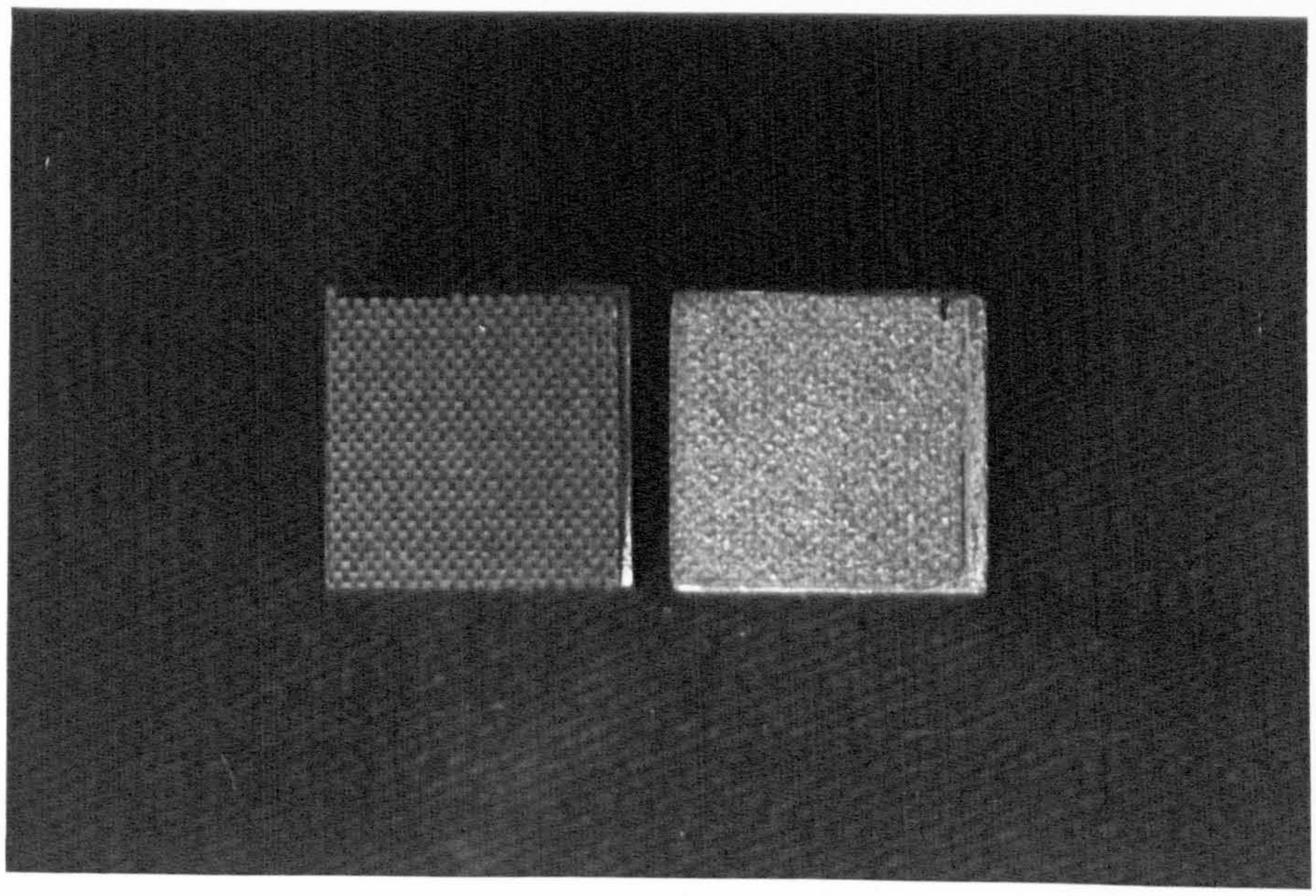

PLATE B.1
FEATURES OF SURFACE OF FRACTURE FOR ADHESIVE TYPE FAILURE

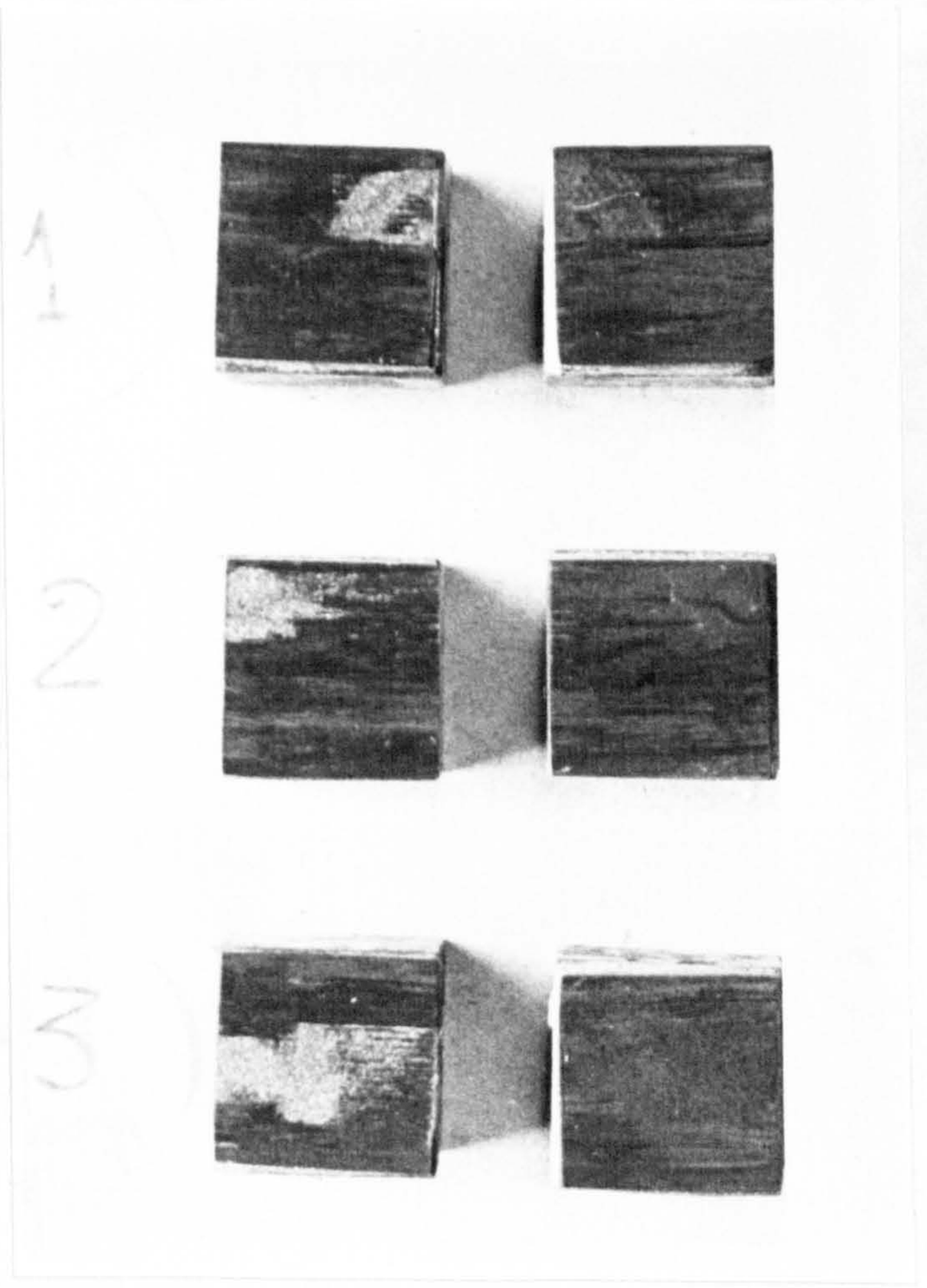

PLATE B.2
INTERLAMINAR TYPE FAILURE (OBTAINED USING ARALDITE 2005 ADHESIVE SYSTEM)

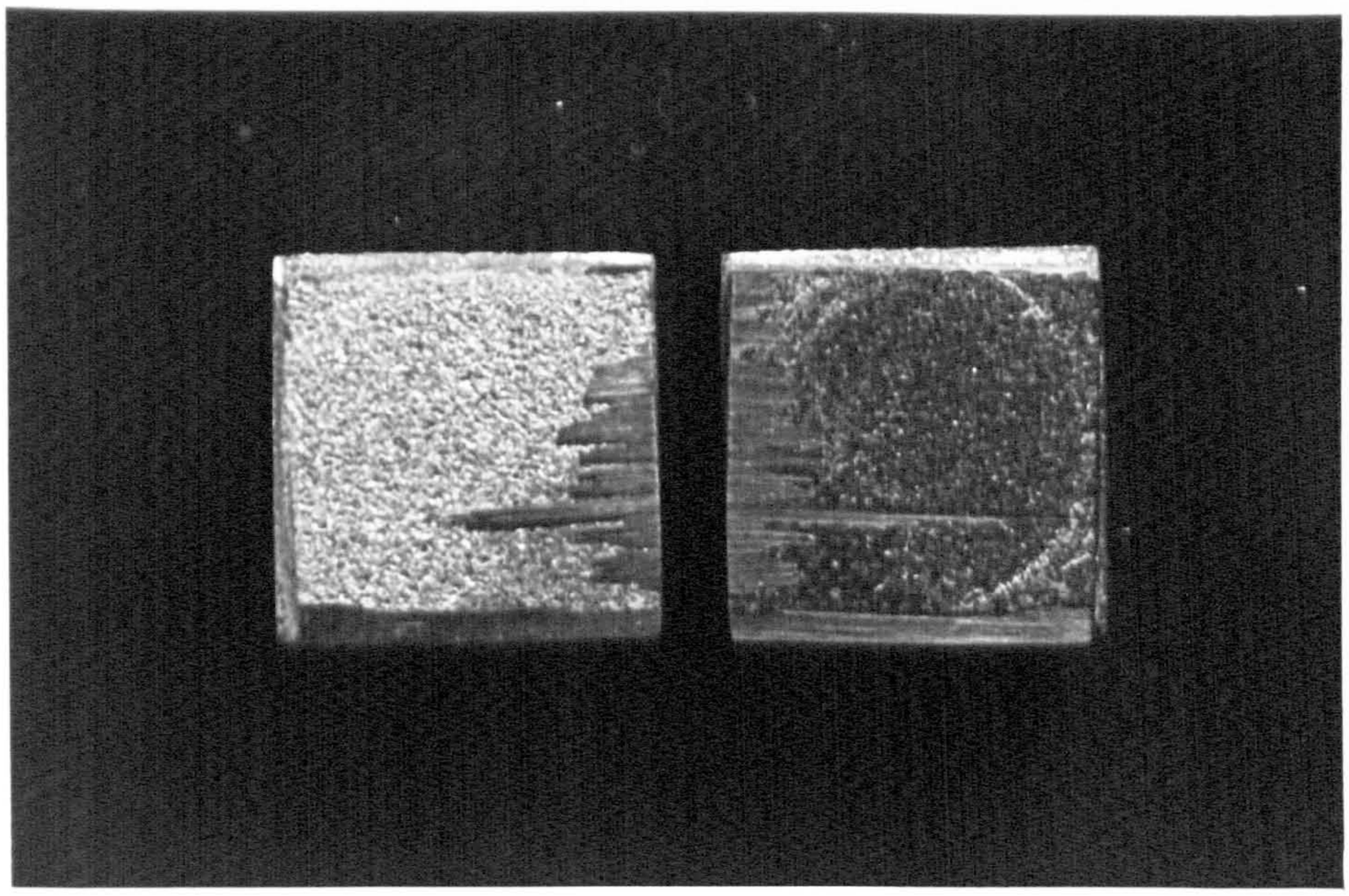

PLATE B.3
FEATURES OF SURFACE OF FRACTURE FOR ADHESIVE TYPE FAILURE

APPENDIX C

CALCULATION OF BLISTER PRE-LOADING SHAPE

*Figures

The initial blister shape (max. deflection at mid-span = 0.1mm) was calculated by employing the theoretical formula:

$$w_o = (\bar{\delta}_o/2)\,[1 + \cos(\pi x/a)] \qquad C.1$$

to tailor the width of the PTFE stripes which were stacked across the CFRP fibres and interlayered as shown in Fig. C.1. An example is shown beside the figure for guidance.

Fig. C.2 gives typical drawing details for the caul plate used in curing the blister CFRP boards.

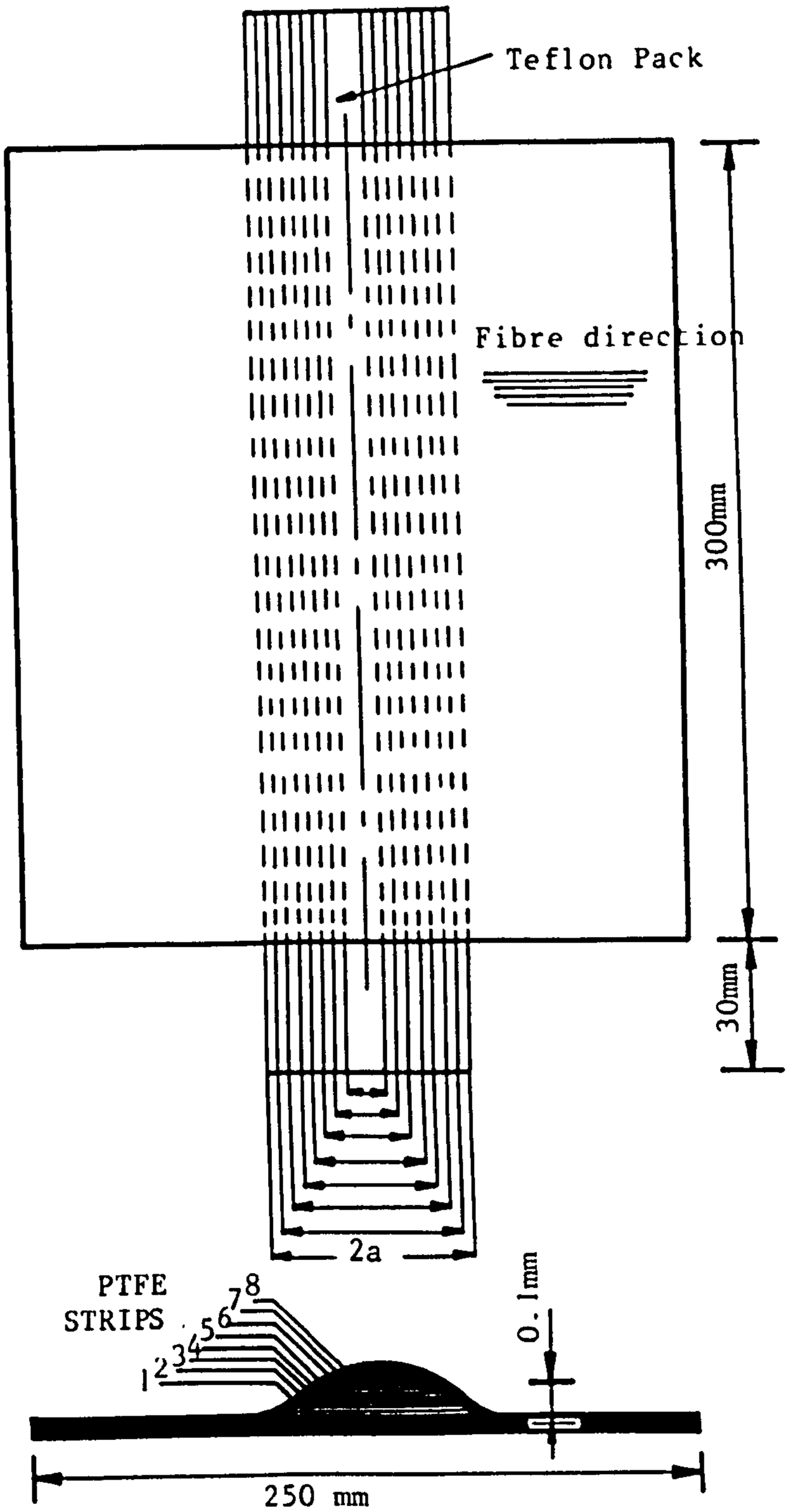

$w_o = (\bar{\delta}_o/2)[1+\cos(\pi x/a)]$ or

$x = \frac{a}{\pi} \arccos(0.25n_{stp}-1)$

n_{stp} = number of strips

Thickness of PTFE = 0.0125mm

Dimensions of PTFE strips

a = 16mm

Strip No.	Strip Width In (mm)
1	32
2	21.3
3	18.6
4	16
5	13.4
6	10.7
7	7.4
8	3.2

Fig. C.1 CFRP BLISTERED BOARD THE BOTTOM PTFE STRIP (No. 1) HAS ITS WIDTH = THE BLISTER SPAN

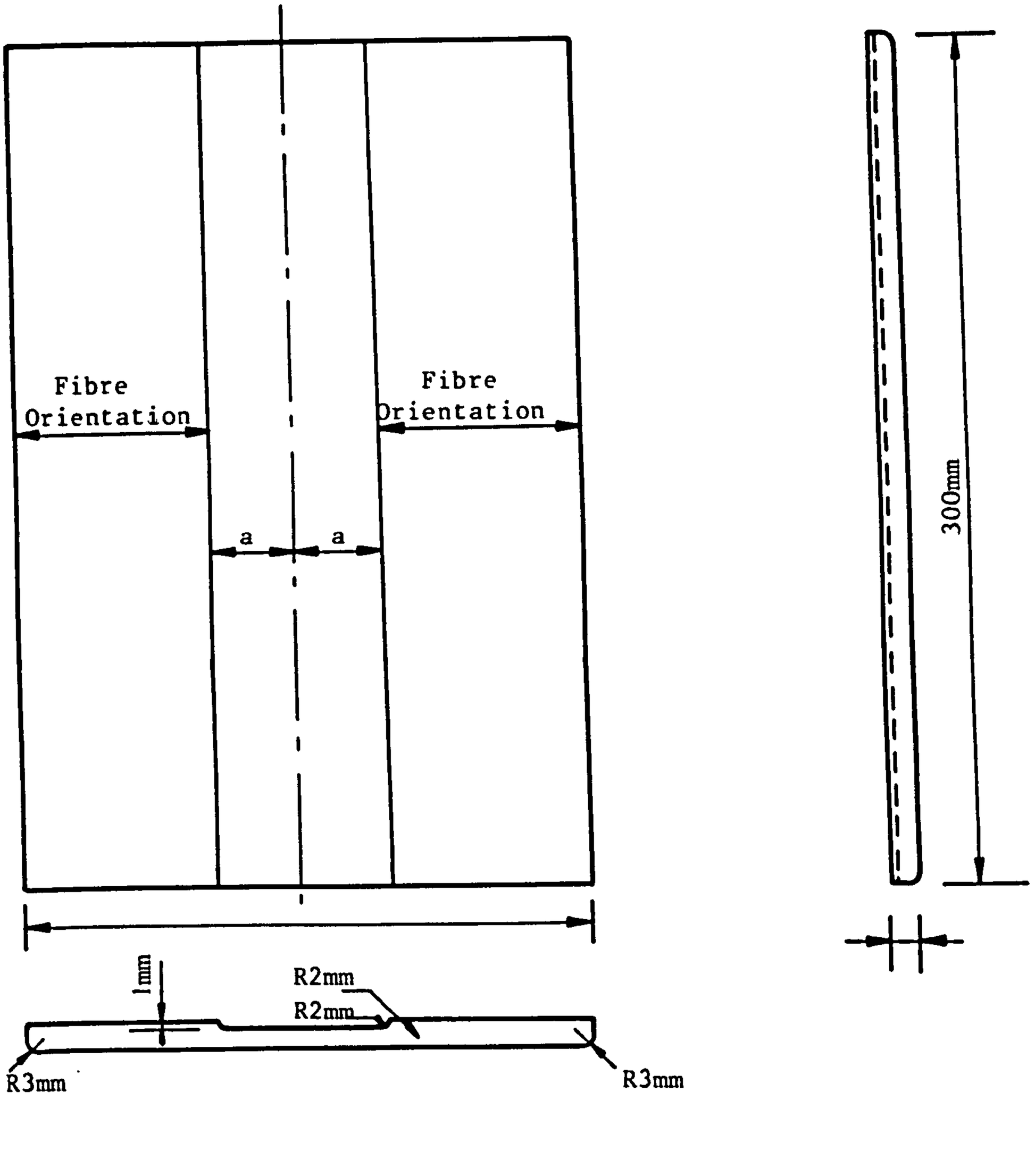

Fig. C.2 GROOVED CAUL PLATE FOR CURING BLISTER CFRP BOARDS

MATERIAL: MILD STEEL 3/16"

REFERENCES

1. Brown, D.S., Eckert, C.H., Kline, C.H., Advanced Polymer Composites - Five Keys to Success. Materials & Design, Vol. 6, No. 5, Oct./Nov. 1985, pp. 203-206.

2. Butler, B.M., Structures. Aerospace America, Dec. 1985, p. 48.

3. Gerharz, J.J., Application of Fibre Composite Materials. RAE Libarary Translation 2045 (Literature Research on the Mechanical Properties of Fibre Composite Materials - Analysis of the State of the Art -), Published by J.J. Gerharz and D. Schütz, Vol. 1, Sec. 11, Aug. 1980.

4. Hadcock, R., Huber, J., Specific Examples of Aerospace Applications of Composites. AGARD Lecture Series No. 124. (Practical Considerations of Design, Fabrication and Tests for Composite Materials), Sec. 12, Oct. 1982.

5. King, R.L., A Production Engineers View of Advanced Composite Materials. Materials & Design, Vol. 3, Aug. 1982, pp. 515-522.

6. The American Institute of Aeronautics and Astronautics, Materials. Aerospace America, Dec. 1985, pp. 50-51.

7. Gerharz, J.J., Mechanical Properties Under Static Loading. RAE Library Translation 2045 (Litrature Research on the Mechanical Properties of Fibre Composite Materials - Analysis of the State of the Art -), Published by J.J. Gerharz and D. Schütz, Vol. 1, Sec. 1, Aug. 1980.

8. Gerharz, J.J., Mechanical Properties under Repeated Loading. RAE Library Translation 2045 (Literature Research on the Mechanical Properties of Fibre Composite Materials - Analysis of the State of the Art -), Published by J.J. Gerharz and D. Schütz, Vol. 1, Sec. 2, Aug. 1980.

9. Gerharz, J.J., Conclusions and Outlooks. RAE Library Translation 2045 (Literature Research on the Mechanical Properties of Fibre Composite Materials - Analysis of the State of the Art -), Published by J.J. Gerharz and D. Schütz, Vol. 1, Sec. 12, Aug. 1980.

10. King, R.L., A Production Engineers Viw of Advanced Composite Materials; Part 2 - The Manufacture of Advanced Composites, Components and Structures -. Materials & Design, Vol. 3, Oct. 1982, pp. 580-588.

11. Bishop, S.M., The Significance of Defects on Failure of Fibre Composites. AGARD Report No. 690, Sept./Oct. 1981.

12. El-Senussi, A.K., Webber, J.P.H., Blister Delamination Analysis in Fibre Reinforced Plastics using Beam-Column Theory with an Energy Release Rate Criterion. Composite Structures, Vol. 5, No. 2, 1986, pp. 125-142.

13. Goree, J.G., Wolla, J.M., Longitudinal Splitting in Unidirectional Composites, Analysis and Experiments. NASA Contractor Report 3881, April 1985.

14. Dorey, G., Fracture of Composites and Damage Tolerance. AGARD Lecture Series No. 124 (Practical Considerations of Design, Fabrication and Tests for Composite Materials), Sec. 6, Oct. 1982.

15. Huth, H., Use of Fracture Mechanics for Fibre Composite Materials. RAE Library Translation 2045 (Literature Research on the Mechanical Properties of Fibre Composite Materials - Analysis of the State of the Art -), Published by J.J. Gerharz and D. Schutz, Vol. 1, Sec. 5, Aug. 1980.

16. Ramani, S.V., Wiliams, D.P., Notched and Unnotched Fatigue Behaviour of Angle-Ply Graphite/Epoxy Composites. ASTM STP 636 (Fatigue of Filamentary composite Materials), 1977, pp. 27-46.

17. Chang, F.H., Gordon, D.E., Gardner, A.H., A Study of Fatigue Damage in Composites by non Destructive Testing Techniques. ASTM STP 636 (Fatigue of Filamentary Composite Materials), 1977, pp. 57-72.

18. Porter, T.R., Evaluation of Flawed Composite Structure under Static and Cyclic Loading. ASTM STP 636 (Fatigue of Filametary Composite Materials), 1977, pp. 152-170.

19. Walter, R.W. et al., Designing for Integrity of Long-Life Composite Aircraft Structures. ASTM STP 636 (Fatigue of Filamentary Composite Materials), 1977, pp. 228-247.

20. Morris, G.E., Hetter, C.M., Fractographic Studies of Graphite/Epoxy Fatigue Specimens. ASTM STP 775 (Damage in Composite Materials), Nov. 1980, pp. 27-39.

21. Badaliance, R., Dill, H.D., Damage Mechanism and Life Prediction of Graphite/Epoxy Composites. ASTM STP 775 (Damage in Composite Materials), Nov. 1980, pp. 229-242.

22. Wang, S.S., Delamination Crack Growth in Unidirectional Fibre-Reinforced Composites under Static and Cyclic Loading. ASTM STP 674 (Composite Materials: Testing and Design - Fifth Conference -), March 1978, pp. 642-663.

23. Greszczuk, L.B., Stress Concentrations and Failure Criteria for Orthotropic and Anisotropic Plates with Circular Openings. ASTM STP 497 (Composite Materials: Testing and Design - Second Conference -), April 1971, pp. 363 - 381.

24. Kocher, L.H., Cross, S.L., Reinforced Cutouts in Graphite Composite Structures. ASTM STP 497 (Composite Materials: Testing and Design - Second Conference -), April 1971, pp. 382-395.

25. Lo, K.H., Wu, E.M., Konishi, D.Y., Failure Strength of Notched Composite Laminates. J. Comp. Materials, Vol. 17, Sept. 1983, pp. 384-398.

26. Pagano, N.J., Pipes, R.B., Some Observations on the Interlaminar Strength of Composite Laminates. Int. J. Mechanical Sciences, Vol. 15, 1973, pp.679-688.

27. Rybicki, E.F., Schmueser, D.W., Fox, J., An Energy Release Rate Approach for Stable Crack Growth in Free-Edge Delamination Problem. J. Comp. Materials, Vol. 11, Oct. 1977, pp. 470-487.

28. O'Brien, T.K., Characterization of Delamination Onset and Growth in a Composite Laminate. ASTM STP 775 (Damage in Composite Materials), Nov. 1980, pp. 140-167.

29. El-Senussi, A.K., Webber, J.P.H., Critical Energy Release Rate during Delamination of Carbon Fibre Reinforced Plastic Laminates. J. of Strain Analysis, 1986 (submitted for publication).

30. Whitcom, J.D., Finite Element Analysis of Instability Related Delamination Growth. J. Comp. Materials, Vol. 15, Sept. 1981, pp. 403-426.

31. Konishi, D.Y., Johnston, W.R., Fatigue Effects on Delaminations and Strength Degradation in Graphite/Epoxy Laminates. ASTM STP 674 (Composite Materials: Testing and Design - Fifth Conference -), March 1978, pp. 597-619.

32. Brock, D., Elementary Engineering Fracture Mechanics, Noordhoff, 1974.

33. El-Senussi, A.K., Webber, J.P.H., On Double Cantilever Beam Technique for Studying Crack Propagation. J. Appl. Physics, Vol. 56, No. 4, 15 Aug. 1984, pp. 885-889.

34. Gurney, C., Hunt, J., Quasi-Static Crack Propagation. Proc. Roy. Soc., London, Series A, Vol. 299, 1967, pp. 508-524.

35. Obreimoff, J.W., The Splitting Strength of Mica. Proc. Roy. Soc., London, Vol. 127, Series A, June 1930, pp. 290-297.

36. Benbow, J.J., Roesler, F.C., Experiments on Controlled Fractures. Proc. Phys. Soc., Series B, Vol. 70, 1957, pp. 201-211.

37. Benbow, J.J., Stable Crack Propagation in Plastics. Proc. Phys. Soc., Vol. 78, 1961, pp. 970-978.

38. Gilman, J.J., Direct Measurements of the Surface Energies of Crystals. J. Appl. Phys., Vol. 31, No. 12, Dec. 1960, pp. 2208-2218.

39. Gillis, P.P., Gilman, J.J., Double-Cantilever Cleavage Mode of Crack Propagation. J. Appl. Phys., Vol. 35, No. 3, March 1964, 647-658.

40. Gillis, P.P., Surface Energy Determinations by Cleavage. J. App. Phys., Vol. 36, No. 4, April 1965, pp. 1374-1376.

41. Srawley, J.E., Gross, B., Stress Intensity Factors for Crackline - Loaded Edge-Crack Specimens. Materials Research & Standards, Vol. 7, April 1967, pp. 155-162.

42. Weiderhorn, S.M., Shorb, A.M., Moses, R.L., Critical Analysis of the Theory of the Double Cantilever Method of Measuring Fracture-Surface Energies. J. Appl. Phys., Vol. 39, No. 3, Feb. 1968, pp. 1569-1572.

43. Burns, S.J., Lawn, B.R., A Simulated Crack Experiment illustrating the Engergy Balance Criterion. Int. J. Fracture Mech., Vol. 4, No. 3, Sept. 1968, pp. 339-345.

44. Ripling, E.J., Mostovoy, S., Corten, H.T., Fracture Mechanics: A Tool for Evaluating Structural Adhesives. J. Adhesion, Vol. 3, 1971, pp. 107-123.

45. Raasch, J., On the Determination of Surface Energy from Cleavage Experiments. Int. J. Fracture Mech., Vol. 7, No. 3, Sept. 1971, pp. 289-300.

46. Kanninen, M.F., An Augmented Double Cantilever Beam Model for Studying Crack Propagation and Arrest. Int. J. Fracture, Vol. 9, No. 1, March 1973, pp. 83-92.

47. Kanninen, M.F., A Dynamic Analysis of Unstable Crack Propagation and Arrest in the DCB Test Specimen. Int. J. Fracture, Vol. 10, No. 3, Sept. 1974, pp. 415-430.

48. Gehlen, P.C., Popelar, C.H., Kanninen, M.F., Modelling of Dynamic Crack Propagation: I. Validation of One-Dimensional Analysis. Int. J. Fracture, Vol. 15, No. 3, June 1979, pp. 281-294.

49. Gates, R.S., Calculation of Stress Intensity Factors for a Double Cantilever Beam Specimen. Int. J. Fracture, Vol. 13, 1977, pp. 710-713.

50. Chow, C.L., Woo, C.W., Fracture Studies with DCB Sepcimen. Int. J. Fracture, Vol. 16, No. 2, April 1980, pp. 121-131.

51. Bonesteel, R.M., Piper, D.E., Davinroy, A.T., Compliance and K_I Calibration of Double Cantilever Beam (DCB) Specimens, Eng. Fracture Mech., Vol. 10, 1978, pp. 425-428.

52. Green, D.J., Hawkins, C.A., Hirlinger, M.M., Double-Cantilever-Beam Testing of a Transversely Isotropic Fibrous Silica Material. J. Am. Ceram. Soc., Vol. 60, No. 1, Jan. 1983, pp. 46-49.

53. Timoshenko, S., Theory of Elasticity. McGraw-Hill, New York, 1934.

54. Griffith, A.A., The Phenomena of Rapture and Flow in Solids. Phil. Trans. Roy. Soc., London, Series A, Vol. 221, March 1921, pp.163-198.

55. Boyd, G.M., From Griffith to COD and Beyond. Eng. Fracture Mech., Vol. 4, 1972, pp. 459-482.

56. Mai, Y.W., Atkins, A.G., Caddell, R.M., On the Stability of Cracking in Tapered DCB Testpieces. Int. J. Fracture, Vol. 11, No. 6, Dec. 1975, pp. 939-953.

57. Hopkins, R.B., Design Analysis of Shafts and Beams, McGraw-Hill, Inc., New York, 1970.

58. Paris, P.C., Sih, G.C., Stress Analysis of Cracks, ASTM STP 381, 1965, pp. 30-83.

59. Atkins, A.G., Lee, C.S., Caddell, R.M., Time-Temperature dependent Fracture Toughness of PMMA. J. Mat. Sci., Vol. 10, 1975, pp. 1381-1393.

60. Mai, Y.W., Atkins, A.G., On the Velocity-dependent Fracture Toughness of Epoxy Resins. J. Mat. Sci., Vol. 10, 1975, Letters, pp. 2000-2003.

61. Mai, Y.W., Atkins, A.G., Crack Stability in Fracture Toughness Testing. J. Strain Analysis, Vol. 15, No. 2, 1980, pp. 63-74.

62. Gurney, C., Mai, Y.W., Stability of Cracking. Eng. Fracture Mech., Vol. 4, 1972, pp. 853-863.

63. Clausing, D.P., Crack Stability in Linear Elastic Fracture Mechanics. Int. J. Fracture Mech., Vol. 5, No. 3, Sept. 1969, pp. 211-227.

64. Ripling, E.J., Mostovoy, S., Patrick, R.L., Measuring Fracture Toughness of Adhesive Joints. Materials Research & Standards, Vol. 4, March 1964, pp. 129-134.

65. Kanninen, M.F., Rybicki, E.F., Brinson, H.F., A Critical Look at Current Applications of Fracture Mechanics to the Failure of Fibre-Reinforced Composites. Composites, Vol. 8, No. 1, Jan. 1977, pp. 17-23.

66. Mostovoy, S., Ripling, E.J., Bersch, C.F., Fracture Toughness of Adhesive Joints. J. Adhesion, Vol. 3, 1971, pp. 125-144.

67. Fourney, M.E. et al., Role of Bond Thickness on Adhesive Failure. Polymer Eng. Sci., Vol. 19, No. 2, Feb. 1979, pp. 114-117.

68. Gledhill, R.A., Kinloch, A.J., Mechanics of Crack Growth in Epoxide Resins. Polymer Eng. Sci., Vol. 19, No. 2, Feb. 1979, pp. 82-88.

69. Phillips, D.C., Tetelman, A.S., The Fracture Toughness of Fibre Composites. Composites, Vol. 3, No. 5, Sept. 1972, pp. 216-223.

70. Marston, T.U., Atkins, A.G., Felbeck, D.K., Interfacial Fracture Energy and the Toughness of Composites. J. Mater. Sci., Vol. 9, 1974, pp. 447-455.

71. Selby, K., Miller, L.E., Fracture Toughness and Mechanical Behaviour of an Epoxy Resin. J. Mater. Sci., Vol. 10, 1975, pp. 12-24.

72. Bascom, W.D. et al., The Interlaminar Fracture of Organic-Matrix, Woven Reinforcement Composites. Composites, Vol. 11, No. 1, Jan. 1980, pp. 9-13.

73. Chai, H., The Characterization of Mode I Delamination Failure in non-Woven, Multidirectional Laminates. Composites, Vol. 15, No. 4, Oct. 1984, pp. 277-290.

74. Keary, P.E. et al., Mode I Interlaminar Fracture Toughness of Composites using Slender Double Cantilevered Beam Specimens. J. Comp. Materials, Vol. 19, March 1985, pp. 154-177.

75. Garg, A.C., Intralaminar and Interlaminar Fracture in Graphite/ Epoxy Laminates. Eng. Fracture Mech., Vol. 23, No. 4, 1986, pp. 719-733.

76. Ditcher, A.K., The non-Linear Stress-Strain Behaviour of Carbon Fibre Reinforced Plastic and its Effect on the Analysis of Laminated Plates and Sandwich Beams. Ph.D. Thesis, March 1981, Aero. Eng. Dept., University of Bristol, U.K.

77. Instron Crack Opening Displacement (C.O.D.) Gauges. Catalogue Numbers: 2670-002, 2670-004 and 2670-006, Manual 1-7-68-2, Instron Lit., Coronation Rd., High Wycombe, Buckinghamshire, U.K.

78. Olster, E.F., Jones, R.C., Toughening Mechanisms in Continuous Filament Unidirectionally Reinforced Composites. Composite Materials: Testing and Design, 2nd Conference, ASTM STP 497, Anaheim, Calif., April 1971, pp. 189-205.

79 Russell, A.J., Street, K.N., Factors Affecting the Interlaminar Fracture Energy of Graphite/Epoxy Laminates. Progress in Science and Engineering of Composites, T. Hayashi, K. kawata & S. Umekawa, Ed., ICCM-IV, Tokyo, 1982, pp.279-285.

80. Gerharz, J.J., Mechanisms of Fatigue Damage and Fatigue Testing. AGARD-LS. 124 (Practical Considerations of Design, Fabrication and Tests for Composite Materials), Oct. 1982, Sec. 7.

81. Stalnaker, D.O., Stinchcomb, W.W., Load History-Edge Damage Studies in Two Quasi-Isotropic Graphite Epoxy Laminates. Composite Materials: Testing and Design, 5th Conference, ASTM STP 674, March 1978, pp. 620-641.

82. Wilkins, D.J. et al., Characterizing Delamination Growth in Graphite-Epoxy. Damage in Composite Materials, ASTM STP 775, Nov. 1980, pp. 168-183.

83. Ewalds, H.L., Wanhill, R.J.H., Fracture Mechanics, Co-publication of Edward Arnold (Lon.) and DUM (Delft, The Netherlands), 1984.

84. Chai, H., Babcock, C.D., Knauss, W.G., One Dimensional Modelling of Fracture in Laminated Plates by Delamination Buckling. Int. J. Solids Structures, Vol. 17, No. 11, 1981, pp.1069-1083.

85. Bottega, W.J., Maewal, A., Delamination Buckling and Growth in Laminates. J. Appl. Mechs. (Transactions of the ASME), Vol. 50, March 1983, pp.184-189.

86. Evans, A.G., Hutchinson, J.W., On the Mechanics of Delamination and Spalling in Compressed Films. Int. J. Solids Structures, Vol. 20, No.5, 1984, pp.455-466.

87. Gillespie, J.W., Pipes, R.B., Compressive Strength of Composite Laminates with Interlaminar Defects. Composite Structures, Vol. 2, 1984, pp.49-69.

88. Williams, M.L., The Fracture Threshold for an Adhesive Interlayer. J. Appl. Polym. Sci., Vol. 14, 1970, pp.1121-1126.

89. Timoshenko, S.P., Gere, J.M., Theory of Elastic Stability. McGraw-Hill, New York, 1961.

90. Hetenyi, M., Beams and Plates on Elastic Foundations and Related Problems. Appl. Mechs. Reviews, Vol. 19, 1966, 95-102.

91. Chai, H., Knauss, W.G., Babcock, C.D., Observation of Damage Growth in Compressively Loaded Laminates. Proc. Soc. Exp. Stress Analysis (SESA), Vol. XL, 1983, pp.329-337.

92. Kunz, S.C., Beaumont, P.W.R., Microcrack Growth in Graphite Fiber-Epoxy Resin Systems During Compressive Fatigue. Fatigue of Composite Materials, STP S69, 1975, pp. 71-91.